Identification and Control of the Laser-based Synchronization System for the European X-ray Free Electron Laser

Vom Promotionsausschuss der
Technischen Universität Hamburg-Harburg
zur Erlangung des akademischen Grades
Doktor-Ingenieur (Dr.-Ing.)

genehmigte Dissertation

von
Dipl.-Ing. Michael Heuer

aus
Kleve

2017

1. Gutachter: Prof. Dr.-Ing. Gerwald Lichtenberg
2. Gutachter: Prof. Dr. Herbert Werner
3. Gutachter: Dr. Holger Schlarb

Vorsitzender des Prüfungsausschusses: Prof. Dr.-Ing. Arne Jacob

Tag der mündlichen Prüfung: 01.09.2017

So eine Arbeit wird eigentlich nie fertig, man muß sie für fertig erklären, wenn man nach Zeit und Umständen das Möglichste getan hat.

(Johann Wolfgang von Goethe)

C

D

Abstract

The European X-ray Free-Electron Laser is currently under construction at the Deutsches Elektronen Synchrotron in Hamburg, Germany. This linear accelerator, with a length of 3.4 km, will generate extremely intense and short X-ray laser light pulses with a duration in the femto-second range and wavelengths down to 0.05 nm. These laser pulses provide physicists with a light source to take a closer look into small structures on atomic scale.

Those precise measurements require timing with an error margin in the femto-second range for most subsystems within the facility. Usually, this timing signal is distributed electrically via coaxial cables. With the new requirements in timing, this kind of distribution is no longer suitable and a new laser-based synchronization system is used. This system generates a laser pulse train via a master laser oscillator and distributes this via optical fiber to multiple end-stations in the facility. The effective length of the optical path inside the fiber is actively stabilized by a link stabilizing unit.

This thesis analyzes this new system from a control point of view. It is shown that the master laser oscillator can be modeled by an integrator, with the $\mathcal{H}_2$ norm as the performance criteria and two filters corresponding to the noise and disturbances of the master laser oscillator itself as well as the electrical oscillator of the facility. Those influences, as well as the dynamic behavior of the master laser oscillator, are identified for a laboratory setup. With these models in hand, different controllers are designed and experimentally evaluated. A sufficient controller performance can be achieved by a PI controller. However, using a feedback controller with a model-based optimization increase this performance, but these require a high order of the controller, which is currently not implementable given the installed hardware.

The second part of this work analyses the link stabilizing units. This is achieved with an attached optical fiber and a timing measurement by an optical cross correlator. If a short optical fiber is connected the system can be approximated by a third order system with a time delay of a few sample. A model is identified and used for controller design. It can be shown that a performance increase by factor of 4.5 can be achieved if an LQG controller, including a model of the time delay, is used instead of the previously used PI controller. Moreover, different approaches for long optical fibers and the operation in the non-linear region of the sensor are shown. These could not be tested in an experiment.

The work closes with an analysis of the overall system and gives suggestions of how to increase the performance of the individual components and of the whole laser-based synchronization system including the attached devices. It will be shown that the optimal performance can be achieved if all systems are connected to the laser-based synchronization system and if the dynamic behavior of the link stabilizing unit and end-station is equal for all subsystems.

F

Contents

J

1 INTRODUCTION

Over the last decades, more and more effort is put into the development of particle accelerators. Projects like the LHC at CERN, the world's largest accelerator, are present in public media.

At the Deutsches Elektronen Synchrotron (DESY), in Hamburg, Germany, two of the current projects are: the Free Electron Laser Hamburg (FLASH) and the European X-ray Free Electron Laser (XFEL) operated by the European XFEL GmbH. The aim of those two facilities is to generate high intensity X-ray laser pulses from an accelerated electron beam. These pulses provide physicist the possibility to take a closer look into small structures on an atomic scale. It will be possible to reveal how complex biomolecules are assembled or even to film the folding and formation of such molecules, [Alt+07].

The smaller accelerator, FLASH, is already in operation for user experiments, and served as experience for the construction of its bigger counterpart, the XFEL. FLASH has a total length of about 315 m with an accelerator section of 150 m. The beam energy goes up to 1.2 GeV and the X-ray laser light has a wavelength down to 4.1 nm, which is the order of molecules. The designed wavelength for the XFEL goes down to 0.05 nm, the order of atoms. To achieve such a wavelength, the required beam energy goes up to 17.5 GeV, the required accelerator length increases to 1.7 km, and the overall length of the facility will be 3.4 km. This is not just a scaling up in the size by a factor of more than ten, e. g. from seven accelerator modules at FLASH to 101 at XFEL, but also of the complexity of the system.

The demanding properties of the X-ray light imply strong control performance requirements for the accelerator section. A lot of different devices all over the facility are participating in the control of the electron beam. To meet the requirements, precise timing between these devices is essential. The increasing size of the facility makes it harder to synchronize these systems in a conventional way, such as with an electrical signal (e.g. distributed via coaxial cables). The synchronization signal needs to be frequently amplified for long distances in the kilometer-range, due to the attenuation of the cables. This additional noise source would add to the timing signal. For this reason, a laser-based synchronization system was proposed in [Kim+04]. Based on this idea, the so-called Laser-based Synchronization (LbSync) system was implemented for FLASH and will be implemented for XFEL ([Win08], [Sch11] and [Sch+13]).

Although this system is cited in more than one hundred publications, it was not analyzed from a control point of view. Thus this work will focus on introducing the control for the LbSync system. The main performance requirements are explained, models for the subsystems are developed, and first control strategies are analyzed.

1.1 Motivation and Research Questions

Presently, the controllers needed for the operation of the LbSync system are heuristically tuned PI controllers. These controllers are not necessarily working at the global optimum of the given performance criterion. This raises the question: can the performance and robustness of the system can be increased by an optimized set of parameters or the usage of modern model-based control techniques?

This is the motivating question for this work. Simple control schemes like PID controller are the dominant types used in industry, [TIA98]. For simple SISO systems, or MIMO systems which can be decoupled, those controllers are a reasonable start and experienced engineers can get suitable results with them. Nevertheless, if the system is more complex or if the edge of the performance limits must be reached, model-based controllers should be used.

These controllers are based on a mathematical description of the system, the so-called plant model, which is to be controlled. The first step in the controller design is to define performance requirements, the closed loop system should fulfill. After that, a model of the plant is identified within the frequency regions of interest. With the model it is possible to design a proper control algorithm that addresses special properties of the plant and the performance requirements. If the final setup does not fulfill the expectations, it is necessary to tune the controller, increase the model accuracy or it could be possible that the requirements can not be reached with the given hardware.

These tasks should be performed for the LbSync system, and the following questions should be answered in this thesis:

1. What are the control challenges of such a system?
2. What is a good model of the Laser-based Synchronization System?
3. Which controller design techniques are suitable for different components?
4. Are there extensions to easily increase the performance?
5. Are there ways to increase the robustness of the different components?
6. What is the optimal solution to control the overall system?

1.2 Structure and Contribution of this Thesis

This work introduces the LbSync system to the control theory community, and explains the systems and the performance measures. Furthermore, it shows how to model such a system and gives inital approaches and methods for the control design. For the benefit of readers with a non-control theory background, important aspects on applied feedback control are emphasized and basic design strategies are shown.

This work is organized as follows: The second chapter explains the LbSync system in more detail, and introduces the hard-, firm-, and software that will be employed. The induced control related properties of these are briefly explained and addressed in the later system analysis and controller design. This work contributes as an inital application and proof of concept for a new firmware rapid prototyping toolset based on MATLAB/Simulink and Xilinx, which was introduced in [Pre+15].

Chapter 3 introduces the required theory. The general control loop is explained as well as the behavior of Analog to Digital Converters (ADCs), Digital to Analog Converters (DACs), and piezoelectric actuators. Moreover, it is shown how the calculation constraints induced by the chosen hardware can be modeled, and gives an introduction in controller design techniques.

Chapter 4 focuses on one of the main LbSync components, the Master Laser Oscillator (MLO). The basic functionality of this system is explained as well as the modeling of the generated laser pulse train. With this, a mathematical model can be identified. The main performance criterion for this system is the minimization of the timing jitter. The modeling of the relevant disturbance and noise sources are analyzed and published in [Heu+14b]. The second part of Chapter 4 focuses on the controller design, and shows the optimization of the performance criterion. The chapter closes with an experimental validation, performed on the final hard- and firmware [Heu+15a; Heu+16].

The second component of the LbSync system, the Link Stabilizing Unit (LSU), is analyzed in Chapter 5. After a brief introduction, the modeling of the dynamic behavior, the characteristic properties and approximations for short and long connected fibers, are shown. The second part focuses on the controller design if the attached fiber link is short [Heu+14a]. Different controller design techniques are discussed and the results of the chosen approaches are shown. The last part of the chapter investigate the changes if long fiber are attached.

The combination of the master laser oscillator, multiple link stabilizing units, and the behavior of this combination is studied in the last chapter. The final goal of the LbSync system is not to optimize the timing jitter of each individual link, but to minimize the timing jitter between these. The influences to this relative jitter is analyzed, and the chapter closes with an global controller design approach.

Possible improvements to the overall system and directions to focus on in subsequent works are discussed in the outlook.

2 OVERVIEW

2.1 European X-ray Free Electron Laser

One of the planned experiments at the XFEL is recording a video of biomolecules [Gün+11]. Such experiments require a small wavelength, and thus high beam energy, which leads to the large number of accelerator modules and the size of the facility, illustrated in Fig. 2.1.

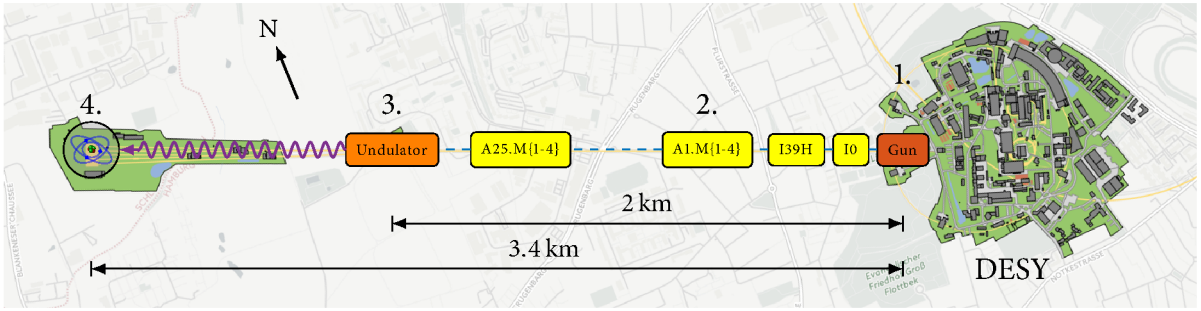

Figure 2.1: Overview of the European XFEL and its surrounding area, see [DM].

The so-called electron gun (1.) triggers the detachment of electrons. This electron bunch, with a charge up to 1 nC, is accelerated by 101 superconducting cryomodules (I0, I39H, A1.M{1-4}, …, A25.M{1-4}) (2.) up to its final energy and a velocity close to the speed of light [Sch10]. At the end of the 2 km long accelerator, the bunch is guided through the undulator (3.), a periodic arrangement of magnets, which forces the electron bunches on a sinusoidal trajectory. This causes the so-called Self-Amplified Spontaneous Emission (SASE) process generating the high energy X-ray laser pulse. These are used in the experiments (4.) at the end of the 3.4 km facility.

To conduct the planned experiments,there are demanding requirements on the electron beam. To meet these, a beam-based feedback is used, requiring the interaction of different spatially distributed subsystems, see [Pfe+12]. On the other hand, the experiment has to be triggered and sampled at an exact time difference.

Thus, a precise synchronization of all subsystems within the XFEL is crucial to achieve the high performance demand. The main timing reference source for the facility is an electrical oscillator with a frequency of 1.3 GHz, the so-called Master Oscillator (MO). Its synchronization signal is distributed by coaxial cables or by the LbSync system to the different subsystems.

2.2 Laser-based Synchronizahosetion System

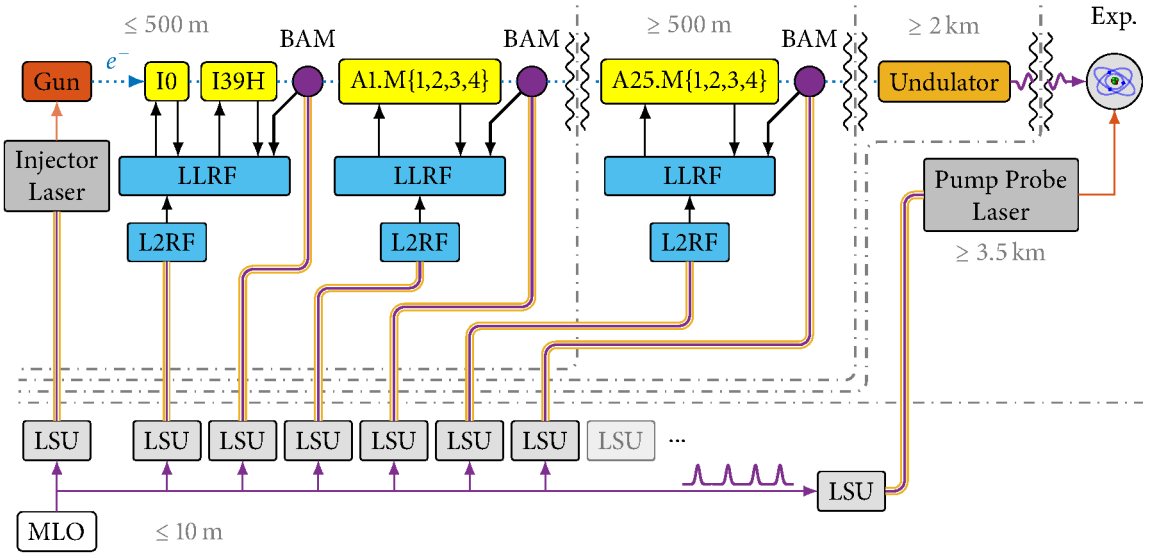

Figure 2.2: Overview of the European XFEL and the laser-based synchronization system.

A simplified diagram of the laser-based synchronization system, connected to various devices in the beamline, is given in Fig. 2.2. In order to accelerate the electron bunch and imprint the required properties, the Low-Level Radio Frequency (LLRF) system controls the amplitude and phase of the acceleration fields in the cryomodules (A{1-25}.M{1,2,3,4}). To increase the performance of this control loop, the Bunch Arrival Time Monitor (BAM) measures the relative time of electron bunches crossing a certain position in the beamline, [Boc12], which is used as a feedback signal for the LLRF system, [Pfe+12]. To get an optimal result, the LLRF system should have a common timing with the BAM.

To provide this precise timing, a laser-based synchronization system is used. It consists of two main parts. The MLO, which generates a laser pulse train at a frequency of 216.67 MHz[1] and the LSU, which stabilizes the optical length of fiber used to distribute the pulse. The MLO and up to 24 LSU are placed on an optical table, where a free-space distribution splits the pulse train and guides it to the LSUs.

Inside the LSU the laser pulse is coupled into a fiber. Due to the high repetition rate and the long spatial extension of the fiber, the arrival time of the pulse train is very sensitive to stress, temperature or humidity changes acting on the fiber. Those disturbances would result in a timing change in the attached device, called timing jitter for high and drift for low frequencies. For this reason, the LSU measures the traveling time inside the fiber and compensates for these changes. This stabilized fiber is connected to the different end-stations like the BAM or the Laser to Radio Frequency (L2RF) converter, which connects the LLRF system.

[1]The sixth harmonic of this fits to the main MO frequency at 1.3 GHz

Figure 2.3: Origami-15 Laser Oscillator.

Table 2.1: Technical specification Origami-15

Description	Value	Unit
Repetition rate	216.67	MHz
Pulse duration	< 200	fs
Wavelength	1550	nm

2.2.1 Master Laser Oscillator

The MLO generates the laser pulse train used to distribute the synchronization signal. A mode-locked laser built by *OneFive GmbH* is used and offers a constant pulse shape, a stable amplitude, and a low timing jitter, [ORIG15]. The frequency of the pulse train can be tuned by a piezo crystal, which changes the cavity length of the laser and so the distance between the pulses. This actuator has a high bandwidth, but a low dynamic range. A second input sets the reference for an internal temperature controller which allows it to tune the frequency in a larger range but with a much lower bandwidth. Some relevant numbers are given in Table 2.1.

If the laser is activated, the frequency of the pulse train is usually far away from the required frequency of 1/6 of the MO frequency and the range of the piezo actuator is not sufficient to compensate for this. For this reason, the secondary input is used. If the frequency of the laser is driven close to the operation range, the control loop of the piezo crystal is closed. As a first error signal, the phase of the 216.67 MHz signal, measured with a photo diode from the pulse train, is used. If this error signal approaches zero, the control input is switched to the phase of the 7-th Harmonic of this signal, which has a higher sensitivity but it is not distinct. This means that this signal approaches zero at multiple phase offsets of the lower frequency, the so-called buckets. Common control related problems of the MLO system are:

The system can not be locked: The closed loop can not be stabilized with the given control parameter.

The laser lock is lost: The controller is turned off due to some unexpected behavior, e. g. if the Root Mean Square (RMS) of the error signal reaches an upper limit.

The laser is in a wrong bucket: Due to the ambiguity of the detection scheme, the control loop stabilizes the laser to a different stable phase, which results in a constant phase offset with respect to the MO.

If possible, the design of the controller should address these problems. All of them result in an error, which can render a user's experiments invalid. The modeling of this device is shown in Sec. 4.1 and the controller design in Sec. 4.2

Figure 2.4: LSU measurement unit.

Table 2.2: Technical specification LSU

Description	Value	Unit
Detector Sensitivity	0.5 . . . 5	$\frac{V}{ps}$
Piezo Sensitivity	19	$\frac{fs}{V}$
Max. Piezo Displacement	2.592	mm
Motor Sensitivity	1	$\frac{fs}{Step}$
Max. Motor Displacement	5.040	m

2.2.2 Link Stabilizing Unit

The optical fibers in the accelerator tunnel are exposed to vibrations, temperature and humidity changes. These disturbances change the optical length of the fiber and thus the arrival time of the pulse at the end station. In response to this, the other major component of the LbSync system, the LSU, is used to stabilize the optical length of a fiber. This is done by optical cross-correlation of the pulses going into the fiber and pulses that are reflected at the end and traveling back to the LSU. If both pulse trains are overlapping, the length of the fiber is a multiple of half the pulse train period. The measurement part is shown in Fig. 2.4 and the control related specification in Table 2.2.

The setup of the device also involves different steps. The sensor only works in a very narrow range. An outer control loop, the coarse tuning, moves the system to the working point of the sensor. This is done via a Motorized Delay Line (MDL) with a mounted mirror. If a valid measurement signal is available, the control loop for a piezo fiber stretcher is closed. Similar to the MLO, the MDL has a large operation range but low bandwidth, and the piezo stretcher a small operation range but a high bandwidth. If the sensor range is left due to disturbances, the locking procedure has to be repeated. Common problems which occur at the LSU system are:

The system can not be locked: With the given controller parameter the system is not stable or the MDL moves too fast and is not capable to detect the working area of the sensor.

The link lock is lost: The controller moves outside the working area and gets unstable, e. g. due to disturbances, and is turned off.

These problems should be addressed in the controller and firmware design. Like in the MLO case, a reduction of the timing jitter at the attached end device is a performance criterion which should be optimized. The modeling of this device is shown in Sec. 5.1 and the controller design in Sec. 5.2. The non-linear sensor and an approach to address its behavior in the controller design is explained in Sec. 5.4.

2.2.3 Attached Devices

Different types of devices need to be synchronized to the precise timing signal of the LbSync system. How to model and control these individually is not in the scope of this work. Nevertheless a brief overview to those devices is necessary to follow the discussion in Sec. 6.2.

Direct Usage - Bunch Arrival Time Monitor (BAM)

Timing jitter and arrival time changes can be introduced through magnetic bunch compressors installed in the accelerator. For this reason, the so-called BAM, is used to measure the timing of the electron bunch at a certain point in the beamline, see [Boc12]. If these signals are additionally used for the cavity field control of the LLRF systems the beam can be stabilized in time by the LLRF controller. This new concept is called beam-based feedback, and is developed in [Pfe14].

Laser to Laser (L2L) - Photo Injector Laser (IL) or Pump Probe Laser (PPL)

The emission of the electron bunch at the gun is triggered by a laser pulse, generated by the Injector Laser (IL), which impacts on the gun cathode. In order to synchronize this process the IL arrival time has to be synchronized to the main pulse train of the LbSync system. Another example is the Pump Probe Laser (PPL). This laser is used to trigger the reaction or to sample a picture of the experiment, dependent on the application and the user experiment. The jitter of this device with respect to the X-ray pulse is responsible for the quality of the picture.

These systems that synchronize another laser to the MLO are so-called Laser to Laser (L2L) systems. It is planned to use the same firmware for both MLO and the L2L systems.

Laser to Radio Frequency (L2RF) - Cavity Control (LLRF)

The cavity controller stabilizes the electric field within the cryo-modules of the accelerator section. This field is used to increase the energy of the accelerated electrons. The requirements in phase and amplitude stability for this field are very demanding and treated in [Sch10] and [Pfe14]. The cavity controller is calculated on a Micro Telecommunications Computing Architecture enhancements for rear I/O and precision timing (MicroTCA.4) crate. To connect this to the LbSync system, a module called Optical Reference Module (REFM-OPT) is used, see [Jan+14]. This device stabilizes a 1.3 GHz reference signal fed by coaxial cables that is used to trigger the sampling of the raw cavity probe signals. Due to this step, the measured signals at the cavity controller are synchronized to the LbSync system.

2.3 Hardware Platform – MicroTCA.4

In the last years, the hardware platform for most control systems at DESY has changed from the previously used Versa Module Europa (VME) system to a new standard called MicroTCA.4.

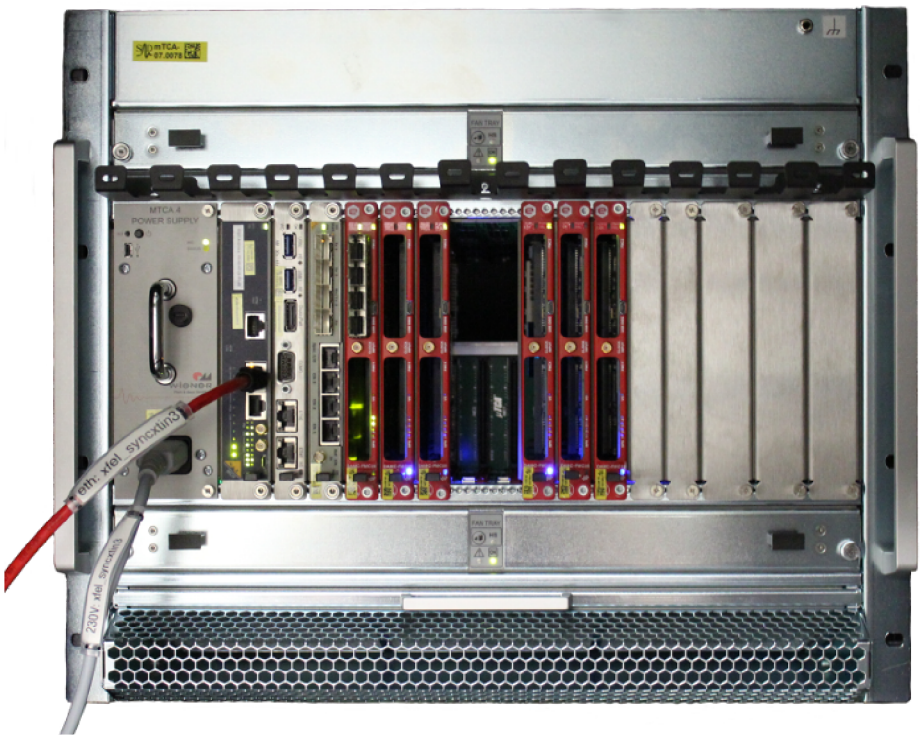

Figure 2.5: MicroTCA4.0 Crate.

Figure 2.5 shows a crate populated with different electronic boards. Boards connected at the front are so-called Advanced Mezzanine Cards (AMCs) and are usually computation boards. At the rear side of the MicroTCA.4 crate, so-called Rear Transition Modules (RTMs) are connected, on which actuators and sensors are placed. In Appendix A the specification of the boards used for the LbSync system are listed.

In this new standard, the fast control algorithms are implemented on a Field-Programmable Gate Array (FPGA). The advantage of this technology change is the increase of the computation speed, ADC, and DAC frequencies. A real-time application on a CPU can achieve sample rates of $< 20\,\mathrm{kHz}$, whereas a Digital Signal Processor (DSP) goes up to $< 200\,\mathrm{kHz}$. With an FPGA computation, frequencies of 200 MHz and more are possible depending on the required application and the complexity of the implemented algorithm.

The main differences between the new MicroTCA.4 and the previously used VME system, from a control theory point of view, are the following:[2]

- The possible control algorithm speed can be increased by a factor of > 100.
- The sampling rate of the actuator increases by a factor of 8 in a two channel operation and 4 with four active channels.
- The internal latency of the control hardware is decreased.
- Additional measurements (e.g. actuator current) are available.
- The algorithm has to be implemented in fixed-point representation instead of floating point values used on a DSP.

2.4 Firmware Platform – Rapid-X

With the new hardware platform based on FPGAs, the firmware development has changed. Previously, the LbSync system, based on VME, was running on DSP, which is programmed in C. For an FPGA, VHSIC Hardware Description Language (VHDL) is required.

The common work flow is to design and simulate an algorithm in *MATLAB/Simulink* and implement it by hand in VHDL. With such a design flow, differences between the implementation and the designed algorithm are hard to find and important implementation details are missed in the simulation. If there are problems, they are usually complicated to analyze. These issues are even more relevant if complex control algorithms come into play, e. g. the implementation can play a huge role for the solution of a state space based model and a bug in a predictive controller approach is impossible to analyze.

For these reasons the implementation of these systems is combined with the tools used in the design phase. The *Xilinx SysGen* Toolbox allows for the simulation of the behavior on the FPGA, concerning fixed point representations and other properties that occur in the implementation. Moreover, this toolbox allows for the generation of the VHDL code from the modeled application. The generated code has no interfaces like actuators, sensors or other components like the memory or the Peripheral Component Interconnect Express (PCIe) interface on the FPGA. *Rapid-X* was introduced in [Pre+14] and [Pre+15].

Hence, the additional toolbox offers components that allow the simulink application designer to connect board related interfaces within the model. If this extended model is generated by *Rapid-X* it is integrated in the common VHDL framework used for the firmware developments and can be directly used on the final system.

[2] The controller and the DAC on the VME LbSync system have a sampling rate of 125 kHz.

These tools bring, the following advantages:

- algorithm design and implementation in the same application,
- the implemented behavior is simulated,
- no VHDL knowledge required for algorithm designer.

One main part of the author's work at DESY was to support the work on this toolbox. The controller and algorithms developed in this thesis are implemented and tested using these tools, [Heu+16]. Moreover, they serve as a test bench for the tools, and a lot of features for the development derived by the requirements for the LbSync firmware. An overview of this firmware is given in Appendix B.

Figure 2.6 shows an example model of an application built with *Rapid-X*. The colored blocks are components given by the newly developed tools.

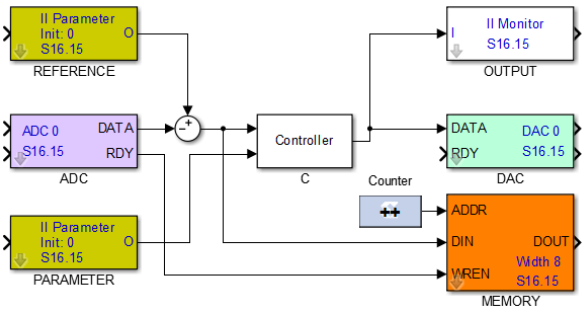

Figure 2.6: Example Rapid-X model.

2.5 Software Framework – MicroTCA4You

To access the different registers of the design firmware, including the fast control algorithm, a software package called MicroTCA4You is needed which includes the required driver and libraries for the communication with the boards. Additionally, there are tools which are directly usable in *MATLAB*, Python or at the command line of the crate operation system,[Kil+14] and [Kil+15].

Those tools are essential for the usage of the system, and the development of part of these was one of the author's tasks in this thesis. Nevertheless, the only implication for control is that this tool is responsible for the data conversion from floating to fixed point values if e. g. control parameter are uploaded to the system.

3 THEORY

After the introduction of the LbSync system, this section introduces the main theoretical control aspects required in this work. Most of the content can be found in classical text books like [SP01], [ÅM08], [DFT92], [FPE14], and [Bay99].

The first part explains the general structure of a control loop and its mathematical representation, followed by the concepts of system norms and the famous Gang of Four, explained in Sec. 3.1.3.

Section 3.2 derives the dynamics of the piezo actuator from the Butterworth-van-Dyke equivalent circuit. Moreover, important properties like hysteresis and creep are briefly introduced.

The concept of system identification is briefly described in Sec. 3.3, and the properties of ADCs and DACs in Sec. 3.4.

Calculations in fixed point numbers are less demanding on the resources of the available computing hardware. For this reason, the implications of choosing these is shown in Sec. 5.

The measure which should be minimized is the timing jitter and phase noise of the system. Section 3.6 introduces these concepts from a control theory point of view.

The theory section closes with the introduction of some basic controller design techniques.

3.1 The General Control Loop

Figure 3.1 shows the general control loop commonly used in the literature, with the plant $G(s)$ and the controller $K(s)$, see e. g. [ÅM08] or [SP01]

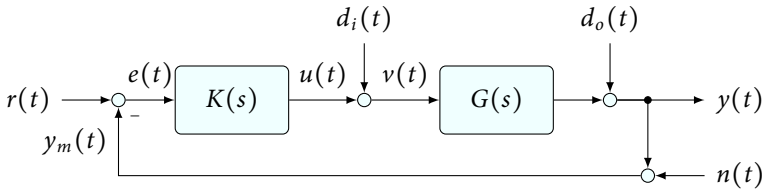

Figure 3.1: Control loop in a one degree of freedom setup.

$r(t)$ is the reference signal which the system output should follow.

$u(t)$ is the controller output which forces the system into the desired state.

$y(t)$ is the output of the plant which can be measured.

$n(t)$ is noise which is added by the measurement but is not part of the desired system output.

$y_m(t)$ is the value visible at the controller, the plant output with the added measurement noise.

$d_i(t)$ is called input disturbance influencing the controller output.

$v(t)$ is the value which is really applied to the plant.

$d_o(t)$ is the disturbance acting on the plant output.

The controller $K(s)$ should generate a signal to the input of the plant $u(t)$ in such a way, that the difference between the plant output and a given reference $r(t)$, i. e. the control error $e(t)$, is minimal. Moreover, unwanted disturbance and noise effects which influences $y(t)$ should be suppressed.

The main disturbances and noise sources for the LbSync system are:

1. Input disturbance $d_i(t)$:
   - Ripple and other effects on the supply voltage
   - Actuator noise and quantization of the DAC
2. Output disturbance $d_o(t)$:
   - Movement of the coarse tuning motor
   - Vibrations and temperature changes of the table with the optical free-space setup
   - Vibrations, temperature and humidity changes of the optical fiber

3. Noise sources $n(t)$:
   - Shot-noise of the photo diode
   - Electromagnetic interference in the measurement path
   - Noise and quantization of the ADC

For the sake of simplicity, the time dependence of the signals is dropped in the following.

3.1.1 System Description

The behavior of a system and the behavior of a controller can be described by the differential equations

$$\dot{x}(t) = f(x, u, t)\,, \tag{3.1a}$$
$$y(t) = g(x, u, t)\,, \tag{3.1b}$$

where f and g are functions depending on the state x, the input u, and the time t.

In this work we will use linear time invariant systems, resulting in

$$\dot{x}(t) = Ax(t) + Bu(t)\,, \tag{3.2a}$$
$$y(t) = Cx(t) + Du(t)\,, \tag{3.2b}$$

where $x(t) \in \mathbb{R}^n$ are the states (internal energy storages), $u(t) \in \mathbb{R}^m$ the inputs, and $y(t) \in \mathbb{R}^l$ the outputs of a system. The matrix $A \in \mathbb{R}^{n\times n}$ is called system matrix, $B \in \mathbb{R}^{n\times m}$ is the input matrix, $C \in \mathbb{R}^{l\times n}$ the output matrix, and $D \in \mathbb{R}^{l\times m}$ is commonly called the feed trough matrix.

If the differential equations are transformed into the frequency domain using the Laplace transformation, the input output behavior for a Single Input Single Output (SISO) system, $l = 1$ and $n = 1$, is given by

$$\frac{Y(s)}{U(s)} = G(s) = C(sI - A)^{-1}B + D = \frac{b_0 + b_1 s + \ldots + b_m s^m}{a_0 + a_1 s + \ldots + a_n s^n}\,, \tag{3.3}$$

where $s = \sigma + j\omega$. The eigenvalues of A and the denominator zeros of (3.3) are the poles and define the dynamic system behavior. Other notations for the system in (3.2) are

$$\begin{bmatrix} \dot{x} \\ y \end{bmatrix} = \begin{bmatrix} A & B \\ C & D \end{bmatrix} \begin{bmatrix} x \\ u \end{bmatrix} \quad \text{and} \quad G(s) = \left[\begin{array}{c|c} A & B \\ \hline C & D \end{array}\right]. \tag{3.4}$$

Amplitude- and Time-Scaling

In most cases, the input and output values are not necessarily in the same order of magnitude [FPE14]. E. g. if up to hundreds of volts or more are applied to a piezoelectric crystal, its strain could be in the range of only a few micrometers. Such a model would have an ill-conditioned representation. Thus a proper scaling is important. This is done by describing the values with respect to their expected maximum denoted by the subscript max, e. g.

$$u_{\text{Scaled}} = \frac{u}{u_{\max}} = S_u u \quad \text{and} \quad y_{\text{Scaled}} = \frac{y}{y_{\max}} = S_y y\,. \tag{3.5}$$

The new scaled system is given as

$$G_{\text{Scaled}}(s) = S_y^{-1} G(s) S_u\,. \tag{3.6}$$

To scale the system in time, the new time unit τ is given by $\tau = S_t t$, leading to

$$\frac{\mathrm{d}x}{\mathrm{d}t} = S_t \frac{\mathrm{d}x}{\mathrm{d}\tau} \quad \Rightarrow \quad \dot{x}(\tau) = \frac{1}{S_t} \cdot Ax(\tau) + \frac{1}{S_t} \cdot Bu(\tau) \tag{3.7}$$

Discrete Time Representation

The system in (3.2) is implemented by the use of its discrete time representation, given by

$$x(kT + T) = \Phi x(kT) + \Gamma u(kT)\,, \tag{3.8a}$$
$$y(kT) = Cx(kT) + Du(kT)\,. \tag{3.8b}$$

The sample instance k and the sampling rate T are given by $t = kT$, and the discrete time matrices are given by

$$\Phi = e^{AT} \quad \text{and} \quad \Gamma = \int_0^T e^{AT} B \,\mathrm{d}t\,. \tag{3.9}$$

Using the Z-Transformation, a SISO system can be written as the transfer function,

$$\frac{Y(z)}{U(z)} = G(z) = C(zI - \Phi)^{-1}\Gamma + D = \frac{b_0 + b_1 z^{-1} + \ldots + b_m z^{-m}}{a_0 + a_1 z^{-1} + \ldots + a_n z^{-n}}\,. \tag{3.10}$$

3.1.2 Signal and System Norms

Some important properties of systems are given by their norms. These norms and their optimization are a main topic in modern model-based controller design, and they will be employed later on.

The transmission of the RMS value of a Linear Time Invariant (LTI) system can be described by its $\mathcal{H}_2$ norm, for SISO systems given by

$$\|G(s)\|_2 = \sqrt{\frac{1}{2\pi}\int_{-\infty}^{\infty} |G(j\omega)|^2 \mathrm{d}\omega}\,. \tag{3.11}$$

Another property is the maximum amplification at a certain frequency given by the $\mathcal{H}_\infty$ norm,

$$\|G(s)\|_\infty = \max_{u\neq 0} \frac{\|y(t)\|}{\|u(t)\|} = \sup_{\omega} |G(j\omega)|\,. \tag{3.12}$$

E. g. consider the bode magnitude plot of the system

$$G(s) = \left[\begin{array}{cc|c} -0.1 & 10 & 1 \\ 1 & 0 & 0 \\ \hline 0 & 1 & 0 \end{array}\right], \tag{3.13}$$

shown in Fig. 3.2 the $\mathcal{H}_\infty$ norm describes the maximum amplification of the signal, while the $\mathcal{H}_2$ norm is the area below the bode plot describing the amplification over all frequencies.

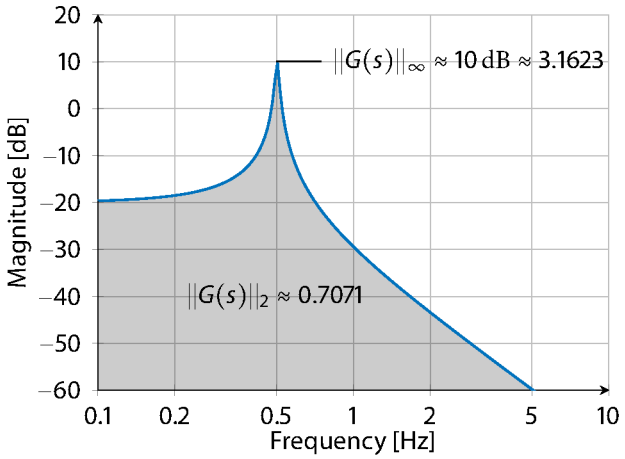

Figure 3.2: Bode magnitude plot of (3.13), describing the $\mathcal{H}_2$ and $\mathcal{H}_\infty$ norm.

3.1.3 Gang of Four

The control loop, shown in Fig. 3.3 has multiple in- and outputs. In many cases, e. g. for the radio frequency field control of the accelerator cavities, the important transfer function $T_{yr}(s)$, with the input r and the output y, is taken into account. But others are also of importance.

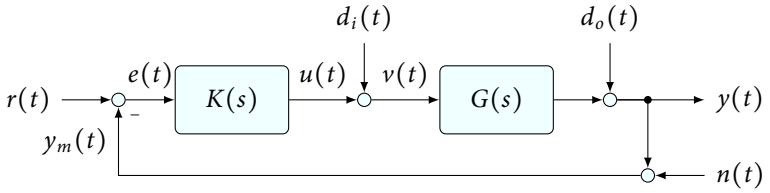

Figure 3.3: Control loop in a one degree of freedom setup.

The so-called Gang of Four (GOF), further explained in [ÅM08], is given by

$$y = \frac{GK}{1+GK}r + \frac{G}{1+GK}d_i + \frac{1}{1+GK}d_o - \frac{GK}{1+GK}n\,, \tag{3.14a}$$

$$y_m = \frac{GK}{1+GK}r + \frac{G}{1+GK}d_i + \frac{1}{1+GK}d_o + \frac{1}{1+GK}n\,, \tag{3.14b}$$

$$e = \frac{1}{1+GK}r - \frac{G}{1+GK}d_i + \frac{1}{1+GK}d_o - \frac{1}{1+GK}n\,, \tag{3.14c}$$

$$u = \frac{K}{1+GK}r + \frac{KG}{1+GK}d_i + \frac{K}{1+GK}d_o - \frac{K}{1+GK}n\,. \tag{3.14d}$$

The individual transfer functions can be summarized as:

$S = \frac{1}{1+GK}$ the sensitivity function describing, i. e. the output disturbance rejection.

$SG = \frac{G}{1+GK}$ the load disturbance sensitivity function.

$KS = \frac{K}{1+GK}$ is the noise sensitivity function, i. e. representing the control effort.

$T = \frac{GK}{1+GK}$ is the complementary sensitivity function, i. e. describing the reference tracking.

For the design of a feedback controller all transfer functions are important [SP01]. If only one of these is optimized, the others may be unsuitable for the control propose. Moreover, they can not be designed independently. They are constrained, which can not be overcome. E. g. the sum of sensitivity and complement sensitivity function is identity, i. e.

$$S + T = I\,. \tag{3.15}$$

This e. g. leads to the following: If the system is optimized for output disturbance rejection ($S \to 0$), this also increases the measurement noise influence ($T \to I$). It is important to find an optimal trade-off between all four transfer functions that satisfy given closed loop requirements.

3.2 The Piezoelectric Actuator

In order to change the resonator length of the MLO or the length of the optical fiber, piezoelectric materials are used to generate the required displacement and/or strain. These elements are the main actuators for the LbSync system and in the following section the main properties and the common way to model them is explained.

3.2.1 Dynamic Behavior

The literature presents various possibilities for modelling such components, depending on the application. In this work, the so-called Butterworth-Van Dyke equivalent circuit, proposed in [Dyk28], is used. This model describes the capacitive behavior, the mechanical resonances, and antiresonances for a piezoelectric material without a load.

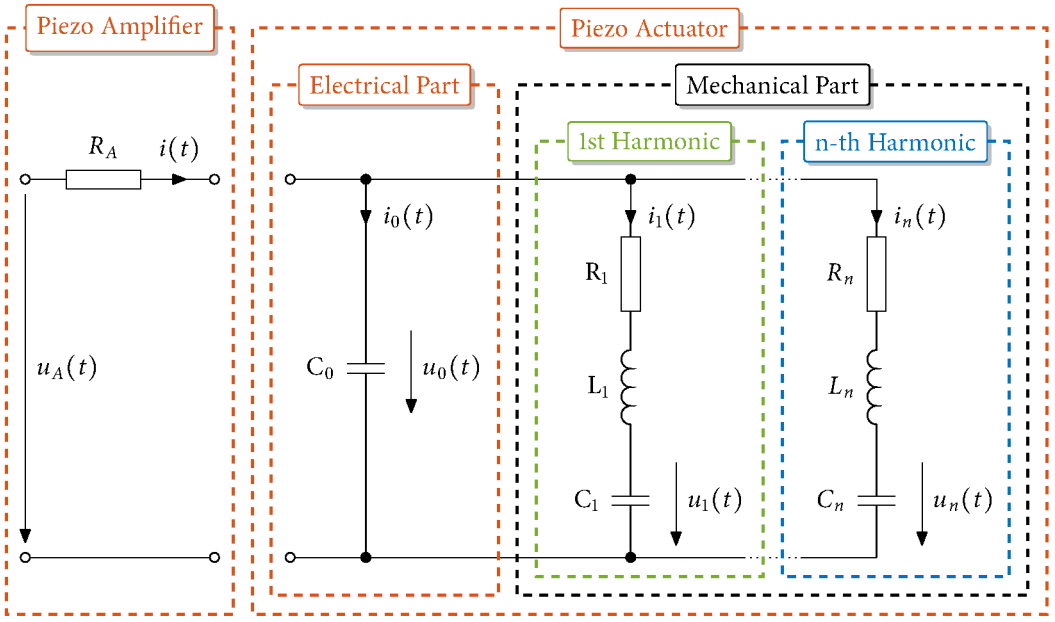

Figure 3.4: Equivalent circuit for the amplifier and piezoelectric actuator.

Figure 3.4 shows the equivalent circuit for the amplifier (left) and the piezoelectric actuator. The middle part shows the real electrical capacity of the piezoelectric component and the right part models the mechanical resonances via an equivalent circuit that behaves the same way as the real mechanical system does. The commonly used electrical and mechanical analogies are e. g. shown in [HB06]. The charge of the capacitor in each branch contributes to the displacement of the piezoelectric actuator's surface. The corresponding inductance drags this displacement back. The resistance models the friction losses that decays this oscillation.

Basic electrical rules can be applied to describe the behavior as a state space model. The amplifier acts as a voltage source with an output resistance. Using Kirchhoff's voltage law gives

$$u_A(t) = i(t)R_A + u_0(t)\,, \tag{3.16}$$
$$u_A(t) = (i_0(t) + i_1(t) + i_2(t) + \ldots + i_n(t))R_A + u_0(t)\,. \tag{3.17}$$

Including the equation for the current $i_0(t) = C_0\dot{u}_0(t)$ at the capacitor, it can be written as

$$u_A(t) = R_A C_0 \frac{du_0(t)}{dt} + R_A \cdot i_1(t) + \ldots + R_A \cdot i_n(t) + u_0(t) \tag{3.18}$$
$$\frac{du_0(t)}{dt} = -\frac{1}{R_A C_0}u_0(t) - \underbrace{\frac{1}{C_0}(i_1(t) + \ldots + i_n(t))}_{\text{additional harmonics}} + \frac{1}{R_A C_0}u_A(t)\,. \tag{3.19}$$

The harmonics are independent from each other and modeled as RCL oscillators. How many of them are taken into account can be decided dependent on the relevant requirements. They are coupled by the voltage drop of their currents floating through the resistor R_A.

For each of the harmonics, the Kirchhoff's rule leads to

$$u_0(t) = i_n(t)R_n + L_n\frac{di_n(t)}{dt} + u_n(t)\,, \tag{3.20}$$
$$i_n(t) = C_n\frac{du_n(t)}{dt}\,. \tag{3.21}$$

Combining the first up to the n-th harmonic with the capacitor of the piezoelectric actuator, the equivalent circuit in Fig. 3.4, is given by

$$\frac{d}{dt}\begin{bmatrix} u_0(t) \\ i_1(t) \\ u_1(t) \\ \vdots \\ i_n(t) \\ u_n(t) \end{bmatrix} = \begin{bmatrix} -\frac{1}{R_A C_0} & -\frac{1}{C_0} & 0 & \ldots & -\frac{1}{C_0} & 0 \\ \frac{1}{L_1} & -\frac{R_1}{L_1} & -\frac{1}{L_1} & \ldots & 0 & 0 \\ 0 & \frac{1}{C_1} & 0 & \ldots & 0 & 0 \\ \vdots & \vdots & \vdots & \ddots & \vdots & \vdots \\ \frac{1}{L_n} & 0 & 0 & \ldots & -\frac{R_n}{L_n} & -\frac{1}{L_n} \\ 0 & 0 & 0 & \ldots & \frac{1}{C_n} & 0 \end{bmatrix} \begin{bmatrix} u_0(t) \\ i_1(t) \\ u_1(t) \\ \vdots \\ i_n(t) \\ u_n(t) \end{bmatrix} + \begin{bmatrix} \frac{1}{R_A C_0} \\ 0 \\ 0 \\ \vdots \\ 0 \\ 0 \end{bmatrix} u_A(t)\,. \tag{3.22}$$

An important other value is the displacement of the piezo. This is, explained by [Pre06, Ch. 4], proportional to the total stored charge of the system, i. e.

$$\Delta l = k(q_c + q_1 + \ldots + q_n)\,. \tag{3.23}$$

3.2.2 Hysteresis and Creep

Despite the linear dynamics, there are also non-linear effects in such an actuator, [PI2014]. The hysteresis effect is shown in Fig. 3.5. If an excitation voltage is applied, the displacement changes in one direction, Δl_e. If this voltage is disabled, the displacement does not reach its initial state but has an offset, Δl_r. An additional voltage step u_r is needed to move it to the initial displacement.

In contrast to the hysteresis, there can be another effect called saturation. If the excitation voltage u reaches a certain value the displacement Δl_s stops, even if the voltage is further increased.

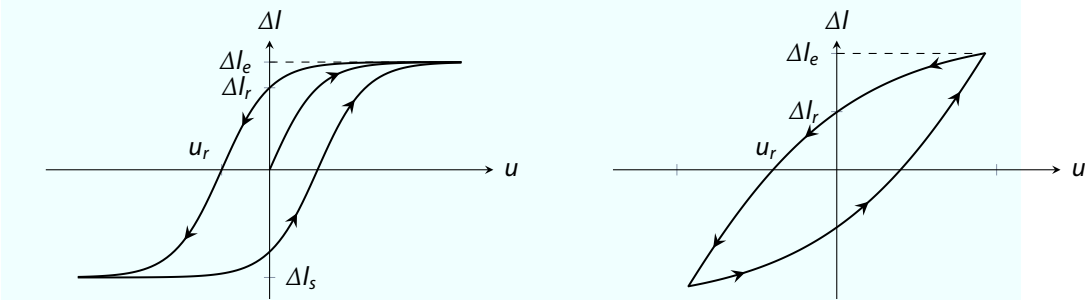

Figure 3.5: Hysteresis with (left) and without (right) saturation.

If an influence of the hysteresis effect is observed in experiments, it is possible to include a compensation scheme as shown in [KK01] and [Jan+06].

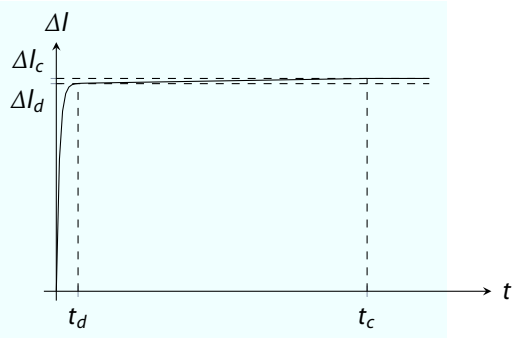

Figure 3.6: Creep behavior in piezoelectric actuators.

Figure 3.6 shows the effect known as creep. The first dynamic excitation ends after a short time t_d and the piezo reaches nearly a steady state displacement Δl_d. This changes very slowly over time to a final displacement, Δl_c. The time of the creep, t_c, is usually in orders of magnitude higher than the time of the piezoelectric dynamics, t_d.

3.3 System Identification

The parameters in the system description (3.2) or the approach in (3.22) are, up to now, not known. An important step, prior to the controller design, is to estimate those parameters. This step is called system identification. Three main methods are distinguished.

White box: All effects are known and the prior knowledge of the system is sufficient to calculate all required parameters.

Gray box: It is assumed, that the structure of the system, like system order, number of resonances, symmetries and other, are known. An experiment is performed to acquire the unknown parameters.

Black box: A general plant description is used, like an LTI system, but all parameters are unknown. Like in the second case, an experiment is performed in order to optimize the model to fit the measured data.

In this work all identification methods are used for different parts of the system. For the last two methods the system has to be excited and the response is measured. Important in this step is that the excitation signal is sufficiently rich to excite the frequency region which is of interest for the latter's closed loop operation. High frequency parts don't need to be modeled if the controller doesn't have to act on them. Low frequency parts are handled by an integral controller behavior. A detailed overview of the system identification procedure can be found in [Lju15] and [Lju99].

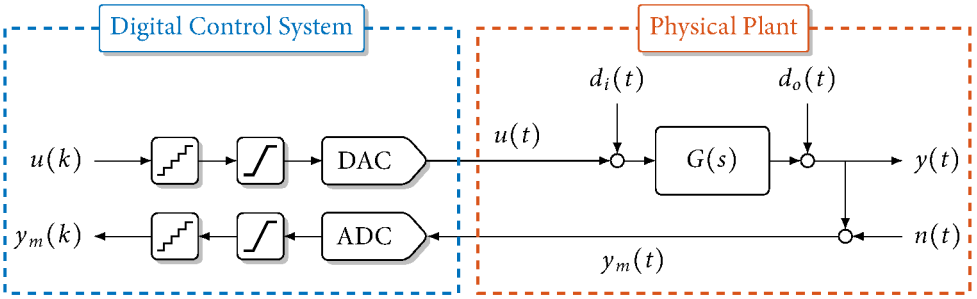

Figure 3.7: Open Loop Setup

Figure 3.7 shows the general setup of an open loop system with digital actuation and measurement. The computed control value $u(k)$ is always quantized, limited, and applied by a zero order hold element to generate the analog control signal $u(t)$. This enters the plant, $G(s)$, generating the system output $y(t)$. After that the ADC measures the system output. Similar to the DAC, the ADC generates a quantized, limited, and time discretized value, $y_m(k)$, of the continuous time measurement, $y_m(t)$. In the experiment for the identification, a pre-generated signal is applied to $u(k)$, while $y_m(k)$ is stored. These two signals are then used to determine the dynamic behavior of $G(s)$.

3.4 ADC and DAC Effects

In a digital control system, the sampling of the analog signal and the generation of the control signal induces important effects that are briefly explained in this section. Those topics are well treated in [LZ06] and also in [Poh95; Smi99; Zöl08] even though they focus on digital audio signal processing. ADC and DAC effects can be modeled by Additive White Gaussian Noise (AWGN) $d_\bullet(t)$ extending (3.2) to

$$\dot{x}(t) = Ax(t) + Bu(t) + B_\bullet d_\bullet(t)\,, \tag{3.24a}$$
$$y(t) = Cx(t) + Du(t) + D_\bullet d_\bullet(t)\,. \tag{3.24b}$$

The matrices $B_\bullet$ and $D_\bullet$ define where and how the effect influences the system.

3.4.1 Sample and Hold

A common way to model ADCs is shown on the left side of Fig. 3.8. It contains a sample and hold unit that is clocked with the sampling rate f_s and converts the continuous signal to discrete, with $t = f_s^{-1} \cdot k$. After that, a quantization maps the analog signal to a digital one.

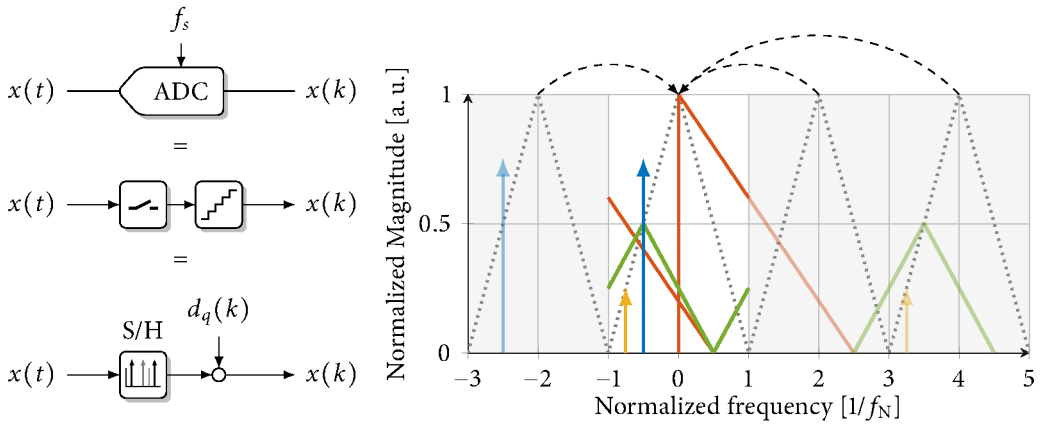

Figure 3.8: Modeling of an ADC as a triggered switch.

The right side shows the effect of the sample and hold unit. Due to the sampling theorem, only signals below the Nyquist frequency $f_N = 0.5\, f_s$ are measurable. If the frequency of a signal is outside this range, it appears to be inside and the even multiples of the Nyquist frequency are mapped to DC, while the odd multiple are mapped to the Nyquist frequency. Usually this is unwanted because it is not possible to distinguish on which frequency the controller should act. For this reason, an anti-aliasing filter is applied in front of the ADC to suppress frequencies larger than the Nyquist frequency. In the case of the LbSync system, this aliasing effect is used to capture the high frequency laser pulse train. The signal appears as a narrow line in a higher Nyquist zone. This allows a technique called under sampling, further explained in Sec. 4.1.3.

3.4.2 Zero-Order-Hold

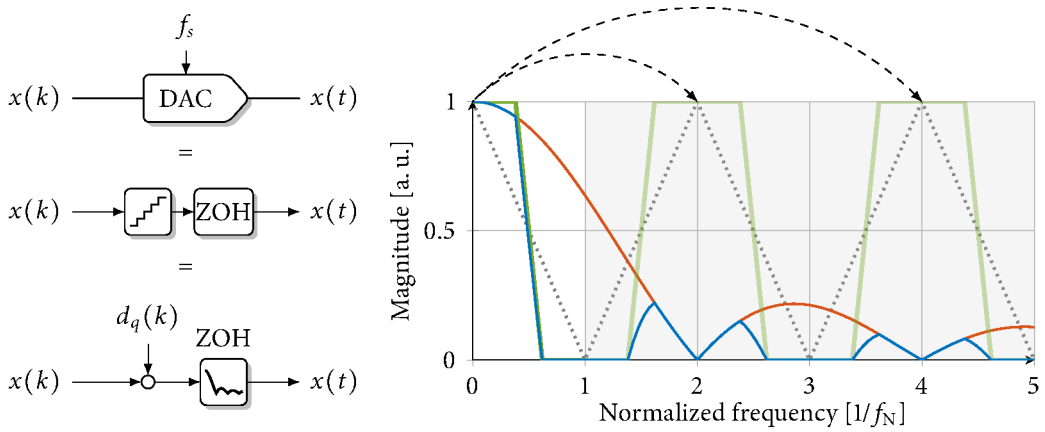

Figure 3.9: Modeling of a DAC as a Zero Order Hold (ZOH) element.

The modeling and the output behavior of a DAC is shown in Fig. 3.9. The quantized digital signal is held between two samples, called zero order hold. Similar to an ADC, the DAC maps the frequency components from the primary Nyquist zone to higher ones, [MT017]. The difference is that the amplitude of these frequency components are shaped with

$$A(f) = \frac{\sin\left(\frac{\pi f_s}{f}\right)}{\frac{\pi f_s}{f}} = \frac{\sin\left(\frac{\pi f_N}{2f}\right)}{\frac{\pi f_N}{2f}}. \tag{3.25}$$

For a continuous time controller design, a common rule is to choose the sampling rate 20 to 40 times faster than the closed loop bandwidth [FPE14]. This rule of thumb can be explained with the DAC behavior. If the sampling rate chosen is high enough, the effect of the zero order hold and the appearance of images is negligible.

The continuous time behavior and transfer function are given as

$$h_{ZOH}(t) = \frac{1}{T}\,\mathrm{rect}\left(\frac{t}{T} - \frac{1}{2}\right) = \begin{cases} \frac{1}{T} & \text{if } 0 \le t \le T; \\ 0 & \text{otherwise.} \end{cases} \tag{3.26}$$

and

$$H_{ZOH}(s) = \frac{1 - e^{-sT}}{sT}. \tag{3.27}$$

3.4.3 Quantization

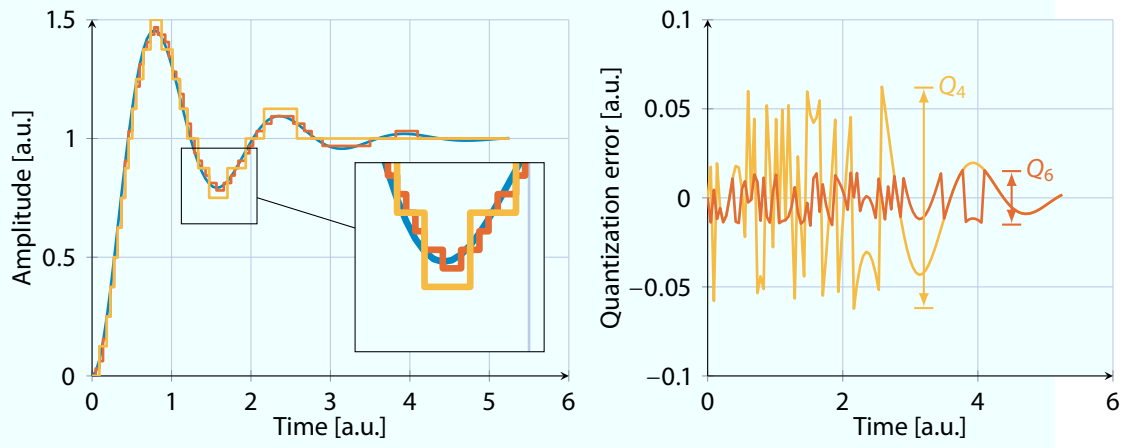

Figure 3.10: Step response (left) and quantization error (right) of this response with 6 (——) and 4 (——) bit compared to the continuous signal (——)

Quantization occurs at the transition from continuous to discrete time data, e. g. using ADCs or DACs. Both elements have a fixed resolution in bits and it is only possible to capture and generate values with this resolution. Figure 3.10 shows the output and the error if different resolutions are available. For a 6 bit resolution with the range from 0 to 2, the signal response (——) and the error of this signal (——) with respect to the continuous value (——) is shown. If the resolution is lowered to 4 bit the error (——) increases, compare to e. g. [Ben48].

To take this behavior into account, the classical quantization model will be used [Wid61]. The error is modeled by AWGN superimposed to the non-quantized signal. The maximum value of this error, the minimum resolution is the quantization step size

$$\Delta Q = \frac{1}{2^N} \cdot x_{max}\,, \tag{3.28}$$

where N is the number of bits and $x_{\max}$ is the dynamic range of the variable in the digital control system. If the error within the range of Q is equally distributed, the power of the error signal is given by

$$\|(e(t))\|_2 = \frac{\Delta Q^2}{12} = d_q^2\,, \tag{3.29}$$

where d_q is the AWGN added in (3.24). For the ADC $B_\bullet = B$ and $D_\bullet = 0$ and for the DAC $B_\bullet = 0$ and $D_\bullet = I$ can be used to model the quantization.

A common approach is that this quantization noise power is equally spread up to the sampling frequency f_s, [HSO11], which gives the constant power density of

$$S(f) = \frac{\Delta Q}{\sqrt{12} \cdot 2 f_s}\,. \tag{3.30}$$

3.5 Finite Word Length Effects

One important property of embedded systems, and of the FPGA based MicroTCA.4 boards, is the computation using finite word length values. The usage of this representation leads to a quantisation in each mathematical operation. This effect can be minimized by calculations with floating point values. For the current system, this is not implemented and these issues have to be taken into account.

The binary representation of fixed point values, and the resulting dynamic range and rounding error is shown in Fig. 3.11. How to compute the parameter minimum, maximum value, and its resolution is given in Table 3.1, compare e. g. [Bom99].

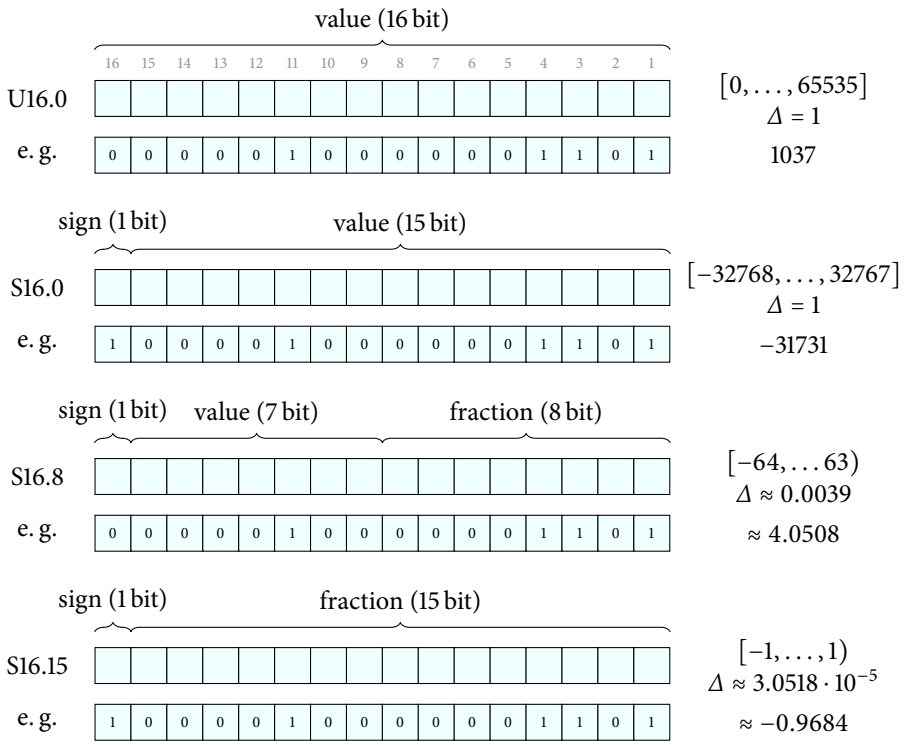

Figure 3.11: Different representation for fixed point numbers.

Table 3.1: Fixed-Point parameter with a total number of N bits and F fractional bits.

Description	Unsigned	Signed
Minimum value	0	$-2^{(N-F-1)}$
Maximum value	$2^{(N-F)} - 1$	$2^{(N-F-1)} - 1$
Delta	2^{-F}	2^{-F}

Disturbance and Noise by fixed point representation

The values in an algorithm calculated with fixed point representation, are quantized in every calculation step. This can also be modeled by AWGN with the appropriate variance,

$$d^2_{\mathrm{FP},\bullet} = \frac{2^{-2F}}{12}\,. \tag{3.31}$$

In contrast to the quantization of the ADC or DAC, the quantization noise induced due to the fixed point calculation is added to every state not only to the in- or outputs. The discrete time model changes to

$$x(k+1) = Ax(k) + Bu(k) + Id_{\mathrm{FP,x}}(k)\,, \tag{3.32a}$$
$$y(k) = Cx(k) + Du(k) + Id_{\mathrm{FP,y}}(k)\,, \tag{3.32b}$$

where I is the identity matrix of the corresponding size.

Change of the dynamic behavior and steady state value

Another common problem is, that the dynamic behavior changes if the parameter in the state space system are rounded to the next representable fixed point value, e. g. [Abr15]. For, e. g.

$$G(s) = \left[\begin{array}{cc|c} 0 & 1 & 0 \\ -17 & -2 & 17 \\ \hline 1 & 0 & 0 \end{array}\right] \text{ and } G(z) = \left[\begin{array}{cc|c} 1 & 3.998\cdot 10^{-4} & 1.36\cdot 10^{-6} \\ -6.797\cdot 10^{-3} & 0.999 & 6.797\cdot 10^{-3} \\ \hline 1 & 0 & 0 \end{array}\right], \tag{3.33}$$

where $G(z)$ is discretized time representation of $G(s)$ with a sampling rate of $f = 2.5\,\mathrm{kHz}$. Hereby, the parameters could be rounded towards zero depending on the fixed point quantization. To reduce the numerical issues, the balanced realization can be used. This transformation leads to states which are as controllable as observable, and is mainly used in model order reduction. As stated in [Lau+87], "other applications of balancing transformations (although not by that name) can be found in signal processing, see, for example, [MR76]". This work proves, that this realization also leads to a minimum round off error during computation and should be performed in applications.

Using the balanced realization, the system is given by

$$G(s) = \left[\begin{array}{cc|c} -0.764 & -4.007 & -1.415 \\ 4.007 & -1.236 & 1.415 \\ \hline -1.415 & -1.415 & 0 \end{array}\right] \text{ and } G(z) = \left[\begin{array}{cc|c} 0.9997 & -0.0016 & -5.665\cdot 10^{-4} \\ 0.0016 & 0.9995 & 5.665\cdot 10^{-4} \\ \hline -1.415 & -1.415 & 0 \end{array}\right]. \tag{3.34}$$

Figure 3.12 shows the response to an input step for the example system with different fixed point representations of the state space system. Figure 3.13 shows the response for different sample times and a constant fixed point representation. The calculation itself is still done in floating point.

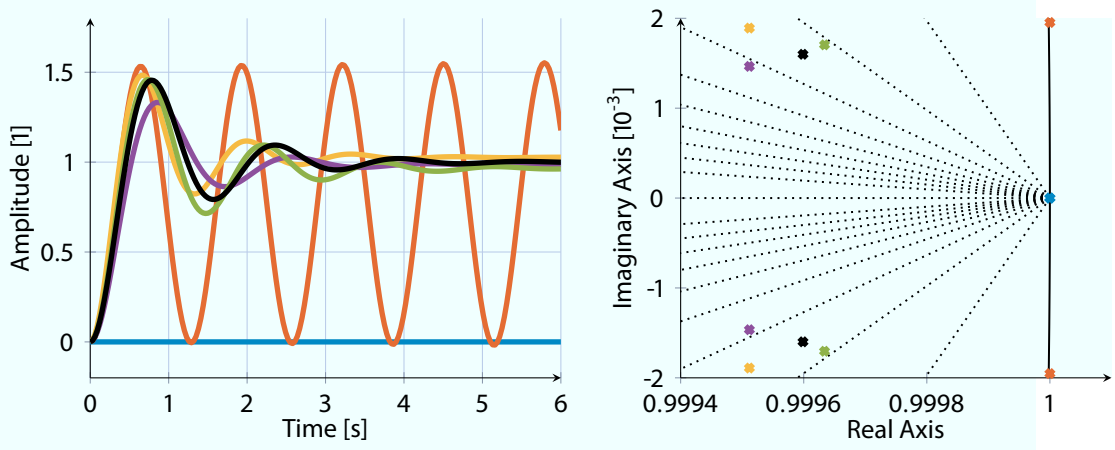

Figure 3.12: Step response (left) and pole location (right) for the example system with a sample rate of 2.5 kHz, 8 (—), 9 (—), 10 (—), 11 (—), 12 (—) fractional bits and calculated in floating point (—)

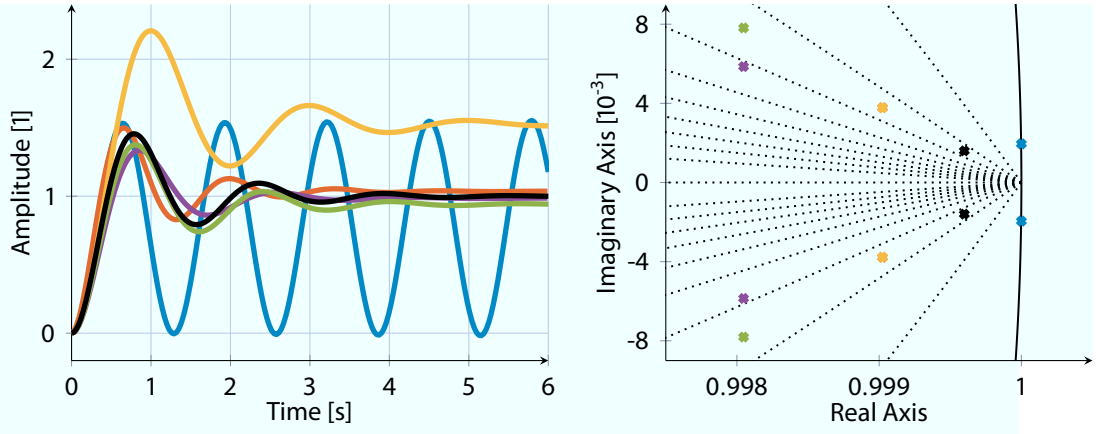

Figure 3.13: Step response (left) and pole location (right) for the example system with 9 fractional bits, sampling frequencies of 2.5 kHz (—), 1.25 kHz (—), 0.833 kHz (—), 0.625 kHz (—), 0.5 kHz (—) and simulated in continuous time (—)

3.6 Timing Jitter and Phase Noise

The laser pulse train generated by the MLO is not an ideal oscillation. There are two major noise effects that occur: amplitude and phase noise. An ideal oscillation $v(t)$ (—), with an amplitude A and a frequency f_c, is given by

$$v(t) = A \sin(2\pi f_c t)\,. \tag{3.35}$$

A real oscillation $v_n(t)$ (—) is given with additional amplitude noise, $A_n(t)$, and phase noise $\phi_n(t)$ (—) by

$$v_n(t) = (A + A_n(t)) \sin(2\pi f_c t + \phi_n(t))\,. \tag{3.36}$$

Phase noise effects especially change the zero crossing of the oscillation. At the connected end station this would result in a changed timing, called timing jitter.

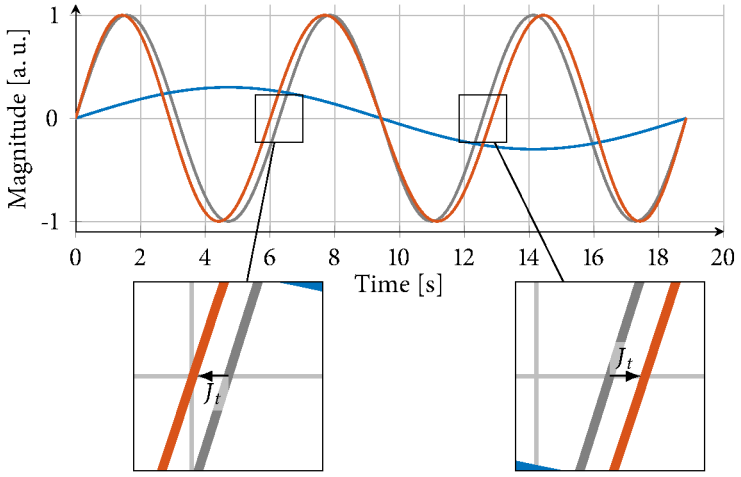

Figure 3.14: Ideal (—) and by phase noise (—) disturbed (—) oscillation with the timing J_t and phase J_ϕ jitter.

Figure 3.14 shows the effect of pure phase noise, which is the dominant behavior of the MLO. The resulting timing jitter is given by J_t .

In most applications the phase noise is measured as a phase difference in radian, which is dependent on the signal's frequency. To evaluate the performance of different setups and the overall behavior it is important to compare this in an absolute time value given by

$$J_t\,[\mathrm{s}] = \frac{J_\phi\,[\mathrm{rad}]}{2\,\pi\,f_c\,\left[\frac{1}{\mathrm{s}}\right]}\,. \tag{3.37}$$

This jitter is the main performance criterion for the LbSync system. The goal is to reduce the timing jitter due to phase noise at the end station. Furthermore, this also has an effect on the measurement in the LSU.

This section shows how these two measures are related, how phase noise can be modeled and how it is transmitted through an LTI system. Section 4.1.2 shows how to model the timing change of the pulse train, while Sec. 4.1.9 shows the concept of timing jitter from the control theory point of view.

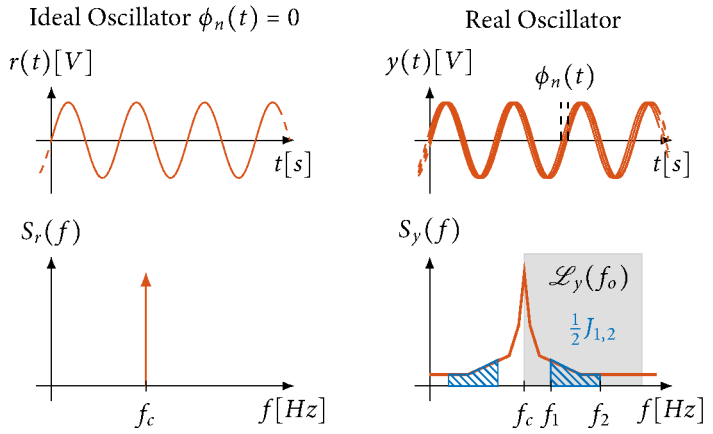

Figure 3.15: Time (upper) and frequency (lower) domain behavior of an ideal (left) and a real (right) oscillation.

Figure 3.15 shows an ideal (left) and a real (right) oscillator in the time (top) and frequency (bottom) domain. The ideal one has a Dirac impulse as its frequency spectrum, which is not true for the real oscillation which has additional components close to the center frequency f_c due to a noise term $\phi_n(t)$, also called phase fluctuation, acting on the phase.

To measure the phase fluctuation $\phi_n(t)$ or the timing jitter directly, different methods are available. The ones used in the LbSync system are:

1. Mixing of the electrical signal with a reference oscillation at the same center frequency is used in the VME setup, explained in Sec. 4.1.3 for the MLO system.
2. An amplitude-phase detection scheme applied to the electrical signal is used in the MicroTCA.4 setup and further explained in Sec. 4.1.3.
3. Direct measurement of the timing difference of the pulse train like used for the LSU systems, see Section 5.1.2.

In the following, the first method is explained in general to introduce the concept of phase noise. The other two are further discussed in Sec. 4.1.3 and Sec. 5.1.2. The signal (3.36), without the amplitude noise, is mixed with a reference oscillation

$$v_r(t) = A_r \sin(2\pi f_r t + \phi_r(t)), \tag{3.38}$$

leading to a lower and upper sideband using trigonometric identities,

$$v_n(t) \cdot v_r(t) = \frac{AA_r}{2} \underbrace{\sin(2\pi f_n t + \phi_n(t) - 2\pi f_r t - \phi_r(t))}_{v_{low}} + \frac{AA_r}{2} \underbrace{\sin(2\pi f_n t + \phi_n(t) + 2\pi f_r t + \phi_r(t))}_{v_{high}} . \tag{3.39}$$

Equation (3.39) can be approximated by

$$v_n(t) \cdot v_r(t) \approx \frac{AA_r}{2}(\phi_n(t) - \phi_r(t)) \approx \frac{1}{K_\phi}\phi_n(t) , \tag{3.40}$$

if the following assumptions hold, see e. g. [Abr02]:

1. Both center frequencies are the same, $f_c = f_r$
2. High frequency components are low pass filtered, $v_{high} \to 0$
3. Small phase fluctuation occur and the small angle approximation holds, $v_{low} = \sin(x) \approx x$
4. The reference oscillator has a much lower noise, $\phi_r(t) \ll \phi_n(t)$

The calibration constant K_ϕ in $[\mathrm{V/rad}]$ is a property of the measurement setup and has to be determined prior to the measurement, as well as if the setup changes.

If a system is not yet stabilized and is in the process of locking, the first assumption, ($f_c = f_r$), doesn't hold. In that case, the measured signal is given by

$$v_n(t) \cdot v_r(t) \approx \frac{AA_r}{2} \sin(2\pi(f_n - f_r)t + \phi_n(t) - \phi_r(t)) , \tag{3.41}$$

where $f_n - f_r = f_b$ is the so-called beat frequency. The dominant behavior of the signal v_n is not the phase fluctuation ϕ_n, but an oscillation within this frequency. An outer control loop, the so-called coarse tuning, is used to move this beat frequency close to zero, which allows the controller to lock the system. After that, the small angle approximation is valid.

The root mean square value of the phase fluctuation is called the integrated timing jitter J_{rad} in $[\mathrm{rad}]$. It can be calculated in the time or in the frequency domain by the theorem of Parseval,

$$J_{\mathrm{rad}}^2 = \|\phi_n(t)\|^2 = \int_0^\infty |\phi_n(t)|^2 \,\mathrm{d}t = \frac{1}{2\pi}\int_{-\infty}^{\infty} \mathscr{L}_{\phi_n}(\omega) \,\mathrm{d}\omega , \tag{3.42}$$

where $\mathscr{L}_{\phi_n}(\omega)$ is the phase noise with the unit $[\mathrm{rad^2/Hz}]$. On commercial measurement devices, e. g. Signal Source Analyzer (SSA), the phase noise is measured in $[\mathrm{dBc/Hz}]$[1]. Choosing this unit leads to an amplitude in-dependency. If the phase fluctuation is small ($0.1\,\mathrm{rad^2}$, [IEEE1139]) it is equal to the unit $[\mathrm{rad^2/Hz}]$.

[1] $[dBc/\mathrm{Hz}]$ is defined as the signal power in an interval of 1 Hz with respect to the total power.

The phase spectrum is

$$S_{\phi_n}(f) = 2 \cdot \mathscr{L}_{\phi_n}(f) = \frac{2 \cdot S_{v_n}(f_c + f)}{A_n A_r} \quad \forall f > 0\,, \tag{3.43}$$

assuming it is symmetric to the center frequency, see [Gar05] and [SLAN256]. The relation between the different spectra is shown in the lower right part of Fig. 3.15. The integrated timing jitter is given as

$$J_{\text{rad}}^2 = \|\phi_n(t)\|^2 = \frac{1}{\pi}\int_0^\infty \mathscr{L}_{\phi_n}(\omega)\,\mathrm{d}\omega = \frac{1}{2\pi}\int_0^\infty S_{\phi_n}(\omega)\,\mathrm{d}\omega\,. \tag{3.44}$$

The integrated timing jitter in [rad] and the phase noise $\mathscr{L}(f)$ in [dBc/Hz] are still dependent on the center frequency. In order to compare the resulting time variation, the timing jitter J_s in [s] and the phase spectrum $S_{\phi_n}(f)$ in [fs^2/Hz] are of interest and given by

$$J_s = \frac{J_{\text{rad}}}{2\pi f_c} \quad \text{and} \quad S_{\phi_n}(f) = 2 \cdot \frac{10^{\frac{\mathscr{L}(f)}{10}}}{(2\pi f_c)^2}\,, \tag{3.45}$$

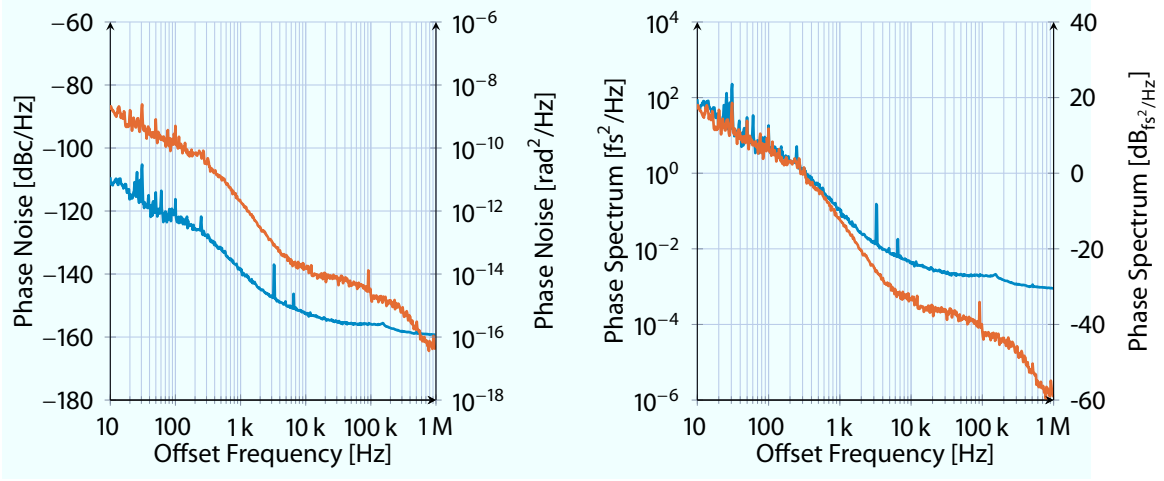

Figure 3.16: Phase noise of the laboratory MO, measured with an SSA at center frequencies of 81.25 MHz (—) and 1.3 GHz (—).

which leads to results not dependent on the amplitude nor on the center frequency, shown in Fig. 3.16. Spectra measured with commercial devices, as well as manually estimated ones, are directly comparable. Moreover, a direct integration can be used to estimate the timing jitter and the parameters are better scaled, from a numerical point of view. For this reason, the phase spectrum will be used further in this work. Moreover, dB$_{\text{fs}^2/\text{Hz}}$ will be defined as dB with respect to the reference of 1 $\frac{\text{fs}}{\sqrt{\text{Hz}}}$ for amplitudes and 1 $\frac{\text{fs}^2}{\text{Hz}}$ for power signals.

3.7 Controller Design

The next section briefly introduces the controller used later in this work. For further information the author recommends classical text books like [ÅM08], [SP01] and [DFT92].

3.7.1 PI Controller

For reference, the currently used Proportional-Integral (PI) controller structure is taken into account, given by

$$K(s) = K_p + K_i \frac{1}{s} = \left[\begin{array}{c|c} 0 & K_i \\ \hline 1 & K_p \end{array}\right] \quad \text{and} \quad K(s) = K_p \left(1 + \frac{1}{T_i s}\right) = \left[\begin{array}{c|c} 0 & T_i^{-1} \\ \hline K_p & K_p \end{array}\right]. \tag{3.46}$$

The control parameters K_p and K_i are heuristically tuned in such a way, that for the MLO, the connected SSA shows a small value for the closed loop timing jitter or for the LSU, the mean controller error $e(t)$ is small.

3.7.2 Linear Quadratic Gaussian Control

The Linear Quadratic Regulator (LQR) controller is given by the control law

$$u(t) = -F\,x(t)\,, \tag{3.47}$$

where F is the so-called state feedback gain chosen such that the cost function

$$V = \int_0^\infty x(t)^T Q x(t) + u(t)^T R u(t)\,dt\,, \quad Q \in \mathbb{R}^{m\times m} \geq 0\,, \quad R \in \mathbb{R}^{n\times n} > 0, \tag{3.48}$$

is minimized for the closed loop. With the system description (3.2) this state feedback gain is given by

$$F = -R^{-1}B^T P\,, \tag{3.49}$$

where P is the positive definite solution to the matrix Riccati Equation

$$PA + A^T P - PBR^{-1}B^T P + Q = 0\,. \tag{3.50}$$

In most cases, not all states $x(t)$ are measurable. Therefore, an observer is used to estimate the states $\hat{x}$. For the observer design, the assumed plant is given by

$$\dot{x}(t) = Ax(t) + Bu(t) + w(t)\,, \tag{3.51a}$$
$$y(t) = Cx(t) + v(t)\,, \tag{3.51b}$$

where $w(t)$ and $v(t)$ are AWGN with

$$E[w(t)w^T(t+\tau)] = Q_e\delta(\tau) \quad \text{and} \quad E[v(t)v^T(t+\tau)] = R_e\delta(\tau)\,. \tag{3.52}$$

The observer $G_{\text{Obsv}}(s)$, estimating $\hat{x}$, is given by

$$\left[\begin{array}{c}\dot{\hat{x}}\\ \hline \hat{x}\end{array}\right] = \left[\begin{array}{c|cc} A-LC & B & L \\ \hline I & 0 & 0\end{array}\right]\left[\begin{array}{c}\hat{x}\\ \hline u\\ y\end{array}\right], \tag{3.53}$$

where the observer gain L is chosen to minimize the estimator cost function

$$V_e = \lim_{t\to\infty} E[(x(t)-\hat{x}(t))^T(x(t)-\hat{x}(t))]\,. \tag{3.54}$$

The solution to this minimization is dual to the previous one. The observer gain L is

$$L = -P_eC^TR_e^{-1}\,, \tag{3.55}$$

where P_e is the positive definite solution to

$$P_eA^T + AP_e - P_eC^TR_e^{-1}CP_e + Q_e = 0\,. \tag{3.56}$$

The combination of optimal state feedback controller and optimal state estimation is known as Linear Quadratic Gaussian (LQG) controller, see e. g. [SP01]. One implementation of this controller, $K(s)$, is given by

$$\left[\begin{array}{c}\dot{\hat{x}}\\ \hline u\end{array}\right] = \left[\begin{array}{c|c} A-LC-BF & L \\ \hline F & 0\end{array}\right]\left[\begin{array}{c}\hat{x}\\ \hline y\end{array}\right]. \tag{3.57}$$

The matrices Q and R and the matrices Q_e and R_e are tuning parameters for the controller and for the observer, respectively. If known, the tuning parameter of the observer should be chosen as the real variance of disturbance and noise, which leads to an optimal estimation of the system states. Moreover, it is important to choose the tuning parameter in such a way, that the dynamics of the observer are faster than those of the closed loop state feedback system.

In order to add an integral behavior to the controller, the design rules can be applied to an augmented plant $G_{Aug}(s)$, given by

$$\left[\begin{array}{c}\dot{x}\\ \dot{x}_i\\ \hline y\\ x_i\end{array}\right] = \left[\begin{array}{cc|c} A & 0 & B \\ C & 0 & 0 \\ \hline C & 0 & D \\ 0 & I & 0\end{array}\right]\left[\begin{array}{c}x\\ x_i\\ \hline u\end{array}\right]. \tag{3.58}$$

An example using colored noise for this design is given in [Bay99, p. 501]. It shows how to handle a 4 Hz oscillation which disturbs the state vector of a second order system.

3.7.3 Extended Kalman Filter

The observer in the previous design assumes, that the plant is linear. If this is not the case in the required operation range, the Extended Kalman Filter (EKF) can be used to add non-linear dynamics, see e. g. [CC09].

The non-linear discrete time system, assumed for the EKF design, is given by

$$x(k+1) = f(x(k), u(k)) + w(k)\,, \tag{3.59a}$$
$$y(k) = h(x(k)) + v(k)\,, \tag{3.59b}$$

which is a more general form of (3.51).

In the first step of this estimator, the new states are calculated based on the previous sample,

$$\hat{x}_k^- = f(\hat{x}_{k-1}, u_k)\,, \quad P_k^- = F_k P_{k-1} F_k^T + Q \tag{3.60}$$

with

$$F_k = \left.\frac{\partial f}{\partial x}\right|_{\hat{x}_{k-1}, u_k}\,. \tag{3.61}$$

After this step, the optimal Kalman gain is calculated by

$$K_k = P_k^- H_k^T (H_k P_k^- H_k^T + R)^{-1}\,, \tag{3.62}$$

with

$$H_k = \left.\frac{\partial h}{\partial x}\right|_{\hat{x}_k^-}\,. \tag{3.63}$$

The last step is the correction of the estimated state and the update of the covariance matrix

$$\hat{x}_k = \hat{x}_k^- + K_k(y_k - h(\hat{x}_k^-))\,, \quad \hat{P}_k = (I - K_k H_k) P_k^- \tag{3.64}$$

Roughly speaking, the EKF is a state observer that is linearized in each sample instance around the current state vector.

3.7.4 $\mathcal{H}_2$ and $\mathcal{H}_\infty$ Optimal Control

In this section a brief introduction of modern controller design based on the minimization of the system norms, introduced in Section 3.1.2, is given. For many performance requirements it is possible to express them in terms of these norms. A controller that minimizes this norm, automatically optimizes its behavior to the given requirements. An introduction to these concepts is given in [SP01] and [ZDG96].

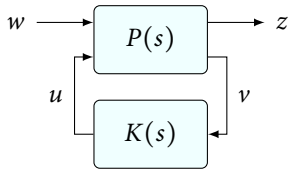

Figure 3.17: General control structure.

The general control structure for these problems is shown in Fig. 3.17, where the generalized plant $P(s)$ and the controller $K(s)$ are given as

$$\begin{bmatrix} \dot{x} \\ \hline z \\ v \end{bmatrix} = \left[\begin{array}{c|cc} A & B_1 & B_2 \\ \hline C_1 & D_{11} & D_{12} \\ C_2 & D_{21} & D_{22} \end{array}\right] \begin{bmatrix} x \\ \hline w \\ u \end{bmatrix} \quad \text{and} \quad \begin{bmatrix} \dot{x}_C \\ \hline u \end{bmatrix} = \left[\begin{array}{c|c} A_C & B_C \\ \hline C_C & D_C \end{array}\right] \begin{bmatrix} x_C \\ \hline v \end{bmatrix}, \tag{3.65}$$

with the exogenous input w, the control variable u, the performance output z and the measurement v. The minimization problem is given by

$$\min_{K(s)} \left\| \mathcal{F}_l(P(s), K(s)) \right\|_n, \quad n \in [2, \infty], \tag{3.66}$$

where $\mathcal{F}_l$ is the lower fractional transformation, and given by

$$\mathcal{F}_l(P(s), K(s)) = P_{zw}(s) + P_{zu}(s)(I + K(s)P_{vu}(s))^{-1}K(s)P_{vw}(s). \tag{3.67}$$

It is possible for the generalized plant $P(s)$ to implement the control loop, shown in Fig. 3.1, and in addition to add weighting filters that are chosen such that the transfer function from w to z gives the cost function to be minimized.

E. g. using the $\mathcal{H}_2$ norm and choosing

$$B_1 = \left[Q_e^{\frac{1}{2}}, 0\right], \qquad B_2 = B, \qquad D_{11} = \mathbf{0}, \qquad D_{12} = \left[0, R^{\frac{1}{2}}\right]^T,$$
$$C_1 = \left[Q^{\frac{1}{2}}, 0\right]^T, \qquad C_2 = -C, \qquad D_{22} = 0, \qquad D_{21} = \left[0, R_e^{\frac{1}{2}}\right],$$

leads to the synthesis of the LQG controller shown in Sec. 3.7.2.

If the $\mathcal{H}_\infty$ norm is used, the norm based synthesis finds a controller that leads to a certain defined behavior for some of the functions in the GOF, see Sec. 3.1.3.

S/KS Problem

Different generalized plants are commonly used. The structure shown in Fig. 3.18 allows one to specify a wanted behavior for the sensitivity function to adjust the performance and for the noise sensitivity function to limit the allowed control action.

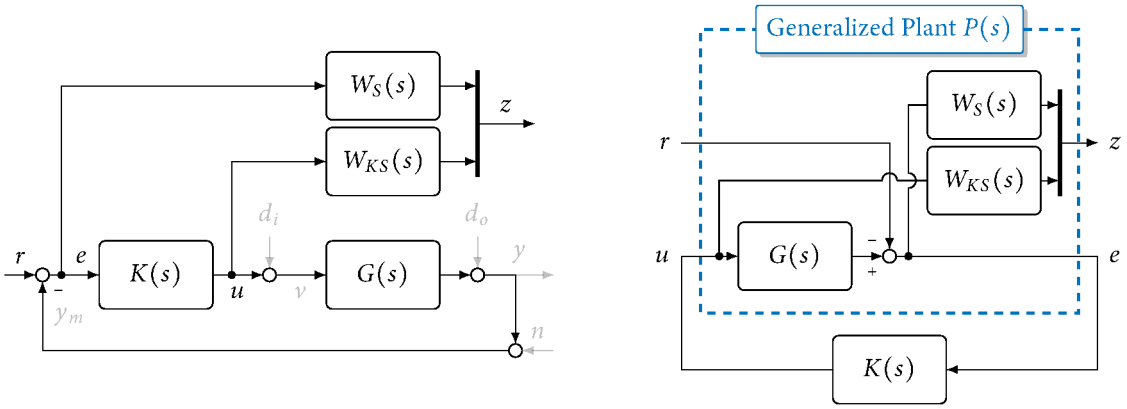

Figure 3.18: Block diagram of the S/KS design in the general control loop (left) and setup in form of a generalized plant (right).

Four Block Problem

If disturbances play a role in control problem, it is possible to extend the generalized plant in Fig. 3.19 by a filter $W_{di}(s)$. This leads to a controller that has a superior input disturbance rejection than the one with the previous design.

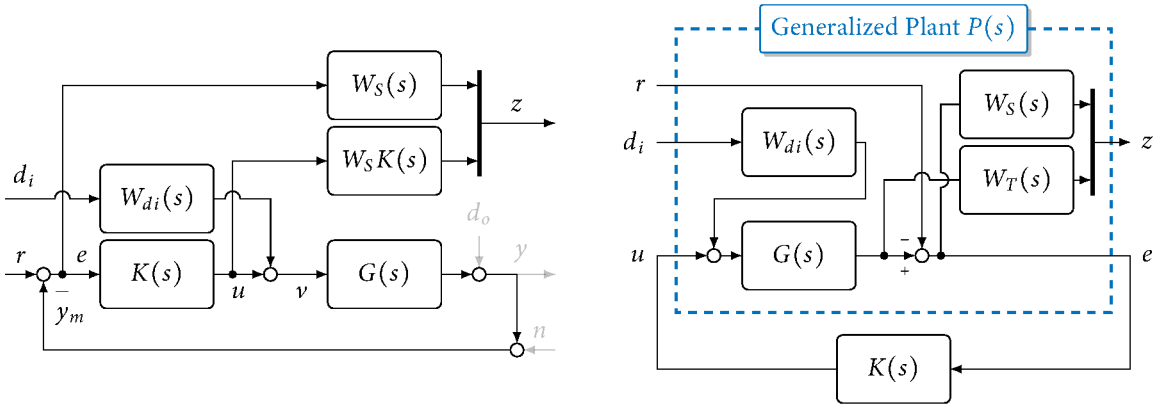

Figure 3.19: Block diagram of the four block design in the general control loop (left) and setup in form of a generalized plant (right).

3.7.5 The Smith predictor

A common problem, which is expected for the LSU, is a time delay between the system and the measurement. If the dynamics and the delay are known, a so-called Smith predictor, introduced in [Smi59], can be used. The author recommends [MP05] or [NC07] for a more expansive account.

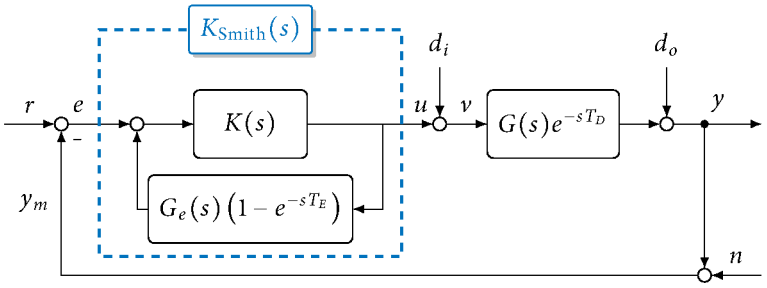

Figure 3.20: Control loop with a Smith predictor.

Figure 3.20 shows a closed controlled loop with the time delayed system $G(s)e^{-sT_D}$ and a controller $K_{\text{Smith}}(s)$, being composed of a controller $K(s)$ and the Smith predictor part below.

The controller output for this loop is given by

$$u = K(s)\left((r - G(s)e^{-sT_D}u) - G_e(s)(1 - e^{-sT_E})u\right) , \tag{3.68}$$

which simplifies to

$$u = K(s)\left(r - G_e(s)u\right) , \tag{3.69}$$

if the input-output behavior of the estimated plant $G_e(s)$ and the real plant $G(s)$ are the same and if the estimated time delay T_E is equal to the real time delay T_D.

The noise sensitivity function for the closed loop is given by

$$KS(s) = \frac{K(s)}{1 + G_e(s)K(s)} \tag{3.70}$$

and the complementary sensitivity function by

$$T(s) = \frac{K(s)G(s)}{1 + G_e(s)K(s)}e^{-sT_D} . \tag{3.71}$$

With this structure, and a constant time delay, the controller $K(s)$ can be designed for delay-free system $G(s)$. The Smith prediction part, placed around the controller, requires a good system model and a precise estimation of the time delay.

4 MASTER LASER OSCILLATOR

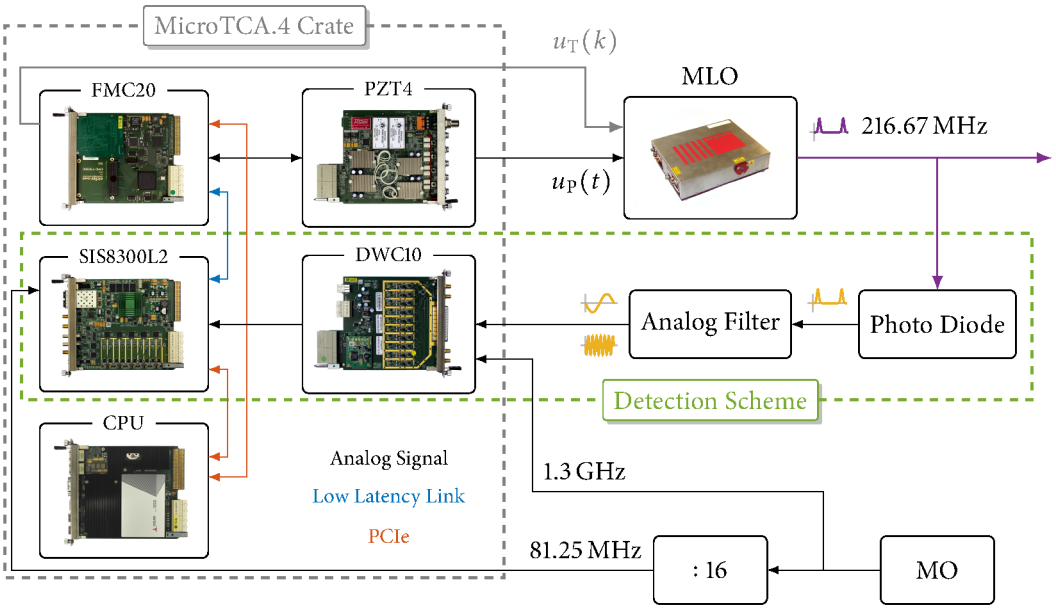

Figure 4.1: Overview of the MLO control scheme discussed in this chapter.

The MLO is the first main component of the LbSync system which will be analyzed. This laser setup is used to generate the pulse train and stabilize its frequency against the electrical MO of the facility. Recent developments are given in [Fel+14] and [Fel+15]. In the following chapter the MLO setup is explained and the characteristic behavior is derived. After that, the system is identified and a suitable model is proposed. The performance limitations for the given setup are shown and different control strategies are evaluated. The chapter closes with an outlook on how to further increase the performance of this individual component.

4.1 Modeling

An overview of the components used for the MLO control scheme is given in Fig. 4.1. The light source for the MLO is a passively mode-locked laser, with a pulse repetition rate of 216.67 MHz. Special properties of this laser are: a pulse duration of < 200 fs, an average power up to $\approx$ 150 mW, and an amplitude noise of less than 0.2% (rms). Moreover, its wavelength of 1550 nm is often used in telecommunication industries. This offers a wide spectrum of available components.

4.1.1 Basic Functionality

The frequency of this laser can be tuned by two actuators, either a piezo crystal or a temperature stage changing the laser cavity length, hence the output frequency $\omega(t)$. It is known, that a piezo crystal has a much higher bandwidth, and it is obvious to expect much better results with this actuator for the frequency tuning. Therefore, the input $u_\mathrm{P}(t)$ is chosen as the main control input. The internal temperature stage, exited by $u_\mathrm{T}(k)$, changes the frequency in a much wider range but much more slowly. It will be used to move the laser to the operation range of the piezo and to compensate for slow drifts in the order of minutes or hours. The influence of these two actuators is shown in Fig. 4.2.

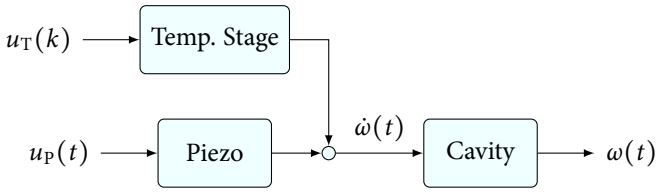

Figure 4.2: Influence of both laser oscillator inputs.

In order to detect the frequency and the phase error with respect to the MO of the generated laser pulses, three detection schemes are currently available. In all cases, the laser pulse train is captured with a photo diode and the resulting electrical signal is filtered and mixed to an intermediate frequency.

These signals enter the MicroTCA.4 crate via a DWC10 down converter board. It is used to pipe the signals trough or convert the signal to the intermediate frequency sampled by a SIS8300L2. This board combines the sampling ADCs and an FPGA with the control algorithm. The control signal $u_\mathrm{P}(k)$ is sent via a Low Latency Link (LLL) over the backplane to an FMC20 board that forwards this signal to the PZT4 piezo amplifier. The high voltage output $u_\mathrm{P}(t)$ of this amplifier is then connected to the piezo in the laser, closing the feedback loop.

The coarse tuning of the laser is implemented on the crates CPU board. The current control signal $u_{\mathrm{P}}(k)$ is read via PCIe and if it reaches a defined threshold the CPU board sends trough a module attached on the FMC20 the signal to tune the laser with the coarse input $u_{\mathrm{T}}(k)$.

4.1.2 Pulse Train

The pulse train, generated by the MLO, will be used as a timing reference at the attached devices. Some of the control objectives introduced later are properties of this pulse train.

Figure 4.3 shows the pulse train measured by a photo diode (——) and the same signal bandpass filtered around 1.3 GHz (——). The timing information is distributed by this signal and each of the peaks corresponds to a clock of the 216.67 MHz MLO, see 2.2. The smaller peaks are caused by the measurement and the detection bandwidth. They are not visible in the optical signal.

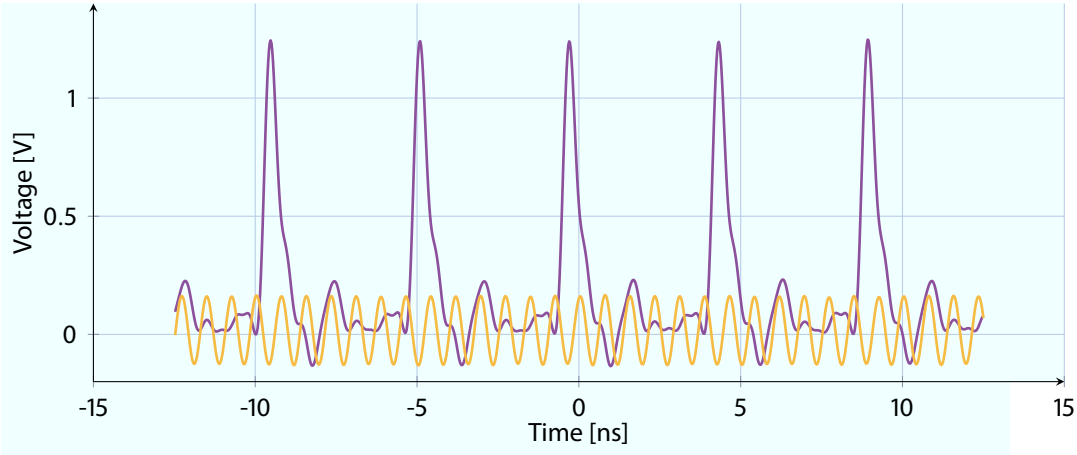

Figure 4.3: Measurement of photo diode (——) capturing the pulse train and the 6th harmonic (——) of this signal

In [Pas08], it is shown, that the shape of mode-locked laser pulse is given by

$$p(t) = P\ \mathrm{sech}^2\left(\frac{t}{\tau}\right) = \frac{P}{\cosh^2\left(\frac{t}{\tau}\right)}, \tag{4.1}$$

where P denotes the maximum pulse power and the Full Width Half Maximum (FWHM) of the pulse is given by the pulse duration parameter τ multiplied by ≈ 1.76. If this shape does not change over time, it is possible to model this pulse train in the time domain as a dirac comb multiplied with this shape, i. e.

$$p(t) = \sum_{k=-\infty}^{\infty} \delta(t + d - kT)\frac{P}{\cosh^2\left(\frac{t}{\tau}\right)}, \tag{4.2}$$

where T is the period time of the pulse train and d is a slight deviation in the pulse position. The period time T and the corresponding length L of the pulse train are given by

$$T = f^{-1} \quad \text{and} \quad L = n^{-1}Tc\,, \tag{4.3}$$

where f is the pulse repetition rate, n the refractive index and the speed of light is given by c.

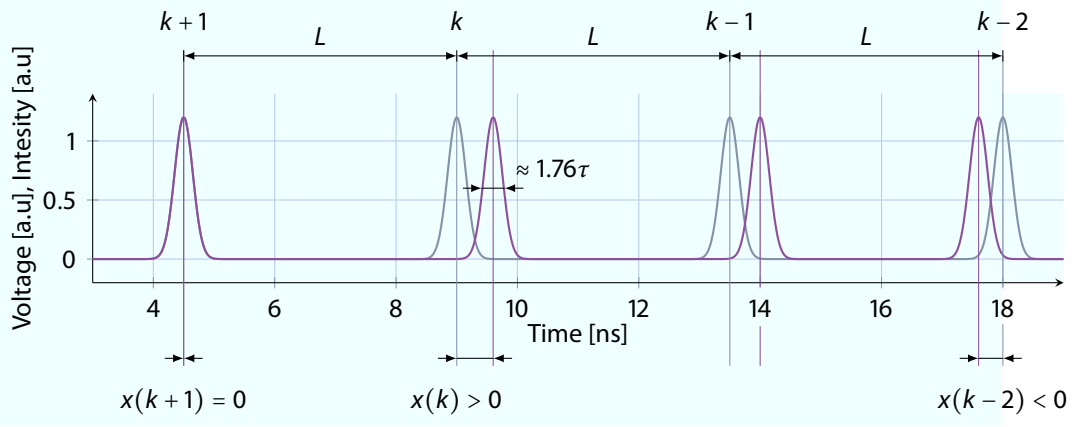

Figure 4.4: State modeling of the pulse train, showing the ideal timed pulse (——) and one with a timing error (——)

Figure 4.4 shows the assumed perfect pulse train (——) that is not known, and the real pulse train (——). At state x we use the difference between these pulses. If we take a look at a certain position in the fiber over time, k denotes a multiple of the time difference after which a new pulse arrives. Moreover, if we take a look at the whole system at one instance of time, L denotes the length difference between two perfectly timed pulses. The important figures of the pules train used for the LbSync system are summarized in Table 4.1.

Table 4.1: Data of the Pulse Train

Description	Value	Unit
Repetition Rate	216.67	MHz
Fiber refraction index	1.446	
Pulse distance T	4.615	ns
Pulse distance L in free-space	1.384	m
Pulse distance L in fiber	0.957	m

4.1.3 Phase Detection Schemes

Before starting the analysis of the dynamic behavior of the MLO, it is important to understand the different detection schemes, shown in Fig. 4.5. These are used to get the relative phase difference between the MO and MLO. If this value goes to zero, both oscillators have the same phase and frequency. All frequencies in these schemes are derived from the main 1.3 GHz master oscillator. For the sake of simplicity, some are rounded or truncated.

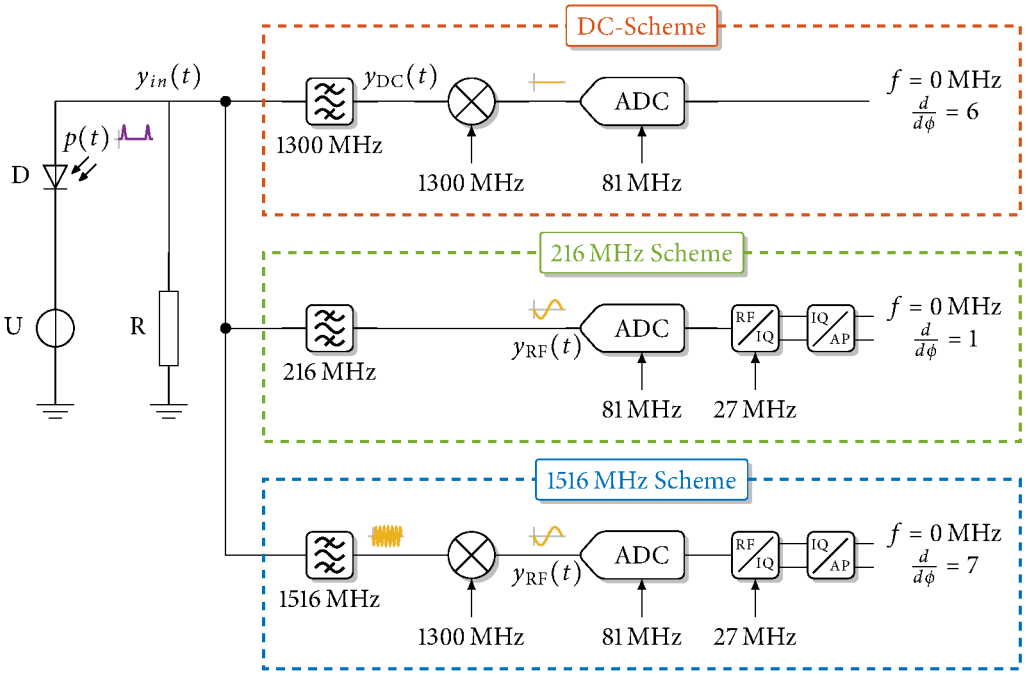

Figure 4.5: Different detection schemes for the MLO signal.

DC-Scheme

The DC-Scheme, shown in the upper part of Fig. 4.5, is previously used in the VME setups and works similar to the procedure introduced in Sec. 3.6. Using a photo diode, the pulse is converted into an electrical signal $y_{in}(t) = kp(t)$, where k denotes the gain of the photo diode, and filtered with a passband of around 1.3 GHz, the sixth harmonic of the pulse train, which gives the signal

$$y_{\mathrm{DC}}(t) = a \cdot \sin(6 \cdot \omega_{\mathrm{P}} t + 6 \cdot (\phi(t) + \phi_n(t))) , \tag{4.4}$$

whereas ω_{P} is the 216.67 MHz repetition rate of the pulse train and $\phi_n(t)$ denotes a phase change of this signal due to a small deviation of the pulse frequency. The signal should be synchronized with the sinusoidal reference signal of the MO,

$$r(t) = \sin(\omega_{MO} t) . \tag{4.5}$$

To get the difference of those signals, both are mixed. The resulting error signal is given by

$$e(t) = r(t) \cdot y_{\mathrm{DC}}(t), \tag{4.6}$$

$$= \frac{a}{2} \underbrace{\sin((\omega_{\mathrm{MO}} + \omega_{\mathrm{MLO}}(t))t + \phi(t) + \phi_n(t))}_{\gamma_{high}} +$$

$$\frac{a}{2} \underbrace{\sin((\omega_{\mathrm{MO}} - \omega_{\mathrm{MLO}}(t))t - \phi(t) - \phi_n(t))}_{\gamma_{low}}, \tag{4.7}$$

$$\dot{\phi}(t) = \omega_{\mathrm{MO}} - \omega_{\mathrm{LO}}(t), \tag{4.8}$$

$$\phi(0) = \phi_0. \tag{4.9}$$

where $r(t)$ is the signal from the MO with the angular frequency $\omega_{\mathrm{MO}} = 2\pi \cdot 1.3\,\mathrm{GHz}$. The signal $y_{\mathrm{DC}}(t)$ generated by the laser pulse train with an angular frequency $\omega_{\mathrm{MLO}}(t)$ and phase noise $\phi_n(t)$ acting on the phase $\phi(t)$. These nonlinear equations are similar to the ones in [Abr02]. In order to linearize the system, the following assumptions are commonly used:

1. The system is close to the operating point, $|\omega_{\mathrm{MO}} - \omega_{\mathrm{LO}}(t)| \to 0$.
2. There are just small phase changes, $\sin(\phi(t)) \approx \phi(t)$.
3. High order harmonics are filtered and therefore the upper sideband vanishes, $\gamma_{high} \to 0$.
4. An input to the laser leads to a linear change around the nominal frequency, i. e. the piezo amplifier bandwidth and the piezo resonances are at higher frequencies than the expected closed loop bandwidth, $\omega_{\mathrm{MLO}}(t) = k u_{\mathrm{P}}(t) + \omega_{\mathrm{MO}}$.

The first assumption allows one to just take a look at the frequency differences, i. e. $r(t)$ as the reference phase and $y(t)$ as the output phase, both with respect to the sinusoidal signal $\tilde{r}(t)$. Assumption 1. and 2. are used to linearize γ_{low} and together with 3. to linearize 4. The last assumption sets the piezo transfer function to a constant gain, which is valid if the piezo is much faster than the frequency changes.

With this simplifications the linearized system dynamics can be described by an integrator, i.e. in the time domain as

$$\dot{\phi}(t) = -k u_{\mathrm{P}(t)}, \tag{4.10}$$

$$e(t) = -\frac{a}{2}(\phi(t) + \phi_n(t)). \tag{4.11}$$

If the phase error $e(t)$, with the given assumption, is zero over time, the input signal is equal in frequency and phase. The phase noise is an output disturbance to the dynamic system given by the transfer function

$$G(s) = \frac{E(s)}{U(s)} = \frac{ak}{2s}. \tag{4.12}$$

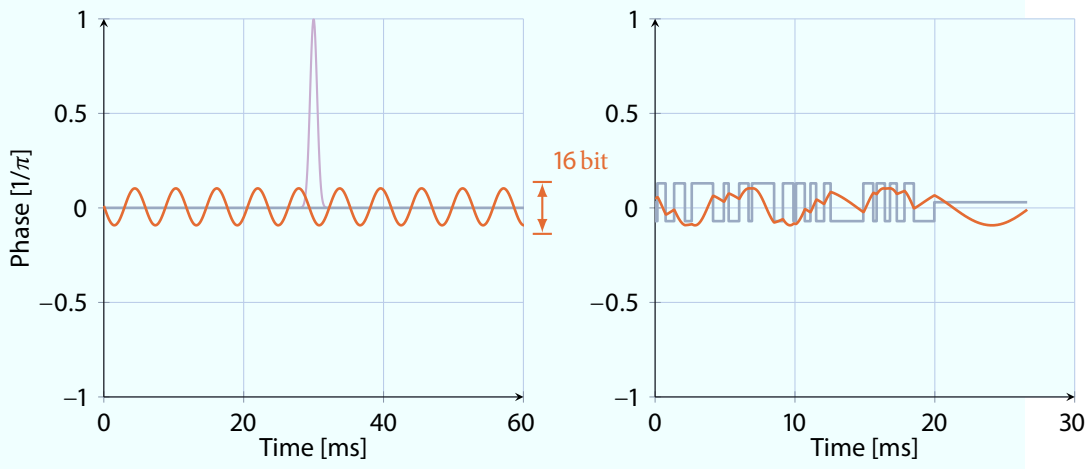

Figure 4.6: Example measurement of the MLO detection scheme. With the optical pulse (—), the excitation signal (—) and the response of the DC channel (—).

This shows, as expected, that the phase shift $\phi(t)$ between both frequencies and therefore the error $e(t)$ will diverge if both frequencies are not equal.

Figure 4.6 shows the measured error signal $\tilde{e}(t)$ of this scheme for an open loop configuration where assumption 1. doesn't hold. The beat frequency is clearly visible and in the right part one can see the integral behavior.

The nonlinear behavior of the DC-Scheme has further disadvantages. The system identification is more complicated and the excitation signal has to be small to keep the output within the linear region. Moreover, in the later closed loop operation, large disturbances can move the system to another stable equilibrium point. Due to the usage of the 6-th harmonic, there are 12 different phases of the pulse where the DC signal has a zero crossing. Just with this signal it is not possible to detect to which of those stable points, the controller moved the loop. The region around these different stable working points is called "bucket" in the LbSync group.

216 MHz and 1516 MHz Scheme

In order to avoid the difficulties with the DC-scheme, it is possible to use other schemes based on an IQ-demodulation of a sampled intermediate frequency.

Fig. 4.7 shows the concept of the demodulation. The measured sinusoidal signal

$$y_{\mathrm{RF}}(t) = A\sin(\omega t + \phi(t)) \tag{4.13}$$

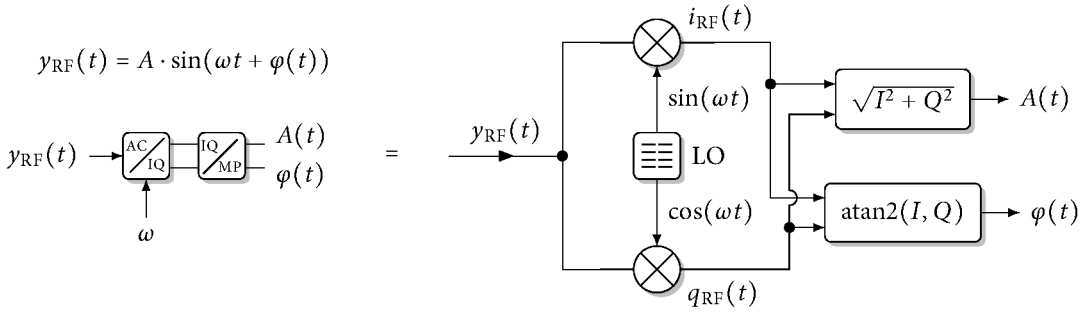

Figure 4.7: Principle of IQ detection with subsequent magnitude phase calculation.

is mixed with the sine and cosine part of the internal oscillator LO,

$$i_{RF}(t) = y_{RF}(t)\sin(\omega t) = \frac{1}{2}A\cos(\phi(t)) - \frac{1}{2}A\cos(2\omega t + \phi(t))\,, \tag{4.14}$$

$$q_{RF}(t) = y_{RF}(t)\cos(\omega t) = \frac{1}{2}A\sin(\phi(t)) + \frac{1}{2}A\sin(2\omega t + \phi(t))\,. \tag{4.15}$$

These two parts describe which part of the oscillation, $y_{in}(t)$, is in phase $i_{in}(t)$ and not in phase $q_{in}(t)$, with respect to the internal oscillator LO.

With a low pass filtered $i_{in}(t)$ and $q_{in}(t)$, the amplitude of the external signal is than given by

$$A(t) = \sqrt{i_{RF}(t)^2 + q_{RF}(t)^2} = \sqrt{\frac{A^2}{4}(\cos^2(\phi(t)) + \sin^2(\phi(t)))} = \frac{A}{2} \tag{4.16}$$

and the phase with respect to the phase of the internal oscillation by

$$\varphi(t) = \text{atan2}\left(A\frac{1}{2}(\cos(\phi(t)), A\frac{1}{2}(\sin(\phi(t))\right)\,. \tag{4.17}$$

If the phase $\varphi(t)$ is zero over time both oscillations have the same phase and frequency.

In both schemes the signal frequency is around 216.67 MHz and the sampling frequency is 81 MHz. As discussed in Sec. 3.4.1., this is called under sampling and due to a lack of an anti-alias filter the frequencies in higher Nyquist zones are mapped to the primary one. In this case we use the 6-th Nyquist zone and end up in a visible frequency of

$$\left(\frac{1}{6} - 3\cdot\frac{1}{16}\right)1.3\,\text{GHz} = \frac{1}{48}1.3\,\text{GHz} \quad \text{i. e.} \quad 216.67\,\text{MHz} - 3\cdot 81\,\text{MHz} \approx -27\,\text{MHz} \tag{4.18}$$

after the sampling. This frequency is the one used for the internal oscillator LO generated by the 81 MHz of the board clock.

Figure 4.8 shows the example measurement with both IQ-demodulation schemes. The main advantage of this scheme is that the phase error is linear in these cases. A possible disadvantage is that additional noise and jitter is added by the ADC, because the exact sampling is the reference. This sampling is triggered by a signal generated from the MO signal.

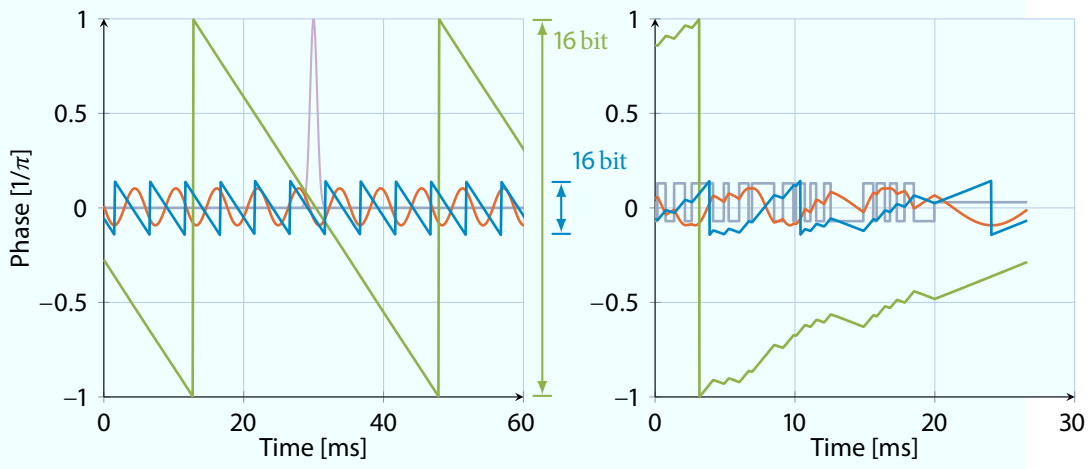

Figure 4.8: Example measurement of the MLO detection scheme. With the optical pulse (—), the excitation signal (—), the response of the DC channel (—), the 216 channel (—) and the 1516 channel (—).

Phase Unwrapping

To combine the sensitivity of the 1516 MHz scheme and the dynamic range of the 216.67 MHz signal a phase unwrapping technique can be used. The main idea is given in [ESQ11].

With this method, the bucket detection stage is not necessary during operation but the system setup requires more steps. From a control point of view, the robustness against disturbances is increased due to the extended dynamic range. The lock will not be lost with this detection method if large disturbances occur and it is not necessary to go through different steps to re-lock the laser.

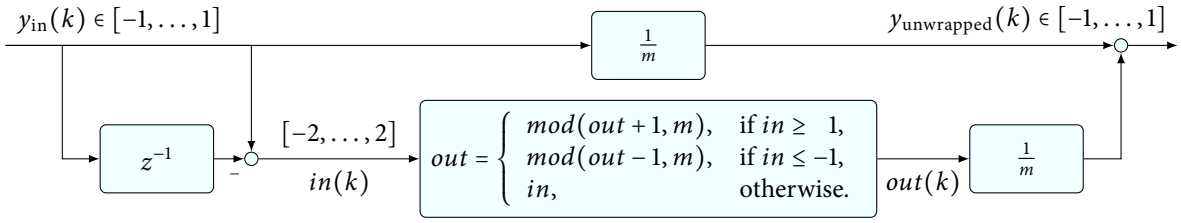

Figure 4.9: Algorithm for the phase unwrapping.

The algorithm implemented for this task is depicted in Fig. 4.9. The input $y_{\text{in}}(k)$ is subtracted from the previous value. If this result is larger than one, there was a jump from the area above 0.5 to the area below −0.5. For a result smaller than one, from the lower to the upper area. As long as the expected frequency change is much smaller than the sampling rate, the jumps indicate a wrap in the binary representation of the value. These wrap arounds can be counted and used to shift the current value to one with fewer wraps.

Figure 4.10 shows this approach. The algorithm was applied on the 1516.67 MHz signal (—) with a parameter set to reach the same dynamic range like the 216.67 MHz signal (—). The unwrapped phase (—) has the same dynamic range than the 216.67 MHz signal but also the same sensitivity than the 1516.67 MHz signal.

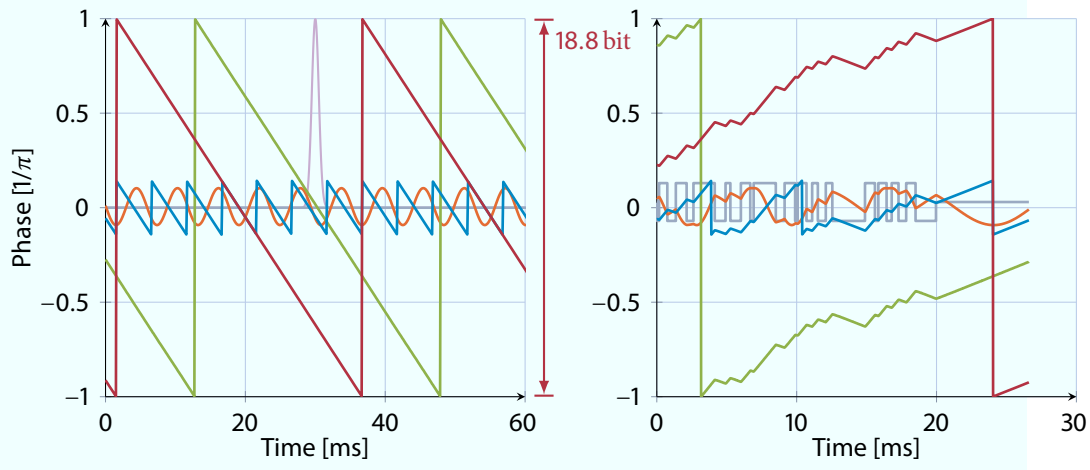

Figure 4.10: Example measurement of the MLO detection scheme. With the optical pulse (—), the excitation signal (—), the response of the DC channel (—), the 216 channel (—), the 1516 channel (—) and the unwrapped channel (—).

With this scheme we can increase the robustness of the laser locking, especial the one of the PPL and the IL, see Sec. 2.2.3. These systems suffer from the occurrence of bucket jumps. This algorithm can capture these events to prevent the controller moving to the wrong stable position.

Comparison

The main advantages and disadvantages of the different schemes are summarized in Table 4.2. The sensitivity of the DC-Scheme is adjustable, which could be used to detect tiny disturbances in the steady state, but this scheme is very sensitive to disturbances that lead to bucket jumps. This could be prevented by using the other schemes. These have a continuous phase mapping and a linear response to phase changes. On the other hand, they require much more FPGA resources, because an IQ and amplitude-phase detection is needed.

As a first approach, the unwrapped 1516 MHz scheme is used. A preferable later solution could be the usage of the 216.67 MHz for the rough estimation and bucket detection. Close to the working point a sensitive DC-Scheme could be used. This combination minimizes the hardware components while maintaining a very good performance. Both signals should be combined with a continuous function to avoid jumps at the transition of both measurements.

Table 4.2: Properties of the different detection schemes used for the MLO

	DC-Scheme	216 MHz	1516 MHz	1516 MHz unwrapped
Sensitivity	adjustable	low	high	high
Calibration required	yes	no	no	no
Linear response	✗	✓	✓	✓
Distinct bucket	✗	✓	✗	constant offset
FPGA resources	low	high	high	very high

4.1.4 Model Structure

With the detection scheme it is possible to get a first model structure for the MLO, which is shown in Fig. 4.11. The signals r, e, φ_{MLO}, y and y_m are phase values with respect to the absolute phase of an ideal oscillation at the system frequency of 216.67 MHz, as described in Section 4.1.2. The plant internal signals ω_{MLO}, ω_{coarse} and ω_{beat} are also frequencies with respect to the system center frequency.

The noise input n_{MO} is the timing error of the MO with respect to a perfect reference oscillator and the timing error of the MLO is modeled by the output disturbance channel d_{MLO}. The sum of n_{MO}, d_{MLO} and φ_{MLO} is the signal y_m, which is measured by the detection scheme.

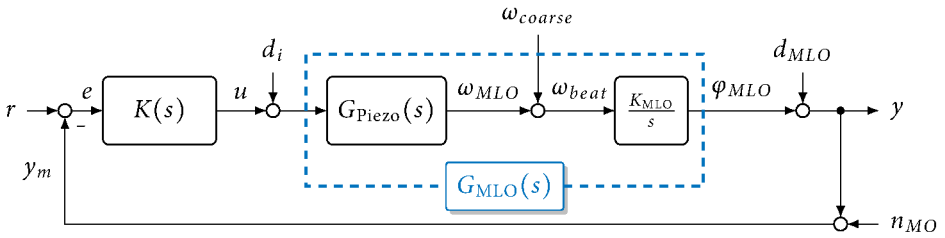

Figure 4.11: Control loop for the MLO system with the timing error of the MO n_{MO}, the timing error of the MLO d_{MLO} and the measurement of the detection scheme y_m.

This model fulfills following important observations:

- A voltage applied to the piezoelectric actuator changes the laser cavity length and therefore the frequency of the laser pulse train.
- The phase noise spectra of MO and MLO don't change with the center frequency.
- The MLO system has an integral behavior.
- A PI controller is required to get a zero steady state error, due to a non zero mean disturbance input.

4.1.5 Control Objectives

Already at the system identification step it is important to have an idea of the performance of the closed loop. The identified model will fit to the behavior of the system in the range where the identification signal excites the system. Differences at frequencies far below that of the closed loop bandwidth will be captured by the integral behavior of the controller, and those far above the region of interest are negligible because the closed loop will not be able to act on them.

For the MLO system the major requirement is to decrease the timing jitter of the laser pulse train. With the basic properties, already discussed in Section 3.6, and the model introduced in the previous section, it is obvious that if the control loop is open $K(s) = 0$ the laser pulse train has the same error as the laser itself. If the closed loop bandwidth was infinite $T(s) = 1$ the laser pulse train would just have the error of the MO. For other configurations, the error of the laser pulse train follows the MO below the closed loop bandwidth and the MLO above. With no other disturbance and noise influences this could be expressed as

$$y(s) = -T(s)n_{MO}(s) + S(s)d_{MLO}(s) \tag{4.19}$$

The left part of Fig. 4.12 shows the phase noise of the laboratory MO (——) and the MLO (——). The expected closed loop bandwidth is given by the intersection of the MO and MLO noise spectra. The closed loop should follow the MO in lower frequencies where it has a lower noise characteristic. For higher frequencies the laser should run open. An important observation is that a controller, which minimizes the absolute noise of the pulse train, is not the one which minimizes the measurement y_m. It should only minimize the measurement error in the range where the MO has a better characteristic. If the error above that point is minimized, the controller imposes a counteraction to the laser pulse train that is an additional noise on y.

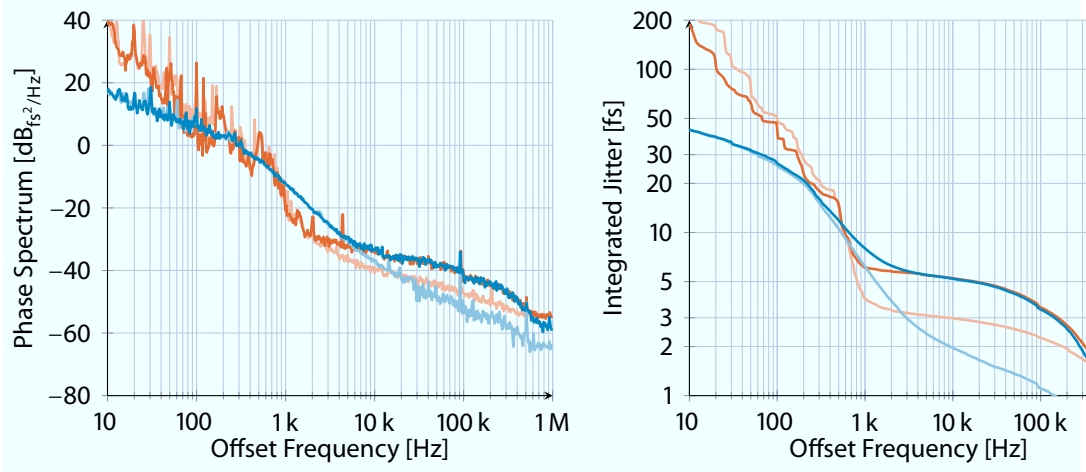

Figure 4.12: SSA phase noise measurement of the lab MO (——) and the OneFive Origami MLO (——), without and with (——), (——) correlations.

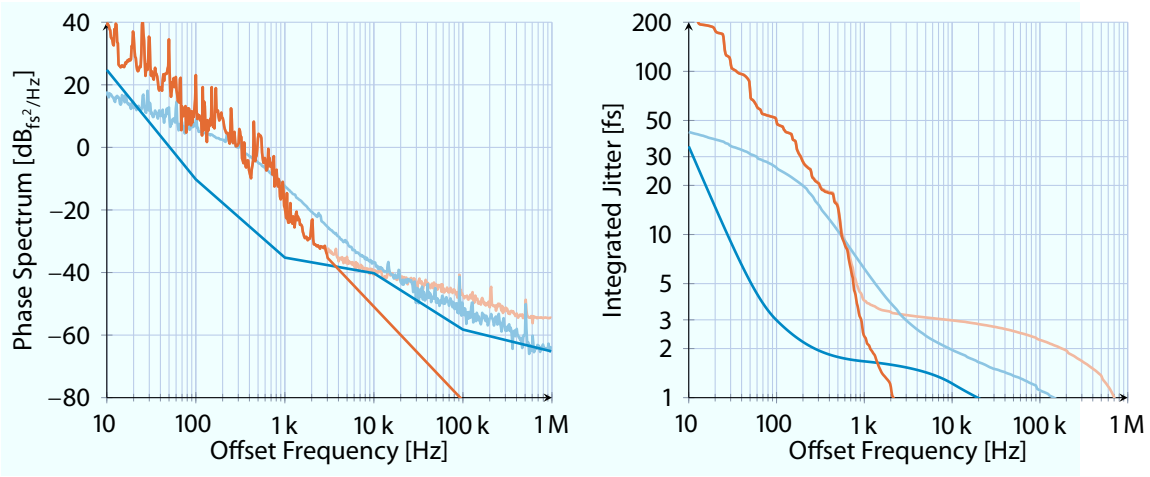

Figure 4.13: XFEL phase noise specification (——), expected phase noise of the MLO (——), lab MO (——) and MLO (——) phase noise measurement.

The integrated timing jitter is shown in the right part of Fig. 4.12, with the laboratory MO (——) and the MLO (——) measured with an SSA. At a level of $-40\,\mathrm{dB_{fs^2/Hz}}$ the inherent noise of the SSA superimposes the measurement. To lower the influence of the measurement device, multiple correlated measurements can be used. The measurement with correlations for the MO (——) and for the MLO (——) shows less influences of the SSA. The characteristic of the lab MO is better in a range below $\approx 1\,\mathrm{kHz}$ and the MLO is better in the range above this value. This leads to an expected closed loop bandwidth of $\approx 1\,\mathrm{kHz}$.

The expected characteristics for the XFEL is given in Fig. 4.13. The specification for the final MO is given in (——), see [Zem+14], and measurements in [Şaf+15] let expect that the phase noise of the MLO (——) decreases like shown. With those data the expected closed loop bandwidth for the XFEL is in a range of $4\,\mathrm{kHz}$.

These assumptions give the expected closed loop bandwidth. For the system identification an excitation signal has to be chosen such that it excites the MLO system in that frequency range, see [Lju99]. In the following a model of the systems dynamic behavior will be identified and after that a model for the coloring filter of the phase noises shown Fig. 4.12 and Fig. 4.13.

4.1.6 Piezo Amplifier

The main actuators for the different applications of the LbSync systems are piezoelectric elements. These ceramics generate a displacement in the range of 10 $^{nm}/_{V}$, the so-called piezoelectric coefficient, if a voltage is applied. High voltages are needed to generate small displacements, and for that purpose the in-house developed PZT4 RTM is used as an amplifier, see [Prz+14].

Dynamic behavior of the Piezo Amplifier

Figure 4.14 shows the simplified circuit of the PZT4. The input voltage, generated by a DAC or an external input, is low pass filtered and fed to an amplifier with a supply voltage of ±100 V.

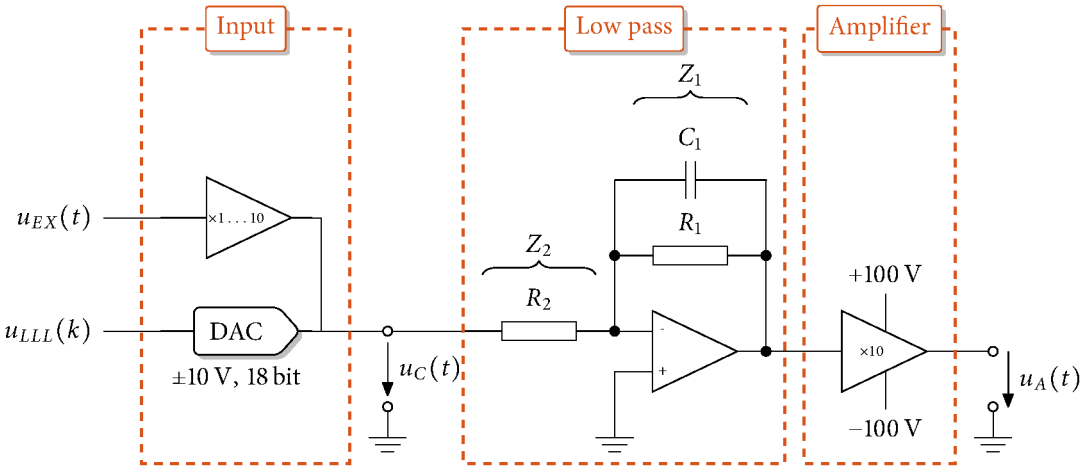

Figure 4.14: Simplified piezo amplifier circuit withighpass its 3 stages.

It is assumed, that the low pass filter can be modeled by a single pole and the amplifier as a constant gain. This leads to the transfer function

$$G_{\text{PZT4,whitebox}}(s) = \frac{u_A}{u_C} = -\frac{Z_2}{Z_1} \cdot G_A = -10 \cdot -\frac{R_1}{R_2} \frac{1}{1 + sR_1C_1}, \tag{4.20}$$

with a negative gain of $G_A = -10$ and ratio of $^{R_1}/_{R_2} = 0.8$. The capacity of C_1 can be adjusted by the software to set the bandwidth of the low pass filter. The steady state gain of the circuit is given by final value theorem as

$$\lim_{s \to 0} G_{\text{PZT4}}(s) = -10 \cdot -\frac{R1}{R2} = 8, \tag{4.21}$$

which gives an operation range of $u_A(t) = \pm 80$ V. In case of the MLO system, the piezo amplifier is used in an unipolar mode with an operation range of $u_A(t) = [0 \ldots 80]$ V.

The transfer function for this well know circuit can be found e. g. in [Hor96].

Validation

To verify the above assumptions a measurement of the frequency response was performed. Figure 4.15 shows the bode diagram of the expected system (- - -), the frequency response measured with a Vector Signal Analyzer (VSA) (——), and of the system identified (——) using *tfest* of the *MATLAB System identification toolbox*. The colors define the setting of the low pass filter, i. e. changing C_1. For the first two settings of 0.3 kHz (——) and 1 kHz (——) the measurement shows that the assumption of a first order system holds. The next two settings, 10 kHz (——) and 50 kHz (——), do not follow the predicted behavior. The slope and phase shift shows that in this frequency region the system behaves as a second order system, even the predicted bandwidth of the PZT4 does not fit anymore.

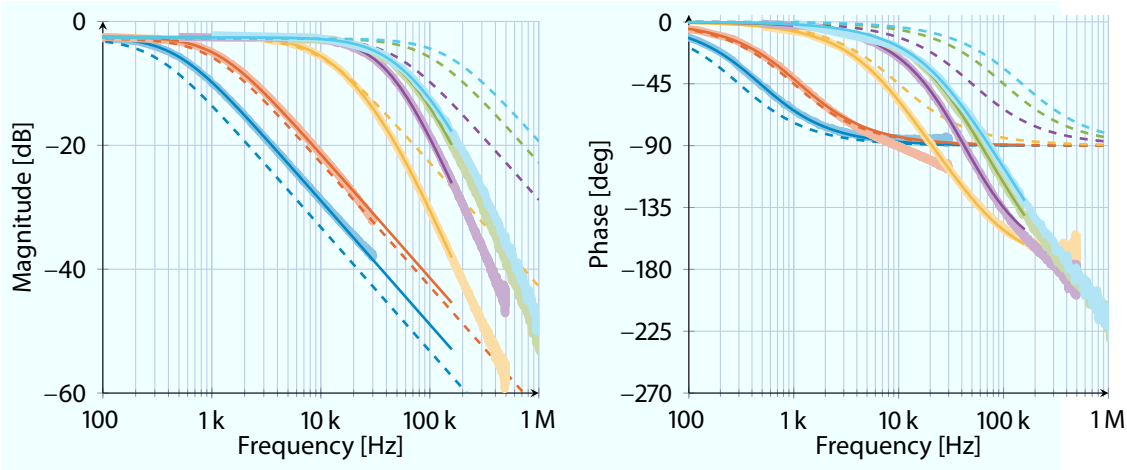

Figure 4.15: Characterization of the PZT4 piezo driver, where dashed lines indicates the white box model, light thick lines the measurement and the thin line the identified behavior. Different low pass filter settings of 0.3 kHz (——), 1 kHz (——), 10 kHz (——), 50 kHz (——), 100 kHz (——) and 150 kHz (——) has been successfully identified.

Table 4.3 shows the location of the identified poles for a chosen low pass filter. Independently of the low pass setting, a pole exists at ≈ 41 kHz and ≈ 1 MHz. A reason for the pole at ≈ 41 kHz could be that the power amplifier adds this additional filter component. The high frequency pole can be caused by different sources, e. g. by the power amplifier, by the cabling of the measurement setup, by the ground layer of the PCB or by other components. This pole can be neglected because it is much higher than the expected closed loop behavior, but the lower one at 41 kHz has to be taken into account. Moreover, one low pass setting above 50 kHz should be replaced by an option without the low pass filter, i. e. $C_1 \to 0$. This would maintain the maximum gain and avoids the unnecessary phase change, whereas the functions to damp higher frequency components of the piezo actuator is still fulfilled.

Table 4.3: Identification of the PZT4

Low pass	Pole Location [kHz]			Fit[%]
0.3 kHz	0.479			98.267
1 kHz	1.128			93.506
10 kHz	10.369	41.842		98.920
50 kHz	42.210	42.210		97.671
100 kHz	41.374	103.368	1048.987	97.473
150 kHz	40.687	160.199	942.667	96.950

The different transfer functions are given by

$$G_{\mathrm{PZT4,1\,kHz}}(s) = \frac{5.355 \cdot 10^3}{s + 7.089 \cdot 10^3}, \tag{4.22}$$

$$G_{\mathrm{PZT4,50\,kHz}}(s) = \frac{5.247 \cdot 10^{10}}{s^2 + 5.163 \cdot 10^5 s + 7.034 \cdot 10^{10}}. \tag{4.23}$$

With an increase of the bandwidth the order of the model also increases due to the multiple poles. If the first low pass is bypassed, the expected transfer function still has a high bandwidth, but lower order, that leading to a reduced order of the controller. This transfer function is given by

$$G_{\mathrm{PZT4,f_{max}}}(s) = \frac{0.8 \cdot 2\pi \cdot 41\,\mathrm{kHz}}{s + 2\pi \cdot 41\,\mathrm{kHz}}. \tag{4.24}$$

This section shows the dire importance of system identification even for these simple systems. The pole that was not considered in the design of the piezo driver is in the range of the later operation. If it is not taken into account, the model for the controller synthesis is not adequate and this will lead to problems in the closed loop behavior.

Conclusion and Uncertainties

The main conclusion of this section is, that the PZT4 is not suitable for operations above 41 kHz. Moreover, if a simple system behavior combined with a high bandwidth is required, the adjustable low pass should contain an option with an open capacitor, i. e. a maximum bandwidth with minimal phase change.

In the current modeling process we did not take noise originated from the operation amplifier and the high power voltage source into account. Moreover, this model did not include saturation effects. It is expected that the operation range is, even with high disturbances, well below the possible dynamic range. If this assumption does not hold, a saturation model should be added.

4.1.7 Dynamic Behavior of the MLO

To identify the dynamic behavior, different identification signals are chosen to excite the system in the required frequency range. A Pseudo Random Binary (PRB) and Band Limited White Noise (BLWN) signal with their spectra are shown in Fig. 4.16 and Fig. 4.17, respectively.

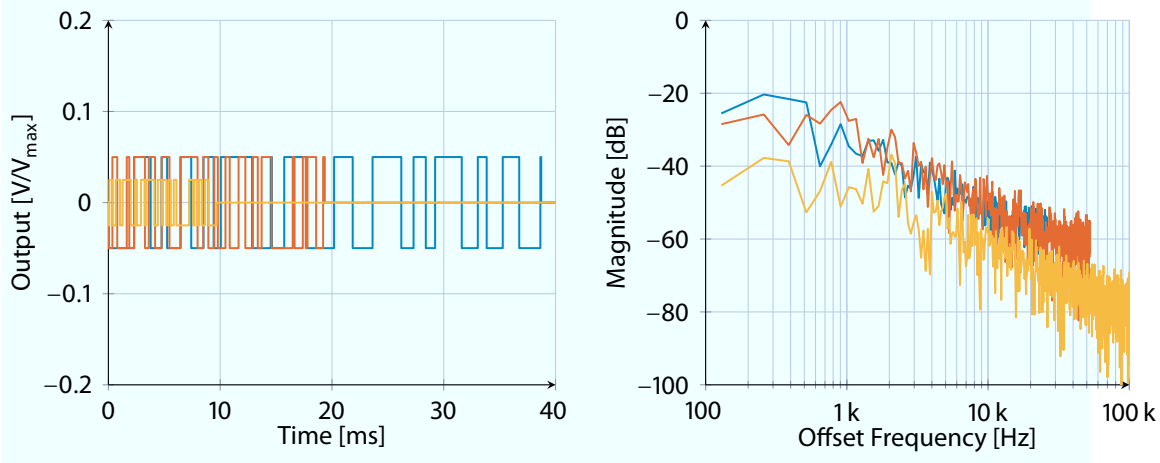

Figure 4.16: Time (left) and frequency (right) domain data of different PRB excitation signals generated with *idinput*, prbs 1 (—), prbs 2 (—), prbs 3 (—)

As a first approach, an open-loop identification is used. The displacement of the laser piezo changes the frequency of the MLO, whereas the phase difference between the MLO and MO is returned by the phase detection scheme. This obviously has an integral behavior and is an open loop unstable system, and should therefore be identified in a closed loop manner. But it is assumed, that the fundamental resonant mode of the piezo is much higher than the region of interest. This could simplify the piezo model to a plain constant gain. Moreover, the external disturbances are at lower frequencies, whereby the system stays very close to the operation point if the excitation signal is applied. This indicates that the system could be modeled by a plain integrator that is, during the excitation, not disturbed that much and could be identified in an open loop setup. Figure 4.18 shows the response to both excitation signals and verifies the assumptions. For this reason, an open loop identification is performed, and it is tested if sufficient model accuracy can be achieved.

As a first step, the free parameter of two different models will be estimated using a grey-box identification.[1] The first model structure assumes that the $G_{\text{Piezo}}(s)$, shown in Fig. 4.11, is identity for the given frequency range. This leads to a plain integrator with an adjustable gain b, as a state space model given by

$$\frac{d}{dt}\left[x_1\right] = \left[0\right]\left[x_1\right] + \left[b\right]u\,, \qquad y = \left[1\right]\left[x_1\right] + \left[0\right]u\,. \tag{4.25}$$

[1] The *MATLAB* function *idgrey* is used for this purpose.

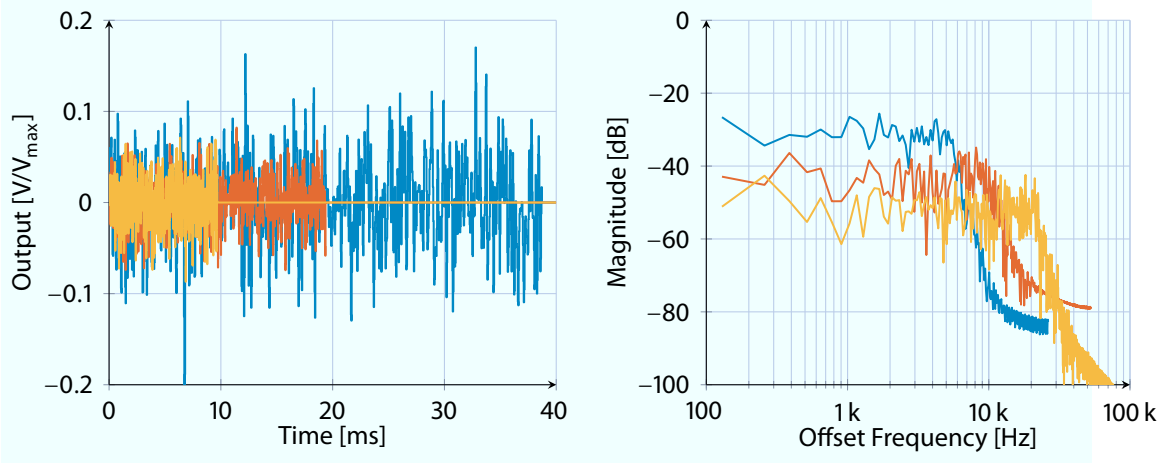

Figure 4.17: Time (left) and frequency (right) domain data of different BLWN excitation signals generated with *idinput*, noise 1 (—), noise 2 (—), noise 3 (—)

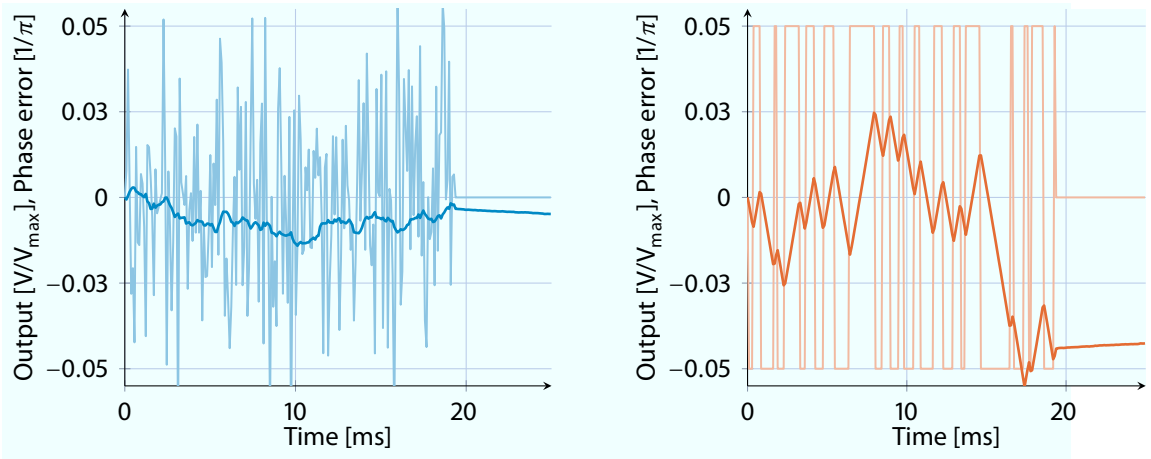

Figure 4.18: Excitation (—) and response (—) to theBLWN signal and to the PRB signal, (—) and (—), show on the left and right plot, respectively.

Sections 4.1.6 and 3.2 showed that the piezo amplifier the piezoelectric actuator itself both have a dominant low pass behavior. Thus, in the second grey box approach, a low pass with adjustable corner frequency a_{22}, is added to the integrator, leading to

$$\frac{d}{dt}\begin{bmatrix} x_1 \\ x_2 \end{bmatrix} = \begin{bmatrix} 0 & 1 \\ 0 & a_{22} \end{bmatrix}\begin{bmatrix} x_1 \\ x_2 \end{bmatrix} + \begin{bmatrix} 0 \\ b \end{bmatrix} u\,, \quad y = \begin{bmatrix} 1 & 0 \end{bmatrix}\begin{bmatrix} x_1 \\ x_2 \end{bmatrix} + \begin{bmatrix} 0 \end{bmatrix} u\,. \tag{4.26}$$

The identification results for various data sets are given in Table 4.4.

Table 4.4: Time domain fit of the data sets compared to their identified model response.

		Structure 1, (4.25)		Structure 2, (4.26)		
Data Set	DS	fit [%]	b	fit [%]	b	pole location of a_{22} [kHz]
prbs 1	4	95.887	568.261	96.205	568.387	8.675
prbs 2	2	87.626	604.978	88.077	605.493	6.694
prbs 3	1	94.388	536.596	95.975	536.739	13.336
noise 1	4	82.455	594.755	82.845	595.717	6.411
noise 2	2	90.280	595.376	91.606	595.942	10.424
noise 3	1	87.647	567.342	91.437	571.223	10.396

The given data shows that the identification of the system gives good results. The left part of Fig. 4.19 depicts a typical response to a noise signal with the measurement (——), the simulation (——), and the error between both (——). A reason for this could be the communication delay between the computing and the actuator board. Hence a time delay is added to the identification process, selected as 5 samples resulting in the smallest overall error signal for all data sets. The new results are given in Table 4.5.

Table 4.5: Time domain fit of the data sets compared to their delayed model response.

		Structure 1, (4.25), delayed		Structure 2, (4.26), delayed		
Data Set	DS	fit [%]	b	fit [%]	b	pole location of a_{22} [kHz]
prbs 1	4	96.435	568.549	96.477	568.566	25.455
prbs 2	2	88.954	601.281	89.038	601.369	16.354
prbs 3	1	96.504	542.904	96.512	542.906	151.241
noise 1	4	82.659	594.173	82.717	594.325	18.116
noise 2	2	94.069	578.771	94.069	578.772	1253.366
noise 3	1	94.497	568.013	94.559	568.064	132.321

If the delay is added, the error signal is minimized. Moreover, the fit identified for structure 1, (4.25), and structure 2, (4.26), is nearly the same. The identified poles of structure 2 have a large spread for the different data sets. So the pole is not dominant, which justifies neglecting the pole for the system model for the excited operation range.

Table 4.6: Validation of model response compared to the different data sets

	b =	540	550	560	570	580
Data Set	DS	fit [%]	fit [%]	fit [%]	fit [%]	fit [%]
prbs 1	4	77.122	77.920	78.566	79.046	79.348
prbs 2	2	92.342	93.388	94.091	94.321	94.024
prbs 3	1	94.772	95.358	95.561	95.334	94.730
noise 1	4	93.672	95.636	97.097	97.140	95.721
noise 2	2	96.061	97.253	98.053	97.940	97.015
noise 3	1	96.891	97.793	97.484	96.253	94.708
average		91.810	92.891	93.476	93.339	92.591

For this reason, (4.25) with a delay of 5 samples is chosen as a model of the MLO. The validation with different values of b is shown in Table 4.6. If b is set to 560, a good average fit for all data sets is achieved. Figure 4.19 is showing the response of two validation data sets to the final MLO model

$$G_{\mathrm{MLO}}(s) = \frac{560}{s} \cdot e^{-s\,t_{\mathrm{MLO}}} \quad \text{with} \quad t_{\mathrm{MLO}} = 11.185 \cdot 10^{-6}\,\mathrm{s}\,. \tag{4.27}$$

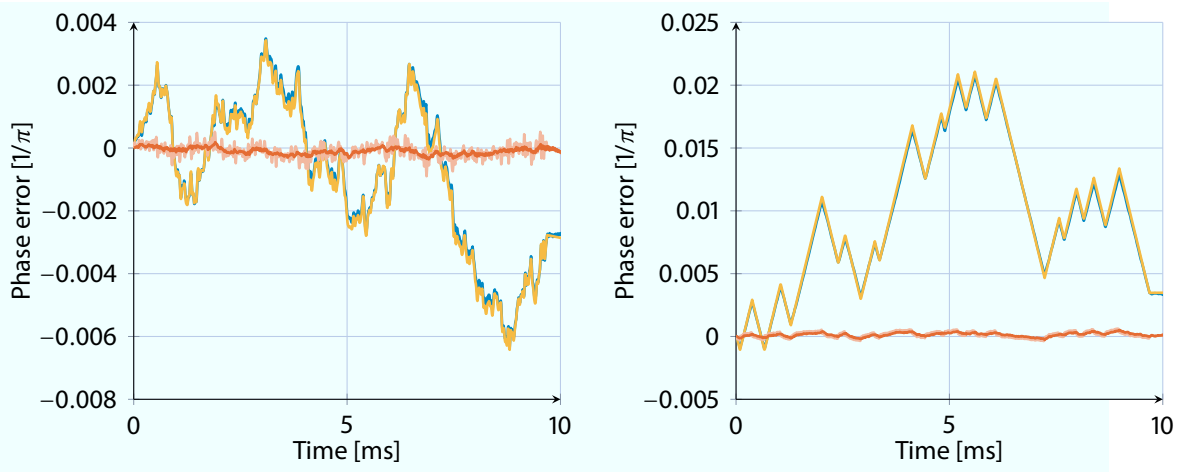

Figure 4.19: Time domain response for the BLWN excitation and the PRB signal with the measurement (—), the simulate response (—), the error of the non-delayed model (—) and the error of the delayed model (—).

4.1.8 Hysteresis and Creep

The last system properties analyzed are the hysteresis and creep behavior of the MLO. As discussed in Sec. 3.2.2 these effects are common for piezoelectric actuated systems.

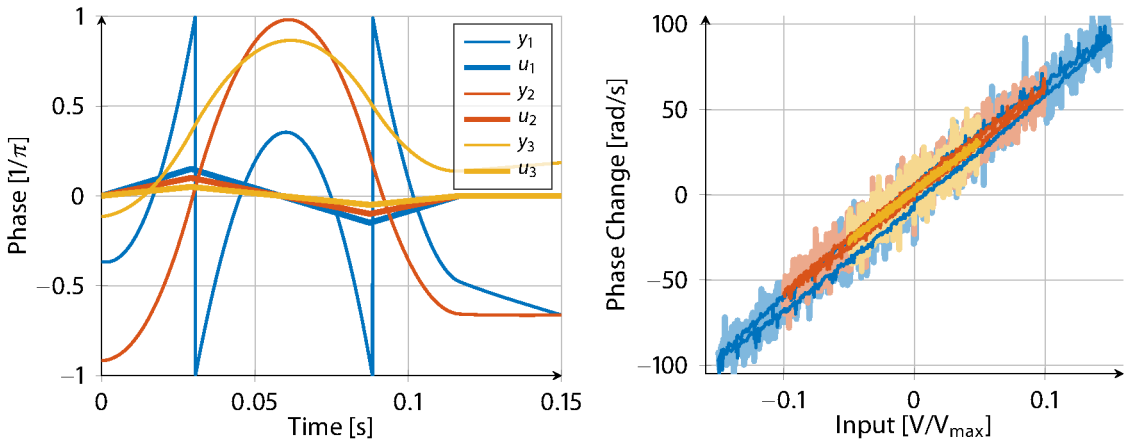

Figure 4.20: Time response (left) and phase change to input voltage behavior (right) for excitations with an amplitude of 5% (—), 10% (—), and 15% (—) of the measurement range

In order to measure this effect, multiple excitations are applied in an open loop close to the nominal operating point. Figure 4.20 shows the result of those measurements. The left plot shows the response y to an excitation with different amplitudes. The right plot shows the change of the response phase in dependence of the applied input voltage, compare to Sec. 3.2.2 . For the raw measurement data, given in the light lines (—), (—), and (—), no hysteresis is visible. If the measured signals are filtered by a 10 sample moving average, normal lines (—), (—), and (—), the expected hysteresis effect becomes visible for excitations above 10% in amplitude.

This experiment shows, that the expected behavior is present, but negligible for the given noise level and expected excitation range. If this effect is increased or the noise level is decreased, it can be further studied using the harmonic balance method, see [LE11].

The creep effect, also mentioned in Sec. 3.2.2 is a very slow effect in the time scale of seconds. All disturbances acting on the system are much faster. For this reason, the integral behavior of the controller will be able to supress this effect which can be neglected.

4.1.9 Phase Noise, Jitter and the $\mathcal{H}_2$ norm

For the controller design, in a model-based framework, it is necessary to describe the phase spectrum with the given system description introduced in Section 3.1.1.

As already mentioned the common approach to model noise in the control framework is the usage of an AWGN signal $\mathcal{N}(0,1)$ with zero mean and a power spectrum $S_n(j\omega) = 1$. If the real noise source is not white, it can be transmitted through a filter $W(s)$ that colorizes the signal in such a way, that is has the same frequency behavior as the real noise source. This filter $W(s)$ is added to the physical plant model to add this noise characteristics, shown in Fig. 4.21. The resulting model, containing the physical plant $G(s)$ as well as additional filters for different properties of the system is the so-called generalized plant $P(s)$.

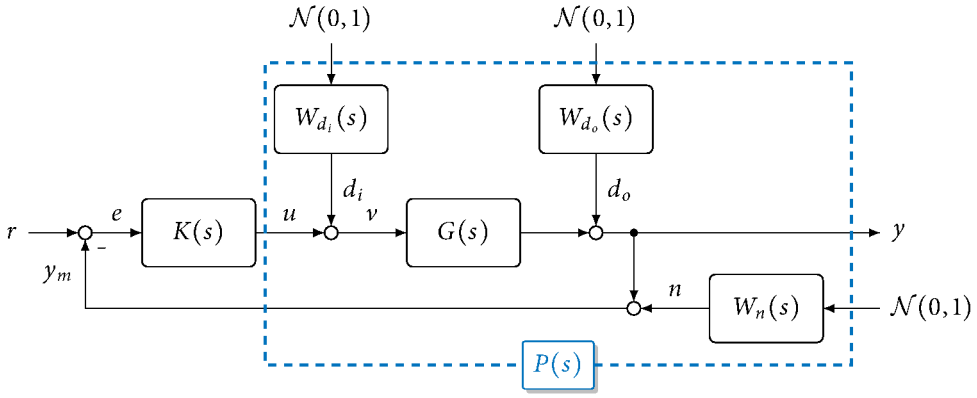

Figure 4.21: Control loop for the MLO system with additional coloring filters.

Consider an input disturbance modeled with an additional filter $W_{d_i}(s)$, shown in Fig. 4.21. The spectrum of the signal $d_i(t)$ is given by

$$D_i(s) = W_{d_i}(s) \cdot 1, \tag{4.28}$$

this means the filter $W_{d_i}(s)$ has to be chosen such that the filter response in the bode plot has the same characteristics as the energy spectrum of the noise signal.

If a power spectrum $S_u(\omega)$ is transfered through an LTI filter $W(s)$, the resulting power spectrum $S_y(\omega)$ is given by

$$S_y(\omega) = |W(\omega)|^2 S_u(\omega), \tag{4.29}$$

where S_u and S_y are power signals and the magnitude, in $[dB]$, in the bode plot is given by $10 \cdot \log_{10}(\bullet)$. If field quantities are used instead, $20 \cdot \log_{10}(\bullet)$ must be used. This leads to the fact that field quantities and the corresponding power signals have the same bode plot. Moreover, the filter $W(s)$ that colors AWGN to an energy signal also thereby colors the power spectrum.

This means that a stable filter with the same bode plot in magnitude $[dB]$ as the power spectrum is suitable to colorize an AWGN input to model noise behavior.

Section 3.1.2 shows that the $\mathcal{H}_2$ norm describes the transmission of the rms value of a signal through an LTI system. The previous discussion shows that the phase noise can be modeled by a filter, $W(s)$, that shapes an AWGN signal. Comparing (3.11) and (3.44) leads to

$$\|G(s)\|_2 = \sqrt{\frac{1}{2\pi}\int_{-\infty}^{\infty} |G(j\omega)|^2 \mathrm{d}\,\omega} = \sqrt{\int_0^{\infty} |g(t)|^2 \mathrm{d}\,t} = \|g(t)\|_2 \,. \tag{4.30}$$

This means, that the timing jitter of a phase noise spectrum is given by the $\mathcal{H}_2$ norm of the filter $W(s)$, which shapes AWGN in such a way that it models the phase noise spectrum. Moreover, the timing jitter of combined and/or derived signals can be calculated with the commonly known rules for the $\mathcal{H}_2$ norm, see e. g. [SP01].

The $\mathcal{H}_2$ norm is infinite for systems with a direct feed-trough, i. e. $D \neq 0$ in 3.2. This is usually the case for the filter $W(s)$ because they model constant noise floor.[2] In that case, the jitter can not be expressed by a finite number and it is common to give the jitter within a frequency range in order to make it comparable.

To compare performances of oscillators, the output jitter is used. It depends on the integration bounds and is given for a certain frequency range as

$$J_{rad,f_1,f_2} = \sqrt{2\int_{f_1}^{f_2} \mathscr{L}(f)\,\mathrm{d}f}, \quad 0 \leq f_1 \leq f_2 \,. \tag{4.31}$$

The direct integration of the signal in the frequency domain is able to handle the bounded range and can be used with raw data, but this requires high computation effort. However, this approach is used in this work.

An other possible solution is to add a low pass to the filter $W(s)$ outside of the region of interest, by using the whole frequency range. This method is used for the controller synthesis part of this work.

A third approach is the use of the frequency limit $\mathcal{H}_2$ norm, shown in [PL12] and [VPA13]. These papers focus mainly on model reduction, but the methods can be adopted in other fields. They are based on frequency limited Gramian, which have already been mentioned in [Gaw04].

New in this section is the obvious relation between timing jitter and $\mathcal{H}_2$ norm. This implies, that it is possible to model the main performance criterion, the phase noise, with a dynamic system excited by AWGN. Moreover, one of the standard performance measures of the control community fits exactly to the differently named one used by the physicists.

[2] E. g. The thermal noise power is given by $P = k_B T \Delta f$. The noise floor at room temperature is −174 dBm/Hz.

4.1.10 Phase Noise Model

Figure 4.22 shows how to model disturbance and noise sources, the phase noise of the MLO and the MO. As introduced in Section 4.1.9, white noise is feed through a filter $W_\bullet(s)$, the so-called coloring filter, before it enters the system. In this case, the noise of the MLO d_{MLO} is modeled by white noise fed through the coloring filter $W_{\mathrm{MLO}}(s)$ and the noise of the MO n_{MO} by $W_{\mathrm{MO}}(s)$, respectively. This section shows how to identify the filters.

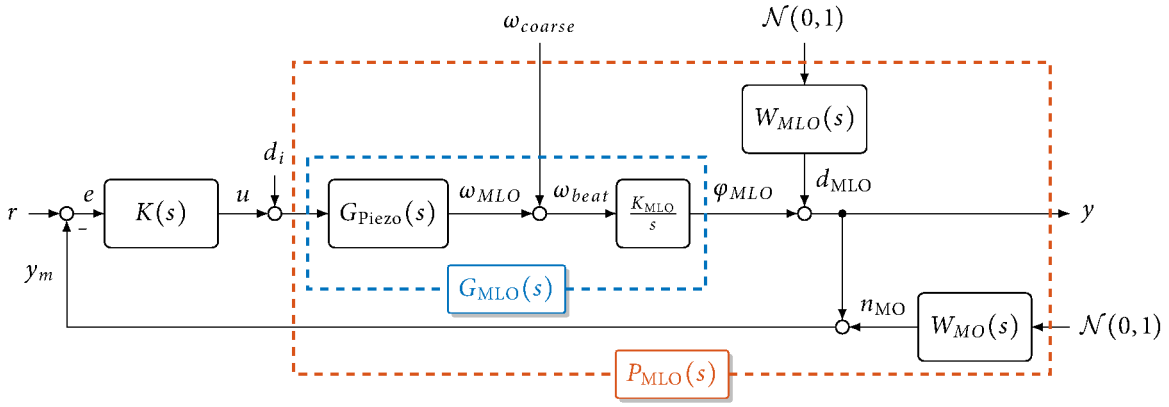

Figure 4.22: Control loop for the MLO system with additional coloring filter.

In the following the MO is not the final oscillator used in the XFEL. At this point of the work, the system is not available for experimental tests. Ergo, the author chose the lab MO in order to compare and evaluate the theory and practice of the different control approaches. If the final MO is available, some of the points discussed in this section as well as in the controller synthesis have to be repeated with the updated model. However, the choice of the controller structure and the proceeding are not affected by the different reference oscillator.

In order to estimate these filters, the noise spectrum in Fig. 4.13 is piecewise linear approximated, and a first assumption for the poles and zeros of a minimum phase filter is made. After that, *MATLAB* and the *fminsearch* Method is used to find a combination of poles and zeros that minimizes the difference of the magnitude of the frequency response compared with the measured spectrum, similar to [Heu+14b]. Figure 4.23 shows the results of this procedure for the MO phase noise and Fig. 4.24 for the MLO phase noise. The integrated error between measurement and the LTI filter is shown in Table 4.7.

The chosen coloring filters are

$$W_{\mathrm{MO}} = 8.9635 \cdot 10^{-4} \frac{(s+481.1)(s+7115)(s+1.186\cdot 10^6)}{(s+114.4)(s+2019)(s+2142)} \quad \text{and} \tag{4.32}$$

$$W_{\mathrm{MLO}} = 8.940 \cdot 10^{-6} \frac{(s+6.116\cdot 10^6)(s+1.454\cdot 10^5)}{(s+1.688)(s+2555)}. \tag{4.33}$$

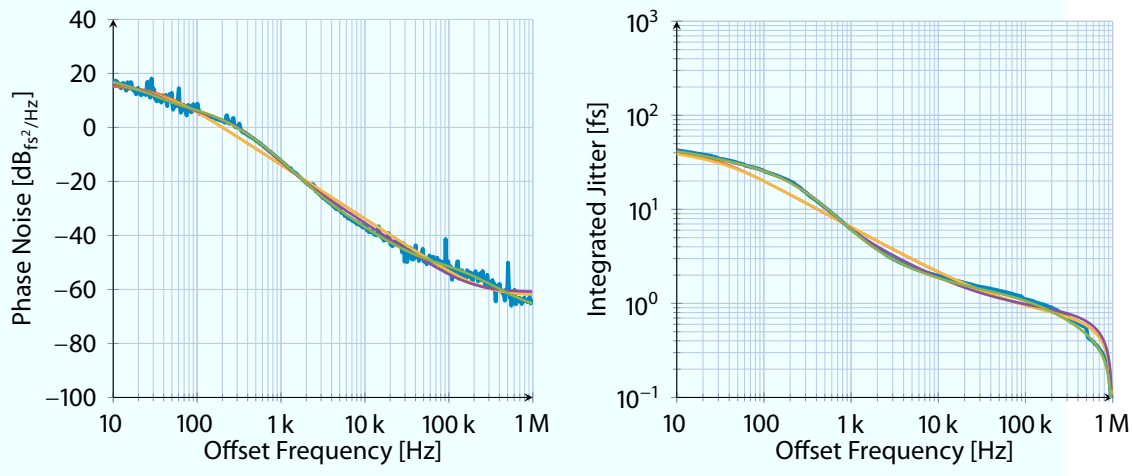

Figure 4.23: Approximation of the MO phase noise (—) with a first (—), second (—), third (—) and fourth (—) oder filter.

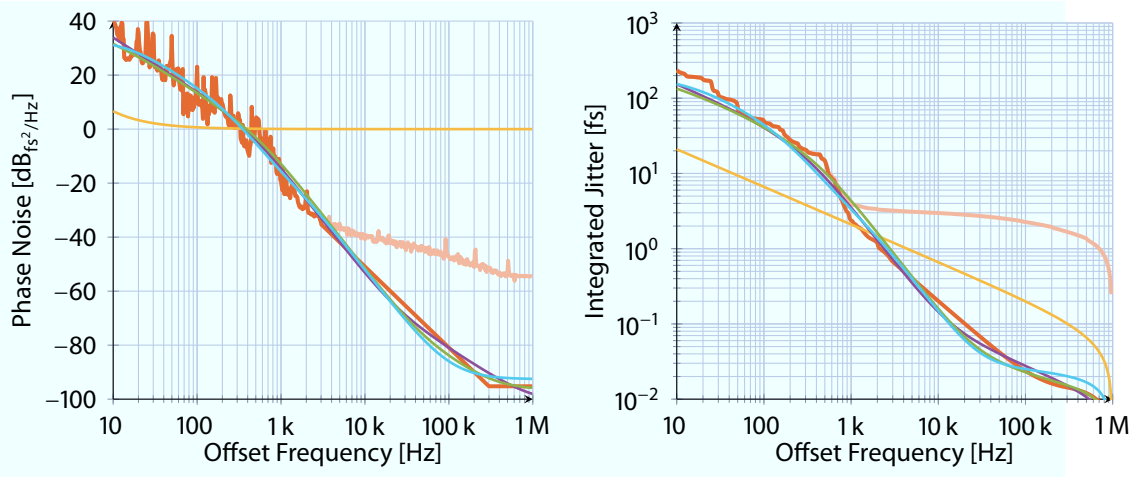

Figure 4.24: Approximation of the MLO phase noise (—) with a first (—), second (—), third (—) and fourth (—) oder filter.

Table 4.7: Integrated jitter of the different phase noise filter.

	MO		MLO	
Model	Error [dB$_{fs^2/Hz}$]	$\mathcal{H}_{2,10\,Hz-1\,MHz}$[fs]	Error [dB$_{fs^2/Hz}$]	$\mathcal{H}_{2,10\,Hz-1\,MHz}$[fs]
measurement	-	42.472	-	235.320
1st order	2.455	39.444	14.773	20.994
2nd order	2.439	38.767	3.610	153.625
3rd order	1.941	41.446	3.925	134.070
4th order	1.353	41.393	4.227	154.375

4.1.11 Measurement Noise

In addition to the MO and MLO phase noise, the measurement with a digital system itself adds further noise components, see Section 3.4. If the measurement adds too much noise, this would be added to the phase noise, which would not be measurable anymore. In such a case, the controller would, for example, follow the measurement noise and not the real MO signal.

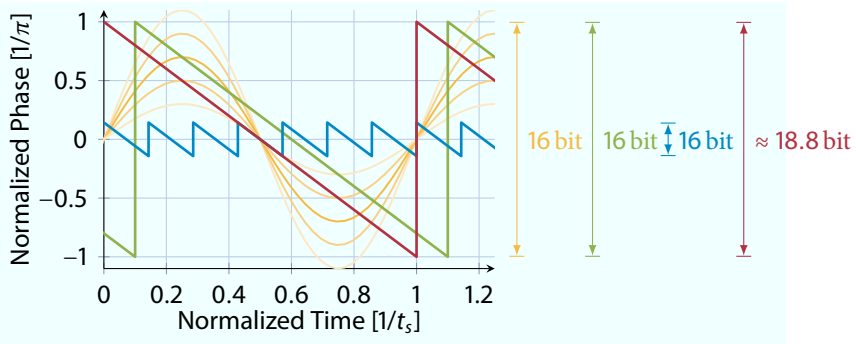

Figure 4.25: Normalized plot of detection scheme with the real phase difference (—), the direct signal (—), and the signal of the 7th harmonic (—).

Figure 4.25 shows the resolution of the different measured signals. The gain of the DC detection scheme (—), see Sec. 4.1.3, is adjustable. This allows one to change the singal precision by losing dynamic range. The 216 MHz (—) and 1516 MHz(—) schemes both have a fixed resolution, precision, and a fixed dynamic range. With the unwrapping algorithm (—), shown in Section 4.1.3, the dynamic range and the resolution can be increased but not the precision.

Table 4.8 shows the intrinsic noise of the ADC sampling process. It assumes that the only source of noise is the quantization and all other sources are negligible. If the 16 bit ADC is use to sample the 216.67 MHz signal, the a quantization noise error is ≈ 71 fs. Sampling the more sensitive 1516.67 MHz signal leads to a reduction to ≈ 10 fs, which is still above the required precision of < 10 fs. This would call for an increase of the ADC resolution.

Table 4.8: Precision for different hardware resolutions

Frequency [MHz]	216				1516			
Period [ns]	4.615				0.659			
	16 bit	18 bit	20 bit	24 bit	16 bit	18 bit	20 bit	24 bit
Delta [10^{-6}]	30.518	7.629	1.907	0.119	30.518	7.629	1.907	0.119
Phase [μrad]	95.874	23.968	5.992	0.745	95.874	23.968	5.992	0.745
Jitter [fs]	70.643	17.661	4.415	0.276	10.065	2.516	0.629	0.004

If it is not possible to increase the ADC resolution, but the sampling rate is much higher than required, oversampling can be used, see [SLAN118]. Multiple measurements are combined into one, with the assumption, that the ADC noise is uncorrelated. This reduces the sampling speed but increases the precision. The new quantization error after the averaging process is given by

$$\Delta e_n = \frac{1}{\sqrt{n}} \Delta e = \frac{1}{n\sqrt{n}} \sum_{k=1}^{n} \Delta e_k \,, \tag{4.34}$$

where Δe_n is the new error which is averaged over n sample with the previous error Δe. For a 16 bit ADC with 81.25 MHz this leads to the expected precisions given in Table 4.9.

Table 4.9: Precision for different averages

Frequency [MHz]	216				1516			
ADC	16 bit at 81.25 MHz				16 bit at 81.25 MHz			
Averages	3	48	96	384	3	48	96	384
Frequency [MHz]	27.083	1.693	0.846	0.212	27.083	1.693	0.846	0.212
Resolution [bit]	0.8	2.8	3.3	4.3	0.8	2.8	3.3	4.3
Jitter [fs]	40.660	10.165	7.188	3.594	5.808	1.452	1.027	0.513

For the later FPGA implementation, a 24 bit representation is chosen, with an oversampling of 48. By the given rate of the ADC clock of 81.25 MHz this would result in a control algorithm clock of 1.693 MHz, which is well above the expected requirements demanded by the closed loop bandwidth. The value was chosen in order to reach the maximum update rate for the piezo amplifier. To get the maximum resolution, the oversampling can be further increased, e. g. to a factor of 384, which still offers a sufficient update rate of 212 kHz for the MLO.

The previous discussion assumes that the ADC samples the phase, which is not true. For the 216 MHz and 1516 MHz schemes an intermediate frequency is sampled from which the phase is calculated, see Section 4.1.3. The relevant calculation in this step is

$$\phi = \operatorname{atan2}(q_{\mathrm{RF}}(k), i_{\mathrm{RF}}(k)) = \operatorname{atan2}(y_{\mathrm{RF}}(k)\sin(\omega k), y_{\mathrm{RF}}(k)\cos(\omega k)) \,, \tag{4.35}$$

where y_{RF} is the intermediate frequency sampled by the ADC and atan2 commonly defined by:

$$\operatorname{atan2}(y,x) = \begin{cases} \arctan(\frac{y}{x}) \,, & \text{if } x > 0, \\ \arctan(\frac{y}{x}) + \pi \,, & \text{if } x < 0 \text{ and } y \geq 0, \\ \arctan(\frac{y}{x}) - \pi \,, & \text{if } x < 0 \text{ and } y < 0, \\ +\frac{\pi}{2} \,, & \text{if } x = 0 \text{ and } y > 0, \\ -\frac{\pi}{2} \,, & \text{if } x = 0 \text{ and } y < 0, \\ \text{undefined} \,, & \text{if } x = 0 \text{ and } y = 0. \end{cases} \tag{4.36}$$

If this signal is quantized with an error $e_{y_{\mathrm{RF}}}$, the error of the phase $\Delta\phi$ is approximated by

$$\Delta\phi = \frac{\partial \operatorname{atan2}}{\partial i}(i,\, q)\,\Delta i + \frac{\partial \operatorname{atan2}}{\partial q}(i,\, q)\,\Delta q = \frac{i}{i^2+q^2}\,\Delta i - \frac{q}{i^2+q^2}\,\Delta q. \tag{4.37}$$

With the amplitude A of the input signal y_{in}, an upper bound for this is given by

$$\Delta\phi \leq \frac{|q|+|i|}{i^2+q^2}\,\Delta y_{\mathrm{in}} \leq \frac{A(|sin(\omega k)|+|cos(\omega k)|)}{A^2}\,\Delta y_{\mathrm{in}} \leq \frac{\sqrt{2}}{A}\,\Delta y_{\mathrm{in}}\,. \tag{4.38}$$

In order to get the minimum quantization error for the phase signal, it is important to use the full dynamic range of the ADC. On the other hand, saturation of the ADC has to be avoided, as this leads to an incorrect calculation of the phase signal. Table 4.10 shows the expected precision of the phase signal for different amplitudes of the intermediate frequency.

Table 4.10: Precision for different amplitudes, an 16 bit ADC at 81.25 MHz and 48 averages.

Frequency [MHz]	216				1516			
Amplitude	1	0.9	0.6	0.4	1	0.9	0.6	0.3
$\sqrt{2}\,A^{-1}$	1.414	1.571	2.357	4.714	1.414	1.571	2.357	4.714
Min. Jitter $[fs]$	10.165	11.294	16.942	33.883	1.452	1.614	2.42	4.840
Max. Jitter $[fs]$	14.376	15.973	23.959	47.918	2.054	2.282	3.4227	6.846

4.1.12 Input Disturbance

The minimal input disturbance, which is acting between controller and plant, is given by the quantization error of the DAC. The model in (4.27) gives the sensitivity of the MLO. The phase change in one second with the full excitation of 80 V is given by

$$\Delta\phi = \frac{560\,\frac{1}{\mathrm{s}^{\mathrm{V}}/\mathrm{V}_{\mathrm{max}}}}{216\,\mathrm{MHz}} = 2.593\,\frac{\mu\mathrm{s}}{\mathrm{s}^{\mathrm{V}}/\mathrm{V}_{\mathrm{max}}}\,. \tag{4.39}$$

The possible timing changes with the different resolutions of the actuator are given in Table 4.11. The DAC used at the piezo driver has a resolution of 18 bit, which results in a timing change, $\Delta\phi$, of 20 atto seconds between two sample, which is well below the resolution of the measurement scheme.

Table 4.11: Timing change dependent on the DAC resolution and frequency.

Resolution [bit]	16		18	
Number $[10^{-6}]$	30.518		7.629	
Timing change $\left[\frac{\text{ps}}{\text{s}}\right]$	79.120		19.780	
Frequency [kHz]	100	1000	100	1000
Timing change $\left[\frac{\text{fs}}{\text{sample}}\right]$	0.791	0.079	0.198	0.020

4.1.13 Conclusion and Uncertainties

The last section showed that the performance criterion for the MLO, the so-called timing jitter, is equivalent to the well known $\mathcal{H}_2$ norm. If the absolute timing jitter is taken into account, the control objective is to minimize the output jitter $\|y(t)\|_2$, which occurs in the region where the noise spectra of the MO and MLO have an intersection point. For this reason, the feedback controller should have an expected closed loop bandwidth of $\approx 1\,\text{kHz}$.

A model of the MLO was identified and extended by the main noise sources, the phase noise of the MO and MLO for a frequency range around the latter's closed loop bandwidth.

If an operation at higher frequencies is required, the low pass behavior of the piezo amplifier and the resonance modes of the piezoelectric actuator can be added to the identification. If the amplitude of the excitation increases or the measurement noise is lowered, the hysteresis should be added to the model.

Up to now, no noise effects of the mechanical vibration, temperature, nor humidity changes are considered. The optical setup will reduce these influences to a minimum. If it turns out that they could be relevant, an acceleration sensor or microphone can be connected to the laser housing and a temperature and/or a humidity sensor on the optical table in order to measure these influences.

To further increase the performance of the system, the detection of the relative phase should be increased in sense of resolution. Moreover, a measurement of the absolute phase should be added in order to directly measure the required performance criterion.

The identification of the piezo amplifier shows, that in addition to the programmable low pass filter, a second pole with a bandwidth of $\approx 42\,\text{kHz}$ is present. For this reason, the author proposes that removing this filter be one of the programmable filter settings. This simplifies the plant model and possibly increases the performance.

4.2 Controller Design

In this section, multiple model-based controllers for the MLO system are designed and theoretical evaluated in a simulation, as well as practically in an experiment. A brief introduction to these controller design approaches was given in Section 3.7. For all plots in this section, the system is scaled in such a way that the maximum expected error is 1 ps and the allowed excitation for this is given by 1 V, see (3.5).

4.2.1 Performance Limitations

To compare the different controllers, an optimal behavior, minimum to timing jitter, of the closed loop is assumed, even thought it is impossible to achieve this behavior.

The performance objective of the control loop is to reduce the output jitter of the MLO pulse train $y(t)$. Under the assumption that just the noise of the MO and MLO is taken into account, it follows from (3.14a) that the resulting output jitter $Y(s)$ is given by

$$Y(s) = T(s)W_{mo}(s) + S(s)W_{mlo}(s) + S(s)G(s)W_{d_i}(s) + T(s)W_n(s)\,, \tag{4.40}$$

$$Y(s) = T(s)W_{mo}(s) + S(s)W_{mlo}(s)\,. \tag{4.41}$$

To minimize the timing jitter, a perfect control loop would have the following behavior,

$$T(s) = \begin{cases} I\,, & \text{if } |W_{mo}(s)| \leq |W_{mlo}(s)|\,, \\ 0\,, & \text{otherwise}\,, \end{cases} \qquad S(s) = \begin{cases} 0\,, & \text{if } |W_{mo}(s)| \leq |W_{mlo}(s)|\,, \\ I\,, & \text{otherwise}\,. \end{cases} \tag{4.42}$$

Figure 4.26 shows the resulting timing jitter with such a theoretical controller for the current setup in the laboratory. The closed loop behavior follows the MO in the frequency range below 1 kHz and the MLO at higher frequencies. The resulting jitter of the closed loop in the range of 10 Hz to 10 kHz is 41.425 fs, which is a lower bound for all other possible controllers.

The resulting complementary sensitivity function, $T(s)$, has a lot of transitions between $T(s) = 1$ and $T(s) = 0$, which would result in a very high order for this controller. Hence a semi-best controller with just one transition at 867 Hz is assumed. This controller and the corresponding closed loop behavior is shown in Fig. 4.27. The resulting timing jitter is 42.068 fs.

Table 4.12 shows the jitter contribution for the MO, MLO, and both controllers. The jitter contribution of the MO is smaller than that of the MLO in ranges below the crossover frequency. The semi-best controller has the same contribution as the MO. The best controller has even lower values, because at some frequencies the laser is slightly better. Above 867 Hz the open laser has a better performance and both controllers have the same jitter contribution, which is the one of the open laser. The main jitter contribution arises from the low frequency noise of the MO. If this could be decreased the closed loop jitter would also be decreased significantly.

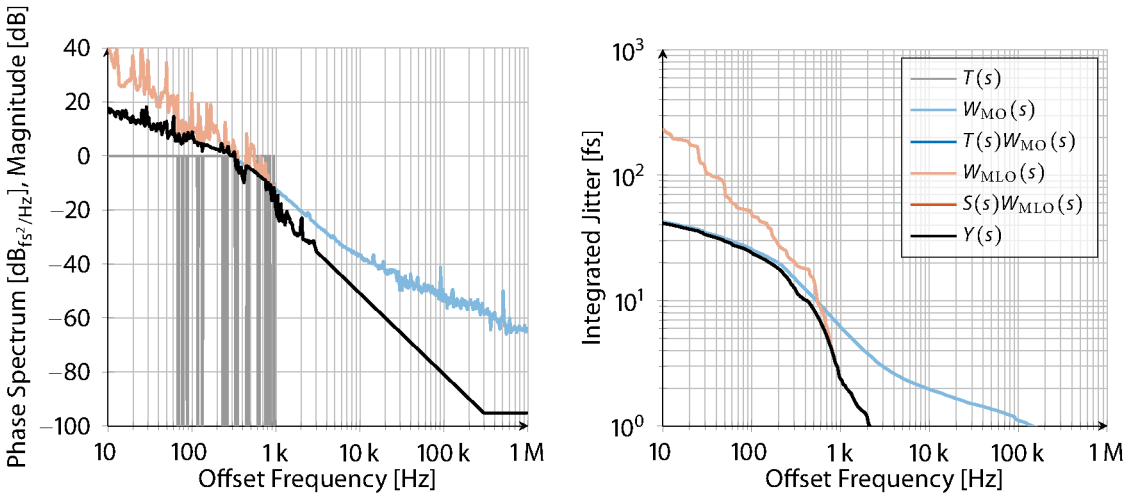

Figure 4.26: Optimal controller to minimize the phase noise and timing jitter

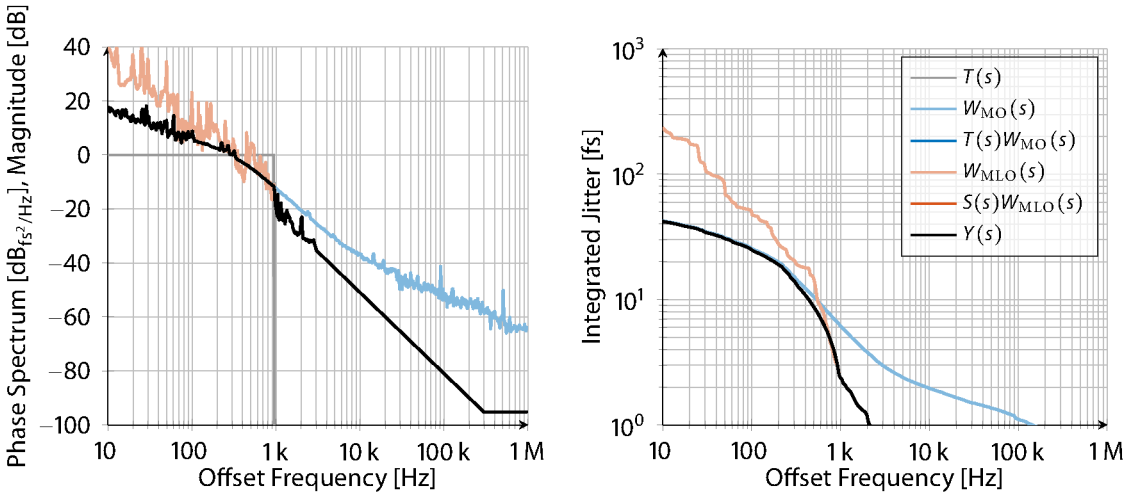

Figure 4.27: Semi-Best controller to minimize the phase noise and timing jitter

Table 4.12: Performance limitation of the ideal MLO loop

Frequency range [kHz]	0.01 . . . 0.1	0.1 . . . 0.5	0.5 . . . 1	1 . . . 5	5 . . . 10	total
MO [fs]	33.542	23.092	8.327	5.600	1.341	42.472
MLO [fs]	226.626	44.964	13.844	2.307	0.339	235.299
K_{Best} [fs]	33.390	22.244	7.967	2.307	0.399	41.425
K_{Semi} [fs]	33.542	23.092	8.277	2.307	0.399	42.068

4.2.2 PI and Optimal PI

In this section the well know PI controller is analyzed. Its advantage is its simple structure, give in Fig. 4.28. Furthermore, there are tuning rules for this kind of controller that do not rely on a system model. For this reason, this controller type is often used as a first approach.

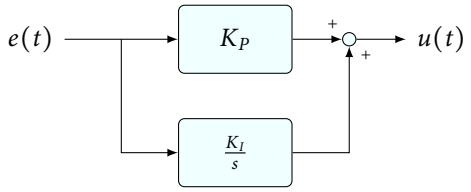

Figure 4.28: Structure of the PI controller

If just the proportional part K_P is used, the closed loop transfer function for the MLO model in Fig. 4.22, from r to y, is given by

$$T_{\mathrm{MLO,P}}(s) = \frac{Y(s)}{R(s)} = \frac{G_{\mathrm{MLO}}(s)K_P}{1 + G_{\mathrm{MLO}}(s)K_P} = \frac{560K_P}{s + 560K_P} = \frac{\omega_{cl}}{s + \omega_{cl}}\,, \tag{4.43}$$

where ω_{cl} is the bandwidth of the closed loop and $P_{\mathrm{MLO}}(s)$ is the MLO model. If K_p is chosen as

$$K_P = \frac{2\pi f_{cl}}{560} = \frac{2\pi\, 867\,\mathrm{Hz}}{560} = 9.728 \tag{4.44}$$

the closed loop bandwidth f_{cl} can be adjusted, whereas the static gain is 1, which gives the impression that the MLO tracks the MO for r equal zero, which is not true. Important at that point is the load disturbance sensitivity function which is given by

$$S_{\mathrm{MLO,P}}(s)G_{\mathrm{MLO}}(s) = \frac{Y(s)}{D_i(s)} = \frac{G_{\mathrm{MLO}}(s)}{1 + G_{\mathrm{MLO}}(s)K_P} = \frac{560}{s + 560K_P} = \frac{560}{s + \omega_{cl}}\,. \tag{4.45}$$

If an input disturbance is given, which is due to the coarse tuning always the case, this disturbance is added to the output phase with the factor $560\,\omega_{cl}^{-1}$. To compensate for this steady state error, an integrator part is added to the controller that leads to

$$T_{\mathrm{MLO,PI}}(s) = \frac{G_{\mathrm{MLO}}(s)(K_P + \frac{K_I}{s})}{1 + G_{\mathrm{MLO}}(s)(K_P + \frac{K_I}{s})} = \frac{560K_P \cdot s + 560K_I}{s^2 + 560K_P \cdot s + 560K_I} \quad \text{and} \tag{4.46}$$

$$S_{\mathrm{MLO,PI}}(s)G_{\mathrm{MLO}}(s) = \frac{G_{\mathrm{MLO}}(s)}{1 + G_{\mathrm{MLO}}(s)(K_P + \frac{K_I}{s})} = \frac{560s}{s^2 + 560K_P \cdot s + 560K_I}\,. \tag{4.47}$$

The static gain of the complementary sensitivity function $T_{\mathrm{MLO,PI}}(s)$ is one, while the static gain of the load disturbance sensitivity function $S_{\mathrm{MLO,PI}}(s)$ is zero. This means the control loop will track the MO and all input disturbances are compensated for.

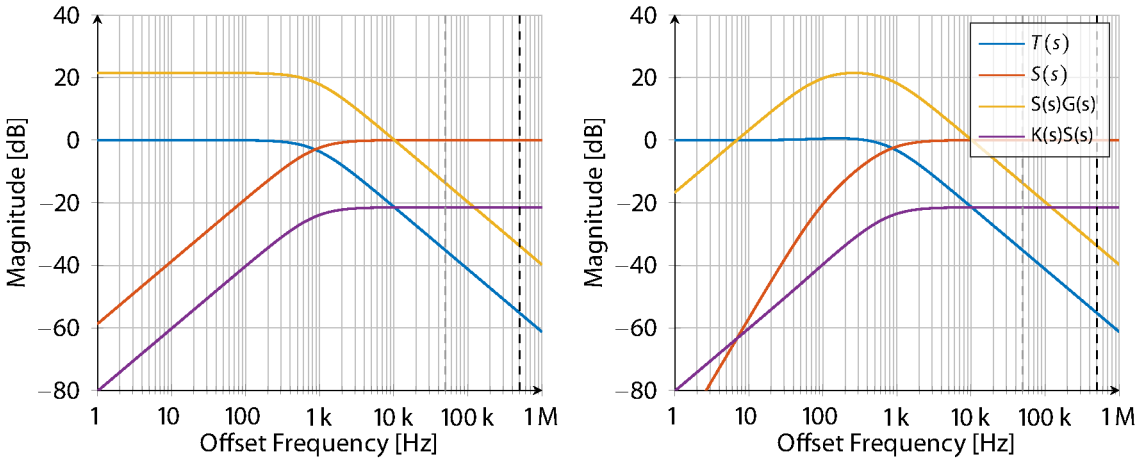

Figure 4.29: Bode diagram for the P (left) and the PI controller (right).

Figure 4.29 shows the resulting gang of four for the P and the PI controller. Both closed loops are stable and have a similarly shaped complementary sensitivity function (——). The important difference is given in the load disturbance sensitivity function $S(s)G(s)$ (——). For the proportional controller (left) it is constant for low frequencies and disturbances are transmitted to y. These disturbances are, e. g. system temperature changes leading to a slow drift of the mean laser frequency ω_{MLO}. With an additional integrator (right), the function $S(s)G(s)$ (——) goes to zero for low frequencies, which means that those disturbances are suppressed by the controller. The integrator gain was chosen manually such that a good disturbance rejection is reached without a peak due to the water bed effect. Figure 4.30 shows the simulation results for this PI controller.

In the next step, the controller parameters are optimized to achieve a minimal timing jitter, based on the measured phase noise data. The *fmincon* function is used to minimize the integrated timing jitter in a range of 10 Hz up to 1 MHz. The closed loop bandwidth of this controller increases to ≈ 2.547 kHz. The simulation is shown in Fig. 4.31. With this increased bandwidth, the spurs in the low-frequency range are suppressed further, which lowers the overall timing jitter. A similar procedure can be implemented using the SSA measurement, which returns the integrated absolute jitter. This value can be used to slightly change the controller bandwidth and adjust the control loop in such a way, that this value is minimized.

Table 4.13 shows the integrated timing jitter for the PI controller. The manually tuned controller has a timing jitter a little above the free running MO. With the optimization, a performance increase of 1.5 fs can be achieved. This is achieved by increasing the closed loop bandwidth to decrease the effects of low frequency peaks that have a high jitter contribution.

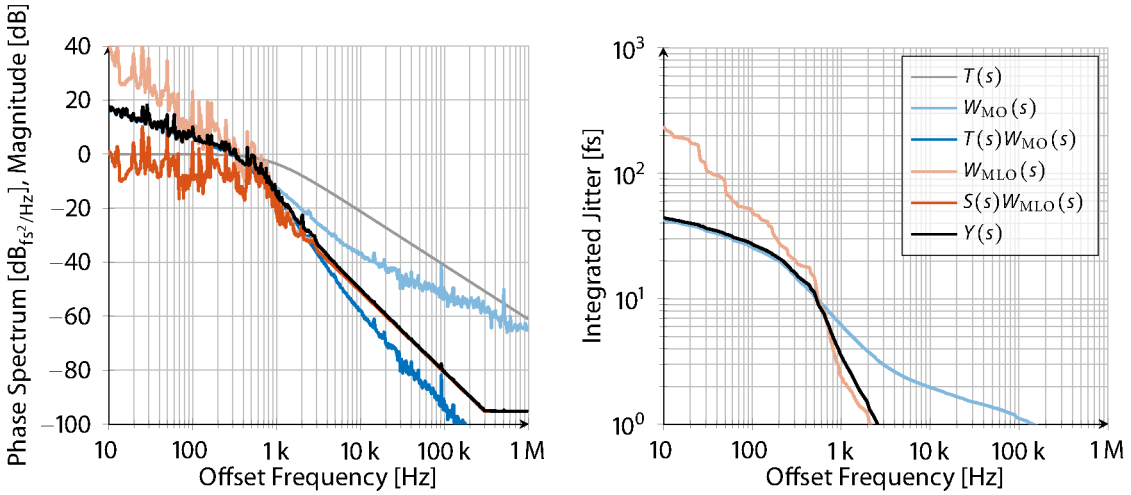

Figure 4.30: Phase noise (left) and timing jitter (right) of the PI controller designed based on the expected bandwidth.

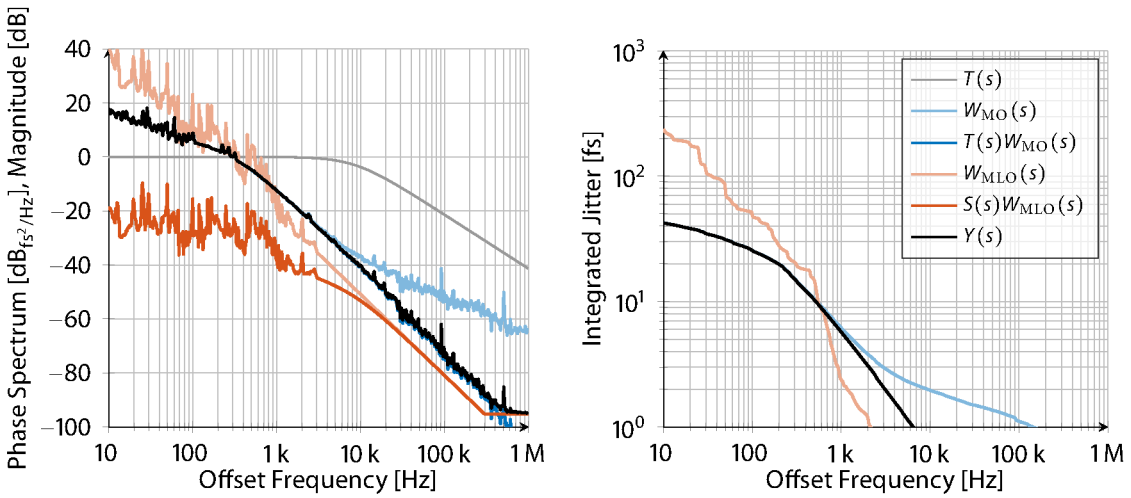

Figure 4.31: Phase noise (left) and integrated timing jitter (right) of the PI controller designed based the minimization of the measured spectra.

Table 4.13: Performance of the PI controller.

Freq. range [kHz]	0.01 . . . 0.1	0.1 . . . 0.5	0.5 . . . 1	1 . . . 5	5 . . . 10	total
MO [fs]	33.542	23.092	8.327	5.600	1.341	42.472
MLO [fs]	226.626	44.964	13.844	2.307	0.339	235.299
K_{PI} [fs]	34.329	24.530	10.255	3.402	0.379	44.104
$K_{PI,\,10\,Hz–1\,MHz}$ [fs]	33.550	23.108	8.358	5.482	1.065	42.430

4.2.3 $\mathcal{H}_2$ Optimal Design with disturbance and noise filter

The different design strategies up to now don't include a model of the colored disturbances and noise. This will be added to the next design approach. The idea is taken from an example in [Bay99], and a first investigation started in [Man15].

Design 1 - SKS

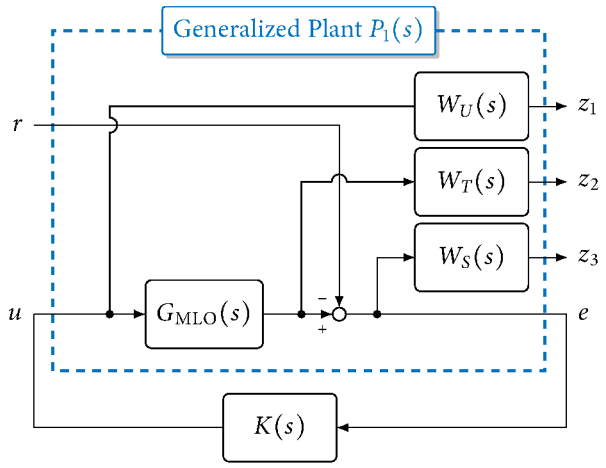

Figure 4.32: Generalized Plant for the first design.

As a first design approach, the generalized plant shown in Fig. 4.32 is used, which is a common choice for $\mathcal{H}_\infty$ optimal control. The filter W_S, W_T, and W_U are used to shape the sensitivity function, complementary sensitivity function, and to penalize the control efford.

In this work we select the noise spectra of the MLO and MO for W_S and W_T, respectively. The filter, W_U, is the tuning knob to limit the control action and is assumed to be constant over all frequencies. Moreover, the $\mathcal{H}_2$ norm is used instead the $\mathcal{H}_\infty$ norm. This leads to the minimization problem

$$\min_{K(s)} \left\| \begin{array}{c} W_U(s) \cdot K(s) \cdot S(s) \\ W_T(s) \cdot T(s) \\ W_S(s) \cdot S(s) \end{array} \right\|_2 . \tag{4.48}$$

In order to solve this problem the tools introduced in [Bal+04] are used.

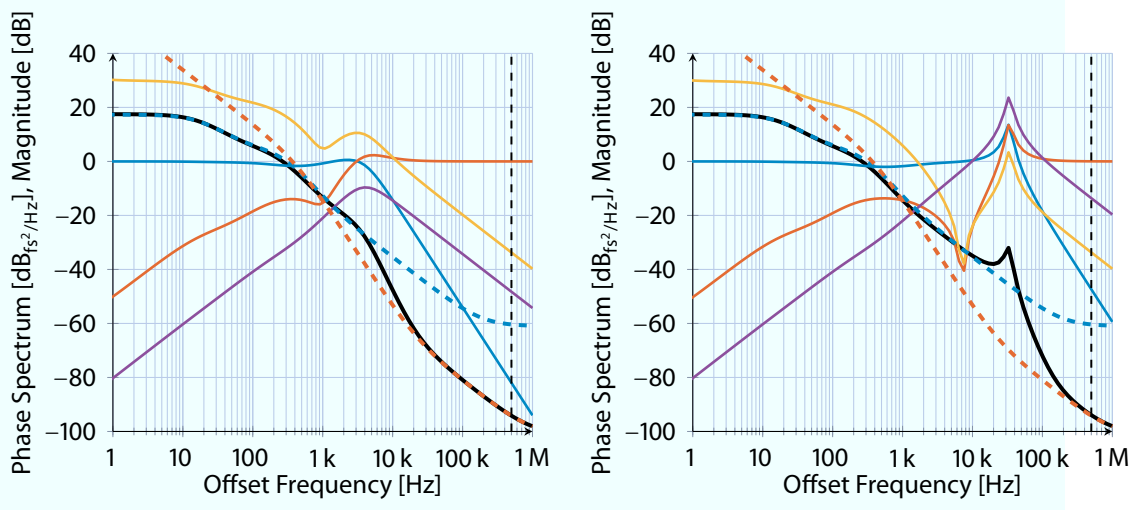

Figure 4.33: GOF for the first design, with (left) and without (right) weight on the controller action, including S (—), T (—), SG (—) and KS (—).

Figure 4.33 shows the GOF for design in Fig. 4.32. The left plot shows the GOF with a small weight on the controller output W_u. The closed loop shows the expected behavior. The total output noise (——) follows the MO (- - -) in the low frequency range and the MLO (- - -) in the high frequency range. The transition between both behaviors, the closed loop bandwidth, is at frequencies a little above the intersection of the noise spectra at 4.712 kHz.

Compared to the PI controller, shown in Fig. 4.30, the optimized loop pushes the sensitivity function (—) down in the range of the transition and increases the bandwidth slightly. This results in a peak response of the sensitivity function of 2.32 dB. The reason for this behavior is, that this increase adds less integrated jitter than it saves with the pushed down area, because the added jitter at higher frequencies is not that costly in terms of the $\mathcal{H}_2$ norm.

The right part of Fig. 4.33 shows the GOF if the control action is not penalized. The bandwidth is increased to 50.791 kHz and a water bed peak appears. This peak at high frequencies again costs less than the further suppressed noises at lower frequencies. In this case, the control action (—) also increases and crosses 0 dB.

Furthermore, Fig. 4.33 shows that $K(s)S(s)$ is not going to zero for low frequencies. This leads to a steady state error if a non-zero mean disturbance input occurs, compare to Sec. 4.2.2.

Design 2 - Four block

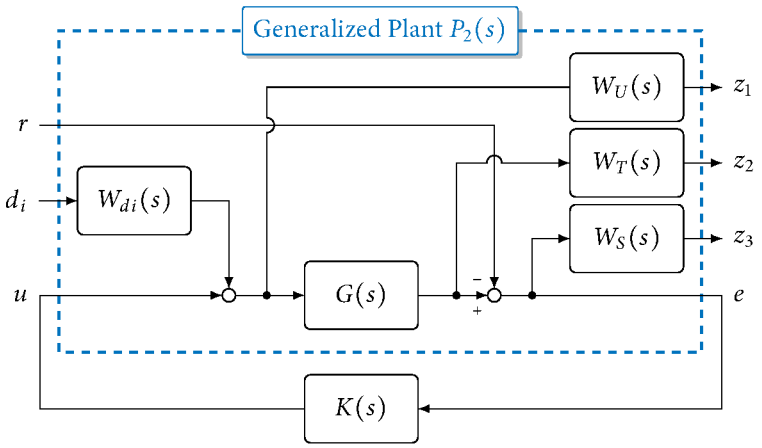

Figure 4.34: Generalized Plant for the second design.

The design, shown in Fig. 4.34, adds a tuning knob $W_{di}(s)$ which penalizes this error.[3] The minimization problem with the additional filter is given by

$$\min_K \left\| \begin{matrix} W_U \cdot K \cdot S & W_U \cdot S \cdot W_{di} \\ W_T \cdot T & W_T \cdot T \cdot G \cdot W_{di} \\ W_S \cdot S & W_S \cdot S \cdot G \cdot W_{di} \end{matrix} \right\|_2 \tag{4.49}$$

The resulting GOF for this design is shown in Fig. 4.35 and the integrated jitter in Fig. 4.36.

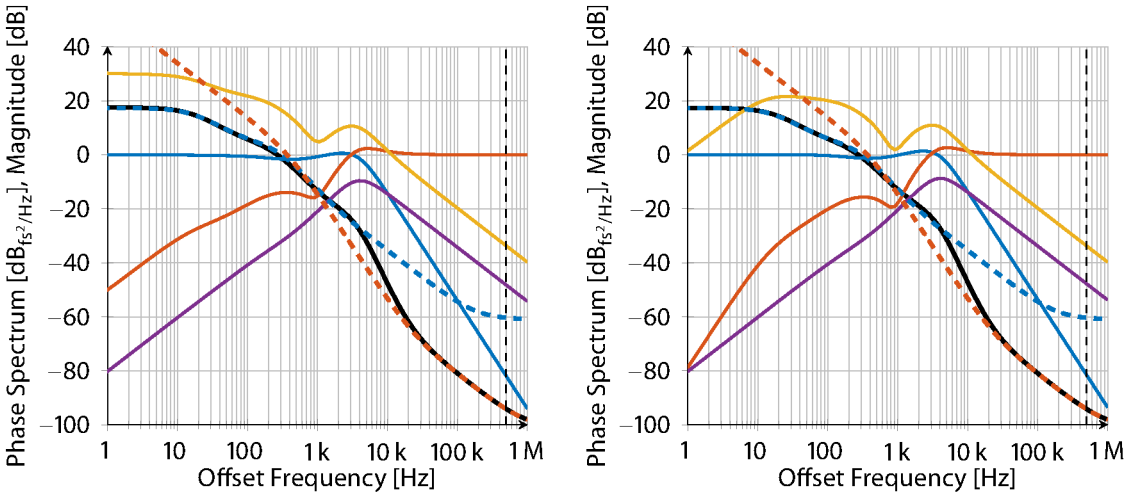

Figure 4.35: GOF of the first (left) and second design (right), with S (——), T (——), SG (——) and KS (——).

[3] Remember, a constant input on this channel is aways given due to the coarse tuning.

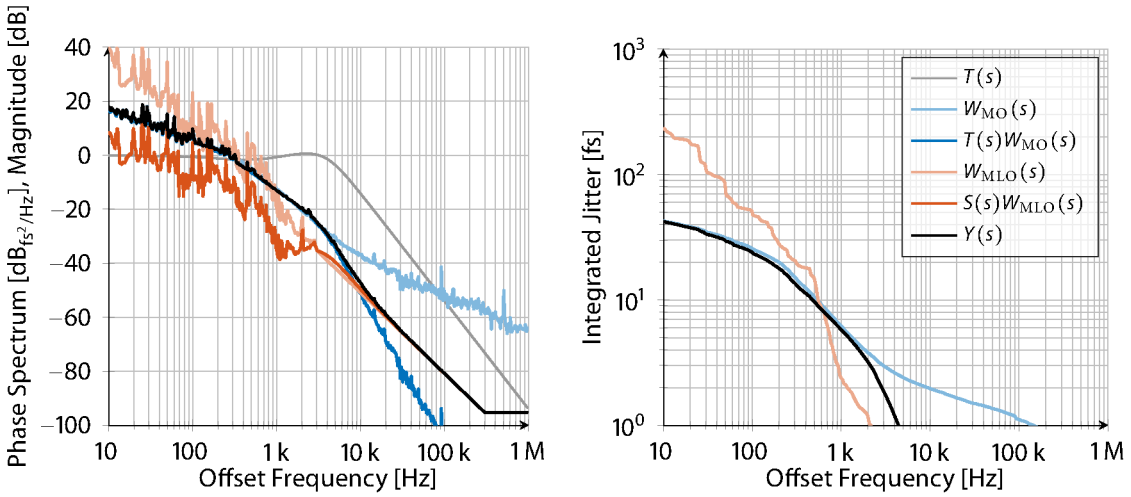

Figure 4.36: Phase noise and integrated timing jitter for the second design.

With the second design it is possible to move $K(s)S(s)$ down at low frequencies and minimize the steady state error. The bandwidth of this design increases to ≈ 5.3 kHz.

Table 4.14 shows the integrated jitter of the different $\mathcal{H}_2$ designs. The lowest jitter is achieved with Design 1 and no controller output penalty. The control action exceeds the allowed range, the controller bandwidth increases above the identified frequency region of the model, and furthermore the controller has a steady state error. The second design has only a ≈ 1% higher jitter value but satisfies all the requirements. For this reason, the second design should be used.

Table 4.14: Performance of the different $\mathcal{H}_2$ controller.

Freq. range [kHz]	0.01…0.1	0.1…0.5	0.5…1	1…5	5…10	total
MO [fs]	33.542	23.092	8.327	5.600	1.341	42.472
MLO [fs]	226.626	44.964	13.844	2.307	0.339	235.299
$K_{\mathcal{H}_2,\,\text{Best}}$ [fs]	34.155	21.109	7.227	4.862	1.336	41.688
$K_{\mathcal{H}_2,\,\text{Design 1}}$ [fs]	34.346	21.406	7.560	5.655	0.726	42.068
$K_{\mathcal{H}_2,\,\text{Design 2}}$ [fs]	34.197	21.724	7.742	6.110	0.776	42.196

4.2.4 Comparison

Table 4.15 summarizes properties, and Table 4.16 summarizes the integrated timing jitter for the closed loop simulation of the different controller developed in the last sections.

Table 4.15: Properties of the different MLO controller.

	K_{Best}	K_{Semi}	K_{PI}	$K_{\text{PI},\bullet}$	$K_{\mathcal{H}_2}$
Realizable	✗	✗	✓	✓	✓
Performance	1	2	5	4	3
Automatic Tunning	✗	✗	✗	✓	✗
FPGA resources	-	-	low	low	high

Table 4.16: Integrated timing jitter in [fs] for the different MLO controller.

Freq. range [kHz]	0.01 . . . 0.1	0.1 . . . 0.5	0.5 . . . 1	1 . . . 5	5 . . . 10	0.01 . . . 10	0.5 . . . 10
MO	33.542	23.092	8.327	5.600	1.341	42.472	10.230
MLO	226.626	44.964	13.844	2.307	0.339	235.299	14.053
K_{Best}	33.390	22.244	7.967	2.307	0.399	41.425	8.326
K_{Semi}	33.542	23.092	8.277	2.307	0.399	42.068	8.623
K_{PI}	34.267	24.487	10.243	3.400	0.379	44.028	10.851
$K_{\text{PI, 500 Hz–1 MHz}}$	33.628	23.273	8.657	4.799	0.575	42.556	10.008
$K_{\text{PI, 10 Hz–1 MHz}}$	33.550	23.108	8.358	5.482	1.065	42.430	10.157
$K_{\mathcal{H}_2\text{, Design 2}}$	34.197	21.724	7.742	6.110	0.776	42.196	9.996

The controller with the lowest closed loop jitter given by K_{Best} is the lower performance bound and not realizable. The integrated jitter for this controller is dominated by the low frequency parts of the MO. The same holds for the second best controller, K_{Semi}, which has just one infinite steep transition in the bode plot.

$K_{\mathcal{H}_2\text{, Design 2}}$ is realizable and leads to the lowest timing jitter. This controller directly minimizes a cost function that the jitter is a part of. To evaluate this cost function, the synthesis algorithm relies on a model of the noise and disturbances. If these are changing, they have to be identified again, and the controller has to be recomputed and tuned. Moreover, the computation efford of this controller depends on the size of the plant and shaping filter.

The optimized PI controller has only a $\approx 1\%$ higher jitter value than the $\mathcal{H}_2$ design. Additionally, it is possible to automatically tune this controller further and react to slightly changing conditions. For this reason, the author suggest to use this approach in combination with an SSA measurement and a slow feedback loop that changes the bandwidth of the PI controller.

The last question of this section is: how to further increase the performance of the MLO system i. e. decreasing the jitter? This can be done via the following approaches:

- The dominant part of the closed loop jitter is given by the MO. Decreasing its jitter in the range below the closed loop bandwidth, would directly decrease the jitter of the MLO system
- The given schemes only measure the difference between MO and MLO, not the absolute jitter. The controller is only able to minimize this error, shown as the red area *e* in the left part of Fig. 4.37. The gray part is not measured and can not be minimized by the control loop. If parts of absolute jitter are measured, e. g. with an optical delay line[4] shown as the orange part in the right part of Fig. 5, these components can be minimized by the controller.

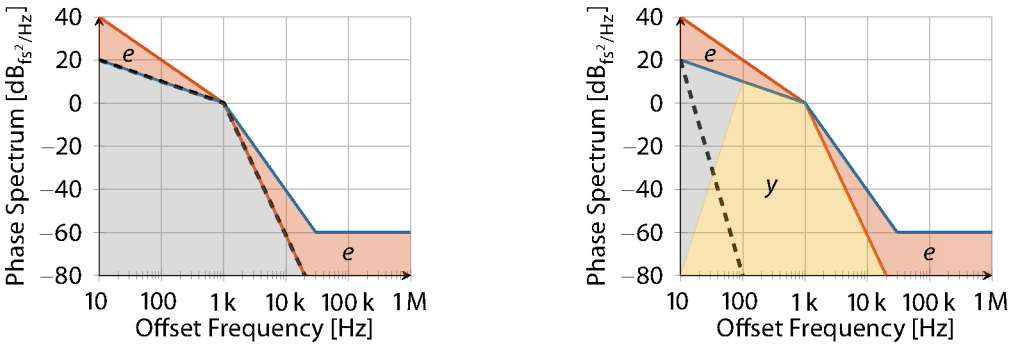

Figure 4.37: Additional phase noise measurement for the MIMO controller.

[4] It is the similar behavior as the links discussed in the next chapter.

4.2.5 Experiments

In the next step the designed controllers are tested in an experiment and the differences between simulation and real behavior is explained. After that, the increase of robustness using the unwrapped signal is shown.

The implementation of the controller is shown in Appendix B. The development of this firmware was one of the major tasks in parallel to the analysis of the LbSync system, [Heu+15a].

PI Design

Figure 4.38 shows the experimental results for the controller, K_{PI}, without any further manual tuning of the real system. This was the first model-based controller used at the MLO system. The MO is given in (——) and the open loop MLO is shown in (——). For the measurement of the closed loop phase noise, an in loop and an out of loop setup is used. In the in-loop configuration (——), the signal of the photo diode connected to the analog filter, shown in Fig. 4.1, is used. In the out-of-loop measurement (——), an own dedicated photo diode captures the signal. If there are additional disturbances due to these photo diodes, the controller suppresses these in-loop measurement, where they are not suppressed in the out-of-loop measurement, i. e. if there are differences between both measurements they could be induced by the measurement path. If multiple measurements are compared, it is important to use the same optical setup and the same settings for amplifieres and attenuators on the measurement boards.

Figure 4.38 shows that the closed loop phase noise follows the reference up to a frequency of 1 kHz, and above that frequency it is below the reference. At 3 kHz and higher, the phase noise is superimposed by the different noise sources, like amplifier, diode, SSA, and others.

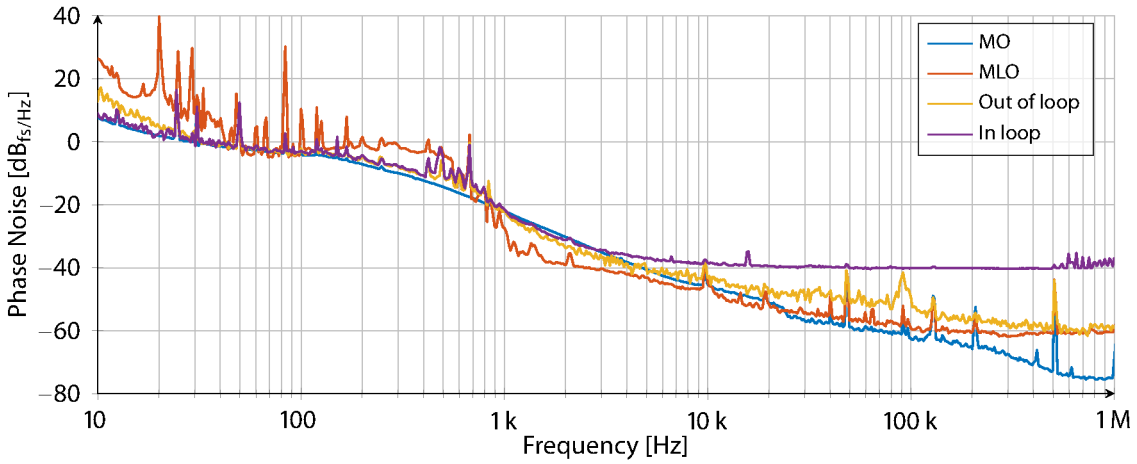

Figure 4.38: Phase noise of the closed loop with the controller C_{PI}.

Unwrapped Phase

The next experiment shows the increase in robustness due to the locking using the unwrapped signal. With the controller C_{PI}, a direct disturbances on the MLO housing did not excited the laser enough to move it to a different bucket. To show the effect, a controller with a ten times smaller closed loop bandwidth was chosen.[5]

Figure 4.39 shows the system response if a disturbance is applied to the MLO housing. On the left side the response with a controller acting on the 1516.67 MHz phase signal (——) and on the right the unwrapped phase signal (- - -), respectively. Moreover, the different stable buckets (- - -) for the 1516.67 MHz signal, w.r.t. the absolute 216.67 MHz phase (——), are shown.

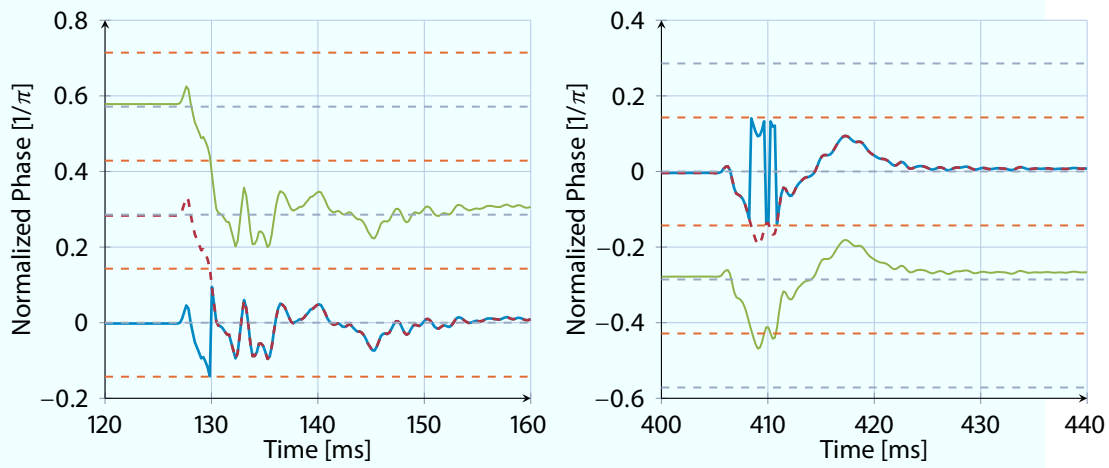

Figure 4.39: Disturbance rejection if locking to the 1516 MHz phase (——) or to the unwrapped phase (- - -), with the 216 MHz phase (——), the buckets (- - -) and the stable equilibrium inside the bucket (- - -).

It is shown, that if a disturbance moves the 1516.67 MHz signal (——) to the boundaries of its dynamic range, the error signal jumps to the opposite region in its dynamic range and the controller stabilizes the MLO at a different bucket. This can be shown by the 216 MHz signal (——), which changes the bucket. This leads to a constant offset with respect to the required steady state value. If the unwrapped (- - -) is used for the locking, introduced in Section 4.1.3, the algorithm detects the jump of the signal and corrects it. This leads to the result that the laser is again locked in the same bucked, shown on the right graph where the 216 MHz signal (——) returns to the same bucket. Moreover, it is shown that the bucket of the unwrapped phase depends on the conditions of the firmware at the start. In the left plot there is a difference of two buckets between the 216.67 MHz signal and the unwrapped 1516.67 MHz on the right plot one bucket. This has to be calibrated after the start, but doesn't change after that.

[5] It is excepted, that subsystems of the XFEL or laser of other facilities are more sensitive to this effect, e. g. if the 37th harmonic, instead of the 7th, is taken for the phase detection.

4.3 Conclusion

This chapter analysed the MLO subsystem of the LbSync system. It was shown what the performance requirements are given by the $\mathcal{H}_2$ norm and how to model the dynamic behavior, the disturbance, and noise sources. After that, inital control strategies were proposed and validated in an experiment.

For the MLO system, the questions raised in Section 1.1 can be answered as follows:

1. The control challenge of the MLO system is the minimization of the absolute timing jitter, which corresponds to the minimization of the $\mathcal{H}_2$ norm of the system output.
2. A suitable model for the MLO system is an integrator. The disturbance and noise effects can be modeled by AWGN filtered by 3rd order LTI systems.
3. A PI controller is sufficient for the MLO system. The controller parameter should be calculated by an LQR approach and tuned with open loop phase noise measurements.
4. A possible way to increase the MLO performance in the sense of phase noise is an additional measurement of the absolute phase.
5. The robustness of the MLO system can be increased by control to the unwrapped phase, which increases the dynamic range of the error signal.

The main limitation of this system is the trade-off between following the MO or the MLO. To reduce the phase noise of the laser pulse train the measure of the absolute phase of the MLO itself and not with regards to the MO could be used. A possible solution for that, an optical delay line, is discussed in the next chapter.

A further step is the evaluation of the shown methods on different subsystems. If other piezoelectric components are used and the piezo resonance is within the locking range, it could be important to add resonances of this actuator and/or take the hysteresis into account. This would lead to a significant difference between closed loop performance of the PI and $\mathcal{H}_2$ optimal controller.

5 LINK STABILIZING UNIT

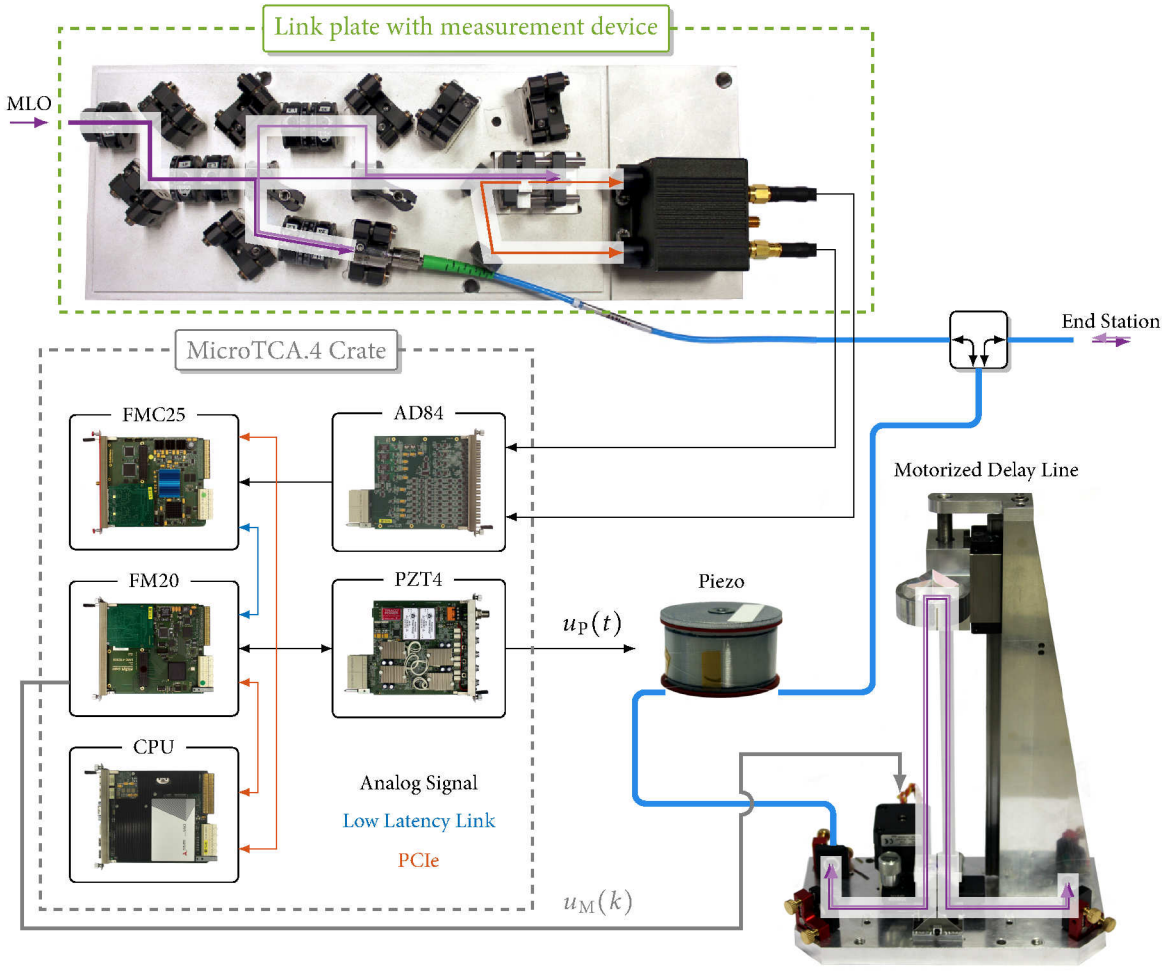

Figure 5.1: Overview of the LSU discussed in this chapter, with a single crate setup and two transmissions through the actuators per up- and downstream of the laser pulse.

The laser pulse train generated by the MLO has to be transmitted to the end stations in the facility by an optical fiber. The LSU is used to keep the pulse travel time within this fiber constant in a range of femto-seconds. This chapter starts by explaining the basic principles of this device. After that a model is developed and identified, and inital control approaches are analyzed and tested. The section closes with the discussion of further improvements for this system.

5.1 Modeling

Figure 5.1 shows a simplified principle of the LSU with the link plate in the upper part. On this plate, the timing difference between a pulse arriving from the MLO and a pulse returning from the end station is measured using an Optical Cross Correlator (OXC). This value is used to stabilize the optical path behind this device.

A piezo stretcher and a MDL are used as actuators. Both are shown in the lower right part of Fig. 5.1. As for the MLO, the piezo stretcher is used as the main actuator and the MDL is used for the coarse tuning. Fig. 5.2 depicts the working principle of both actuators applying a small length change $\Delta l(t)$ to the total optical path length $L(t)$.

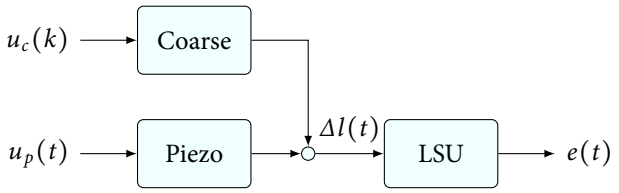

Figure 5.2: Influence of both laser oscillator inputs.

In order to increase the sensitivity, the piezo is passed twice and the MDL twelve times for the up- and downstream path. For the measurement, it is required to add a Dispersion Compensating Fiber (DCF) in order to compensate for pulse broadening. With this, and the length of the fiber L_{Fiber} itself, the total optical length, which the pulse travels through, is given by

$$L = \underbrace{2 \cdot L_{\text{Piezo}} + 12 \cdot L_{\text{MDL}} + 2 \cdot L_{\text{DCF}} + L_{\text{Fiber}}}_{L_{\text{upstream}}} + \underbrace{2 \cdot L_{\text{Piezo}} + 12 \cdot L_{\text{MDL}} + 2 \cdot L_{\text{DCF}} + L_{\text{Fiber}}}_{L_{\text{downstream}}} . \tag{5.1}$$

The length L_{Piezo} is the 40 m long fiber around the piezo stretcher, see [PZ2], L_{MDL} is the 1 m long single path in the MDL, L_{DCF} is the length of the DCF and L_{Fiber} is the length of the fiber. In the laboratory setup a short link with $L_{\text{Fiber,short}} \approx 10\,\text{m}$ and $L_{\text{DCF,short}} \approx 1\,\text{m}$, leading to $L_{\text{short}} \approx 184\,\text{m}$, and a long link with $L_{\text{Fiber,long}} \approx 3.6\,\text{km}$, $L_{\text{DCF,long}} \approx 240\,\text{m}$ and $L_{\text{long}} \approx 8.324\,\text{km}$ are available.

For the LSU setup, an AD84 is used to capture the measurement data. These are piped to an FMC25 that hosts the control algorithm. The calculated control value is transmitted via a low latency link to the FMC20 board, setting the piezo voltage to a new value.

In the final setup the detection and control part (AD84 and FMC25) will be in a different crate than the actuator part (FMC20 and PZT4), which could increase the system latency.

In the following section, the model for the spatially extended optical fiber will be developed. After that, the measurement of the optical length is explained with its influences the control application. With the fiber and the measurement combined, the whole model for the LSU is presented.

5.1.1 Pulse Train in an Optical Fiber

The optical pulse train is explained and modeled in Section 4.1.2. Figure 5.3 shows, how this pulse train is transmitted through a simple piece of fiber. If the length of this fiber is an n-th multiple of the laser period length L, it acts as a pure constant time delay.

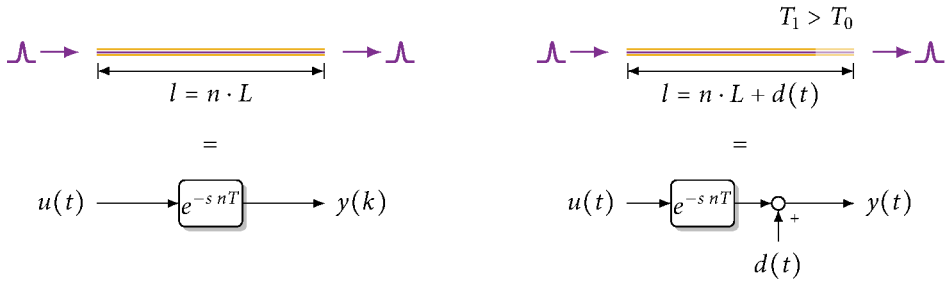

Figure 5.3: Modeling of the optical fiber.

During manufacture and assembly, the length will not fit perfectly to this multiple, which can be modeled by a constant part in the disturbance, $d(t)$. Dynamical parts in $d(t)$ are induced by, for example: temperature or humidity changes and vibrations acting on the fiber. If these influences caused a length change of $\geq 0.5L$, the time delay in the model would change. This is not expected for the LbSync system, which leads to a time invariant time delay.

The total timing error of the pulse, at the fiber end, is given by

$$y(t) = e^{-s\,nT} u(t) + d(t)\,, \tag{5.2}$$

where the initial timing error of the incoming pulse is $u(t)$ and the disturbance $d(t)$ is small compared to the period length of the pulse train.

With the optical displacement given in the data-sheet [PZ2], the maximum change of the optical length, due to the piezoelectric actuator is given by

$$\Delta l_{\text{Piezo}} = 4 \cdot 8.1 \frac{\mu\text{m}}{\text{V}} \cdot 80\,\text{V} = 2.592\,\text{mm} \ll L = 0.975\,\text{m}\,. \tag{5.3}$$

The possible optical change by the MDL is given by

$$\Delta l_{\text{Motor}} = 4 \cdot 6 \cdot 21\,\text{cm} = 504\,\text{cm} \approx 5 \cdot L\,. \tag{5.4}$$

Both actuators in combination are used to compensate for fast fluctuation and long term drifts. The maximum operation range of both is smaller than the period length of the pulse. This leads to the conclusion that, for this model of the LSU system, different but constant time delays nT are given and only the disturbance $d(t)$ varies in time.

5.1.2 Measurement with an Optical Cross Correlator

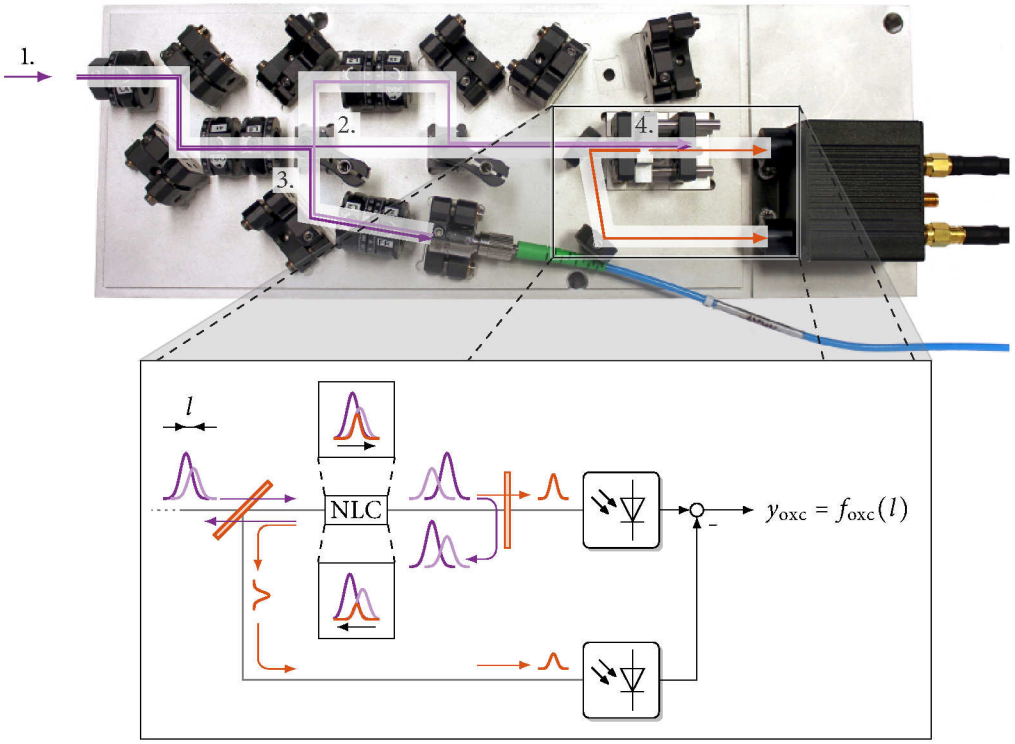

Figure 5.4: Measurement principle of the LSU.

The measurement, used to keep the optical fiber length constant, is the time difference of a pulse coming from the MLO and one coming from the end station. If both pulses arrive at the link plate at the same time, the optical length is a multiple of the pulse repetition rate.

The upper part of Fig. 5.4 shows the link plate where the optical setup for this measurement is realized. If a pulse from the MLO (——) enters the LSU (1.), it is split (2.), and a small fraction is branched off and goes directly to the OXC (4.). The main part (3.) is coupled into the fiber and goes through the actuators to the end-station in the accelerator. There, the pulse is partially reflected and travels back the way to the link plate. This returning pulse (——) and the fraction of the subsequent pulse are guided through an OXC which is used to determine the timing difference.

The lower part of Fig. 5.4 shows this. A non-linear crystal generates a correlation (——) of the two pulses (——) and (——). Behind the crystal, the correlation is sampled by a photo diode and both pulses are reflected back trough the crystal. This generate a second correlation (——), also sampled by a photo diode. Due to the birefringence of the crystal a group delay between both differentially polarized pulses is given which enables the implementation of balanced cross correlation, see [Kim+07].

The difference of the two correlations, for pulses with the shape given in (4.1), is given by

$$f_{oxc}(l) = \frac{P_+}{cosh^2\left(\frac{d_+ + l}{a_+}\right)} - \frac{P_-}{cosh^2\left(\frac{d_- - l}{a_-}\right)} + b\,, \tag{5.5}$$

and its derivative by

$$\frac{\mathrm{d}f_{oxc}(l)}{\mathrm{d}l} = \frac{2\,P_+\,sinh\left(\frac{d_+ + l}{a_+}\right)}{a_+\,cosh^3\left(\frac{d_+ + l}{a_+}\right)} + \frac{2\,P_-\,sinh\left(\frac{d_- - l}{a_-}\right)}{a_-\,cosh^3\left(\frac{d_- - l}{a_-}\right)}\,. \tag{5.6}$$

The maximum power of the correlation pulses $P_+\,, P_-$ is dependent on the laser power of the MLO. The duration parameters $a_+\,, a_-$ are dependent on the fiber components and can drift with temperature or humidity changes, which slightly changes the fiber's properties. The position $d_+\,, d_-$ of those pulses are dependent on the mechanical setup and are constant. The constant bias voltage of the balanced detector b is subtracted from the measurement and can be neglected. With the separation of constant and time-varying parameters, (5.5) is given as

$$f_{\mathrm{oxc}}(l(t), \rho(t), p) \quad \text{with} \quad \rho(t) = [P_+(t), P_-(t), a_-(t), a_+(t)] \quad \text{and} \quad p = [d_+, d_-]\,, \tag{5.7}$$

where $l(t)$ is the length change of the fiber, $\rho(t)$ are drifts with a much lower frequency, and p are constant parameters.

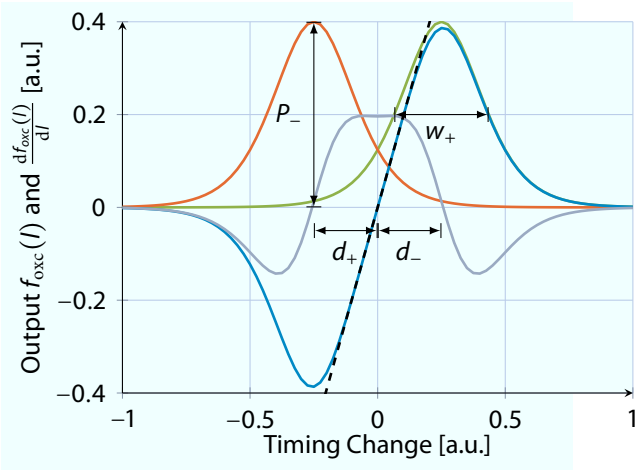

Figure 5.5: Non-linear function of the OXC measurement used for the LSU.

Figure 5.5 shows a typical OXC function, with the positive (——) and negative (——) correlation pulse, the combination of both (——), and the first derivative of this function (——). The full width at have maximum of the pulse is given by $w_+ \approx 1.76 \cdot a_+$.

If the duration and position parameter are chosen in the right way, a small region, close to the zero crossing, can be approximated by a linear function. In this region, where the sensor is usually operated in, the timing difference between both pulses is proportional to the measurement output.

5.1.3 Modeling of the Optical Fiber

This section shows how to model an optical fiber in combination with the given relative measurement discussed in the last section. The main question to be addressed is, if it is possible to detect length changes at the end of the fiber.

Single fiber solution

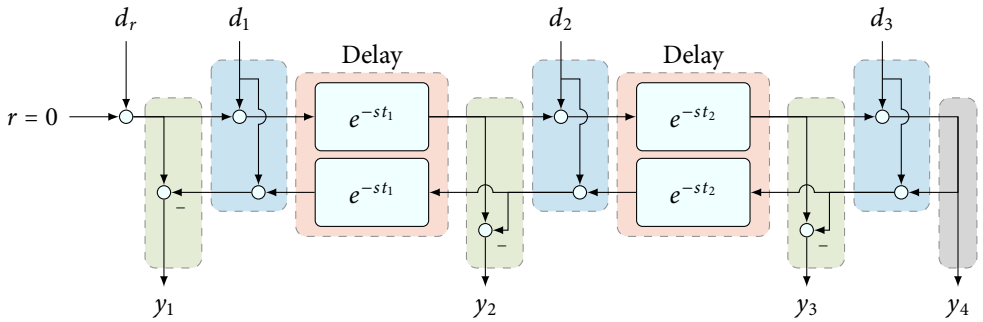

Figure 5.6: Block Diagram of the optical fiber with a mirror at the end, including the reference input r, different disturbance inputs $d_\bullet$, and measurement positions $y_\bullet$.

Figure 5.6 shows a block diagram for the timing of the laser pulse train where a single fiber is used for the up- and downstream transmission. In the following, the time or frequency dependence is omitted for the signals. The timing error of the incoming pulse train is given by d_r and the reference value r can be used to achieve a constant shift of the pulse train. The disturbance inputs $d_{1,2,3}$ are small length changes – compared to the period length of the pulse train – at different positions of the fiber. If an actuator, such as a piezo stretcher, is attached at a point of the fiber, the length change due to the actuator acts like a disturbance. Later, the length change induced by the piezo stretcher Δl is considered at the position of d_1.

The disturbance, d_1, is active at the beginning and d_3 is active at the end of the fiber. Choosing the delays t_1, t_2, d_2 can model a disturbance at an arbitrary point of the fiber. At the end of the fiber link, a part of the pulse, y_4, is used for the end-station and the other part is reflected back through the fiber. This output y_4 should be stabilized, but it is not measurable in the final setup. The available measurement is given at y_1.

Based on this structure, the solution with one fiber can be modeled with the transfer function,

$$y(s) = G(s)d(s), \quad \text{where} \tag{5.8}$$

$$G(s) = \begin{bmatrix} e^{-s(t_1+t_2)} & e^{-s(t_1+t_2)} & e^{-s(t_2)} & 1 \\ 0 & 0 & 0 & -2 \\ (1-e^{-s(2t_2)})e^{-s(t_1)} & (1-e^{-s(2t_2)})e^{-s(t_1)} & -1-e^{-s(2t_2)} & -2e^{-s(t_2)} \\ 1-e^{-s(2t_1+2t_2)} & -1-e^{-s(2t_1+2t_2)} & (-1-e^{-s(2t_2)})e^{-s(t_1)} & -2e^{-s(t_1+t_2)} \end{bmatrix} \tag{5.9}$$

and

$$y(s) = \begin{pmatrix} y_4 \\ y_3 \\ y_2 \\ y_1 \end{pmatrix}, \quad d(s) = \begin{pmatrix} d_r \\ d_1 \\ d_2 \\ d_3 \end{pmatrix}, \quad t_3 = t_1 + t_2 . \tag{5.10}$$

The behavior for a very short fiber, where one pulse from the MLO is correlated with itself inside the OXC, is given by setting the time delays t_1 and t_2 to zero. The transfer matrix in that case is given by

$$G(s)|_{t_1=t_2=0} = \begin{bmatrix} 1 & 1 & 1 & 1 \\ 0 & 0 & 0 & -2 \\ 0 & 0 & -2 & -2 \\ 0 & -2 & -2 & -2 \end{bmatrix}. \tag{5.11}$$

This gives a first impression of the fiber properties. Dependent on the input of a disturbance and the position of the measurement device, different disturbances are observable or not. The end-station y_4 always gets all disturbances, see first row of (5.11), while the measurement device detects only disturbances in the fiber after they occur, compare the following rows. Moreover, the disturbances of the MLO are not visible at the measurements but at the end-station, see first column.

In the final setup, the input d_1 is used for the actuator and the output y_1 for the measurement. The steady state y_1 should be controlled to zero. It follows that

$$y_1 = 0 \Rightarrow d_1 = -d_2 - d_3 . \tag{5.12}$$

From this, it follows, for the steady state, that

$$y_4 = d_r + d_1 + d_2 + d_3 = d_r - d_2 - d_3 + d_2 + d_3 = d_r . \tag{5.13}$$

This means that with the single fiber, where disturbances are equally added up- and downstream, given it is a short fiber, it is possible to cancel the disturbances that are behind the measurement device. Disturbance before that device are not observable in this case and the controller is not capable of compensating for these.

Two fiber solution

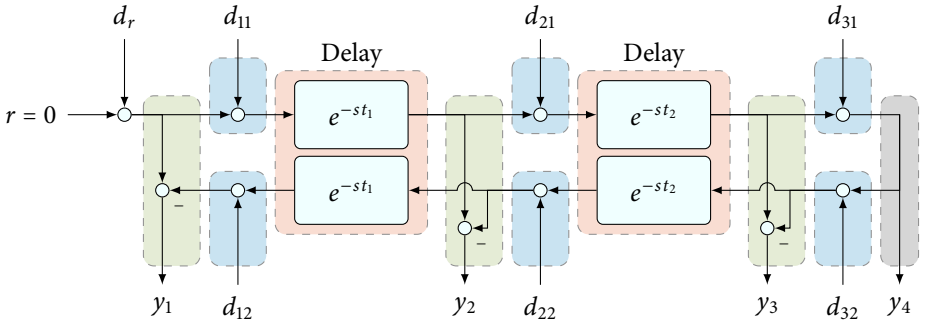

Figure 5.7: Block Diagram of the setup with two optical fibers, a mirror at the end, the reference input r, different disturbance inputs $d_\bullet$, and measurement positions $y_\bullet$.

The second example is shown in Fig. 5.7. This block diagram depicts the case if two different fibers are used for the down- and upstream or if the path in the actuator chain is not symmetrical. Thus the total disturbance input is given by

$$d(s) = \begin{pmatrix} d_r & d_{11} & d_{12} & d_{21} & d_{22} & d_{31} & d_{32} \end{pmatrix}^T , \tag{5.14}$$

where $d_{\bullet 1}$ are the disturbances acting on the upstream and $d_{\bullet 2}$ on the downstream path, respectively. The transfer matrix for a short link is than given by

$$G(s)|_{t_1=t_2=0} = \begin{bmatrix} 1 & 1 & 0 & 1 & 0 & 1 & 0 \\ 0 & 0 & 0 & 0 & 0 & -1 & -1 \\ 0 & 0 & 0 & -1 & -1 & -1 & -1 \\ 0 & -1 & -1 & -1 & -1 & -1 & -1 \end{bmatrix} . \tag{5.15}$$

In this case, the fiber end gets all upstream disturbances (first row) but the measurement devices observes all up- and downstream disturbances. For the steady state control case with the actuator on d_{11} and the measurement y_1, it follows that

$$y_1 = 0 \Rightarrow d_{11} = -d_{21} - d_{31} - d_{32} - d_{22} - d_{12} \quad \text{and} \tag{5.16}$$

$$y_4 = d_r - d_{32} - d_{22} - d_{12} . \tag{5.17}$$

If, for example, a disturbance is present on channel d_{31} and exactly the opposite disturbance enters on channel d_{22}, the pulse timing on y_3 changes whereas the timing on y_1 stays the same. This unwanted behavior justifies the single fiber solution and shows that it is important to pass all actuators on the up- and downstream path in the same way. This example was not done in one of the first LSU designs [KK10]. A similar discussion, from a non-system-theoretic point of view, is performed in [Sch11] and leads to the same results.

Bode diagram of the fiber transfer function

In the case of a spatially extended fiber, the whole transfer matrix (5.9) is required. There are two characteristic functions depending on the fiber length. These are

$$G_{y_1 d_r} = G_r(s) = \quad 1 - e^{-s\,2t_3} \quad \text{and} \tag{5.18}$$

$$G_{y_1 d_1} = G_d(s) = -1 - e^{-s\,2t_3}\,, \tag{5.19}$$

where t_{12} is the delay due to the fiber. The other parts of (5.9) are just combinations of these two with different and additional time delays.

The bode diagram of these transfer functions is shown in Fig. 5.8. $G_r(s)$ is given on the left and $G_d(s)$ on the right side. A short fiber of 114 m (—) with a traveling time of $2t_3 = 0.558\,\mu$s , a fiber of 416m (—) and $2t_3 = 4.076\,\mu$s, and a long fiber of 4.162 km (—) and $2t_3 = 40.760\,\mu$s are shown.

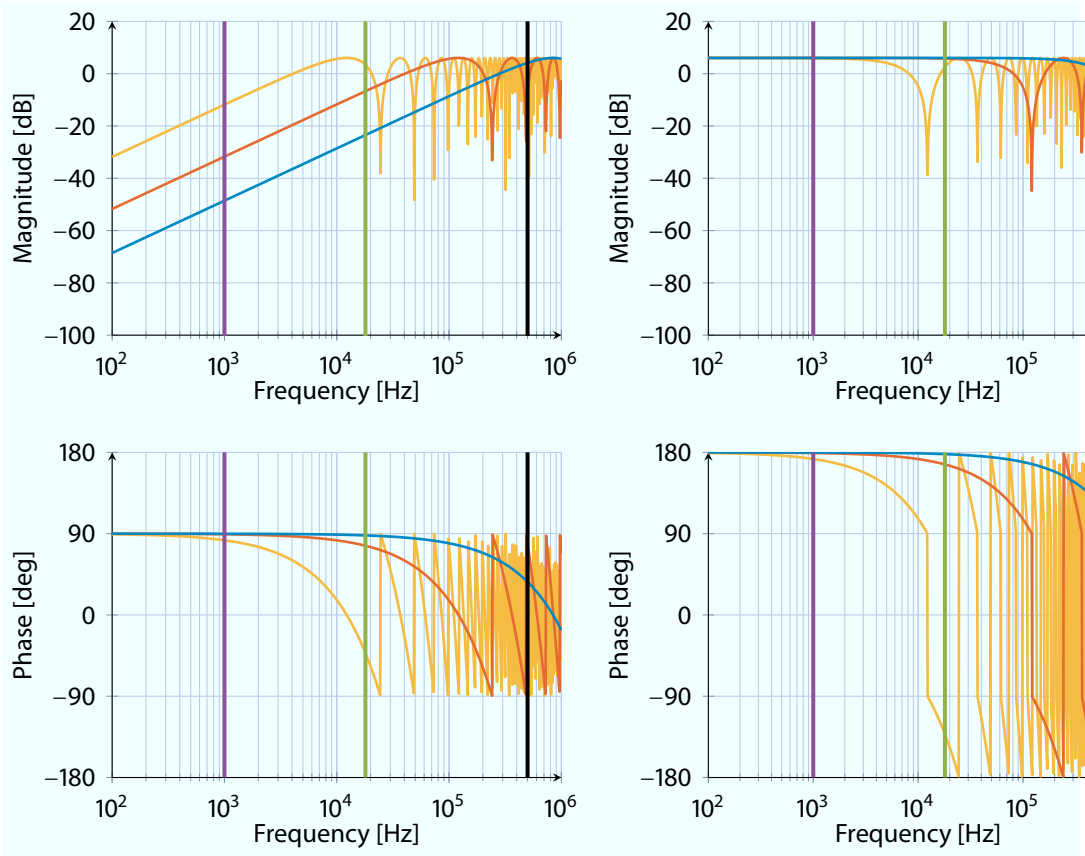

Figure 5.8: Bode diagram of G_r (left) and G_d (right) for the short test link (—), the FLASH link (—), and the long test link (—) with the piezo resonance (—), the MLO bandwidth (—), and the DAC sampling rate (—)

The magnitude of $G_r(s)$, i. e. the transfer from the MLO to the measurement, goes to zero for small frequencies. Dependent on the fiber length, the magnitude increases to a maximum of $\approx$ 3 dB for higher frequencies. After that, maxima and zero transmissions are repeated. For spatially extended fibers this also means low frequency disturbances induced by the MLO are not transmitted. Higher frequencies can be transmitted with a maximum gain of 2.

For the transfer function, $G_d(s)$, a similar behavior can be observed. For low frequency disturbances the gain is given by $\approx$ 3 dB. After a first cancellation the same behavior as at $G_r(s)$ is given. An important point is that the minima of $G_d(s)$ are the cancellation of $G_r(s)$ and vice versa.

Figure 5.9 shows the same bode diagram from the top view to visualizes the fiber length dependence. The frequency is given on the x-axis, the y-axis denotes the length of the fiber and the magnitude is indicated by the greyscale.

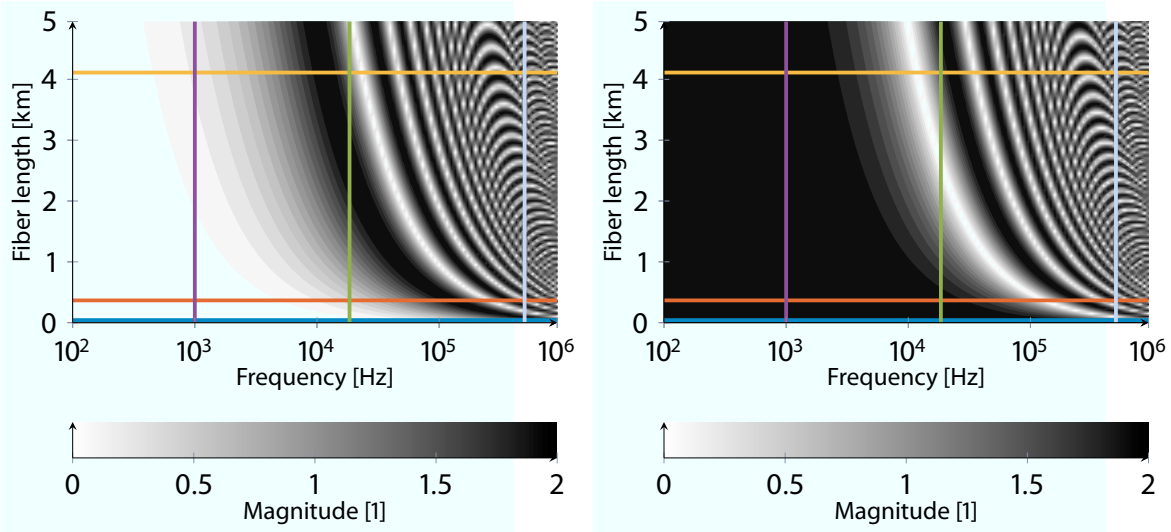

Figure 5.9: Amplitude plot of G_r (left) and G_d (right) for the short test link (—), the length of FLASH (—) and the long test link (—) with the first piezo harmonic (—), the MLO bandwidth (—) and the DAC sampling rate (—).

For a short link length with $t_3 \to 0$, the approximation

$$G_r(s) \approx 0 \quad \text{and} \quad G_d(s) \approx 2\,, \tag{5.20}$$

can be used and shows the behavior observed in previous experiments. Changes from the MLO are not measurable on the sensor but those due to length deviations of the fiber are.

If long links ($L \gg 2\,\text{km}$) in combination with high frequencies ($f \gg 10\text{kHz}$) are used, like in the XFEL, these effects are relevant. In the succeeding subsections, the dynamic behavior of available link setups are identified. With these measurements, the theoretical assumptions are validated.

5.1.4 Control Objectives

For the MLO system the control objective is to find a controller minimizing the integrated timing jitter of the pulse train. The same objective is given for the LSU. Compared to the MLO, there is no known major disturbance that should be suppressed. The behavior which should be optimized is the weak damped oscillation of the piezo crystal. For this reason, the dynamic behavior around the first harmonic of that piezo crystal will be identified.

5.1.5 Model Structure

For the final link setup, the timing error of the MLO enters at d_r, the measurement is installed at position y_1, and the piezo acts on position d_1. This leads to the setup, shown in Fig. 5.10. In the upper part the fiber is modeled as discussed in the previous section. $G_{\text{Piezo}}(s)$ is the transfer function of the piezo, which describes the fiber length change, Δl, generated by an applied voltage u. The non-linear measurement function of the OXC is given by f_{oxc}.

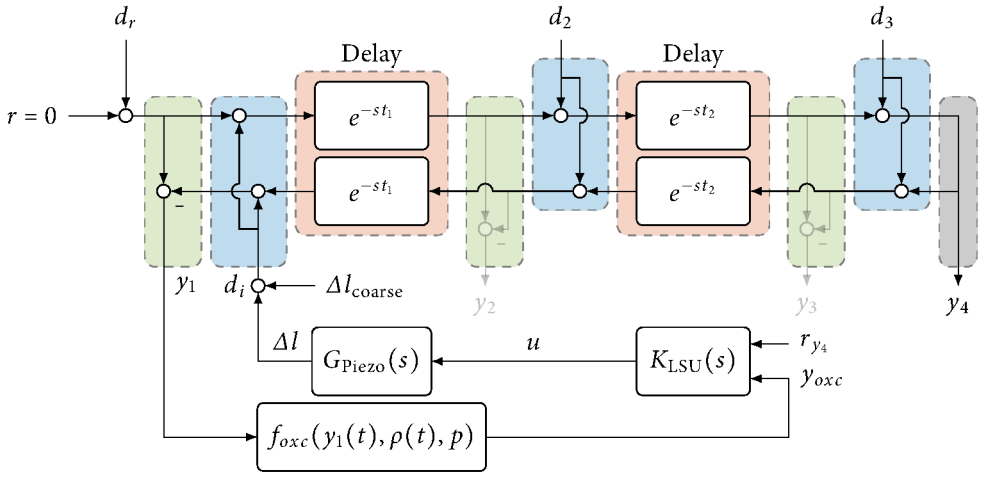

Figure 5.10: Block Diagram of the optical fiber with the measurement function f_{oxc}, the controller $K_{LSU}(s)$, and the piezo $G_{\text{Piezo}}(s)$.

It is assumed, that the piezo stretcher is a linear system, shown in 3.2. In a first step, its transfer function, $G_{\text{Piezo}}(s)$, has to be identified. Even if the attached fiber is changed, this transfer functions stays the same. To minimize the effects of the fiber, this identification is performed with a short laboratory fiber with a total optical length of ≈ 114 m. As shown in the previous section this simplifies the fiber to a gain of two for frequencies $\ll 200$ kHz.

In the second step, a longer fiber is attached to validate the theoretical assumptions of the previous section. With the same piezo but a different fiber, the change in the dynamic behavior is related to this changed component.

5.1.6 Dynamic behavior with a short optical fiber

In the first approach, a white box model, based on the Butterworth-Van Dyke equivalent circuit, introduced in Sec. 3.2, is used for the fiber stretcher. The different circuit components, shown in Table 5.1, are given in [PZ2] and [PZT4].

Table 5.1: Data of the piezoelectric fiber stretcher.

	Electrical Part	1st Harmonic	2nd Harmonic
Resistance [Ω]	5	20	3.3
Inductance [mH]	-	15	0.7
Capacitance [nF]	75	5	12

With these values, the model for the piezo actuator $G_{\text{Piezo}}(s)$, mapping an excitation u_0 in [V] to an optical fiber length change Δl in [fs], is given by

$$\begin{bmatrix} \dot{u}_0 \\ \dot{i}_1 \\ \dot{u}_1 \\ \dot{i}_2 \\ \dot{u}_2 \\ \hline \Delta\dot{l} \end{bmatrix} = \left[\begin{array}{ccccc|c} -2.67\cdot10^6 & -13.3\cdot10^6 & 0 & 13.3\cdot10^6 & 0 & 2.67\cdot10^6 \\ 66.7 & -1.33\cdot10^3 & -66.7 & 0 & 0 & 0 \\ 0 & 200\cdot10^6 & 0 & 0 & 0 & 0 \\ 1.43\cdot10^3 & 0 & 0 & -4.71\cdot10^3 & -1.43\cdot10^3 & 0 \\ 0 & 83.3\cdot10^6 & 0 & 0 & 0 & 0 \\ \hline 12.67 & 0 & 12.67 & 0 & 12.67 & 0 \end{array}\right] \begin{bmatrix} u_0 \\ i_1 \\ u_1 \\ i_2 \\ u_2 \\ \hline u \end{bmatrix}. \tag{5.21}$$

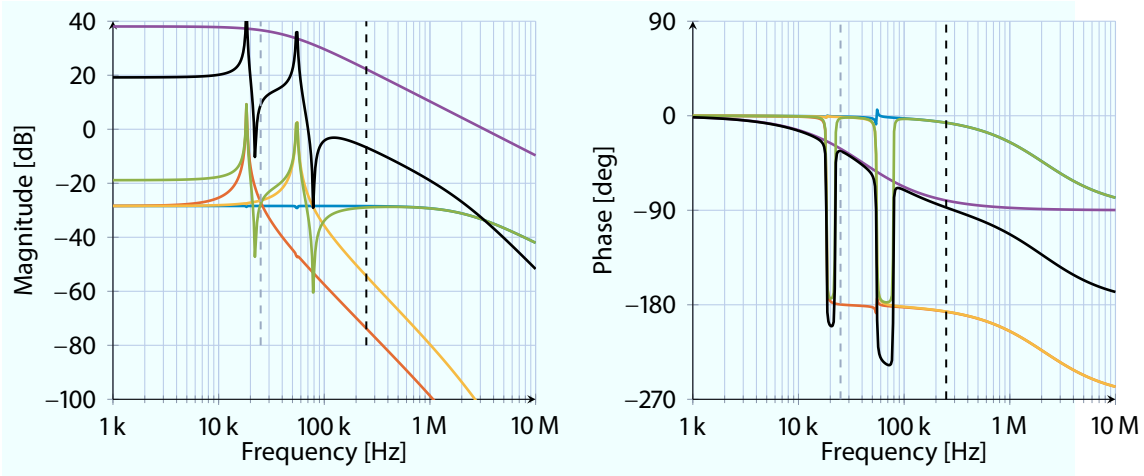

Figure 5.11: Bode diagram for piezoelectric actuator normalized to a length change of 1 ps, with the electrical part (—), the 1st (—), and 2nd Harmonic (—), the length change Δl (—), and the length change including the PZT4 (—).

Figure 5.11 shows the transfer function of the PZT4 (—), the electrical part of the piezo (—), both harmonics (—) and (—) and the combined displacement Δl (—).

Adding the sensitivity of the OXC and the simplification for a short fiber yields

$$G_{\text{Short}}(s) = -2 \cdot f_{\text{oxc}} \cdot G_{\text{Piezo}}(s)\,. \tag{5.22}$$

The expected response of the white box model (—) and the measured response (—) are shown in Fig. 5.12. To compare both measurements, it is crucial to capture the measurement function f_{OXC} and normalize their responses. The current pulse power and the pulse shape can be different, which changes the slope in the linear range. However, the normalized (—) response in [ps] can be compared with the white box model.

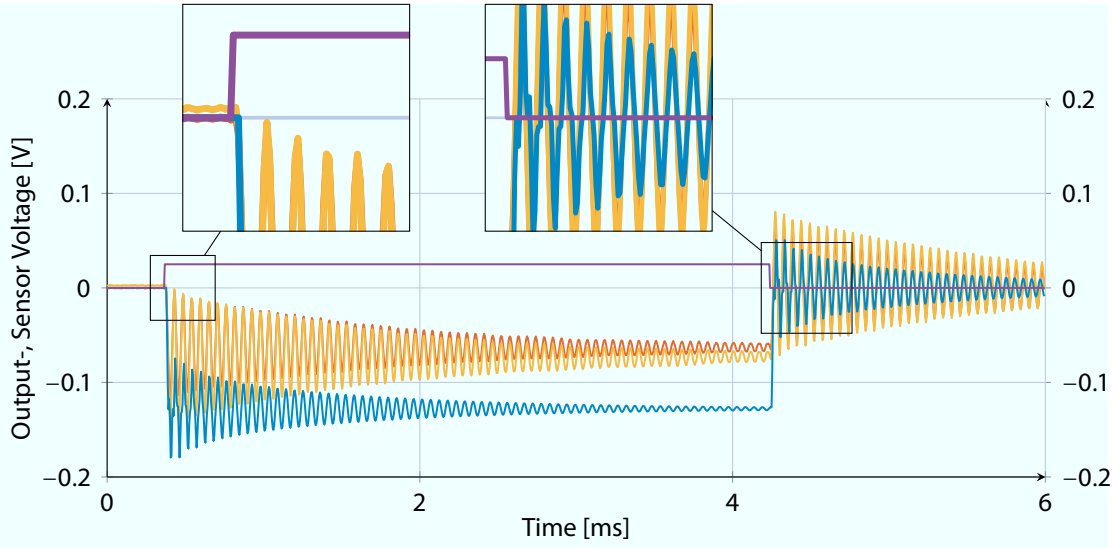

Figure 5.12: Step response of the short links setup $G_{\text{Short}}(s)$, showing the excitation voltage (—), the sensor measurement in $[\frac{\text{V}}{\text{V}_{\text{max}}}]$ (—) and in [ps] (—), and the white box model response (—) in [ps].

According to [PZ2], the first harmonic of the piezo stretcher is at a frequency of 18 kHz, which is confirmed by the measurement in Fig. 5.12. The second harmonic at 56 kHz leads to an additional oscillation shown the right magnified part. This effect is not observed in the measurement. One reason could be that this oscillation is damped more than the white box model assumes. An other possibility is that this mode excites the piezo stretcher in a shears movement that does not change the perimeter and therefore the fiber length. The principle modes of a thin-walled cylinder are e. g. illustrated in [WM05].

Furthermore, the damping of the first mode and the static gain of the white box model do not match with the experiment. To validate the theoretical model, the system is excited with PRB

and BLWN signals in order to perform a black box identification using the subspace identification method.

As a first step, the system order is estimated using the sorted singular values of the Hankel matrix. A selection of characteristic measurements are given in Table 5.2.

Table 5.2: Singular values of the Hankel matrix for different measurements.

	f_{max} [kHz]	1st	2nd	3rd	4th	5th	6th	7th
steps	-	5.774	5.326	0.2631	0.1056	0.08177	0.06484	0.05424
prbs 2	50	2.274	2.092	0.09332	0.07500	0.07119	0.06113	0.05739
prbs 4	25	19.854	18.484	0.4948	0.1679	0.1164	0.04638	0.01696
noise 1	100	1.569	1.469	0.08839	0.04336	0.03391	0.01815	0.01313
noise 4	25	19.924	18.489	0.2992	0.07749	0.01328	0.009518	0.007852

The first two singular values are in the same order of magnitude and much higher than those that follow. This indicates a dominant second order behavior, in this case the first piezo harmonic. The third singular value is an order of magnitude lower, but still higher than what follows, indicating an additional pole. In the classical model it is assumed that this low pass is given by the capacitance of the piezo. Figure 5.11 shows the bode plots of the transfer function of this part (——) and the low pass due to the piezo amplifier (——). The crossover frequency of this low pass is at a much smaller frequency. For this reason, this third pole is very likely induced by the piezo amplifier. For the high frequency excitations, the fourth and fifth singular values are indicating a second pole pair, the second piezo harmonic.

For $G_{\text{Piezo}}(s)$ a third order model and a fifth order model are identified using the *n4sid* method. The left part of Fig. 5.13 shows the poles and zeros for a third, and the right part for a fifth order model.

The third order model shows a light damped pole pair at $\approx 18\,\text{kHz}$ for all runs. The pole at the range of the PZT4 low pass is identified for all data sets except the step excitation. In that case the pole is estimated at higher frequencies.

The PRB signals and the fast noise excitation lead to the same results using the fifth order model. The poles at the first and second harmonic and the low pass of the piezo amplifier are identified at expected positions in the complex plane. However, zeros are not fitting with the white box model. The identified complex zero is at a little lower frequency as the second pole pair and not at a higher one as predicted. In the case of the step response, the single pole is estimated at a higher frequency than expected. For the low frequency noise excitation the second pole pair does not fit.

Prior to the identification process, the time delay, shown in the left magnified part of Figure 5.12 is estimated and removed from the data set. Even though the right half plane zeros in the

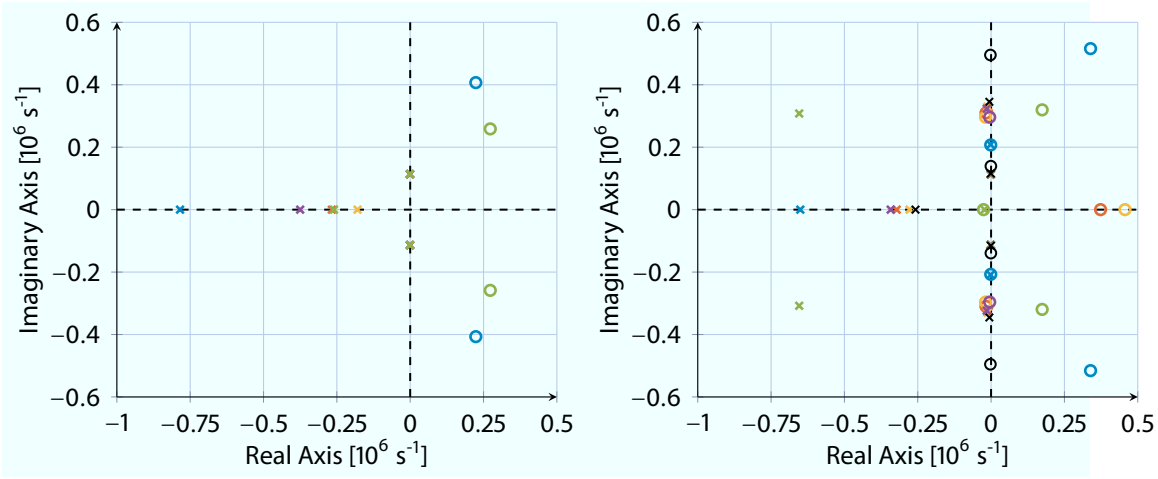

Figure 5.13: Poles and zeros of $G_{\text{Short}}(s)$, identified with the data set steps (——), prbs 2 (——), prbs 4 (——), noise 1 (——) and noise 4 (——), and the white box model (——).

identification are sensitive to further small variation of the data alignment. This could be caused by time delays modeled by those zeros.

The estimated delay amounts to three to four samples of the computing frequency of 500 kHz, i. e. 6 to 8 μs. This delay and its variation could be induced by the LLL, and the communication between the computing AMC and the FMC20 sending the data to the PZT4. In the final setup the control value is send via an optical link to a different crate. This scheme includes three LLL communication lines and four boards. It is likely that the time delay for this setup will increase.

Table 5.3 shows the cross validation of the two model types with respect to the other data sets. For the third order model the one identified using the prbs 1 data shows the best fit in the time domain and for the fifth order model the one identified from the prbs 4 data set.

Table 5.3: Cross validation of the different measurements and models for the LSU.

	3rd order model					5th order model				
	steps	prbs 1	prbs 4	noise 1	noise 4	steps	prbs 1	prbs 4	noise 1	noise 4
steps	95.64	87.28	85.75	91.56	79.56	82.47	74.59	85.97	70.74	77.97
prbs 1	72.10	89.88	89.71	84.23	77.18	57.56	55.68	82.78	44.30	77.34
prbs 4	74.38	91.97	93.18	87.86	77.48	59.73	50.22	82.11	37.61	76.01
noise 1	79.22	84.91	84.91	87.04	71.13	62.97	45.56	76.39	33.59	69.98
noise 4	53.27	78.03	77.02	67.87	93.38	47.50	53.91	72.74	45.19	89.37
avg.	74.92	86.41	86.11	83.71	79.75	62.05	55.99	80.00	46.28	78.13

Figure 5.14 shows the bode plot for the third (left) and the fifth order model (right).

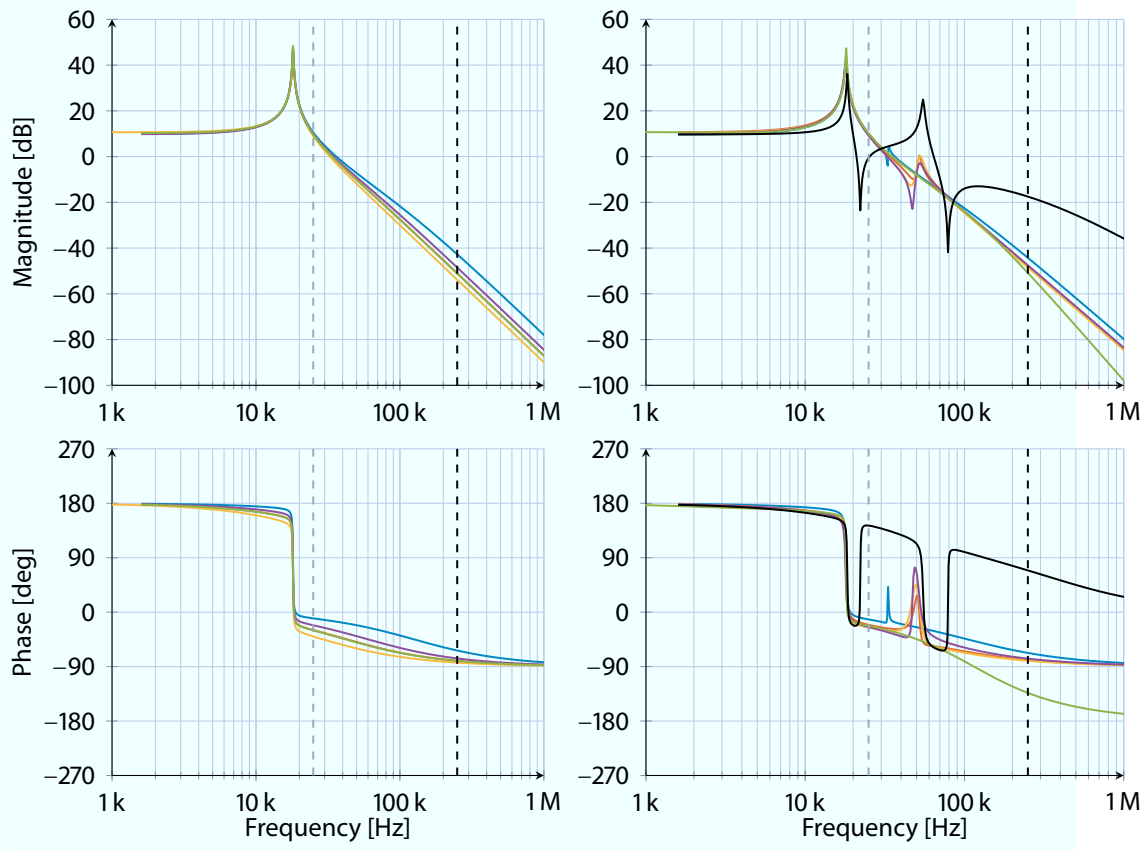

Figure 5.14: Bode diagram for $G_{\text{Short}}(s)$ with three (left) and five (right) states, identified with the data set steps (—), prbs 2 (—), prbs 4 (—), noise 1 (—), and noise 4 (—), and the white box model (—), normalized to a timing change of 1 ps.

The chosen third order model $G_{\text{Short}}(s)$ is given by the state space model,

$$\begin{bmatrix} \dot{x}_1 \\ \dot{x}_2 \\ \dot{x}_2 \\ \hline y \end{bmatrix} = \left[\begin{array}{ccc|c} -666.7 & 1.137 \cdot 10^5 & 0 & 3.203 \cdot 10^5 \\ -1.137 \cdot 10^5 & -666.7 & 0 & 1.273 \cdot 10^5 \\ 0 & 0 & -1.818 \cdot 10^5 & 5.542 \cdot 10^5 \\ \hline 0.7876 & 0.5756 & -0.7747 & 0 \end{array}\right] \begin{bmatrix} x_1 \\ x_2 \\ x_3 \\ \hline u \end{bmatrix}. \tag{5.23}$$

In the following, the model equation and controller parameter are scaled in time by 1000, according to Sec. 3.1.1, and the negative sign of the plant is removed in order to use a negative feedback with positive tuning parameter. This has numerical advantages and simplifies the tuning, but requires a rescaling prior to uploading the controller to the real system.

Moreover, the model (5.23) includes the small link approximation (5.20) leading to a factor 1/2 if used for long links.

5.1.7 Dynamic behavior with a long optical fiber

In the next step, a ≈ 3 km long fiber is connected to the LSU to validate the assumptions given in the previous section. The simplification for the short fiber (5.20) is thus not valid anymore, and the model, shown in Fig. 5.15, should be used. This model is a simplification of Fig. 5.10.

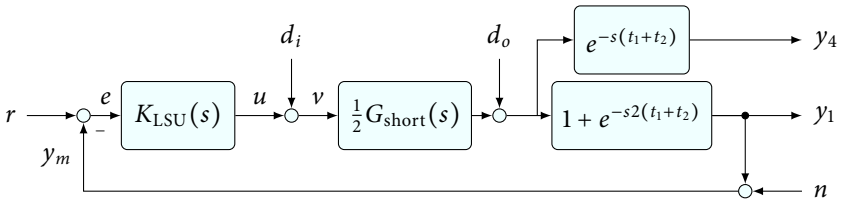

Figure 5.15: Control loop for the long link setup, with the additional link end output y_4.

The transmission zeros of the fiber transfer function (5.19) are an important property of this system. These lead to the step response depicted in Fig. 5.16. For the short link of 114 m (——), the measured response (left) has a factor two larger amplitude compared to the response at the link end (right). If the link length is increased to 1 km or 2 km, the amplitude of the oscillation decreases while the steady state gain remains the same. The response at the end-station is just delayed by the length of the fiber. The frequency and amplitude is not changing. If the fiber reaches a length of 2.824 km, the timing change of the upstream pulse induced by the oscillation of the piezo resonance and the one of the downstream pulse are compensated. The oscillation of the piezo mode is not visible at the measurement even though this vibration is present at the end-station. The same occurs if disturbances are present in the accelerator. If the elements in (5.9) are zero for certain frequencies at certain fiber positions the influence can not be detected.

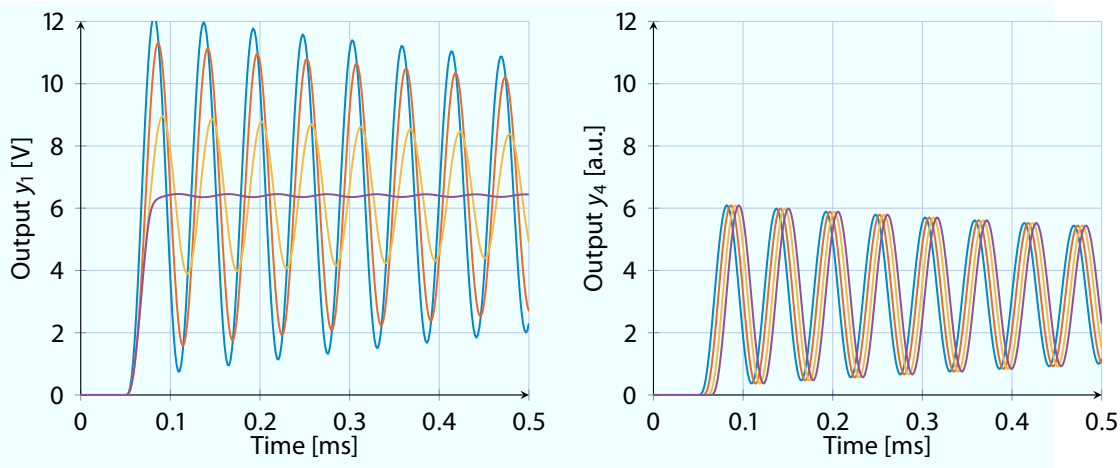

Figure 5.16: Simulated output y_1 (left) and y_4 (right) to a step input of the open loop LSU with the short (——), 1 km (——), 2 km (——), and a 2.824 km (——) long fiber.

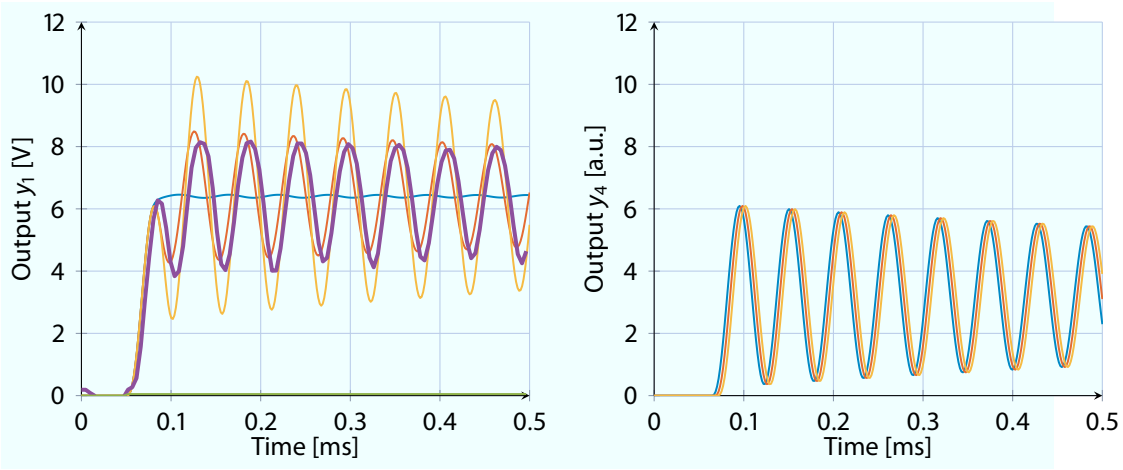

Figure 5.17: Simulated output to a step input of the open loop LSU with a 2.824 km (——), 3.5 km (——), and the maximum fiber of about 4.162 km (——) compared to the scaled measurement of an experimental link with a 4 km (——) long fiber.

Figure 5.17 shows the behavior if the link length is increase above this point. With a length of 3.5 km (——) to 4.162 km (——) the amplitude of the oscillation increases. A characteristic property ot the time response is the first oscillation before 0.1 ms, where only the timing change of the downstream pulse is measurable at the LSU. After the travel time, the upstream pulse arrives at the sensor and the full magnitude is visible. This predicted behavior is then measured (——).[1]

With the short fiber, $G_{\text{short}}(s)$, the transfer function, from Δl to y_1, for the long fiber is given by

$$G_{\text{Long}}(s) = \frac{1}{2} G_{\text{Short}}(s)\left(1 + e^{s2t_3}\right), \tag{5.24}$$

where $t_3 = t_1 + t_2$ is the pulse travel time inside the fiber for the up- or downstream path. With the length of the fiber l, the refractive index n and the speed of light c, given by $t_1 = t_2 = lnc^{-1}$. The fiber with its output y_4 can be modeled as shown in Fig. 5.18.

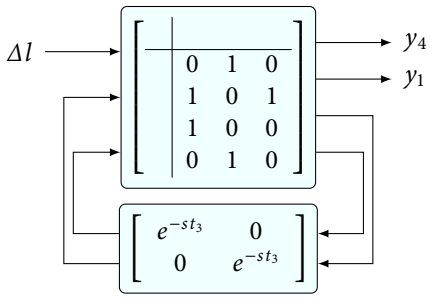

Figure 5.18: LFT model of the fiber link

[1] Due to a different OXC gain, the response is scaled to have the same steady state value as Fig. 5.16.

5.1.8 Dynamic behavior with the non-linear measurement function

In the next modeling step, the non-linear characteristic of the OXC measurement, introduced in Sec. 5.1.2, is added. This behavior is important to take into account if the disturbances are large, due to a long fiber or if the measurement principle is used in the L2L application.

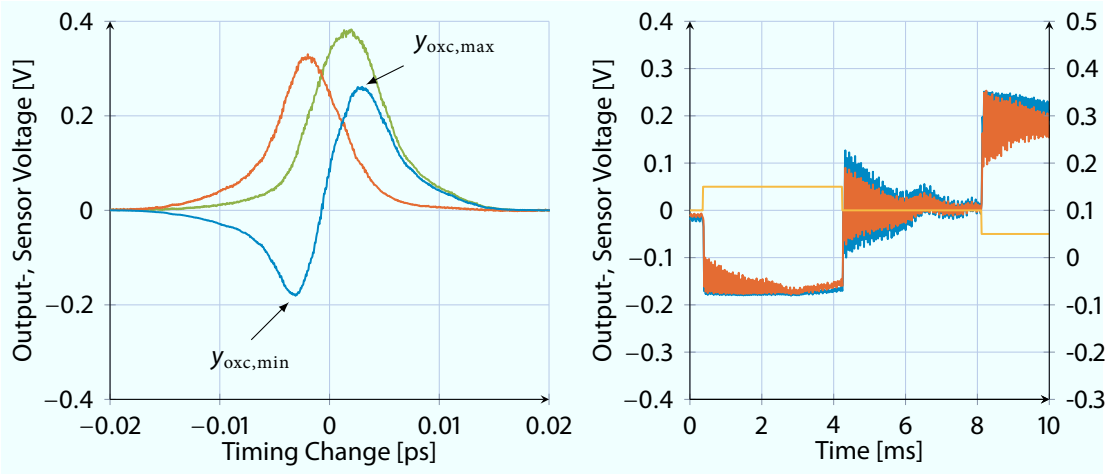

Figure 5.19: Typical measurement of f_{OXC} (left) with the positive (—), negative (—), and the difference (—) of the correlation pulses, and a step response leaving the linear region (right) with the additional excitation (—).

The left part of Fig. 5.19 shows a typical measurement function, captured by a voltage sweep with the piezo stretcher. The difference of the minimum $y_{oxc,min}$ and maximum $y_{oxc,max}$ is typically given due to the optical setup as a maximum timing change of ≈ 500 fs. If the system is operated outside this region the behavior shown on the right part of Fig. 5.19 is given. Even though the piezo stretcher oscillation is unchanged the measurement does not show this behavior anymore. The timing changes outside of $y_{oxc,min}$ to $y_{oxc,max}$ are mirrored back to the linear range.

The non-linear system for the LSU is given by the combination of (5.23) and (5.5) leading to

$$\dot{x} = A_{\text{Short}}\, x + B_{\text{Short}}\, u \tag{5.25a}$$

$$y_m = \frac{P_+}{cosh^2\left(\frac{d_+ + 2(C_{\text{Short}} x + d_\bullet)}{a_+}\right)} - \frac{P_-}{cosh^2\left(\frac{d_- - 2(C_{\text{Short}} x + d_\bullet)}{a_-}\right)}, \tag{5.25b}$$

where the matrices are given by (5.23), which is structured as follows

$$\left[\begin{array}{c} \dot{x} \\ \hline y \end{array}\right] = \left[\begin{array}{c|c} A_{\text{Short}} & B_{\text{Short}} \\ \hline C_{\text{Short}} & 0 \end{array}\right] \left[\begin{array}{c} x \\ \hline u \end{array}\right]. \tag{5.26}$$

5.1.9 Laser Power Dependency of the Measurement Function

In Fig. 5.20 a low frequency voltage sweep at the piezo stretcher is performed and the OXC measurement function for the short setup is shown. An Erbium-Doped Fiber Amplifier (EDFA), located in the fiber behind the actuators, amplifies the laser pulse in the LSU and has an direct influence on the parameters P_+ and P_- in (5.5). Different Laser Diode Driver (LDD) currents, i. e. pulse power settings, are measured. The positive and negative diode responses are given in the left plot, whereas the different signals from the OXC are given in the right plot.

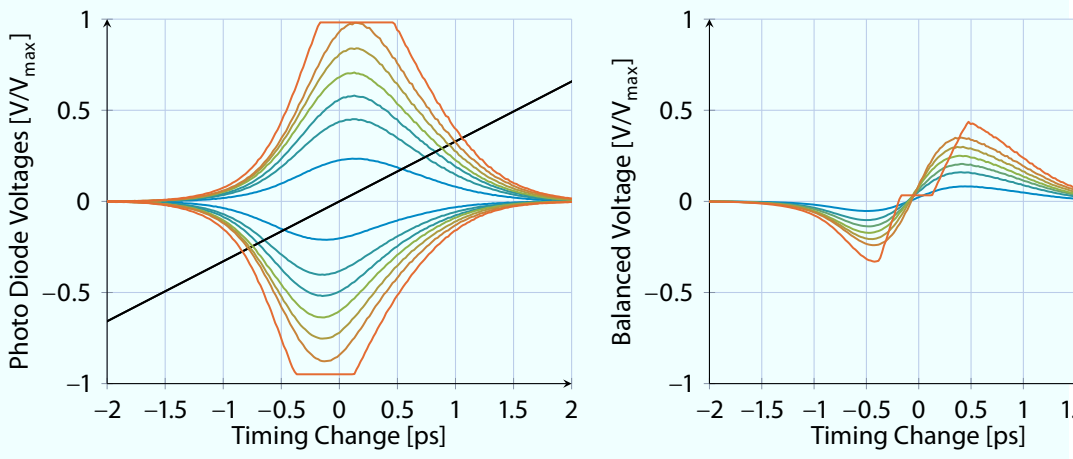

Figure 5.20: Measurement of f_{OXC} with different LDD currents, of 250 mA (——), 300 mA (——), 325 mA (——), 350 mA (——), 375 mA (——), 400 mA (——), and 450 mA (——). The applied normalized piezo voltage during the sweep is given in (——).

The LDD current has a direct influence on the OXC sensitivity and is chosen such, that the slope in the linear range has a high value without saturating the single diode input channel. With a current of 350 mA (——), the sensitivity[2] within the linear range of the short link setup with the AD84, and $V_{max} = 2.339\,\mathrm{V}$ is given by

$$\dot{f}_{\mathrm{OXC}}(\Delta l)\big|_{\Delta l(0)} \approx \left(799\,\frac{\mathrm{fs}}{\mathrm{V}/\mathrm{V}_{\mathrm{max}}}\right)^{-1} \approx \left(0.34\,\frac{\mathrm{fs}}{\mathrm{mV}}\cdot 1\,\mathrm{V}\right)^{-1} \approx 2.94\,\frac{\mathrm{mV}}{\mathrm{fs}}\cdot 1\,\frac{1}{\mathrm{V}}\,, \tag{5.27}$$

The timing change during the voltage sweep, shown in Fig. 5.20, is given by

$$\Delta l(t) = \underbrace{4\cdot 19\,\frac{\mathrm{fs}}{\mathrm{V}}}_{k_{lsu}}\cdot\underbrace{40\,\mathrm{V}}_{k_{pzt4}}\cdot u(t)\,, \tag{5.28}$$

where $u(t)$ is the applied normalized voltage in a range of ± 1, k_{pzt4} is static gain of the piezo amplifier and k_{lsu} is the static gain of the piezo stretcher in the given setup, compare to [PZ2].

[2] $\mathrm{V}/\mathrm{V}_{\mathrm{max}}$ is used to emphasis that normalized voltage implemented on the FPGA with a range of –1 to 1 is used.

5.1.10 Time Varying Behavior of the Measurement Function

Section 5.1.2 shows, that the OXC measurement depends on the alignment of the optical setup and different pulse parameter, like pulse amplitude and width. Besides the optical length, a temperature and humidity change also influences these parameter. This leads to a slowly varying measurement function f_{oxc}.

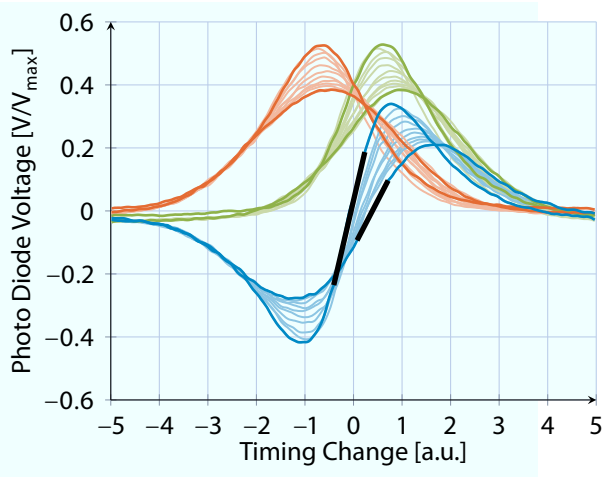

Figure 5.21: Measurement of f_{OXC} over several days, with minimum and maximum of the positive (—), the negative (—), the difference of both correlation pulses (—), and the minimum and maximum sensitivity (—).

Figure 5.21 shows the maximum and minimum variation of f_{oxc} (—) over a period of three days. All parameters, i. e. the amplitude, the width, and alignment of the single pulses (—) and (—) are variable with time.

The amplitude and width variation leads to a changing gain,[3] with a minimum of ≈ 0.30 and a maximum of ≈ 0.66. This leads to a gain variation of ±37.5%. From this observation follows the requirement, that the designed controller has to be robust against this gain change. If the nominal value is unknown, the controller has to be robust against twice the gain variation which is ±75%. If the system is operated over a longer time, and the minimum and maximum gain is known, the robustness can be adjusted accordingly in order to increase the performance.

Another important property, shown in Fig. 5.21, is the variation of the pulse alignment, d_+ and d_- in (5.5), leading to a bias of the measurement changes. In the general control loop, shown in Fig. 3.1, this can be modeled by a non-zero mean at the noise channel $n(t)$. New link setups are designed in such a way, that this effect is minimized if it is induced by thermal expansion of the link plate. For this reason, this measurement should be repeated with the final setup for further validation.

[3] The shown measurement is not calibrated, thus units are omitted.

5.1.11 Input and Output Disturbances

In the next step, the main disturbances are analyzed for the LSU. Possible input disturbances for that system are

- Quantization of the DAC
- Fluctuation of the PZT4 high voltage power supply

Output disturbances of the loop, shown in Fig. 5.10, are e. g.

- Vibration, humidity, and temperature changes of the fiber
- Vibration, humidity, and temperature changes of the optical setup
- Phase noise of the laser pulse train

The influences are superimposed on the output and should be minimized by the closed loop operation. To achieve this, the sensitivity function should be small, $S(s) \ll 1$ for the frequencies ranges where the disturbances occur.

The quantization error is, according to Sec. 3.4.3, given by

$$e_{\Delta t} = 4 \cdot 19 \frac{\text{fs}}{\text{V}} \cdot 80\,\text{V} \cdot \frac{1}{2^N}\,. \tag{5.29}$$

The pulse passes the piezo four times where the piezo sensitivity is 19 fsV^{-1}, according to [PZ2]. The piezo is excited by an DAC with N bit. Table 5.4 shows the values for common ADC resolutions. The ADC that is used at the PZT4 has 18 bit, as for the MLO system.

Table 5.4: Timing Change dependent on the ADC resolution and frequency.

Resolution [bit]	14	16	18
Numerical Value [10^{-6}]	122.070	30.518	7.629
Voltage [mV]	4.883	1.221	0.305
Timing Change [fs]	0.371	0.093	0.023
Optical Path Length Change [nm]	158.203	39.551	9.888

The lower limit in timing change shown in Table 5.4 is well below the required range of $\ll 1$ fs. The same is true of the influence of the PZT4 high voltage power supply. For that the voltage read back is used. Even with the added noise of the ADC to this channel, the RMS value of the read back is 2.4 mV, which leads to an upper limit of the input disturbance of 0.181 fs.

Temperature and humidity changes are occurring in the frequency range of hours. These effects are captured by the integral behavior of the controller and by the coarse tuning to avoid a steady state error.

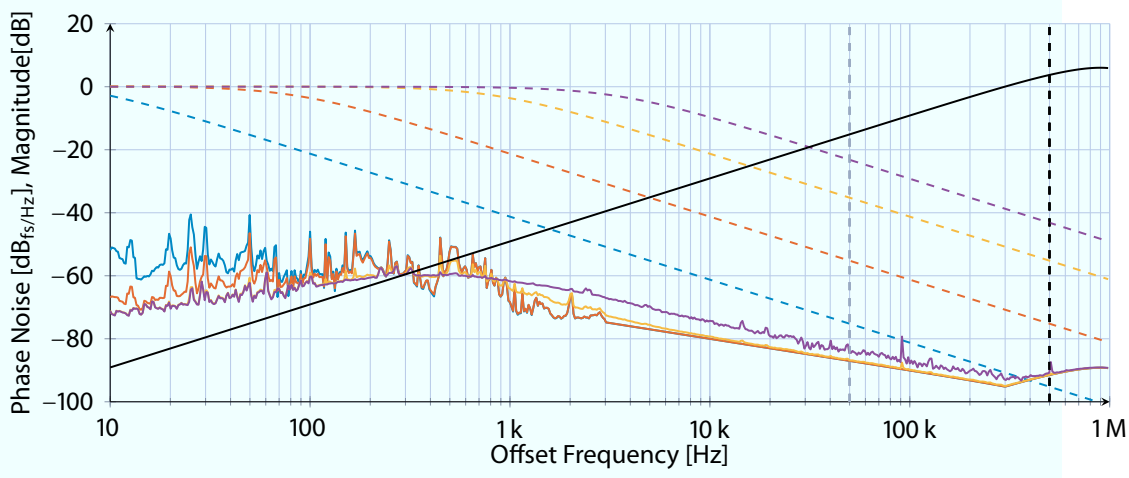

Figure 5.22: MLO phase noise transmitted to the measurement for short links with a locking-bandwidth of ≈ 10Hz (——), ≈ 88Hz (——), ≈ 873Hz (——), and ≈ 3.464kHz (——).

Figure 5.22 shows the phase noise of the disturbance induced by the MLO for the short test link. The phase noise of the pulse train depends on the MLO complementary sensitivity function (- - -) and is transmitted to the end of the link. This phase noise is decreased by the fiber transfer function (——) for the measurement, as introduced in Sec. 5.1.3.

In the frequency range below the intersection of MO and MLO, an increase of the MLO closed loop bandwidth leads to a decrease of the disturbance acting on the LSU, by the reduction of the MLO jitter. In the range above this intersection an increase leads to an amplification of the disturbance, due to the fiber transfer function that increases the sensitivity at those frequencies. In order to avoid disturbances in the range of the LSU closed loop bandwidth, the MLO controller should not be tuned too aggressively.

The measurement of this behavior is given in Fig. 5.23. For a low bandwidth setting (upper left) a low frequency oscillation is visible and disappears for a higher bandwidth (upper right). If the bandwidth is further increased (bottom) a high frequency disturbance of the signal is visible, which fits to the theoretical prediction.

Figure 5.24 shows the MLO disturbance if the fiber length is changed. The short links (——) has the maximum disturbance at ≈ 200 Hz to ≈ 800 Hz at a level of −60 $dB_{fs/Hz}$. If the length is increased, (——) and (——), the disturbance is amplified by the same factor as the length change until the notch occurs due to the fiber transfer function (5.18).

To suppress all occurring disturbances mentioned in this section, the closed loop bandwidth can be chosen in the range of the piezo dynamics.

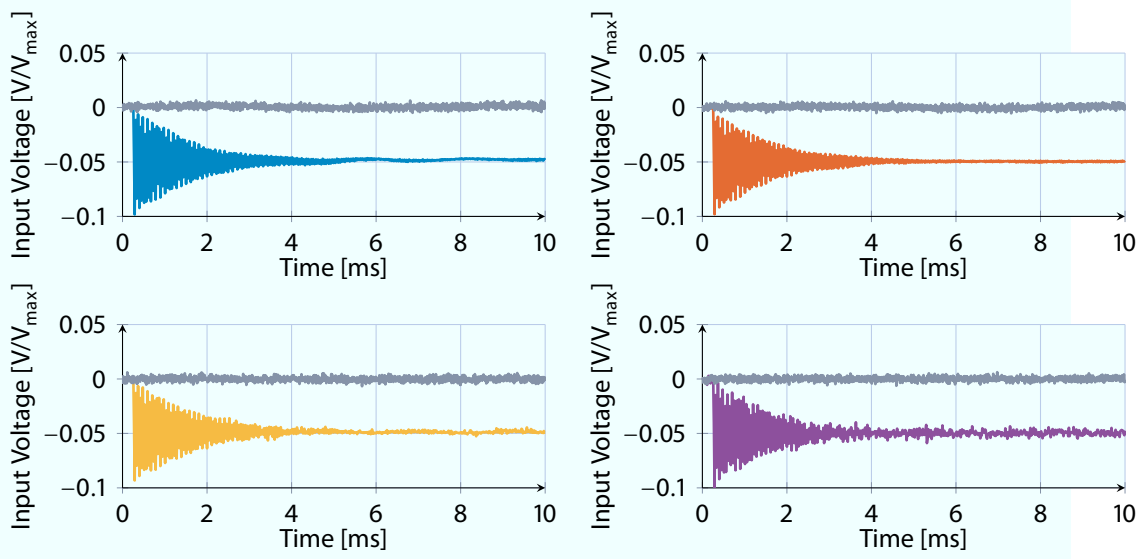

Figure 5.23: Step response of the LSU with a short fiber with a MLO locking-bandwidth of ≈ 10Hz (——), ≈ 88Hz (——), ≈ 873Hz (——), and ≈ 3.464kHz (——).

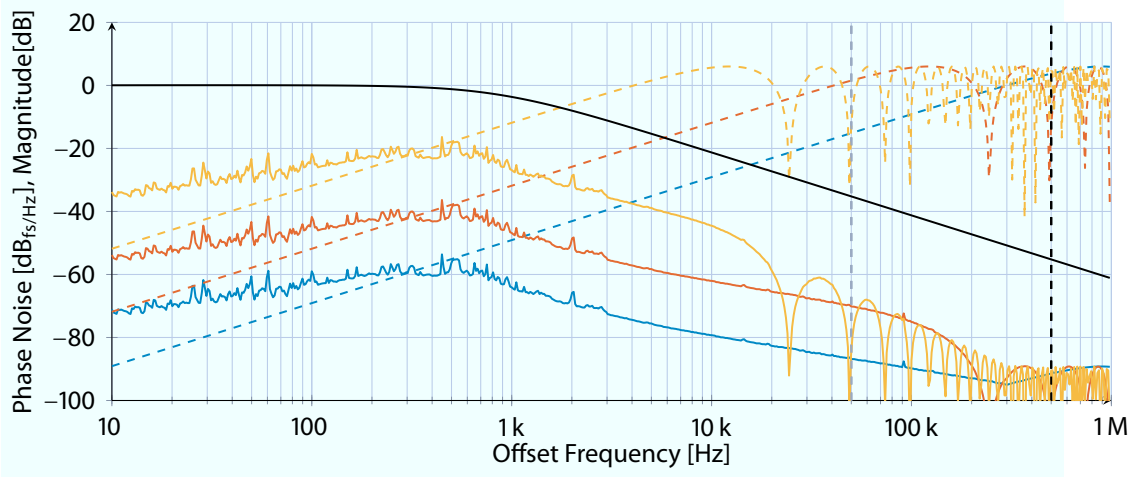

Figure 5.24: MLO phase noise measurable as a disturbance at the link with the short (——), the FLASH (——), and the longest XFEL (——) fiber, the relevant transfer fiber functions (- - -), and the complementary sensitivity function of the MLO loop (——).

5.1.12 Measurement Noise

The minimum measurement noise for the LSU is given by the input quantization and the sensitivity of the OXC measurement. The signal of the OXC is captured with an AD84 RTM with a resolution of 16 bit. The sensitivity of the measurement depends on various parameters and is usually in a range of 468 $\frac{\text{fs}}{\text{V/V}_{\text{max}}}$ to 4678 $\frac{\text{fs}}{\text{V/V}_{\text{max}}}$, leading to the lower error bound shown in Table 5.5, which is well below the requirements.

Table 5.5: Timing Change dependent on the ADC resolution and frequency.

Resolution [bit]	16		18	
Number [10^{-6}]	30.518		7.629	
Sensitivity $\left[\frac{\text{fs}}{\text{V/V}_{\text{max}}}\right]$	468	4678	468	4678
Timing Change [fs]	0.014	0.143	0.004	0.036

Other noise sources are e. g.

- Non-linearities, shot noise, and voltage bias of the photo diode
- Vibration, humidity, and temperature changes of the optical setup
- Amplitude fluctuations of the pulse train
- Additional light captured by the photo diode

An important point in the general control loop, see Fig. 3.1 is, that the disturbances d_o should be in a lower frequency range than the noise n. If this is the case and the closed loop bandwidth is placed in between, the disturbance is transmitted with $S(s) \ll 1$ and the noise with $T(s) \ll 1$.

If both, disturbance and noise, are in the same frequency range, equation (3.15) limits the performance. If the disturbance is suppressed, ($S(s) \ll 1$) the noise n is added to the output, $T(s) \approx 1$. On the other hand, if the controller doesn't react to the noise, $T(s) \ll 1$, the disturbance d_o is passed to the output y, $S(s) \approx 1$.

The measured output y_m, visible on the control system, doesn't have this behavior. The transfer function from d_o to y_m and the one from n to y_m are both given by $S(s)$. The in-loop jitter y_m is lower if the bandwidth increases but the noise, acting below the closed loop bandwidth, is added to the output y that is not visible in y_m. This could give the wrong assumption about the proper choice of the control loop bandwidth.

An intuitive example, which depicts this effect of low frequency measurement noise is shown in Fig. 5.25. Additional light in the laser room is captured by the photo diode and visible in the open loop (left). This ≈ 100 Hz noise is added to the measurement y_m (——).

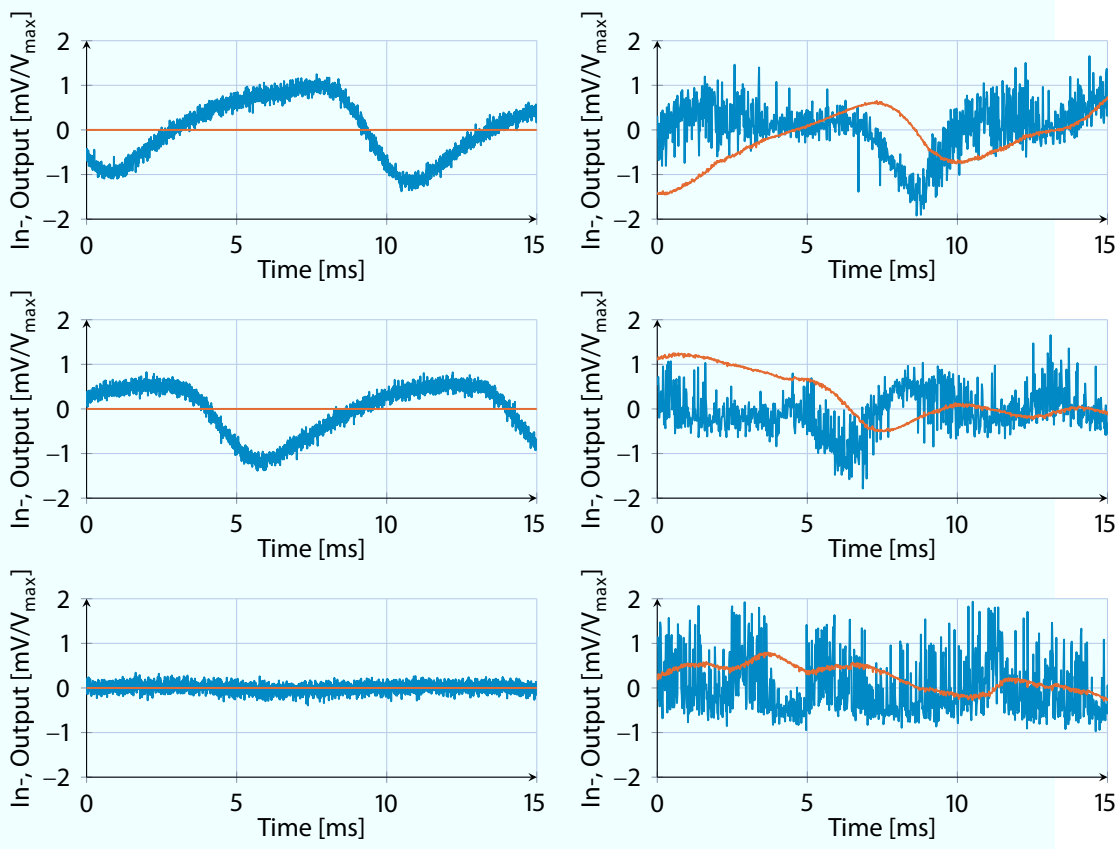

Figure 5.25: Open loop (left) and closed loop (right) response, with no LSU plate cover (top), with LSU cover (middle) without light in the laser room (bottom), with the OXC measurement (——) and the controller output (——).

If the feedback loop is closed[4], the controller output compensates parts of this effect and the inverse of the noise is visible at the controller output (——). With $y_m(t) = y(t) + n(t)$ it is obvious, that, if the in-loop signal $y_m(t)$ has a reduced effect on this noise $n(t)$, the out-of-loop signal $y(t)$ has added the inverse of this unwanted component.

If the LSU plate cover is closed (middle) the additive noise is only slightly reduced. Still, the lenses at the balanced detector capture the ambient light. This effect is e. g. gone (bottom) if the cover of the LSU is currently placed as shown in Fig. 5.26, where both lenses are fully covered. Other ways are to fully close the cover of the optical table or turn the light in the laser room off. This shows, that the cover of the LSU plate should be extended to cover the lenses of the balanced detector. This would allow maintenance work on the optical table without imprinting the ambient light on the end-station of the links.

[4]The PI controller designed in Sec. 5.2.1 is used.

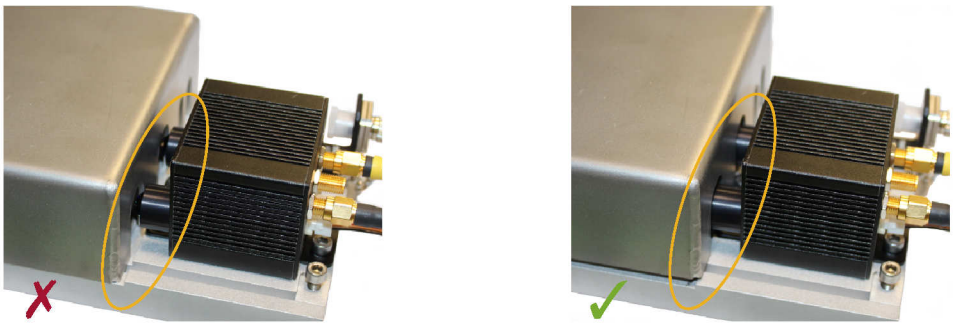

Figure 5.26: Picture of the LSU cover with the influence of ambient light (left) and corrected LSU cover (right) to avoid this noise influence.

In Fig. 5.25 an other issue is also shown. The noise and/or disturbance seems to depend on the measured position. Figure 5.27 shows this behavior with an OXC calibration by a slow voltage sweep. The noise around the measurement (—) depends on the output voltage, i. e. the measurement position (—).

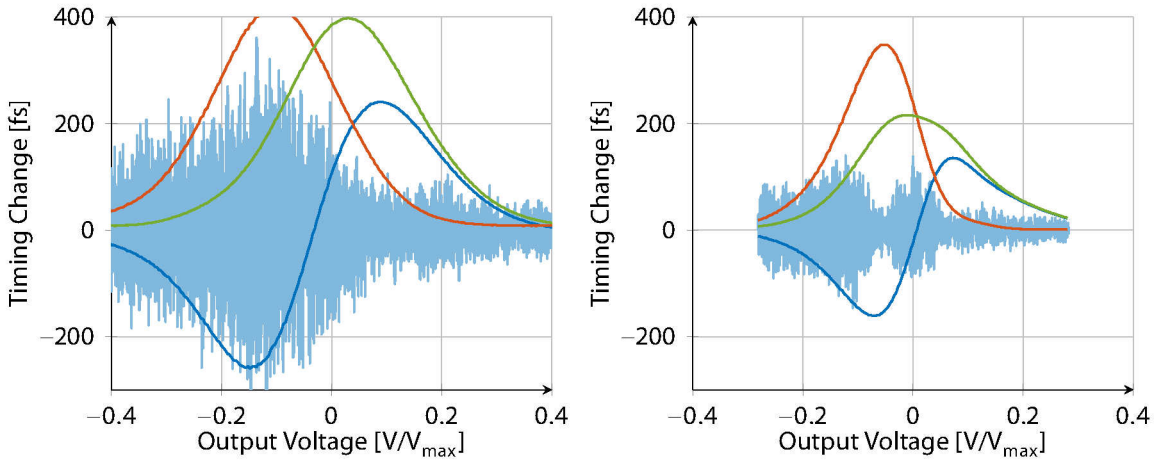

Figure 5.27: Noise, amplified by 100 (—), induced by a bad (left) and a proper (rigth) optical setup, with both photo diodes (—) and (—), and the balanced signal (—).

For a disturbance occurring on the pulse train before the measurement, it is expected that the envelope of this effect is shaped like the derivative of the measurement function $f_{\mathrm{OXC}}(\Delta l)$. This is not the case. It is thus reasonable to assume that this is a noise effect, entering the control loop at the noise input $n(t)$.

The measurement using the OXC and a balanced detector is sensitive to the mechanical setup. This section emphasized some of the, partly unknown, noise properties of this sensor. Those effects should be studied further to allow an optimized controller design, e. g. the knowledge of the noise can be used in the design introduced in Sec. 3.7.2.

5.1.13 Additional State Access by Current Measurement

The excitation of the piezo stretcher Δl is not directly measurable. The transfer function of the fiber and the characteristic of the OXC measurement are superimposed. Moreover, the different disturbance and noise effects are added with frequency components below the piezo resonance. This imposes limitations that could not be overcome with this setup.

If there is another measurement to access $G_{\text{Piezo}}(s)$ it could be possible to decouple the task of damping piezo vibrations and therefore to optimize the link behavior. This could lead to a simpler controller design and gives more degrees of freedom for the overall control. Such an additional measurement is the piezo current. As stated in Sec. 3.2, the charges of the equivalent circuit are related to the displacement of the piezo surface, whereas the current is related to the velocity of this displacement.

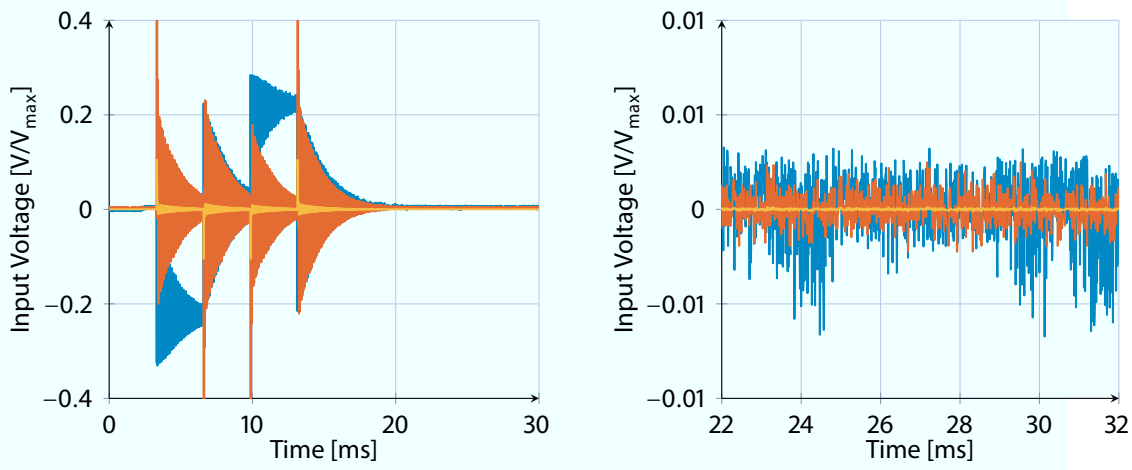

Figure 5.28: Response of the LSU to multiple steps, with balanced detector signal (——), the current (——), and the current scaled to the same dynamic range (——).

Figure 5.28 shows the current (——) compared to the measurement of the OXC (——) for a step applied to the piezo. The right part shows the noise in the steady state. If the raw measurements are compared, the current noise is in the range of the last 5 of 18 bit, which is 1/44 of the OXC noise. If the current signal is amplified by a factor of 20, (——), the same dynamic range for an excitation is reached. Still, the noise is 1/2 of the OXC noise even though also the ADC noise is also multiplied by this factor.

An important advantage is that the new measurement is not influenced by the fiber transfer function nor transformed by the non-linear mapping of the OXC, for these reasons the difficulties in Sec. 5.1.7 and Sec. 5.1.8 are neglected. The transmission zero of the fiber is not present and the oscillation of a link with an unsuitable link length can be suppressed. The control of the piezo dynamics and the rejection of fiber disturbances can be decoupled using a Multiple

Input Multiple Output (MIMO) controller or a cascaded control structure, dependent on the later designed bandwith for both purposes.

An inner control loop can be used to highly damp the piezo dynamics, while an outer loop sets the required length change, Δl, which stabilizes the optical length of the link. Due to the PZT4 read-back update rate of only $f \approx 110\,\text{kHz}$, which is just five times faster than the piezo resonance, and the FMC20 board that is not synchronized to the computation board, leading, from the controller point of view, to a variable time delay of about one or two samples, this analysis was postponed. It is reasonable to increase the sampling rate and synchronize both boards. This is possible with modifications at the hardware and firmware level. If these changes are done, the explained strategy should be investigated and studied further.

5.1.14 Hysteresis and Creep

In the last step, the hysteresis and creep, introduced in Sec. 3.2.2, are analyzed. Like in the MLO case, a slow triangle voltage is applied in the open loop and the response is captured.

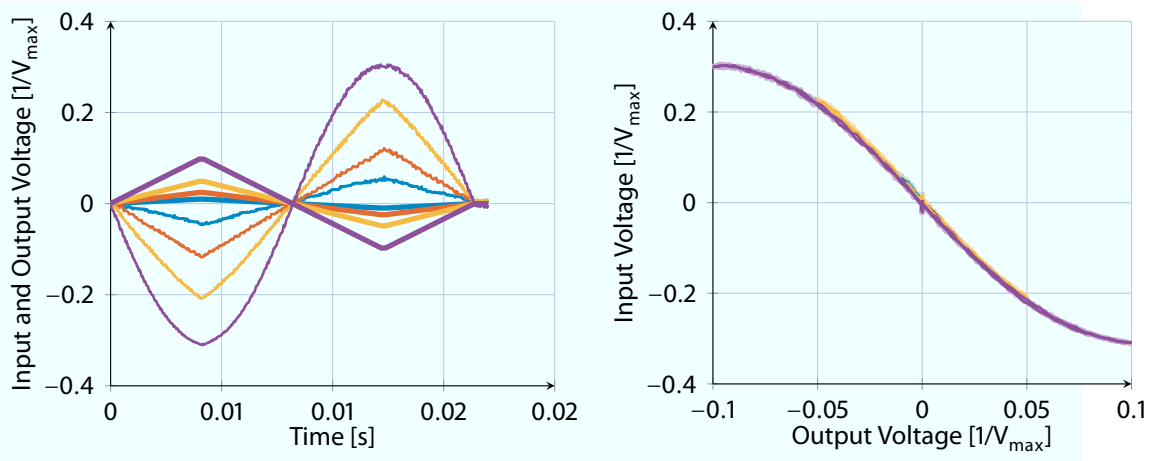

Figure 5.29: Time response (left) and measurement change to input voltage behavior (right) for excitations with an amplitude of 1% (—), 2.5% (—), 5% (—), and 10% (—) close to the working point.

The left part of Fig. 5.29 shows the excitation and the measured response for different amplitudes. The right part of Fig. 5.29 shows the measured sensor voltage dependent on the applied voltage. The hysteresis effect is not visible for the piezo stretcher in the LSU. If the amplitude is increased, the non-linearity due to the measurement function is more dominant, which is the saturation like behavior of (—) left side of Fig. 3.5.

The creep is also negligible for the LSU. To compensate for the disturbances acting on the system, an excitation of the controller is required, which is much faster than this effect.

5.1.15 Conclusion and Uncertainties

This section showed the modeling of the LSU. The dynamic properties of the system are given by the behavior of the piezo crystal, the piezo amplifier, the measurement with an OXC and a balanced detector adding a non-linear measurement function. If the spatial length of the fiber is extended, a time delay component is added. From a control theory point of view, the stabilization of the LSU is a disturbance rejection problem.

The piezo dynamics can be modeled by a third order system, modeling the first resonance and the low pass behavior of the piezo amplifier. The resonances are predicted by a Butterworth-Van Dyke equivalent circuit, but the expected zeros are not measured. If this is observed later it should be analyzed. Moreover, the current model only contains one resonance mode, which could be increased.

The resulting transfer function of the spatially extended fiber is discussed in Sec. 5.1.3 and published in [Heu+15b]. The transfer function for the fiber with the differential measurement contains a transmission zero. If the fiber reaches a critical length the mode of the piezo dynamics can be hidden and the phase of the transfer function changes. This has to be considered in the controller design and imposes limitations. An additional fast measurement of the piezo current can be used that has no transmission zeros.

The measurement by the OXC is sensitive to various influences and changes its gain over time. The initial gain can be calibrated, but for the time dependent changes the controller should be designed to be robust against these. If the OXC should be used outside the linear region an EKF can be used as a first approach.

Additionally, some main disturbance and noise effects are shown. A main issue for this system is that they could be in the same frequency regions. If this is the case, both disturbance and noise, can not be compensated for at the same time. The discussion shows, that the closed loop bandwidth is limited by the expected noise of the measurement setup. If the bandwidth is decreased to minimize disturbances, it is not allowed to have noise in the same frequency region. For this reason, a further analysis and classification of the contributing disturbance and noise effects should be done.

5.2 Linear Controller Design for Short Links

In this section, a controller for the LSU with a short fiber is developed. The general control loop is used with the plant $G_{\text{short}}(s)$, i. e. the third order model identified in Sec. 5.1.6.

5.2.1 PI Design

Like in the MLO case, the first control approach is the PI controller implemented on the VME system. It will be used as a reference for performance comparisons of the following designs. The transfer function is given by

$$K(s) = K_p + \frac{K_i}{s} = K_p\left(1 + \frac{1}{sT_i}\right) \quad \text{with} \quad T_i = \frac{K_p}{K_i}\,. \tag{5.30}$$

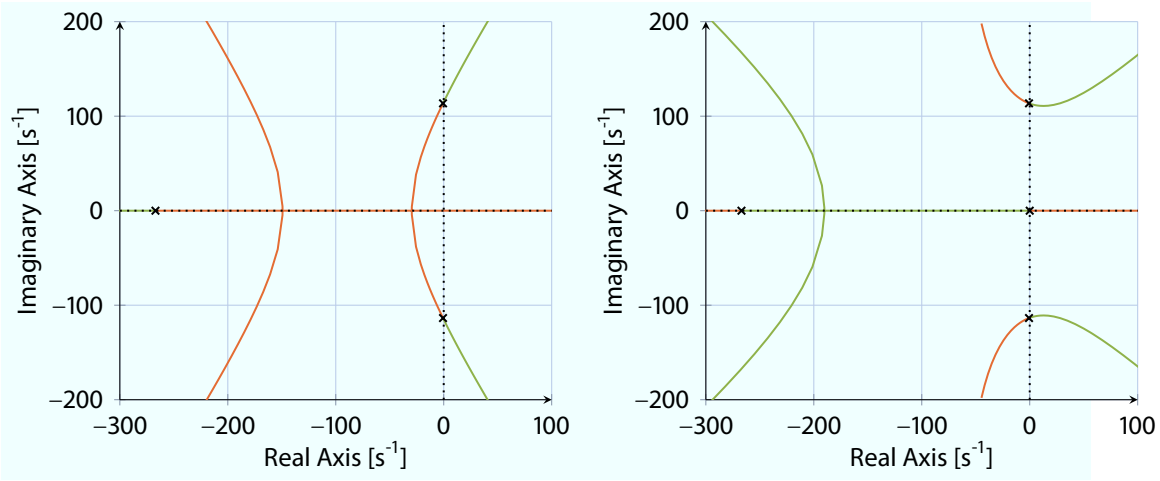

Figure 5.30: Root locus plot for the plant $G_{short}(s)$ together with a proportional controller (left) and an integral controller (right), with a positive (—), and a negative (—) K_P (left) and K_I (right).

Figure 5.30 shows the root locus plot if only a proportional gain (left) or an integral gain (right) is used. A positive (—) K_P leads to the instability of the pole pair and a negative (—) to a damping of the piezo resonance. Due to a non-zero mean disturbance, d_o, an integral behavior is required to move the output y to zero (as in 4.2.2). With only an integral part in the controller the closed loop is just stable for small positive values (—) of K_I. If the value is increased, the pole pair moves to the Right Half Plane (RHP) leading to an unstable closed loop.

If an PI controller is used, the closed loop contains a zero defined by

$$s + \frac{1}{T_i} = s + \frac{K_i}{K_p} = 0\,. \tag{5.31}$$

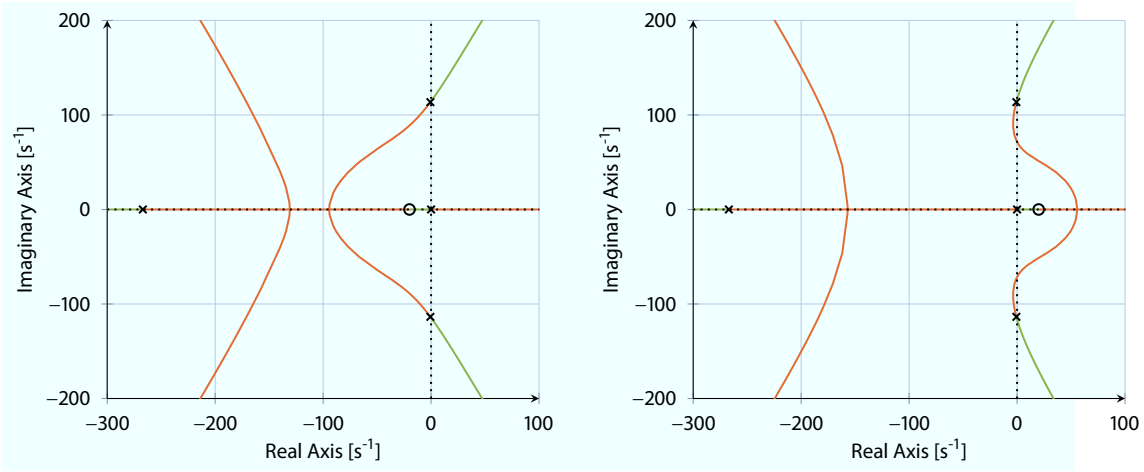

Figure 5.31: Root locus plot for the PI controller with positive T_i (left) and negative T_i (right) and with positive (——) and negative (——) K_P.

The left part of Fig. 5.31 shows the root locus plot for $T_i = 0.05$ with a positive (——) and a negative (——) proportional gain. In this setup, the zero is in the Left Half Plane (LHP) but it is not possible to decrease the oscillation and increase the damping of the pole pair without moving the integrator pole into the unstable RHP.

For this reason, the root locus with a $T_i = -0.05$ and a positive (——) and a negative (——) proportional gain is shown in the right part of Fig. 5.31. The drawback of this setup is an undershoot of the step response due to the RHP zero. On the other hand it is possible to lower the frequency and increase the damping of the dominant pole pair.

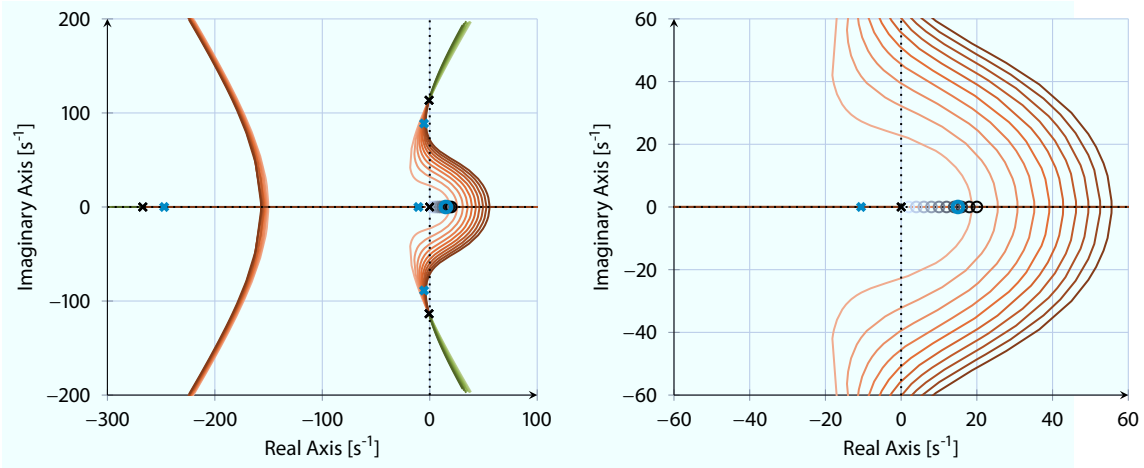

Figure 5.32: Root locus plot for PI controller with a negative K_P and a negative T_i in a range from 5 (——) to 0.05 (——). The right side shows a zoom of the origin.

Figure 5.32 shows this plot for different positive T_i in a range from 5 (—) to 0.05 (—), and a negative one in the same range, (—) to (—). The initial poles (—) move along those trajectories for different loop gains. The RHP zero moves further to the right for a smaller T_i, which minimizes the undershoot of a step response. On the other hand, a larger ratio prohibits moving the closed loop poles to a high damping and smaller frequencies. Moreover, the closed loop is less robust to changes in the loop gain.

The closed loop poles of the heuristically tuned controller (—) are shown in Fig. 5.32. The time domain response of the closed loop to a test sequence is shown in Fig. 5.33. At a time of 0.5 ms a reference change of 0.1 ps is applied. After that a step disturbance on $d_i(t)$ with a size of $\frac{0.1}{3.202}\,\frac{\mathrm{V}}{\mathrm{V_{max}}}$ leading to an open loop output change of 0.1 ps followed by a 0.1 ps step on $d_o(t)$ at 2.5 ms and the same step on the noise input $n(t)$ at the time of 3.5 ms.

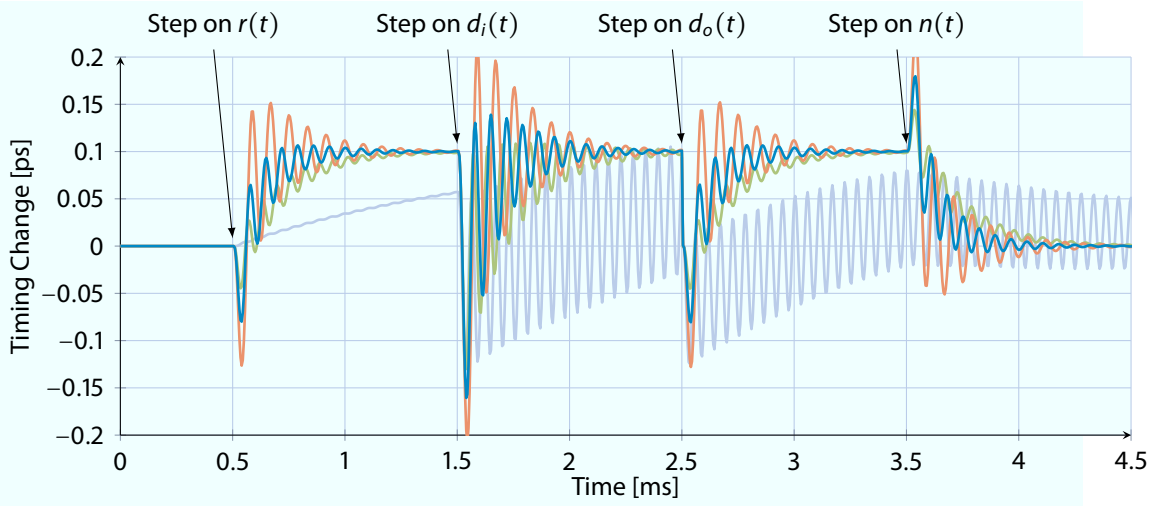

Figure 5.33: Simulated response of the heuristically tuned PI controller (—) and the previous used integral controller (—) to the test sequence with nominal plant. Furthermore, the assumed plant variation are shown by an increased gain (—), a decreased gain (—) gain.

Compared to the previous controller, $K_{\mathrm{PI,old}}$ (—), the heuristically tuned controller K_{PI} (—) has a much faster response and the resonance of the piezo is much more damped in the case of disturbance and noise inputs. Still, it shows some oscillation. More over, the closed loop of K_{PI} shows an undershoot due to the RHP zero, which is an unwanted behavior.

Section 5.1.10 showed that the gain of the OXC function can vary during the operation, which changes the loop gain. An 37.5 % (—) increased and decreased by the same factor (—) still leads to a stable behavior but changes the damping of the resonance.

The controller K_{PI} has a reasonable behavior but the resonance should be further reduced using other controller design methods.

5.2.2 LQG Design

The LQG controller design finds an optimal controller with respect to the cost function defined in (3.48) and introduced in Sec. 3.7.2. Due to the coarse tuning, the mean value of d_o is non-zero that requires the design with integral action, shown in Fig. 5.34.

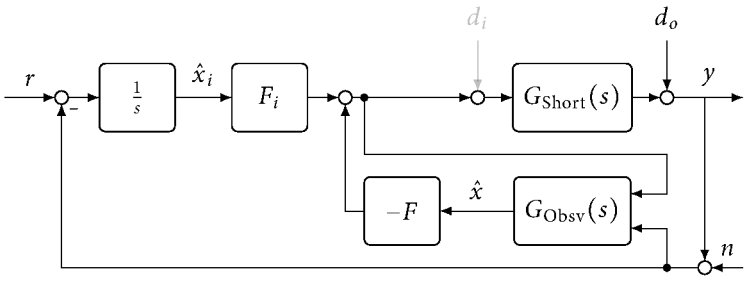

Figure 5.34: Block diagram of the LQG controller with integral action used for the LSU.

In the first step, the observer $G_{\text{Obsv}}(s)$ is designed according to Sec. 3.7.2, with the tuning parameter Q_e and R_e. The tuning parameter Q and R for the design of F and F_i are chosen as

$$Q = \begin{bmatrix} C^T \cdot \rho_y \cdot C & 0 \\ 0 & \rho_i \end{bmatrix} \quad \text{and} \quad R = \rho_u \tag{5.32}$$

with the output matrix C leading in the SISO case to the cost function

$$V = \int_0^\infty \rho_y y^2(t) + \rho_i x_i^2(t) + \rho_u u^2(t)\, dt\,. \tag{5.33}$$

The new scalar tuning parameter ρ_y, ρ_i and ρ_u can be used to optimize the closed loop response. The damping of the output y can be minimized by increasing ρ_y and convergence speed by an increase of ρ_i. The control efford can be penalized by an increase of ρ_u, which leads to a slower response of the system.

If the controller tuning should be allowed to the operators in the control room of the accelerator, these tuning knobs are suitable. By a common rule of thumb, the closed loop is not destabilized by tuning these parameters, if the real part observer poles are chosen four times faster than the poles of the closed LQR loop. Moreover, the poles of the closed loop system should be a factor of 20 below the sampling rate, [DFT92]. Both conditions should be checked prior the control parameter upload.

Figure 5.35 shows the closed loop response to the test sequence of an LQG controller with

$$\rho_y = 1\,, \quad \rho_i = 2.5 \cdot 10^3\,, \quad \rho_u = 25\,, \quad Q_e = \begin{bmatrix} 1 & 1 & 1 \end{bmatrix}^T \cdot \begin{bmatrix} 1 & 1 & 1 \end{bmatrix}, \quad R_e = 0.5\,. \tag{5.34}$$

The undershoot of the previous design is not present anymore. Moreover, the oscillation of the pole pair is further damped, for the reference tracking as well as for the disturbance and noise rejection. The largest pole of the closed loop system is at $\approx 42\,\text{kHz}$.

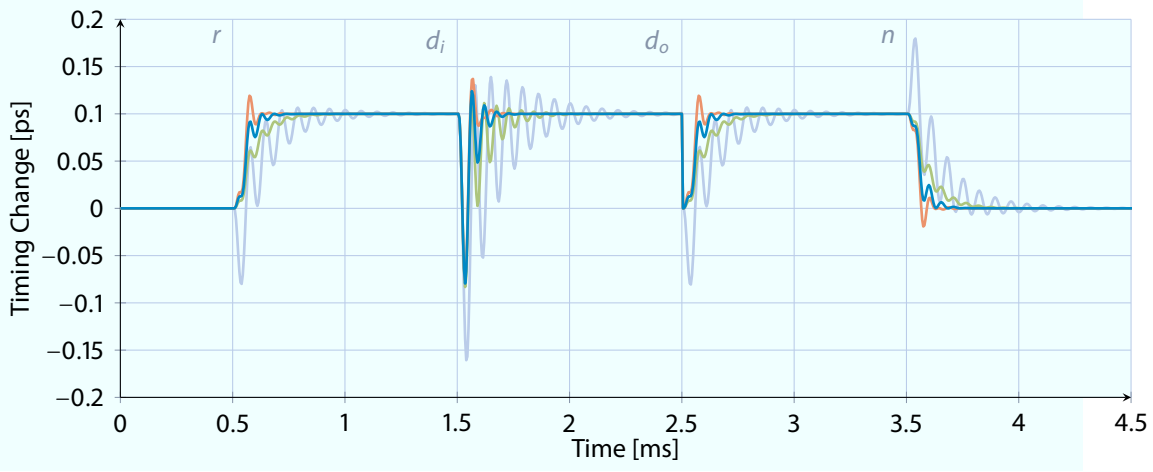

Figure 5.35: Response of the LQG controller with nominal (——), increased gain (——) and decreased gain (——) plant compared to the heuristically tuned PI controller (——).

5.2.3 S/KS and Four Block Design

The next design strategies based on the norm optimization, introduced in Sec. 3.7.4. The transfer functions $S(s)$ and $KS(s)$ are weighted with the generalized plant shown in Fig. 3.18 where the $\mathcal{H}_\infty$ norm from r to z is minimized.

The GOF of the resulting closed loop is shown in Fig. 5.36. The filter $1/W_S(s)$ (- - -) for the sensitivity function $S(s)$ (——), chosen such that low frequency components, i. e. up to the piezo resonance, are suppressed and the filter $1/W_{KS}(s)$ (- - -) which limits the controller action.

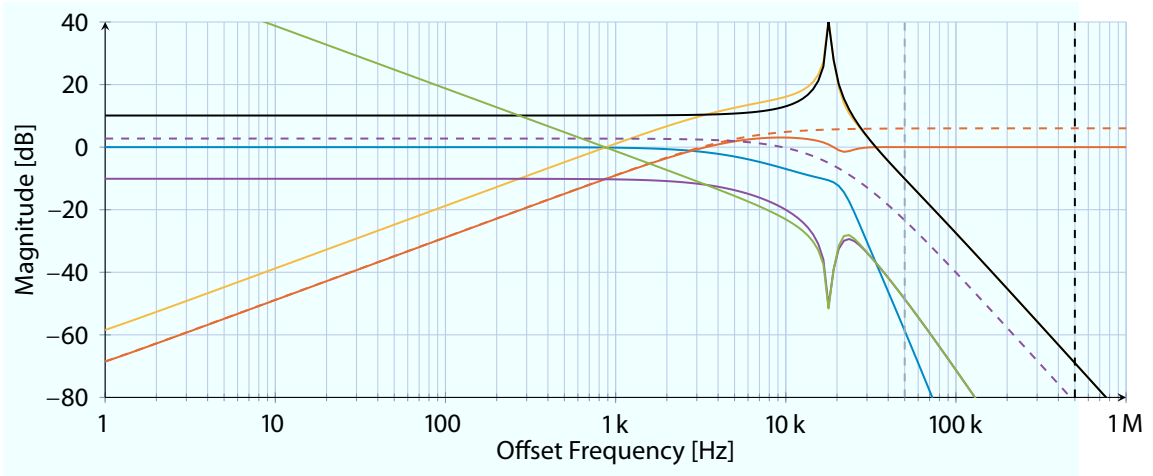

Figure 5.36: GOF for the S/KS design, including $S(s)$ (——), $T(s)$ (——), SG (——), KS (——), the weighting filter $1/W_S(s)$ (- - -) and $1/W_{KS}(s)$ (- - -) and the plant (——).

With this generalized plant the peak in SG (——) is not suppressed leading to a controller which is very sensitive to input disturbances. This is visible in the response to the test pattern, shown in Fig. 5.37. The dynamic behavior for the reference tracking at 0.5 ms is good whereas the closed loop starts ringing for a disturbance input at 1.5 ms.

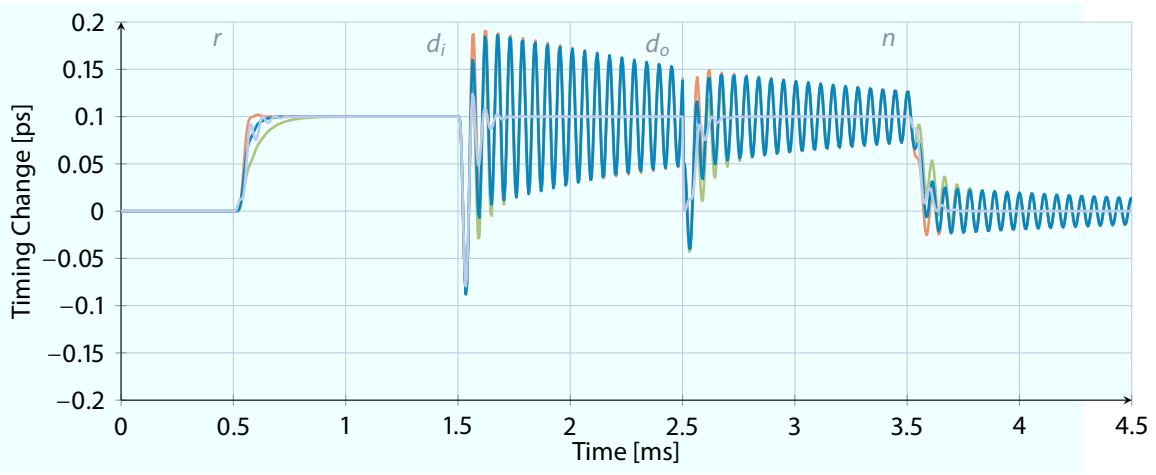

Figure 5.37: Response of the S/KS controller to test sequence with nominal (——), increased gain (——) and decreased gain (——) plant compared to the LQG controller (——)

The disadvantage of the previous design leads to the next one. In this case also the disturbance channel d_i is weighted. The generalized plant for this case is shown in Fig. 3.19 in Sec. 3.7.4. The resulting GOF is shown in Fig. 5.38.

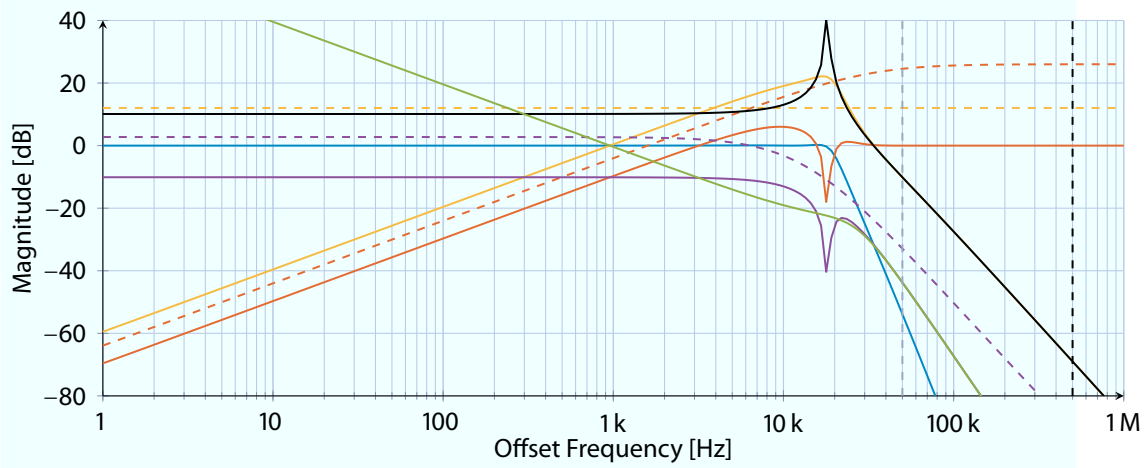

Figure 5.38: GOF for the four block design, including S (——), T (——), SG (——), KS (——), the weighting filter W_S^{-1} (- - -), W_{KS}^{-1} (- - -), and W_{di}^{-1} (- - -) and the plant (——).

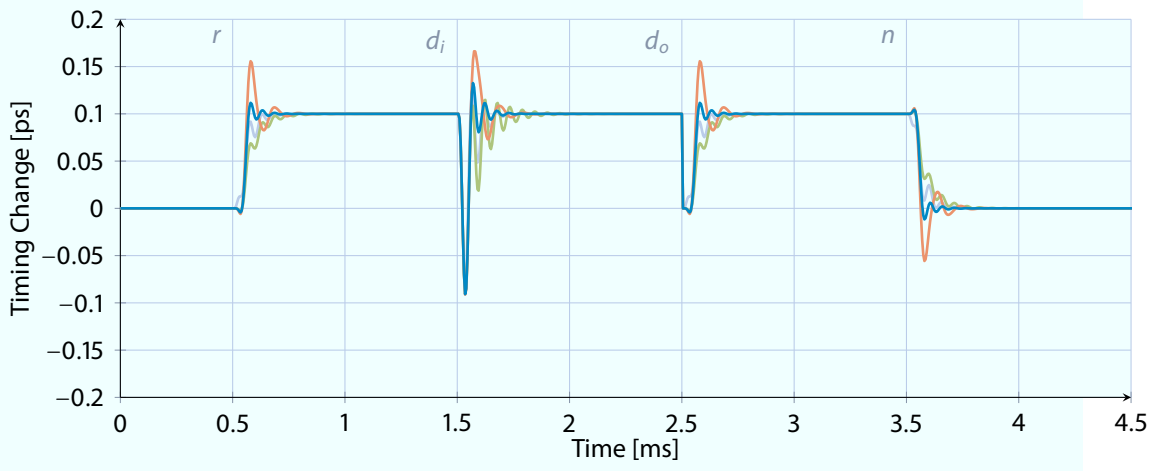

Figure 5.39: Response of the four block controller with nominal (——) plant gain, increased gain (——) and decreased (——) plant compared to the LQG controller (——)

5.2.4 Comparison

Table 5.6 summarizes the properties of the different designs for the short link setup. The model based controller show a performance increase compared to heuristically tuned K_{PI}. If a more sophisticated controller is used, the undershoot can be reduced and a further increase of the performance is given.

Table 5.6: Properties of the different LSU controller.

	$K_{\mathrm{PI,old}}$	K_{PI}	K_{LQR}	K_{SKS}	K_{4B}
Performance rating	5	3	2	4	1
Automatic tunning	✗	✗	✗	✗	✗
State Space Size (n_x, n_i, n_o)	2, 1, 1	2, 1, 1	4, 1, 1	7, 1, 1	7, 1 ,1
FPGA resources	low	low	medium	high	high

The four block design has a slightly better response but a bigger controller order. The seventh order system is currently not implementable on the used FMC25 computing board. Consider the direct implementation of the state space system equation shown in (3.8) with four states one input and one output. For that case 24 multiplication units are required. If the number of states is increased up to seven the number of multiplication units increases to 63. It is possible to reduce the number of units by changing the algorithm to a serial implementation which requires an increased computation clock for the controller. The amount of multiplication units on the current FMC25 board was not sufficient to implemented four controller with seven states in *Rapid-X* even if a serial algorithm is used. For this reason, only the LQR controller will be tested in the experiment.

5.2.5 Experiments

This section shows the experimental results of the LSU system at the XFEL. Compared to the identification in previous section, the hardware changes from the SIS83000L to the FMC25. Moreover, the setup and the link changes and the controller parameters are adjusted to the new measurement gain $f_{\mathrm{OXC}}(y)\big|_{y=0}$. The development of the firmware used for this experiments is shown in Appendix B and was one of the major tasks. In a first step the closed loop properties are validated. After that, the PI and LQG controller are compared against each other.

P Controller

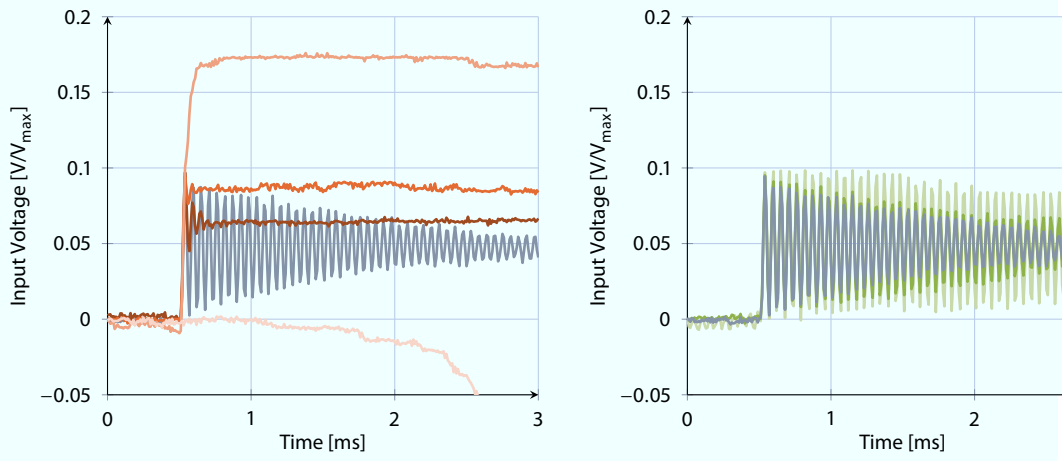

Figure 5.40: Measured response of the open loop (—) and the P controller with a gain of −0.05 (—), −0.1 (—), −0.15 (—), −0.2 (—), 0.001 (—), and 0.002 (—).

Figure 5.40 shows the measured response of the P controller to an input disturbance step on d_i. The system behavior fits with the prediction shown in the root locus plot in Fig. 5.30.

If a negative K_p is chosen (left part), the oscillation is damped e. g. with values of −0.05 (—) and −0.1 (—). For a value of −0.15 (—) the closed loop poles are located on the real axis and no oscillation occurs. If the gain is further increased to −0.2 (—) the loop is unstable.

The response with small positive values of K_p is shown in the right part of Fig. 5.40. They decrease the damping compared to the open loop behavior (—), e. g. 0.001 (—) and 0.002 (—) until an unstable behavior is reached at ≈ 0.00275.

The same experiment is performed with a pure integral controller. The stable range is given by $K_i = 0 \ldots 6.25$. In this range the damping is slightly decreased until the unstable condition is reached.

PI Controller

Figure 5.41 shows the measured response of K_{PI} to the sequence also used in the simulation. The step on the disturbance output d_o at 2.5 ms can not be performed with the given setup and is omitted. The undershoot of the response is given like predicted by the simulation, shown in Fig. 5.33. The oscillation, on the other hand, is damped much more than expected.

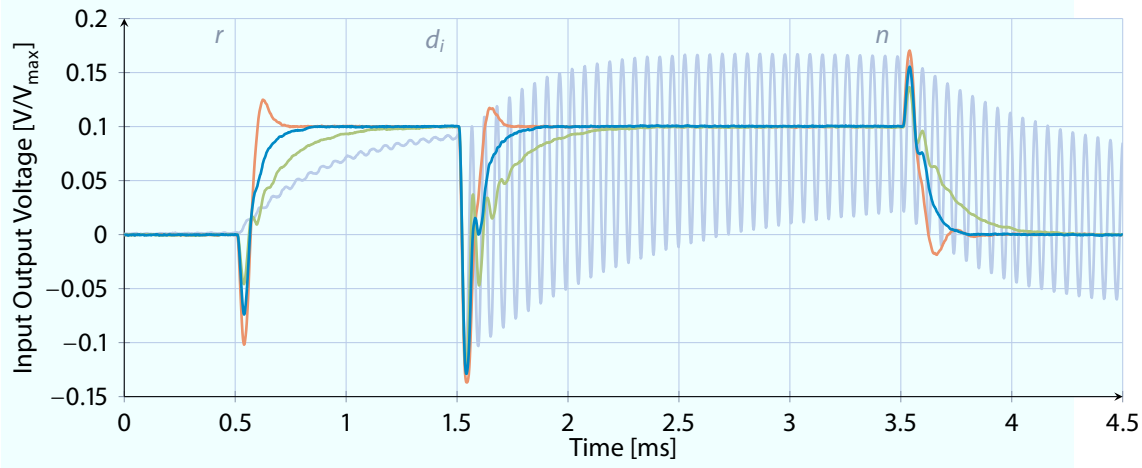

Figure 5.41: Measurement of the proposed PI controller with a nominal (—), increased (—) and decreased (—) OXC gain and of the former used controller (—).

Compared to the previous control parameter (—) the suggested one (—) has a much faster time response and suppresses in- and output disturbances.

If the loop gain, due to the OXC is decreased by ≈ 37.5% (—) the response is slower than the one with the matched plant gain. If the gain is increased (—) by the same amount, the response has a small overshoot.

The measurement shown in Fig. 5.41 is performed with an optimized link in terms of measurement noise. This noise depends on the proper choice of the optical setup on the LSU plate, the correct length of the DCF, the light power and more properties. Comparing the first 0.5 ms of Fig. 5.40 and Fig. 5.41 shows the difference between a link with low and with high measurement noise, respectively. The following measurements are performed with the same link setup and the same optical power, like used in Fig. 5.41.

Time delay of the final setup

The discrepancy in the oscillation can be explained by the time delay in the control loop. The measurements for the system identification, see Sec. 5.1.6, are performed with a different hardware setup and the small delay, shown in Fig. 5.12, was neglected. The time delay of the final hardware, FMC25 with AD84 and FMC20 with PZT4 is depicted in Fig. 5.42.

The response to a step (—) for a firmware with 500 kHz (—) and 1 MHz (—) and the internal LLL communication is shown, as well as the response if the AD84 DAC is used with the external input of the PZT4 (—) and (—), respectively. The internally computed model (—), used for comparison, starts with a delay of 2 samples which are given by the application part of the firmware. The response of the measurement starts 5 (500 kHz) and 10 samples (1 MHz) after the excitation. This leads to a time delay of ≈ 10 μs, which is true for the LLL and the external connection. A direct connection between ADC and DAC of the AD84 leads also to delay of ≈ 10 μs, leading to the conclusion that this could be induced by the ADC sampling.

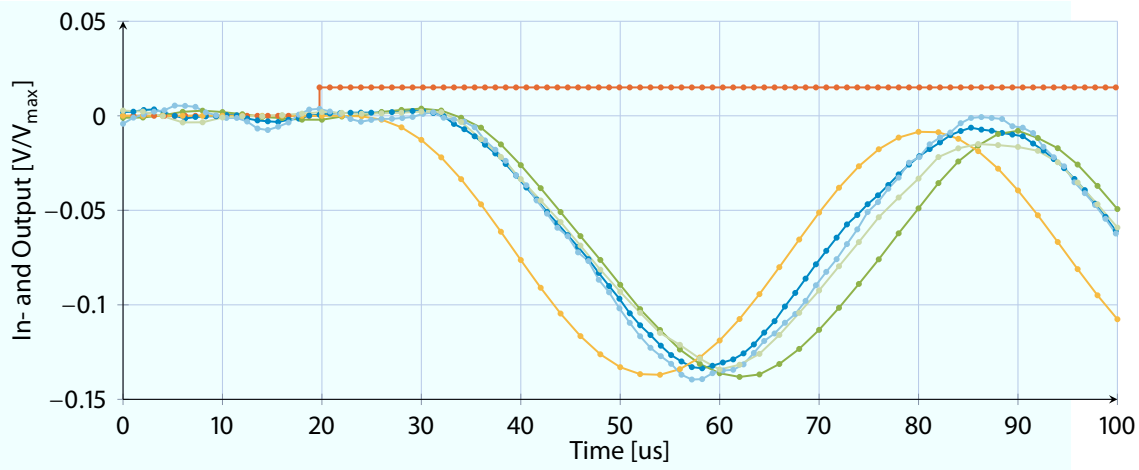

Figure 5.42: Response to a reference step (—), with a 500 kHz (—) and 1 MHz (—) firmware with LLL and with external connection (—), (—) compared to the model (—).

With this additional delay taken into account, the time response changes like shown in Fig. 5.43.

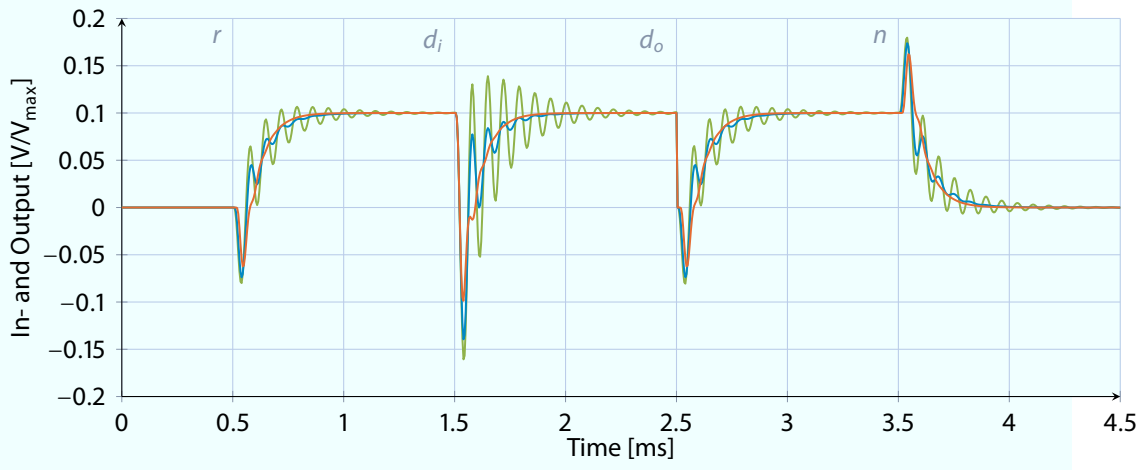

Figure 5.43: Simulation of the proposed PI controller without (—) with an additional time delay of 2.5 μs (—) and 10 μs (—).

The oscillation of the response decreases if the delay is slightly increased and below the half of the delay margin of 21.4 μs. If the delay increases the oscillation appears again until the loop gets unstable if the delay exceeds the delay margin. The simulated behavior fits the measurement given in Fig. 5.41. This behavior can be explained with the bode diagram of the closed loop shown in Fig. 5.44.

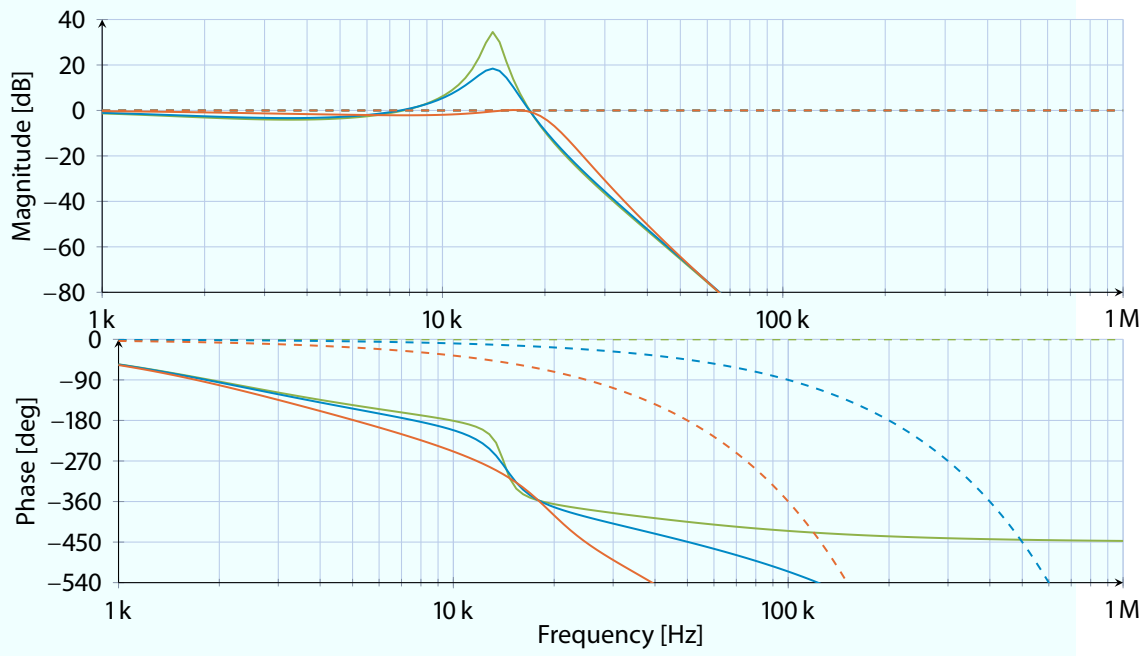

Figure 5.44: Bode diagram of the closed loop using a PI controller without (——) with an additional time delay of 2.5 μs (——) and 10 μs (——) with the corresponding open loop transfer functions of the time delays (- - -) and (- - -) and the unit gain (- - -).

If the delay of the control hardware increases, the resonance peak is lowered. If the delay increases above the delay margin the closed loop is not stable anymore. Coincidentally the new hardware hits a delay which increases the performance of the system.

LQG Controller

The LQG design approach is tested next. The controller K_{LQG}, designed in Sec. 5.2.2 is not stable. Figure 5.45 shows the achievable response if the controller parameters are chosen as

$$\rho_y = 1 \quad \rho_i = 2.5 \cdot 10^3 \quad \rho_u = 50 \quad Q_e = \begin{bmatrix} 10 & 0 & 0 \\ 0 & 10 & 0 \\ 0 & 0 & 1 \end{bmatrix} \quad \text{and} \quad R_e = 0.5\,. \tag{5.35}$$

The behavior of the nominal gain (——) is, due to requirement to change the parameter, much slower than the simulated one. Moreover, the piezo resonance is only weakly damped. If the

gain is increased (—) an overshoot occurs and for a decreased (—) gain the rise time response decreases. The oscillations remain unchanged.

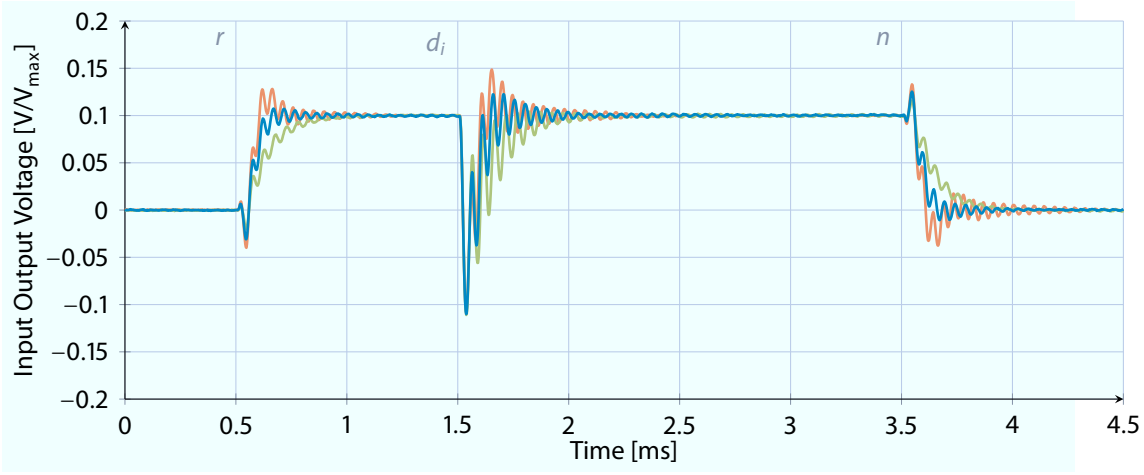

Figure 5.45: Measurement of the LQG controller with an additional time delay of nominal plant (—) and with increased plant gain (—) and decreased plant gain (—).

This raises the question if this behavior can also be explained by the additional time delay and if this can be predicted by the identified system model. The simulation of the LQG controller with and additional time delay is shown in Fig. 5.46. If the time delay increases the controller does not damp the oscillation due to the phase change.

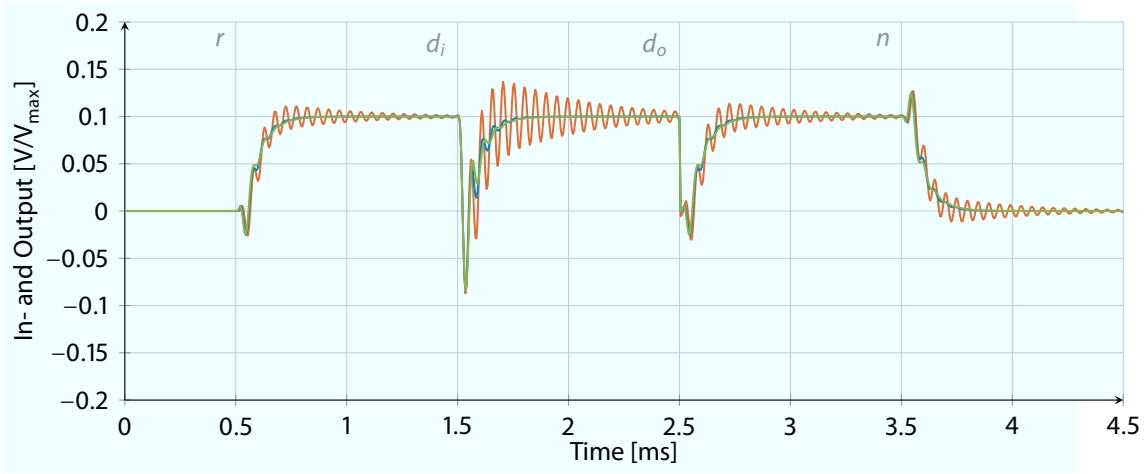

Figure 5.46: Simulation of the LQG controller with an additional time delay of nominal plant (—), increased plant gain (—) and decreased plant gain (—).

LQG Controller with Pade Approximation

A common approach to handle time delays is the pade approximation, see e. g. [SP01], given by

$$e^{-st} \approx \frac{1 - k_1 s + k_2 s^2 - \ldots \pm k_n s^n}{1 + k_1 s + k_2 s^2 + \ldots + k_s^n} \,. \tag{5.36}$$

A 2nd order pade approximation is added to the system model (5.23), which increases the model order from 3 to 5. For this system the augmented LQG controller in Sec. 3.7.2 is designed. The required controller order increases, due to the integrator, to 6. The result of this new controller $K_{\mathrm{LQG,pade}}$ is shown in Fig. 5.47. The design parameters are chosen as

$$\rho_y = 1\,, \quad \rho_i = 2.5 \cdot 10^3\,, \quad \rho_u = 25\,, \tag{5.37a}$$

$$Q_e = \begin{bmatrix} \sqrt{10} & \sqrt{10} & 1 & 1 & 1 \end{bmatrix}^T \cdot \begin{bmatrix} \sqrt{10} & \sqrt{10} & 1 & 1 & 1 \end{bmatrix}\,, \quad R_e = 0.5\,. \tag{5.37b}$$

With the modeled time delay the synthesis controller is stable in contrast to the design in (5.35). Moreover, the response is much faster and the closed loop more stabl. This allows to further tune the controller. Compared to the PI controller, the overshoot is smaller and the response faster.

The drawback of this approach is that it is not yet possible to implement four of these controllers on the final hardware. Nevertheless, with the *Rapid-X* tools it was easily possible to build a firmware which hosts only two controller in order to validate this approach in an experiment.

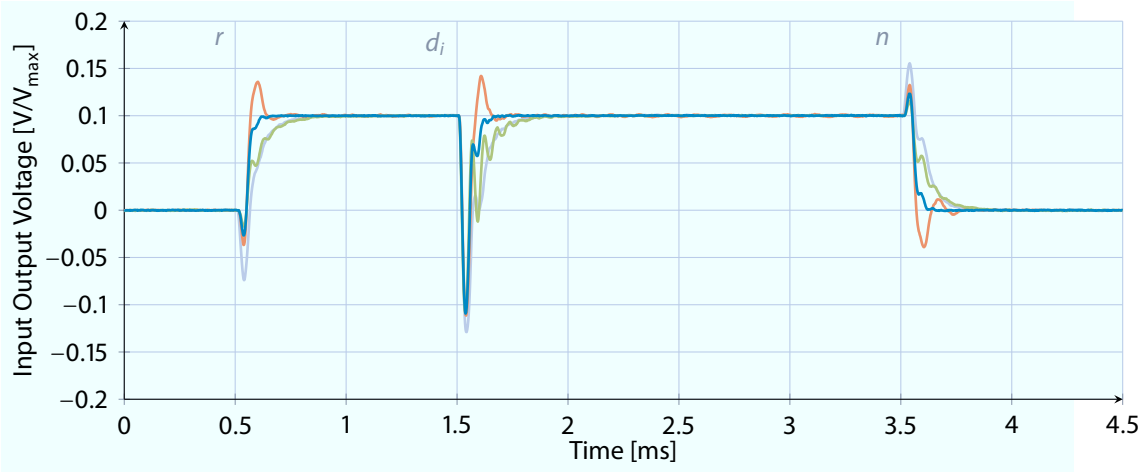

Figure 5.47: Measurement of the LQG controller with pade approximation for the additional time delay, with the nominal (—), increased (—) and decreased gain (—) plant compared to the PI controller (—)

In-loop timing jitter

Up to now, the measurements are in-loop signals y_m, given in [V/Vmax]. To convert those into actual timing jitter the sensitivity of the optical setup has to be calibrated like introduced in Sec. 5.1.9. The sensitivity for the given measurement is $\approx 2.9\ \frac{\mathrm{mV}}{\mathrm{fs}}$ or $\approx 789\ \frac{\mathrm{fs}}{\mathrm{V/V_{max}}}$.

Table 5.7: Steady state performance of the in-loop error y_m for the LSU controller.

Time	1 s, 3 measurements				12 h with 1 s Interval		
	$K_{\mathrm{PI,old}}$	K_{PI}	K_{LQR}	$K_{\mathrm{LQR,pade}}$	$K_{\mathrm{PI,old}}$	K_{PI}	$K_{\mathrm{LQR,pade}}$
Max peak $[mV/V_{max}]$	6.040	2.518	2.764	2.171	13.069	9.079	4.875
Mean peak $[mV/V_{max}]$	-	-	-	-	4.833	3.020	2.258
RMS $[mV/V_{max}]$	1.045	0.380	0.443	0.276	1.205	0.415	0.273
Max peak [fs]	4.766	1.987	2.181	1.714	10.312	7.163	3.847
Mean peak [fs]	-	-	-	-	3.813	2.383	1.782
RMS [fs]	0.825	0.300	0.349	0.218	0.951	0.328	0.215

The performance of the controller in-loop signal is given in Table 5.7. The long term measurement are taken over a period of 12 h at night of three consecutive days. The RMS and the peak to peak values are calculated over a measurement interval of 1 s. The maximum and the mean of these peak to peak values are higher than the ones of a single short measurement. The reason for this is that, over the long measurement time, the motor coarse tuning is activated. This leads from a single interval to higher peak values.

The table shows, that for the long term measurement, including motor movements, the RMS of the in-loop timing error can be reduced from 0.951 fs to 0.328 fs if the model-based PI controller is used. Furthermore, the model-based LQG controller with pade approximation leads to 0.215 fs, which is a reduction by a factor of 4.4 compared to the previously used PI controller and a further reduction by 1.5 compared to the optimized PI controller.

The peak to peak value indicates the overshoot to be the result of a motor movement. This value is also decreased from a mean of 3.813 fs for the previous controller to 2.283 fs for the model-based PI and to 1.782 fs to the LQG controller. In the current setup, the coarse tuning is activated in the range of minutes. This time should be increased to avoid the disturbances induced by the movement.

The next important step is the comparison and validation of the out-of-loop signal y_4. At the end of this work the required setup was not available. Nevertheless, the given data show that the LQG controller with pade approximation should be used for the current setup.

5.2.6 Conclusion

The performed experiment shows that the prediction of the model, identified in Sec. 5.1.6, models the real plant behavior. An important property, shown in the experiments, is the time delay inside the control loop. Even thought the inter-board communication is optimized, the whole loop, including ADC and DAC sampling and readout, is of importance for the control task.

For the PI controller the resonances of the piezo are not well damped without the delay. If the plant delay is added to the controller synthesis the phase change decreases the resonance peak in the closed loop. For the LQG controller the opposite is the case. Without the time delay, the internal model suppresses the piezo resonances. With an un-modeled additional time delay this is not true anymore and the performance of the delayed PI controller is superior.

In the last step, the time delay is added to the system model and with this new model the LQG controller is designed. This strategy leads to a controller that is able to suppress the resonance modes and has a fast step response for all inputs of the GOF.

This controller has the best performance, but it is not possible to implement four controllers in parallel on the current hardware. An upgrade is scheduled that should allow this design. In the mean time, the delayed PI controller with the second best performance can be used. If it is possible to decrease the delay, the 4th order LQG controller can be chosen. Nevertheless, a shift to boards with more capabilities will allow for a more sophisticated controller, which could in turn increase the performance.

The close loop with the LQG controller is unstable if it is moved to a non-linear region of the OXC measurement, which could occure e.g. by a physical disturbance to the optical table. A possible solution for this drawback will be briefly explained in Sec. 5.4.

Not shown are links with a poor optical setup. The measurement noise and linearity in the working point depends strongly on a proper setup. And with those also the performance of the closed loop.

5.3 Controller Design for Long Links

If the short link approximation is not valid anymore, see (5.20), but the LSU is operated in the linear range, the control loop in Fig. 5.15 can be used, which is a simplification of the model structure shown in Fig. 5.10. The purpose of the controller is to minimize the timing error at y_4, the output at the end-station, although only y_1 is measured. Remember, for the short links y_4 has half the magnitude of y_1, which changes if a longer fiber length is taken into account.

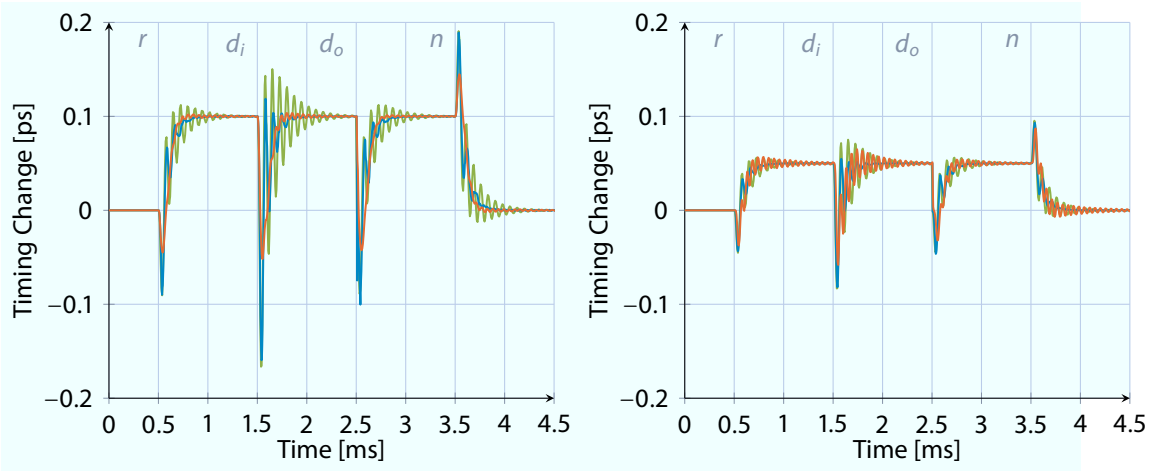

Figure 5.48: Simulation of the PI controller without internal time delay and with a short (——) a 412 m (——) and a 2.542 km (——) long fiber.

Figure 5.48 shows the response of the measured output y_1 (left) and the response of the end-station output y_4 (right) to the test sequence in the closed loop with the controller $K_{\mathrm{PI}}(s)$. For a short fiber (——) the resonance of the piezo is given at the in-loop error signal (left) as well as on the end station signal y_4 (right). The same is true e. g. for links of the length of FLASH (——). If the fiber length is increased close to the critical length of 2.824 km, e. g. to 2.542 km (——), the resonance is only given at the end-station and not on the in-loop signal. The reason for this is the transmitting zero of the fiber, due to the time delay, which cancels this frequency. This example shows, that the response at the end-station, for the long links planed for XFEL, can be disturbed by the piezo resonance or vibration inside the tunnel even if the links have an undisturbed in-loop error signal. Moreover, if the fiber length is further increased, the measured phase is rotated, see Sec. 5.1.7, which leads to an unstable closed loop.

To cope with this delay and the transmission zeros, the following approaches are e. g. possible:

1. Compensate the delay using the smith-predictor introduced in Sec. 3.7.5.
2. Controller design with a delay in the system model, using the Pade approximation, see Sec. 5.2.5.
3. Suppress the piezo vibration using a current read-back, compare to Sec. 5.1.13.

Section 3.7.5 shows how to compensate a constant time delay by subtracting the time delayed model and control the un-delayed simulation of the plant. For the LSU the plant consists of an un-delayed response combined with the delayed on. Therefore, Fig. 5.49 shows the LSU control loop where the prediction and the plant part are swapped compared to the standard design.

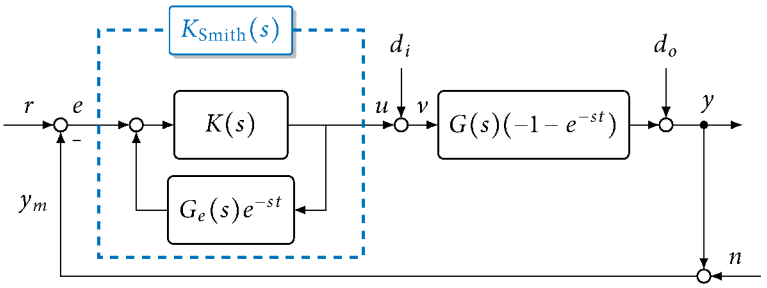

Figure 5.49: Smith predictor approach for the link.

Without the Smith predictor the closed loop with the optimized PI controller is unstable for a the longest XFEL link with a length of 4.162 km. Figure 5.50 shows the response (——) if the Smith predictor is used as a first approach. The added prediction leads to a stable closed loop with a wanted behavior for $T(s)$ at 0.5 ms. Nevertheless, an input disturbance leads to an oscillation of the resonance mode. Moreover, the offset of in- and output disturbance can not be compensated by the integral part of the controller. The reason for that is the changes structure of the LSU compared to the standard Smith approach. In order to compensate those steady state errors, a high pass filter is added to the smith-prediction part in the controller, similar to methods discussed in [NC07]. With this modification the response (——), shown in Fig. 5.50, has no steady state error.

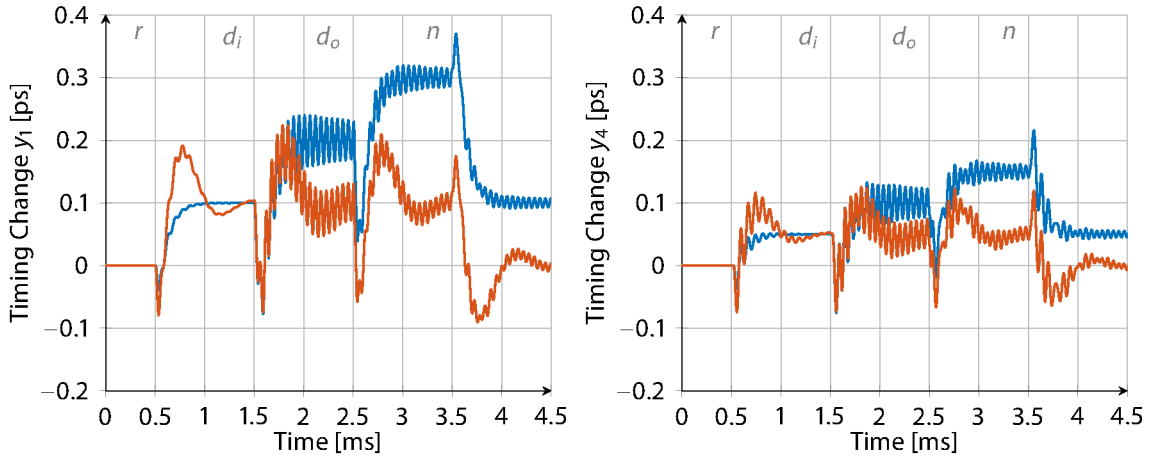

Figure 5.50: Simulated response at the measurement (left) and at the end station (right) of the long link without (——) and with (——) high-pass filter in the Smith predictor.

In order to increase the damping of the input disturbance function, a pade approximation of the link dynamic is added to the plant model as a second approach. If the fiber length is known the fiber dynamics, shown in Fig. 5.18, can be added to the plant model. This extended plant model is than used in the LQG design, explained in Sec. 3.7.2.

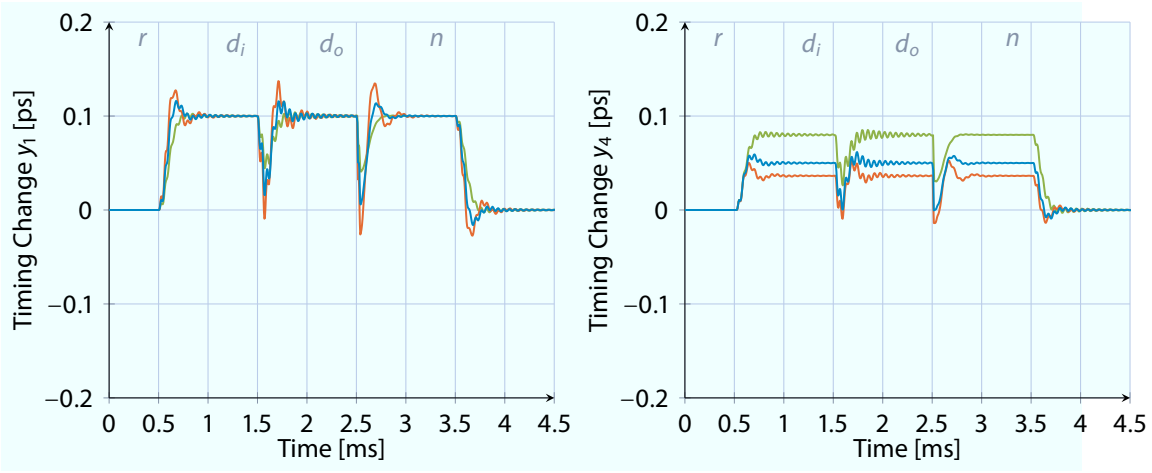

Figure 5.51: Simulated response at the measurement (left) and at the end station (right) for the long link with LQG controller with pade approximation with the nominal (——), increased (——) and decreased gain (——).

Figure 5.51 shows the response of this controller. The oscillation is damped for the sensor output y_1 (left) as well as for the end station output y_4 (right). The drawback of this solution is shown on the right plot. If the gain changes, the approximation of the fiber leads, in this control structure, to a steady state error at the end station output y_4 which is unwanted if a reference has to be tracked. This should be further studied in subsequent works if a reference tracking becomes necessary.

The last approach, the suppression of the piezo resonances by measurement of the current, is not possible due to the slow sampling of the signal. Moreover, the pade approximation will lead to an increase of the system and controller order which does not fit on the available FPGA. The first approach on the other hand only requires a time delay e. g. a buffer, which are available. For this reason, the Smith predictor is implemented in the firmware. Nevertheless, at the end of this work, no long links have been available at XFEL. Tests of this approach should be performed if those are available.

5.4 Non-linear Controller Design

While performing the experiments in Sec. 5.2.5, an important disadvantage of the LQG design was observed. This controller is unstable in the non-linear parts of the OXC measurement. For this reason, the PI controller has to be used to close the loop. If the system is close to the working point, the controller can be switched in order to increase the performance.

If the system moves outside the linear region with the activated LQG controller, a large oscillation occurs and the lock is opened. This occurs when, for example:

- the LSU activated outside the linear region
- there is a fast drift compared to the coarse tuning update rate, the integral part of the controller saturates and the system moves outside the linear range.
- a disturbance $\approx 250\,\mathrm{fs}$ occurs the dynamic response moves outside the linear range.

These points are usually not relevant for the operation phase, because

- the system should be in a steady state and is not activated or deactivated.
- the saturation of the integrator already leads to a disallowed timing error. Both the dynamic range of the controller and the coarse tuning update rate, have to be adjusted accordingly.
- there is no work going on in the laser room and hence there should be no big disturbances. If there are disturbances, the performance is already degraded to an unwanted level.

Nevertheless, it is desirable that the LSU system also be stable during the commissioning phase, where these problems can occur. A common way to achieve this is to take this non-linearity into account through the usage of the EKF, briefly introduced in Sec. 3.7.3. Comparing the system assumption (3.59) for the EKF with the discrete version of the non-linear system (5.25) leads to

$$x(k+1) = \underbrace{\Phi_{\mathrm{Short}}\, x(k) + \Gamma_{\mathrm{Short}}\, u(k)}_{f(x(k),u(k))} \tag{5.38a}$$

$$F_k = \frac{\partial f}{\partial x} = \Phi_{\mathrm{Short}} \tag{5.38b}$$

$$y_m(k) = \underbrace{\frac{P_+}{cosh^2\left(\frac{d_+ + 2(C_{\mathrm{Short}} x(k) + d_\bullet)}{a_+}\right)} - \frac{P_-}{cosh^2\left(\frac{d_- - 2(C_{\mathrm{Short}} x(k) + d_\bullet)}{a_-}\right)}}_{h(x(k))} \tag{5.38c}$$

$$H_k = \frac{\partial h}{\partial x} = C_{\mathrm{Short}} \cdot \left(\frac{2\,P_+\, sinh\left(\frac{d_+ + C_{\mathrm{Short}} x(k)}{a_+}\right)}{a_+\, cosh^3\left(\frac{d_+ + C_{\mathrm{Short}} x(k)}{a_+}\right)} + \frac{2\,P_-\, sinh\left(\frac{d_- - C_{\mathrm{Short}} x(k)}{a_-}\right)}{a_-\, cosh^3\left(\frac{d_- - l}{a_-}\right)} \right). \tag{5.38d}$$

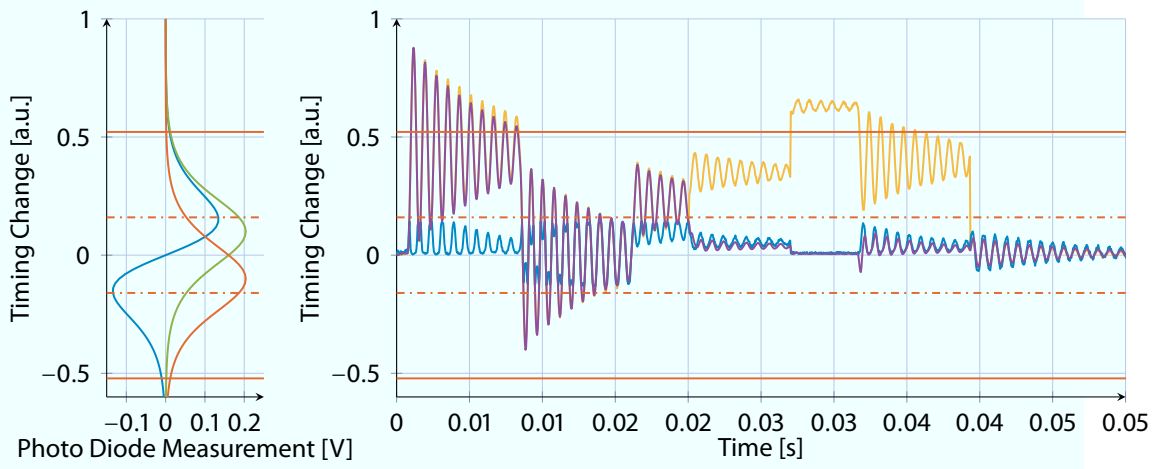

Figure 5.52: Simulation of the open loop state estimation using a the difference signal of the OXC with the real timing change (——), the measured signal (——), and the estimated timing change (——).

The simulation for this first approach is depicted in Fig. 5.52. The EKF is capable of capturing a reference step and small disturbance steps close to the linear region. If a large disturbance occurs the estimation diverges from the real system response. The reason for this is the non-uniqueness of the measurement function.

The second approach uses each of the photo diodes channels. Actually, these are measured individually in order to calibrate a possible offset and to minimize electrical interferences on the difference signal. Now the two signals allow the proper estimation of the LSU states of the non-linear model.

With both diodes, the output function of the non-linear system changes to

$$y_m(k) = \underbrace{\begin{bmatrix} \frac{P_+}{\cosh^2\left(\frac{d_+ + 2(C_{\text{Short}}x(k) + d_\bullet)}{a_+}\right)} \\ \frac{P_-}{\cosh^2\left(\frac{d_- - 2(C_{\text{Short}}x(k) + d_\bullet)}{a_-}\right)} \end{bmatrix}}_{h(x(k))}, \tag{5.39}$$

$$H_k = \frac{\partial h}{\partial x} = \begin{bmatrix} C_{\text{Short}} \cdot \frac{2P_+ \sinh\left(\frac{d_+ + C_{\text{Short}}x(k)}{a_+}\right)}{a_+ \cosh^3\left(\frac{d_+ + C_{\text{Short}}x(k)}{a_+}\right)} & C_{\text{Short}} \cdot \frac{2P_- \sinh\left(\frac{d_- - C_{\text{Short}}x(k)}{a_-}\right)}{a_- \cosh^3\left(\frac{d_- - C_{\text{Short}}x(k)}{a_-}\right)} \end{bmatrix}^T. \tag{5.40}$$

The response of the open-loop state estimation is shown in Fig. 5.53. The disturbance occurring at the maximum of the difference signal can be tracked with this configuration, because the combination of both individual diodes leads to a defined change, which is unique for the direction of the timing change.

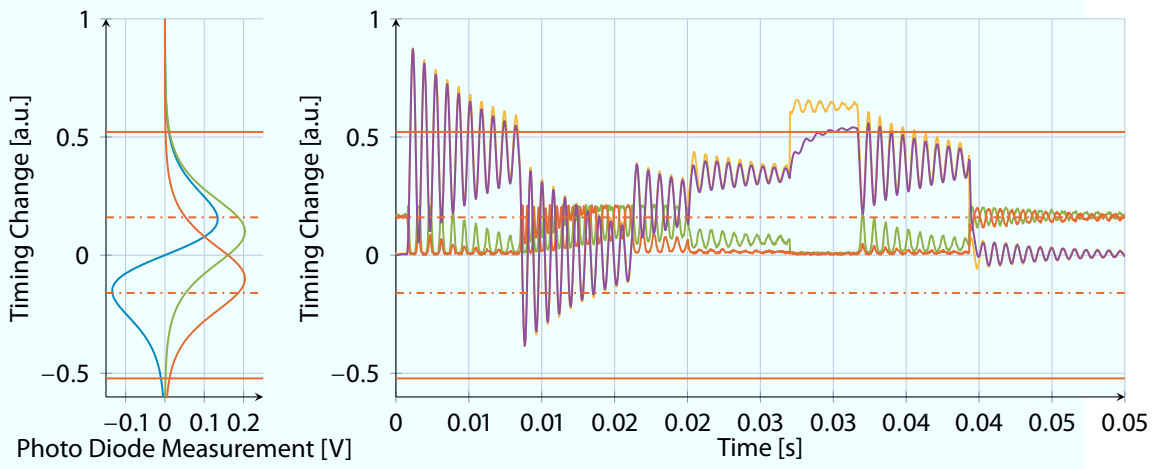

Figure 5.53: Simulation of the open loop state estimation using both photo diode signals with the real timing change (—), the positive (—) and negative (—) photo diode signal, and the estimated timing change (—).

This second approach leads to an extended working region that includes both edges of the non-linear measurement functions. This technique can be used for the LSU as well as for other applications using this sensor, e. g. the L2L setup.

The common arguments against the usage of an EKF are

- the calculation of $h(x(k))$, and the derivative $H(x(k))$, may be too demanding in terms of resources and clock cycles.
- the calculation of the matrix inverse in (3.62) may be too demanding in terms of resources and clock cycles.

In the given case, both functions just have one argument and only a limited range is required. For this reason, it is possible to interpolate between grid points stored in a one dimensional look-up-table, which decreases the required calculations. The matrix inverse in the first approach is the inverse of a scalar value and for the second approach the inverse of a two by two matrix, which is possible to implement. Still the disadvantage of this method is the increased number of multiplications required on the computation hardware.

5.5 Conclusion

This chapter analysed the LSU subsystem of the LbSync system. It was shown that a third order model can be used to mathematically model the behavior of the piezo driver and the fiber stretcher. A time delay is given by the spatially extended fiber and the measurement principle leads to a non-linear measurement function. After that modeling part, first control strategies are proposed and validated in experiments. The applicable controller with the best performance is the LQG controller that was designed with an additional pade approximation.

For the LSU system, the questions raised in Section 1.1 can be answered as follows:

1. The control challenge of the LSU system is the minimization of the external influences, e. g. the transmission of output disturbances.
2. A suitable model for the piezo fiber stretcher actuated with the PZT4 is a 3rd order model. The sensor shows a non-linear measurement function and the length of the connected fiber model to a time delay that leads to a transmission zero.
3. Right now, the best possible controller for the LSU system is the optimized PI controller. If less than 4 links are required per computation board, the order of the controller could be increased or if the delay in ADC can be reduced, the LQG controller should be used to increase the performance.
4. A possible way to increase the LSU performance for long links is to add the measurement of the piezo current to overcome the transmission zero.
5. The robustness of the LSU system can be increased by the usage of an extended Kalman filter, which is capable of estimating the piezo states despite the non-linear measurement function and/or to add the current read-back that is not influenced by the OXC measurement.

6 OVERALL SYSTEM

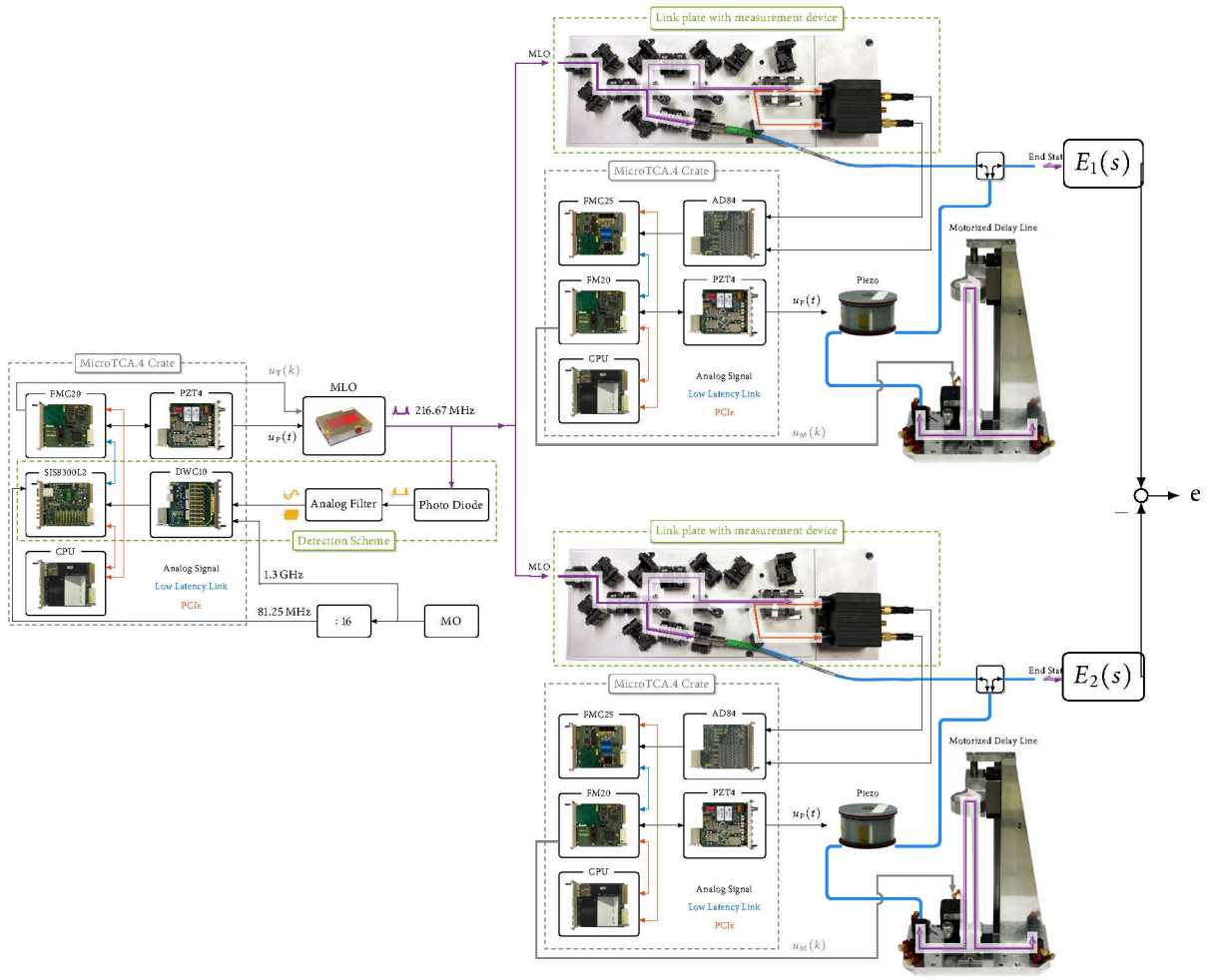

Figure 6.1: Overview of a LbSync System with the MLO and two LSUs.

The last chapter of this work will focus on the interaction of the different subsystems. The main control goal is not to optimize each of the systems individually, but to minimize the timing error between the different end-stations. This chapter shows the behavior of this error difference with the strategies developed up to now. After that, ways to improve the behavior of the overall system are analyzed.

6.1 Modeling

Figure 6.2 combines the different components of the LbSync system in an overall block diagram. In the upper left part the MLO is modeled with its coloring filter, W_{MO}, generating the electrical synchronization signal. Below that, the MLO is given with its coloring filter, W_{MLO}, and the control loop with the plant $P_{\mathrm{MLO}}(s)$ and the MLO controller $C_{\mathrm{MLO}}(s)$. Two LSUs, discussed in detail in Sec. 5, are shown in the center. In the right part of Fig. 6.2, different end stations $E_\bullet(s)$ with output signals $z_\bullet$ can be seen. The difference signal to be minimized is given by $v_\bullet$.

The end station $E_0(s)$ is connected to the MO with a conventional coaxial cable, shown in the upper part. The more complex LbSync system with the MLO, and two LSUs L_1 and L_2 is shown in the lower part. Each of the LSUs has one end station, $E_1(s)$ and $E_2(s)$, respectively.

The different input channels for the overall system are

n_{MO}, d_{MLO}	which are the noise effects of the MO and MLO. The colored noise is generated by AWGN $N(0,1)$, transmit trough the filter $W_{\mathrm{MO}}(s)$ and $W_{\mathrm{MLO}}(s)$, explained in Sec. 4.1.9.
n_{MLO}	models noise added by actuator chain of the MLO, i. e. DAC, PZT4 and others.
u_{MLO}	is the control action generated by the MLO controller.
y_{MLO}	is the absolute timing error of the laser pulse train generated by the MLO.
d_{coaxial}	models the additional timing error induced by a coaxial distribution of the synchronization pulse. This disturbance is assumed to be much higher than the timing errors induced by disturbances on the optical fiber.
d_1, d_2	are noise effects acting only on the fiber of one LSU and not on the others.
d_{12}	is a common noise effect which acts on the fiber of both LSU.
$e_\bullet$, $u_\bullet$, $dl_\bullet$	are the control errors measured by the OXC, the control actions and the resulting piezo length changes of the LSU.
y_1, y_2	are the timing errors of the laser pulse train at the end station.
$z_\bullet$	are the timing errors of the real measurement devices connected to the end stations. For the whole machine operation the minimization of those fluctuations are the final requirement.
$v_\bullet$	are the timing differences between the relevant measurements.

The performance measure of interest is the timing jitter between the different end stations. This is the error, $v_\bullet$, between the output of the different end stations, e. g. v_{01} for the difference between end station $E_0(s)$ and $E_1(s)$. If these errors tend to zero all attached devices get the synchronization signal at exactly the same time.

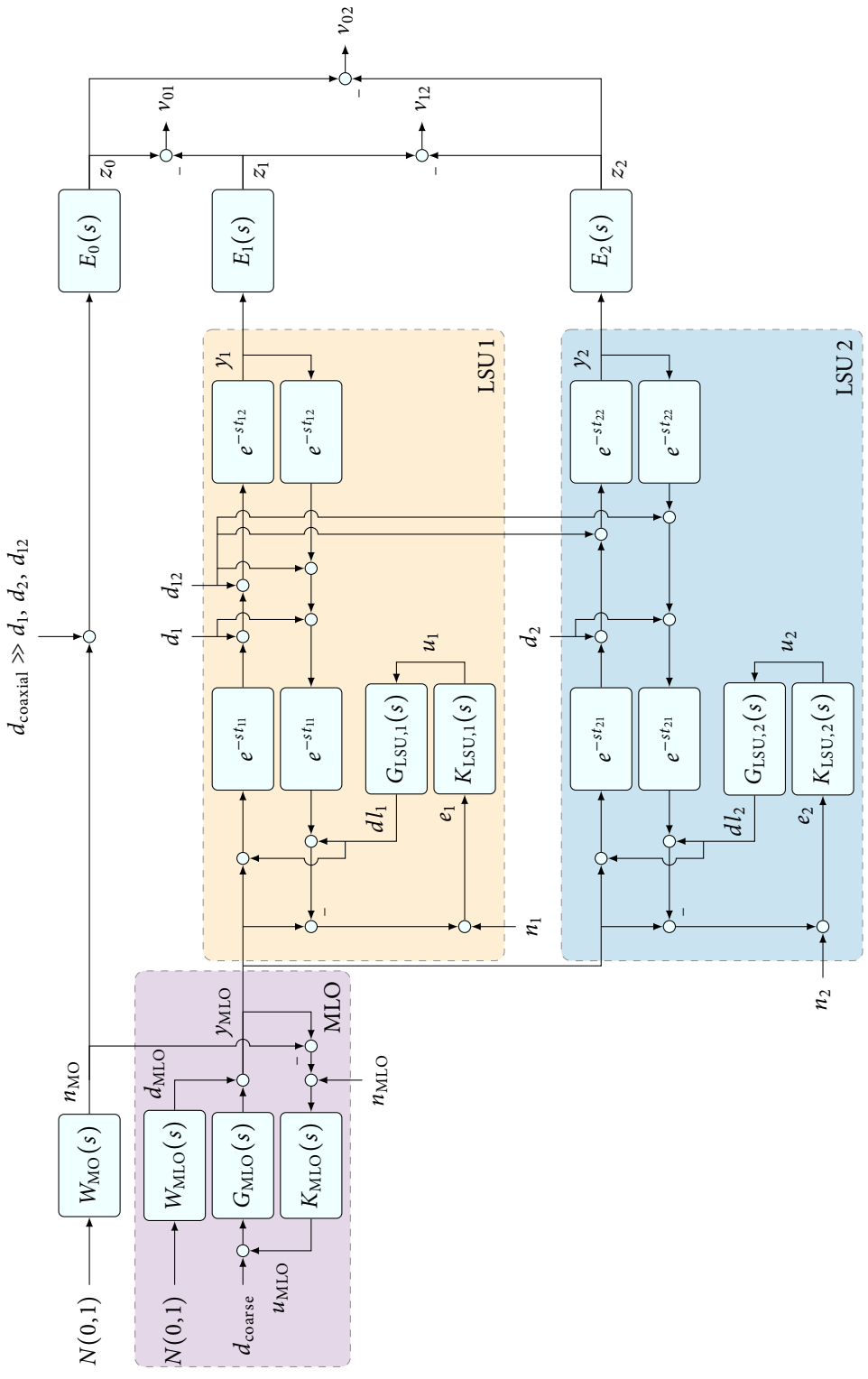

Figure 6.2: Block diagram of the LbSync system with MO, MLO subsystem, two LSU with the end stations $E_1(s)$ and $E_2(s)$. All signals are expressed in phases w.r.t. the ideal phase of the absolute 216.67 MHz reference signal.

6.1.1 Control Objectives

In the operation of the facility many systems are working together. The beam-based feedback requires measurements of the BAM, the pump probe laser has to be synchronized to the electron beam and many other subsystems depend on each other. In order to optimize the performance, it is important that these systems take their measurements and/or perform their calculations at the same time.

In terms of the overview in Fig. 6.2, it means that the relative timing jitter $\nu_\bullet$ should go to zero, i. e. the $\mathcal{H}_2$ norm for all system inputs to $\nu_\bullet$ should be minimized. The final performance specification for this timing difference is given by $\approx 1\,\mathrm{fs}$.

6.1.2 Dynamic Behavior

The timing error at the output of an end-station connected to a coaxial cable is given by

$$z_0 = E_0(s)(n_{\mathrm{MO}} + d_{\mathrm{coaxial}})\,, \tag{6.1}$$

where the disturbance signal d_{coaxial} has a very high contribution and can not be avoided. If the electrical signal is directly used without an additional Phase Locked Loop (PLL), e. g. for the clock of an LLRF crate, the end station is given by the transfer function

$$E_0(s) = 1\,. \tag{6.2}$$

This means that the output is the sum of the two disturbance. If a laser system, e. g. a PPL, is connected to the coaxial link, the relevant end station dynamics $E_0(s)$ is given by the closed loop transfer function of this subsequent control loop, which could also have additional noise sources. These are neglected in this discussion.

The transfer functions of the LbSync systems are more complex. The absolute timing error of the laser pulse train after the MLO, which enters the different LSU, is given by

$$y_{\mathrm{MLO}} = \underbrace{\frac{G_{\mathrm{MLO}}(s)K_{\mathrm{MLO}}(s)}{1 + G_{\mathrm{MLO}}(s)K_{\mathrm{MLO}}(s)}}_{T_{\mathrm{MLO}}(s)}(n_{\mathrm{MO}} + n_{\mathrm{MLO}}) + \underbrace{\frac{1}{1 + G_{\mathrm{MLO}}(s)K_{\mathrm{MLO}}(s)}}_{S_{\mathrm{MLO}}(s)} d_{\mathrm{MLO}}\,. \tag{6.3}$$

As discussed in Chapter 4, this is a trade-off between following the MO and the measurement noise $T(s) \to 1$, and following the phase noise of the free running MLO $T(s) \to 0$, i. e. in that theoretical cases the pulse train timing error has a limit value of

$$y_{\mathrm{MLO}} \approx \begin{cases} d_{\mathrm{MLO}}, & \text{if } T(s) \to 0, \\ n_{\mathrm{MO}} + n_{\mathrm{MLO}}, & \text{if } T(s) \to 1. \end{cases} \tag{6.4}$$

With the discussions in Chapter 5, the timing change at the end of the LSU $\bullet$, $y_\bullet$ is given by

$$y_\bullet = e^{-st_{\bullet 3}}(y_{\mathrm{MLO}} + dl_\bullet) + e^{-st_{\bullet 2}}(d_1 + d_2)\,, \tag{6.5}$$

with the one way time delay through the fiber

$$t_{\bullet 3} = t_{\bullet 1} + t_{\bullet 2} \tag{6.6}$$

and the length change of the piezoelectric actuator by

$$dl_\bullet = P_{\mathrm{LSU},\bullet}(s)C_{\mathrm{LSU},\bullet}(s)e_\bullet\,. \tag{6.7}$$

The timing error measured by the LSU, simplified by neglecting the OXC non-linearity, is

$$e_\bullet = -(1 + e^{-s2t_{\bullet 3}})dl_\bullet + (1 - e^{-s2t_{\bullet 3}})y_{\mathrm{MLO}} - (1 + e^{-s2t_{\bullet 2}})e^{-st_{\bullet 1}}(d_\bullet + d_{12}) + n_\bullet\,. \tag{6.8}$$

Combining (6.8) and (6.7) gives

$$dl_\bullet = \frac{P_{\mathrm{LSU},\bullet}(s)C_{\mathrm{LSU},\bullet}(s)((1 - e^{-s2t_{\bullet 3}})y_{\mathrm{MLO}} - (1 + e^{-s2t_{\bullet 2}})e^{-st_{\bullet 1}}(d_\bullet + d_{12}) + n_\bullet)}{1 + P_{\mathrm{LSU},\bullet}(s)C_{\mathrm{LSU},\bullet}(s)(1 + e^{-s2t_{\bullet 3}})}\,. \tag{6.9}$$

With (6.5),(6.6) and (6.9) , the timing error at an end station is given by

$$\begin{aligned} y_\bullet = {} & \underbrace{\left(1 + \frac{P_{\mathrm{LSU},\bullet}(s)C_{\mathrm{LSU},\bullet}(s)(1 - e^{-s2t_{\bullet 3}})}{1 + P_{\mathrm{LSU},\bullet}(s)C_{\mathrm{LSU},\bullet}(s)(1 + e^{-s2t_{\bullet 3}})}\right)}_{T_{y_\bullet, y_{\mathrm{MLO}}}} e^{-st_{\bullet 3}} y_{\mathrm{MLO}} \\ & + \underbrace{\left(1 - \frac{P_{\mathrm{LSU},\bullet}(s)C_{\mathrm{LSU},\bullet}(s)(1 + e^{-s2t_{\bullet 2}})e^{-s2t_{\bullet 1}}}{1 + P_{\mathrm{LSU},\bullet}(s)C_{\mathrm{LSU},\bullet}(s)(1 + e^{-s2t_{\bullet 3}})}\right)}_{T_{y_\bullet, \mathrm{d}_\bullet}} e^{-st_{\bullet 2}}(d_\bullet + d_{12}) \\ & + \underbrace{\left(\frac{P_{\mathrm{LSU},\bullet}(s)C_{\mathrm{LSU},\bullet}(s)}{1 + P_{\mathrm{LSU},\bullet}(s)C_{\mathrm{LSU},\bullet}(s)(1 + e^{-s2t_{\bullet 3}})}\right)}_{T_{y_\bullet, \mathrm{n}_\bullet}} e^{-st_{\bullet 3}} n_\bullet\,. \end{aligned} \tag{6.10}$$

The difference at two end stations is given by

$$\nu_{12} = E_1(s)y_1 - E_2(s)y_2\,, \tag{6.11}$$

and depends on the connected end station, $E_1(s)$ and $E_2(s)$. In the case of the LbSync system, a directly connected end station, i. e.

$$E_\bullet(s) = 1\,, \tag{6.12}$$

is an example of a BAM. Other lasers where the timing difference is measured with an OXC and with a system connected via the L2RF module have an additional dynamics $E_\bullet(s) \neq 1$.

Short fiber

If a very short fiber, $t_{\bullet\bullet} \to 0$, is connected, (6.10) can be simplified to

$$y_\bullet = y_{\mathrm{MLO}} + \underbrace{\left(1 - \frac{2 \cdot P_{\mathrm{LSU},\bullet}(s) C_{\mathrm{LSU},\bullet}(s)}{1 + 2 \cdot P_{\mathrm{LSU},\bullet}(s) C_{\mathrm{LSU},\bullet}(s)}\right)}_{S_{\mathrm{LSU},\bullet}(s)} (d_\bullet + d_{12}) + \underbrace{\left(\frac{P_{\mathrm{LSU},\bullet}(s) C_{\mathrm{LSU},\bullet}(s)}{1 + 2 \cdot P_{\mathrm{LSU},\bullet}(s) C_{\mathrm{LSU},\bullet}(s)}\right)}_{\frac{1}{2} T_{\mathrm{LSU},\bullet}(s)} n_\bullet \,. \quad (6.13)$$

The timing difference between two end stations stabilized with the LbSync system is given by

$$\begin{aligned} v_{12} = & \underbrace{\left(E_1(s) - E_2(s)\right) y_{\mathrm{MLO}}}_{x} + \underbrace{\left(E_1(s) S_{\mathrm{LSU},1}(s) - E_2(s) S_{\mathrm{LSU},2}(s)\right) d_{12}}_{y} \\ & \pm \underbrace{E_\bullet(s) S_{LSU,\bullet}(s) d_\bullet}_{d} \pm \underbrace{\frac{1}{2} E_\bullet(s) T_{\mathrm{LSU},\bullet}(s) n_\bullet}_{n} \,, \end{aligned} \quad (6.14)$$

and leads to the following observation for a negligibly short fiber:

- The timing error of the laser pulse train y_{MLO} is a common mode effect, if the dynamic behavior of the end stations $E_\bullet(s)$ are equal and therefore cancels. If the end stations are not equal, the resulting jitter can just be minimized by minimizing y_{MLO}.
- The timing change by common disturbances on the fiber d_{12} is minimized if the sensitivity function combined with the end station dynamics is the same for all link combinations.
- Uncorrelated disturbances, $d_\bullet$, can be reduced by minimizing of the $\mathcal{H}_2$ norm of the sensitivity function, by reducing the disturbances them-selfs or by placing the fiber spatially close to each other, which leads to correlated disturbances.
- The influence of measurement noise, $n_\bullet$, can be reduced by minimizing the $\mathcal{H}_2$ norm of the complementary sensitivity function or by reducing the noise itself.

If one of the end stations is connected with the electrical synchronization and the other with the LbSync system, the resulting timing difference is given by

$$\begin{aligned} v_{0\bullet} = & E_0(s)(n_{\mathrm{MO}} + d_{\mathrm{coaxial}}) - E_1(s) T_{\mathrm{MLO}}(s)(n_{\mathrm{MO}} + n_{\mathrm{MLO}}) - E_1(s) S_{\mathrm{MLO}}(s) d_{\mathrm{MLO}} \\ & - E_1(s) S_{\mathrm{LSU},\bullet}(s)(d_\bullet - d_{12}) + \frac{1}{2} E_1(s) S_{\mathrm{LSU},\bullet}(s) n_\bullet \,. \end{aligned} \quad (6.15)$$

With the theoretical assumption, that the MLO is locked tight to the MO over the whole frequency range $T_{\mathrm{MLO}}(s) \to 1$, $S_{\mathrm{MLO}}(s) \to 0$, it can be simplified to

$$\begin{aligned} v_{0\bullet} = & \quad E_0(s)(n_{\mathrm{MO}} + d_{\mathrm{coaxial}}) + E_1(s)(n_{\mathrm{MO}} + n_{\mathrm{MLO}}) \\ & + E_1(s) S_{\mathrm{LSU},\bullet}(s)(d_\bullet + d_{12}) + \frac{1}{2} E_1(s) S_{\mathrm{LSU},\bullet}(s) n_\bullet \,, \end{aligned} \quad (6.16)$$

which draws the following:

- If the bandwidth of the MLO is maximized and the end stations have the same dynamics, the noise of the MO becomes a common mode effect. Still, the disturbance d_{coaxial} and the measurement noise in the MLO loop n_{MLO} are present at the timing difference.
- Correlated and uncorrelated disturbances, d_{12} and $d_\bullet$, can be reduced by minimizing of the $\mathcal{H}_2$ norm of the sensitivity function of the LSU or by reducing the disturbances itself.
- Uncorrelated measurement noise, $n_\bullet$, can be reduced by minimizing the $\mathcal{H}_2$ norm of the complementary sensitivity function or by reducing the measurement noise itself.

Long fiber

If both compared links have long attached fibers, the time delay has an influence on the timing difference. Assuming a Smith prediction with an ideal plant model for the individual link,[1]

$$C_{\text{LSU},\bullet} = \frac{\tilde{C}_{\text{LSU},\bullet}}{1 - P_{\text{LSU},\bullet} e^{-s2t_{\bullet 3}} \tilde{C}_{\text{LSU},\bullet}}, \tag{6.17}$$

as given in Section 5.3, the timing behind the LSU (6.10) can be simplified to

$$\begin{aligned} y_\bullet = & \underbrace{\left(1 + \frac{P_{\text{LSU},\bullet}(s)\tilde{C}_{\text{LSU},\bullet}(s)(1 - e^{-s2t_{\bullet 3}})}{1 + P_{\text{LSU},\bullet}(s)\tilde{C}_{\text{LSU},\bullet}(s)}\right)}_{T_{y_\bullet, y_{\text{MLO}}}} e^{-st_{\bullet 3}} y_{\text{MLO}} \\ & + \underbrace{\left(1 - \frac{P_{\text{LSU},\bullet}(s)\tilde{C}_{\text{LSU},\bullet}(s)(1 + e^{-s2t_{\bullet 2}})e^{-s2t_{\bullet 1}}}{1 + P_{\text{LSU},\bullet}(s)\tilde{C}_{\text{LSU},\bullet}(s)}\right)}_{T_{y_\bullet, \text{d}_\bullet}} e^{-st_{\bullet 2}}(d_\bullet + d_{12}) \\ & + \underbrace{\left(\frac{P_{\text{LSU},\bullet}(s)\tilde{C}_{\text{LSU},\bullet}(s)}{1 + P_{\text{LSU},\bullet}(s)\tilde{C}_{\text{LSU},\bullet}(s)}\right)}_{T_{y_\bullet, \text{n}_\bullet}} e^{-st_{\bullet 3}} n_\bullet . \end{aligned} \tag{6.18}$$

With the complementary sensitivity function

$$\tilde{T}_\bullet(s) = \frac{P_{\text{LSU},\bullet}(s)\tilde{C}_{\text{LSU},\bullet}(s)}{1 + P_{\text{LSU},\bullet}(s)\tilde{C}_{\text{LSU},\bullet}(s)} \tag{6.19}$$

and a length change at the end of the fiber, given by

$$t_{2,2} = t_{1,2} + \Delta t \quad \Rightarrow \quad t_{2,3} = t_{1,3} + \Delta t\,, \tag{6.20}$$

[1] Remember that the non-time delayed part of the standard Smith predictor is in inside the plant for the LSU.

the timing difference at the end of two end station is given by

$$\begin{aligned} \nu_{12} = \quad & \left(E_1(s) - E_2(s)e^{-s\Delta t}\right) e^{-st_{1,3}} y_{\mathrm{MLO}} && + \left(E_1(s)\tilde{T}_\bullet(s) - E_2(s)\tilde{T}_\bullet(s)e^{-s\Delta t}\right) e^{-st_{1,3}} y_{\mathrm{MLO}} \\ & && - \left(E_1(s)\tilde{T}_\bullet(s) - E_2(s)\tilde{T}_\bullet(s)e^{-s3\Delta t}\right) e^{-s3t_{1,3}} y_{\mathrm{MLO}} \\ & + \left(E_1(s) - E_2(s)e^{-s\Delta t}\right) e^{-st_{1,2}} d_{12} && - \left(E_1(s)\tilde{T}_\bullet(s) - E_2(s)\tilde{T}_\bullet(s)e^{-s\Delta t}\right) e^{-s(2t_{1,1}+t_{1,2})} d_{12} \\ & && - \left(E_1(s)\tilde{T}_\bullet(s) - E_2(s)\tilde{T}_\bullet(s)e^{-s3\Delta t}\right) e^{-s(2t_{1,3}+t_{1,2})} d_{12} \\ & \pm E_\bullet(s)\tilde{T}_\bullet(s)e^{-st_{\bullet,3}} n_\bullet\,, && \pm \left(E_\bullet(s)(1 - \tilde{T}_\bullet(s)(1 + e^{-s2t_{\bullet 2}})e^{-s2t_{\bullet 1}})\right) e^{-st_{\bullet 2}} d_\bullet \end{aligned} \quad (6.21)$$

This leads to the following:

- If the fiber to the end station has a different length, the disturbance of the MLO is no longer a common mode effect, even if the combination of complementary sensitivity function and the end station dynamic are the same. The influence can be reduced by minimization of the absolute timing jitter y_{MLO}, which requires a MLO controller as designed in Sec. 4.2, and not one with a high bandwidth.
- Correlated disturbances are canceled if the combination of link and end station dynamics are similar and if the difference of the link lengths is small ($\Delta t \to 0$).
- Like in the short fiber case, uncorrelated disturbances and noise influences can only be reduced by minimizing the effect itself.

6.1.3 Conclusion and Uncertainties

The overall LbSync system, based on the individual components discussed in Sec. 4.1 and Sec. 5.1 was developed in the last section. For this analysis both models are combined and the assumption and uncertainties of each of the model also applies for the overall description.

6.2 Controller Design

The previous section showed that a minimal jitter between the output of the end-stations can be achieved if the combination of LSU and end station $E(s)$ have the same dynamic behavior.

In the following, $\mathcal{H}_\infty$ model matching is briefly illustrated, which is based on minimization of the system norms explained in Sec. 3.1.2. The idea is given in [DFT92]. With this design approach it is possible to design a controller that leads directly to a desired closed loop behavior.

Two short links with different end stations are taken into account in this example. One of the links is connected to a BAM that uses the pulse train directly, i. e. $E(s) = 1$. The other link is connected to a L2RF system, where a bandwidth of 5 kHz is assumed.[2] The requirement is that both link end-stations should behave in the same way.

Figure 6.3 shows the response to the test sequence, see Sec. 5.2.1, of the closed loop with $K_{\mathrm{lqr}}(s)$ as the controller. The timing of the BAM (——) directly changes whereas the timing after the L2RF (——) component changes slowly due to its low pass behavior. The timing error between both end stations (——) should be minimized.

The response to a reference step is faster for the BAM timing error than for the L2RF. Increasing the speed of the response leads to an increase of the controller bandwidth, which exceeds the limits of the given hardware. For this reason, the response of the BAM will be slowed down to fit to the L2RF response.

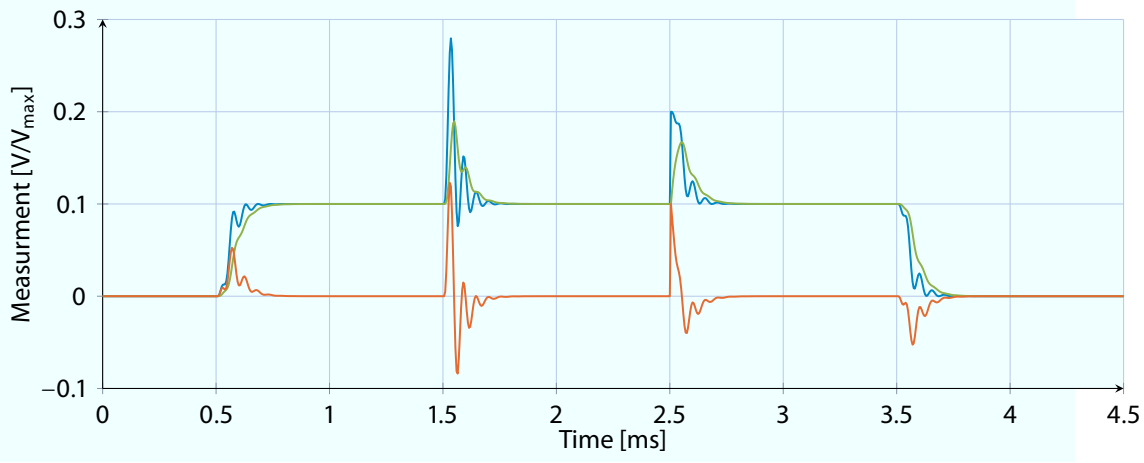

Figure 6.3: Simulation of the timing error after the BAM (——) end-station, the L2RF (——) end-station and the difference between both (——) if the associated LSU is excited by the test sequence.

[2] The actual bandwidth for the end-station has to be analyzed.

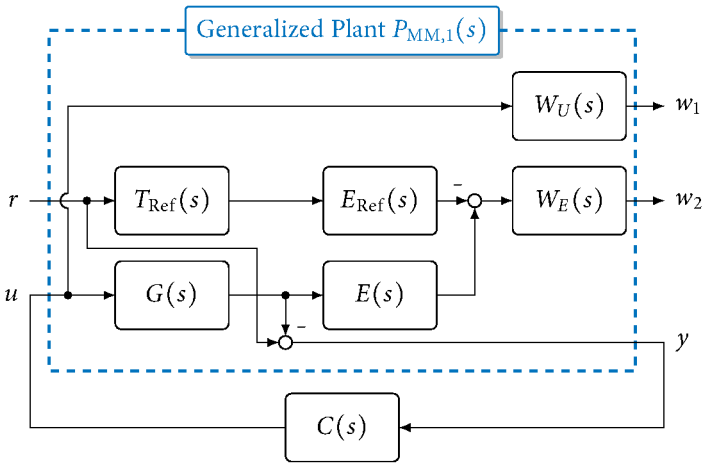

Figure 6.4: Generalized plant for the model matching design 1

Design 1

As a first approach for the first task, the generalized plant shown in Fig. 6.4 is used. A reference complementary sensitivity function $T_{\text{Ref}}(s)$ and an end station $E_{\text{Ref}}(s)$ are chosen. The designed controller $K(s)$ for the link $G(s)$ with the end station $E(s)$ should lead to the reference dynamics. The two weighting functions, $W_{\text{u}}(s)$ and $W_{\text{e}}(s)$, can be used to penalize the control efford and the difference between the behavior in the frequency domain.

The resulting step response is shown in Fig. 6.5. The dynamic behavior for the reference step at 0.5 ms can be tracked well, but the resonance peak in the input disturbance function is not suppressed, which leads to the oscillation if an input disturbance occurs, compare to Sec. 5.2.3.

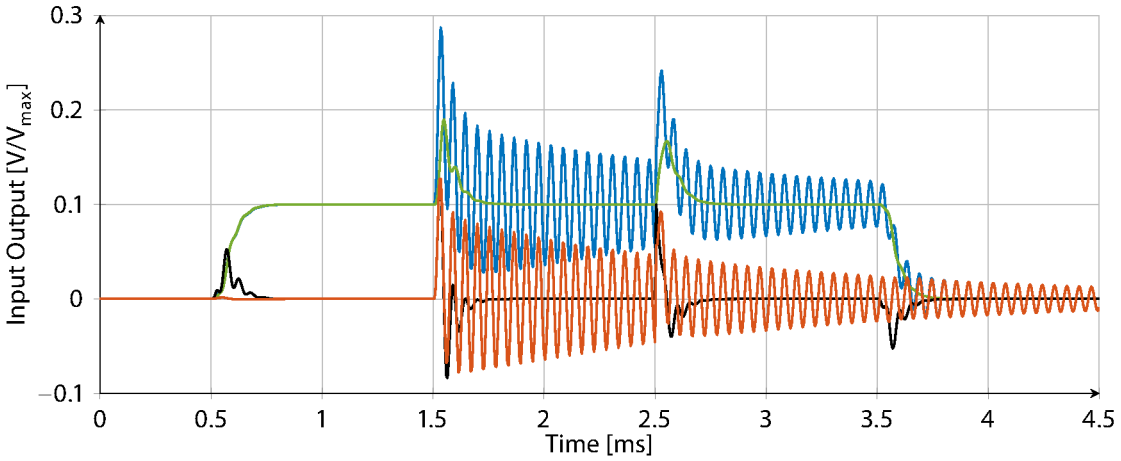

Figure 6.5: Simulation of the error after the BAM (——) and the L2RF (——) end-station with the difference (——) for the first design compared the previous difference (——).

Design 2

The second approach adds a weight, $W_{di}(s)$, to penalize this oscillation. The generalized plant is shown in Fig. 6.6 and the response for a designed controller in Fig. 6.7.

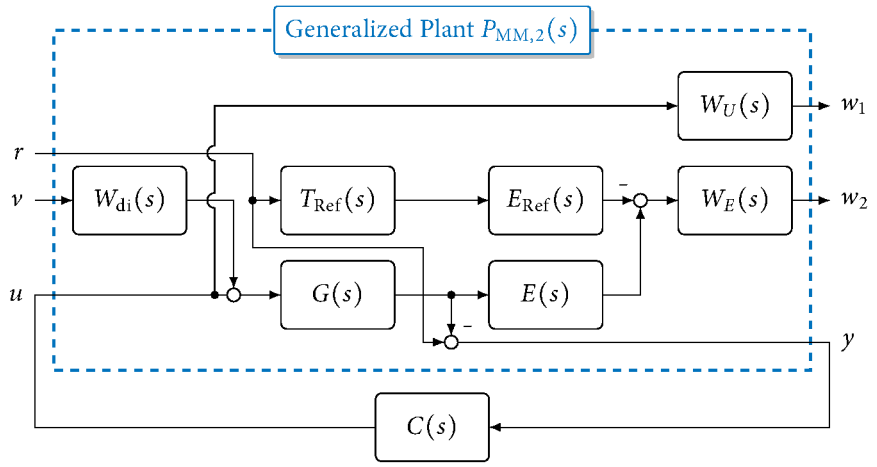

Figure 6.6: Generalized plant for the second model matching design.

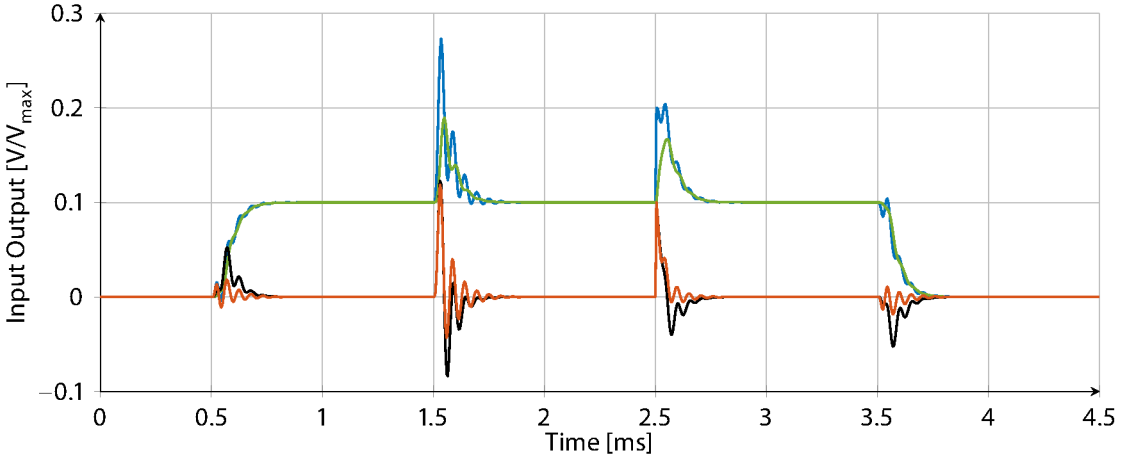

Figure 6.7: Simulation of the error after the BAM (——) and the L2RF (——) end-station with the difference (——) for the second design, compare to the previous difference (——).

The result of this design shows a significant reduction of the input disturbance oscillation. On the other hand, the fitting of the reference step decreases. The RMS error between Fig. 6.3 and Fig. 6.7 improves by ≈ 20%, thus the the fastest dynamics inside the controller increases from ≈ 45 kHz to ≈ 50 kHz. The drawback of this approach is the increased controller order from 4 to 12. Moreover, the design relies on the precise characterization of the end-station dynamics. Without a feedback it is not possible to act on disturbances and uncertainties inside the end-station.

6.3 Conclusion

In this section, the overall system was analyzed. The best performance can be achieved if the clock for all end-stations is derived from the LbSync system. The coaxial distribution should be used as an auxiliary input to reach the working point easily. After that, the LbSync system should be the reference. In this case, common mode errors like the MO and MLO influences as well as common disturbances don't effect the timing difference between the end stations.

Moreover, this section shows that it is not important to minimize the jitter of each individual system, but to design the different systems in such a way, that the dynamic behavior is equal. If this is the case, disturbances are resulting in the same timing error at the different end stations and the difference goes to zero. E. g. it makes sense to choose a controller which does not lead to an optimal reference tracking for the LSUs that are connected to BAMs. The controller should be changed in such a way, that it superimposes the same dynamic behavior for all LSU end station combinations. With this choice, the timing difference at the end stations can be minimized.

For the overall system, the questions raised in Section 1.1 can be answered as follows:

1. All subsystems should be connected and synchronized to the LbSync system.
2. The control challenge of the overall system is the minimization of the relative timing jitter between the outputs of the end-stations.
3. A suitable model for the overall system is the combination of the models developed for the individual components.
4. A model matching controller should be used to impose the same dynamic behavior for all combinations of LSU and end-station.
5. A possible way to increase the overall performance is to reduce the influencing disturbance and noise effects and update the LSU controller like discussed.
6. The robustness of the overall system could be increased by increasing the robustness of the individual components.

7 SUMMARY AND OUTLOOK

7.1 Summary

In this work, the LbSync system at the European X-FEL is considered. This linear accelerator will generate extremely intense X-Ray pulses to perform measurements on an atomic scale. In order to achieve the requirements of these experiments, the subsystems, used to accelerate the electron beam and to sample the probe, have to be synchronized in the range of femto-seconds. For this purpose, the LbSync system is used, which contains two main components: the MLO to generate the laser pulses, and the LSUs used to stabilize the optical fiber that distributes those pulses.

Section 4.1.2 shows the modeling of this laser pulse train. Important properties of this pulse train are the phase noise and the timing jitter, which are explained in Sec. 3.6. These properties can be expressed in the common control theory framework by shaping filters at noise channels in combination with the $\mathcal{H}_2$ norm, which is discussed in Sec. 4.1.9.

In the next step, the MLO is discussed, and it is shown how to optimize the dynamic range of the measurement, see Sec. 4.1.3. After that, Sec. 4.1.7 shows how to derive and identify the mathematical model for the MLO and Sec. 4.1.10 shows how to include the timing jitter into the model. Using this model, the parameter of the previously used PI controller are optimized and validated in an experiment. Furthermore, a controller design based on the pulse properties is discussed in Sec. 4.2.3.

The model of the optical fiber, used to transmit the pulse to the end-station is discussed in Sec. 5.1.1 and a model for the LSU, used to stabilize this fiber, is identified in Sec. 5.1.6. With this model, different controllers are designed and validated in experiments. Section 5.2.5 shows that these controllers can achieve a performance increase by a factor of 4.5 compared to the previously used controller. If a long optical fiber is used, the model of the fiber has to be included in the controller design. This is shown in Sec. 5.3. Another extension is the usage of the non-linear region of the sensor. This can be used to increase the robustness of the control scheme and is shown in Sec. 5.4.

The last chapter of this work combines the model of the MLO and two LSUs, which gives a mathematical description of the LbSync system. The main properties are shown in Sec. 6.1 and first controller designs based on $\mathcal{H}_\infty$ model matching are discussed in Sec. 6.2.

7.2 Outlook

The next steps of the controller development for the LbSync system should be the systematical validation of the predicted properties for long links and the combination of multiple links in an out-of-loop measurement. During the work on this project this was not possible due to the missing available hardware setup.

If the out-of-loop measurement shows a coupling between different signals of MLO, LSUs, and of the LSUs with respect to each other, the error signals of each device could be used by the others to reach a common mode variation that increases the overall performance.

Another important extension could be the usage of the actual piezo current in a cascaded feedback loop. This work showed at several points, that this could lead to a simplified, but cascaded control structure.

In order to increase the MLO performance, the measurement of the absolute phase noise of the laser oscillator should be tested, e. g. with a LSU without a fiber. If it can be shown, that the absolute phase noise can be measured, a MIMO controller should be used, acting on both error signals.

A similar approach should be used for the L2L. Up to now, a two step approach is used. In the first step the second laser is locked to the disturbed RF signal of the MO and if it reaches the working point the controller switches to the precise LbSync system. The robustness of this scheme can be increased if both error signals are combined, e. g. by a Kalman filter.

Another possible way to increase the robustness of the L2L system is the usage of the nonlinear Kalman filter, which takes the sensor function into account.

For all controller designs it could be analyzed whether it is advantageous to include the fixed point property in the synthesis step of the feedback controller design.

A MicroTCA.4 – Board Specification

SIS8300L2 – Computation AMC

The control algorithm and logic will run on one of two computation boards. The *SIS8300L* manufactured by *Struck Innovative Systems* is shown in Fig. A.1. This board will be used to run the algorithm for the MLO. The technical details are listed in Table A.1.

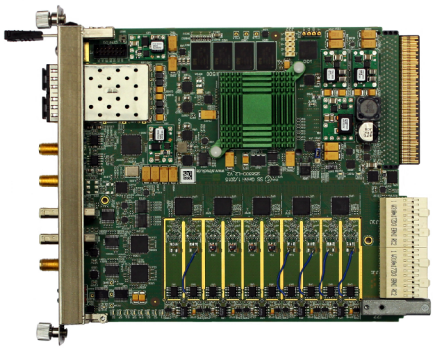

Figure A.1: SIS8300L2 Computation AMC

Table A.1: Technical specification SIS8300L2

Description	Value	Unit
Max. Algorithm clock	125	MHz
ADC voltage range	±1.2	V
Max. ADC frequency	125	MHz
ADC resolution	16	bit
DAC voltage range	±1.2	V
Max. DAC frequency	125	MHz
DAC resolution	16	bit

DWC10 – Downsampling RTM

In order to use the ADC of the struck board an RTM has to be attached. The *DWC10* is shown in Fig. A.2. This is one of these boards and will be used to mix high frequency signals to an intermediate frequency which will be transmitted to the *SIS8300L* and digitalized there. Some of the channels are bridged to fed through low frequency and DC signals. Technical details are listed in Table A.2.

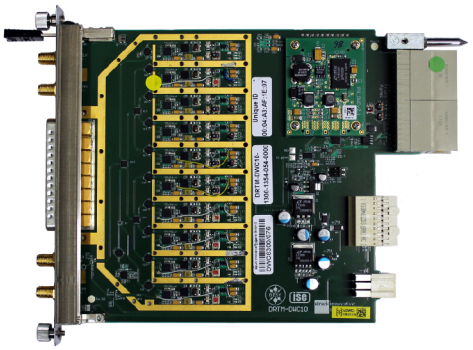

Figure A.2: DWC10 RTM

Table A.2: Technical specification DWC10

Description	Value	Unit
Input Channel	10	
Input Range	±1	V

SIS8900 – ADC Pipe-through RTM

In the inital laboratory tests, the SIS8900, shown in Fig. A.3, was used to pipe-through signals from a single ended input to the ADC inputs of the SIS8300L board. The relevant technical specification are given in Table A.3.

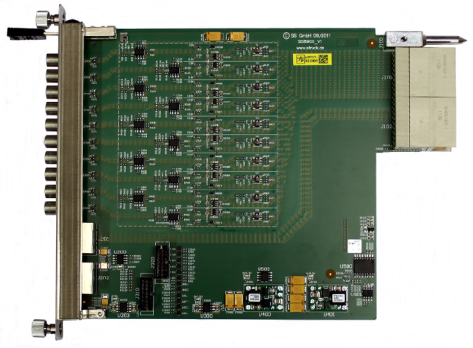

Figure A.3: SIS8900 RTM

Table A.3: Technical specification SIS8900

Description	Value	Unit
Input Channel	10	
Input Range	±1	V

FMC25 – Computation AMC

The other computation board is the *FMC25* manufactured by *CAEN ELS* and shown in Fig. A.4. This board will used for the LSU units. Additionally, this board holds up to two cards which drive the motors of the optical delay lines, used for the coarse tuning of the LSU. This board does not contain any ADC or DAC and requires an RTM offering these. Technical details are listed in Table A.4.

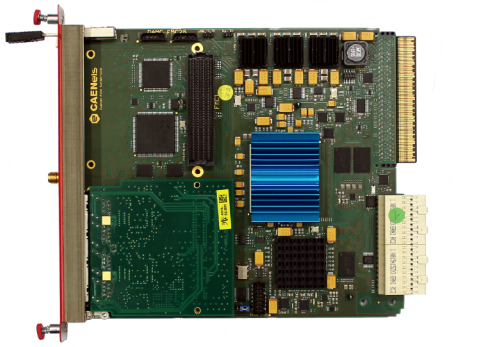

Figure A.4: FMC25 Computation AMC

Table A.4: Technical specification FMC25

Description	Value	Unit
Max. Algorithm clock	50	MHz

AD84 – ADC and DAC Combination

For this reason, the *AD84* RTM, shown in Fig. A.5, is used. Technical data are given in Table A.5.

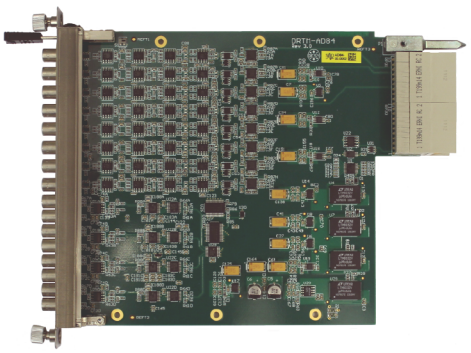

Figure A.5: AD84 RTM

Table A.5: Technical specification AD84

Description	Value	Unit
ADC Channel	8	
ADC Range	≈ 2.4	V
ADC Resolution	16	bit
ADC Frequency	2	MHz
DAC Channel	4	
DAC Range	≈ 1	V
DAC Resolution	16	bit
DAC Frequency	1	MHz

FMC20 PZT4 – Piezo- and Motor-Driver Combination

To drive the piezoelectric actuators, high voltages are required which the DAC outputs of the previous boards do not offer. For this reason, a power amplifier, the *PZT4*, shown in Fig. A.6, is needed. This board is connected to an *FMC20* AMC which receives control data via an LLL and pipes them through the *PTZ4*. Important properties of this board are given in Table A.6.

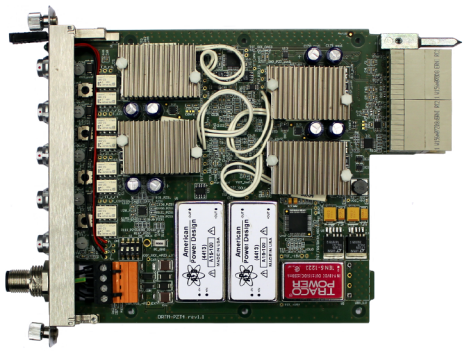

Figure A.6: PZT4 Piezo Amplifier Board

Table A.6: Technical specification PZT4

Description	Value	Unit
Output Channel	2 or 4	
Output Range	±80	V
Output Resolution	18	bit
Output Frequency	0.5 or 1	MHz
Voltage Sensor Resolution	16	bit
Voltage Sensor Frequency	≈ 110	kHz
Current Sensor Resolution	16	bit
Current Sensor Frequency	≈ 110	kHz

CPU and X2 Timer

This boards holds the operating system and runs the server which supervises and control the applications which run on the computation boards. The *X2-Timer* board receives the machine trigger which can used to synchronize the data acquisition with respect to the bunches in the accelerator.

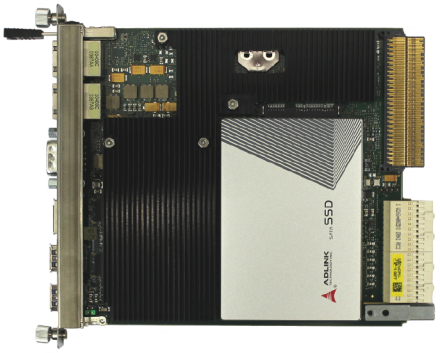

Figure A.7: CPU Board

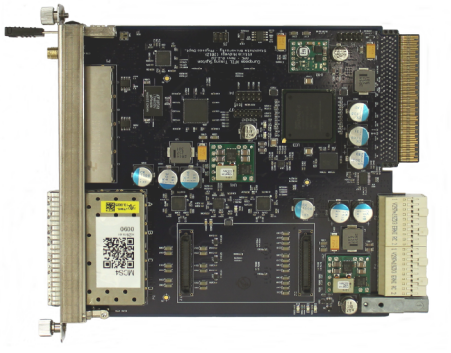

Figure A.8: X2 Timer Board

B Firmware Overview

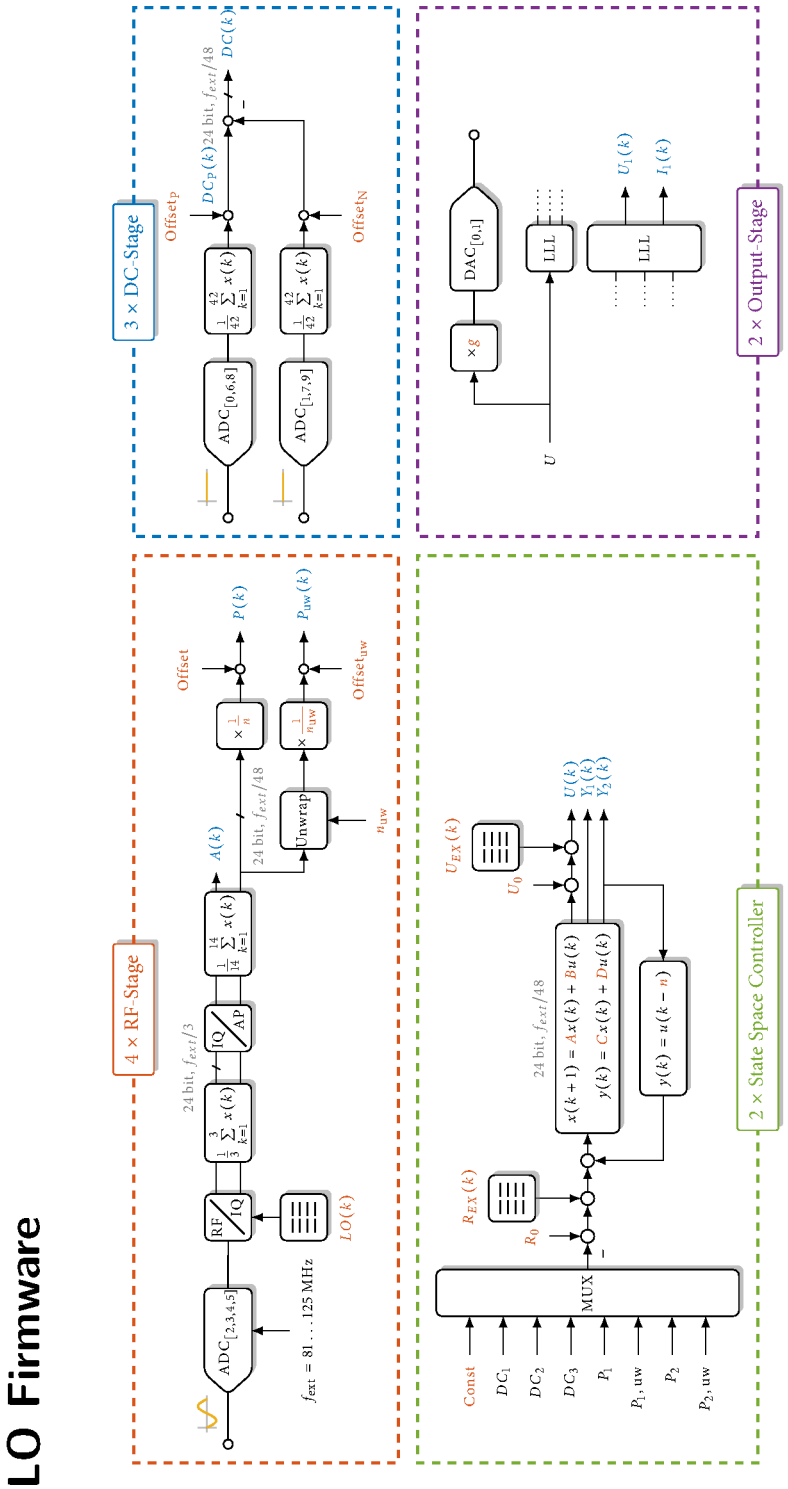

Figure B.1: Simplified block diagram of the MLO firmware.

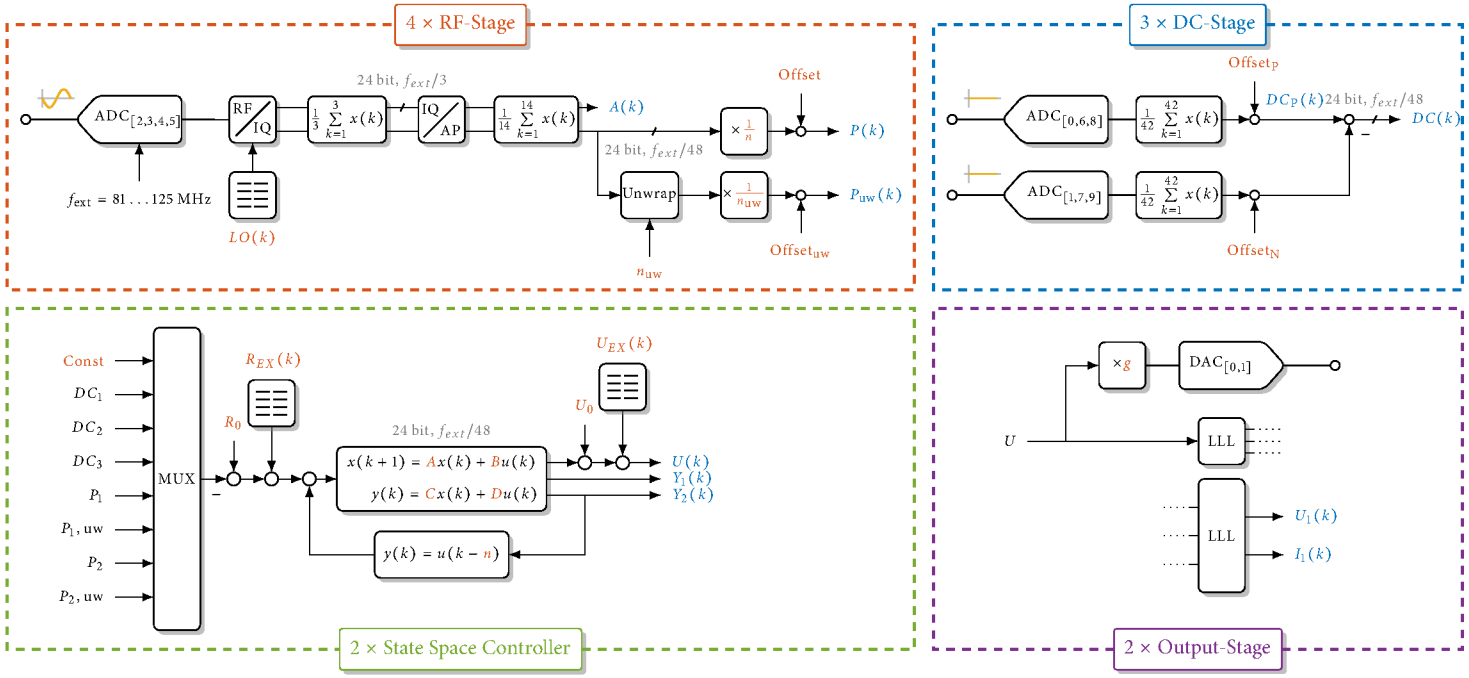

Figure B.2: Simplified block diagram of the MLO firmware.

List of Abbreviations

ADC	Analog to Digital Converter
AMC	Advanced Mezzanine Card
AWGN	Additive White Gaussian Noise
BAM	Bunch Arrival Time Monitor
BLWN	Band Limited White Noise
DAC	Digital to Analog Converter
DCF	Dispersion Compensating Fiber
DESY	Deutsches Elektronen Synchrotron
DSP	Digital Signal Processor
EDFA	Erbium-Doped Fiber Amplifier
EKF	Extended Kalman Filter
FLASH	Free Electron Laser Hamburg
FPGA	Field-Programmable Gate Array
FWHM	Full Width Half Maximum
GOF	Gang of Four
IL	Injector Laser
L2L	Laser to Laser
L2RF	Laser to Radio Frequency
LbSync	Laser-based Synchronization
LDD	Laser Diode Driver
LHP	Left Half Plane
LLL	Low Latency Link

LLRF	Low-Level Radio Frequency
LQG	Linear Quadratic Gaussian
LQR	Linear Quadratic Regulator
LSU	Link Stabilizing Unit
LTI	Linear Time Invariant
MDL	Motorized Delay Line
MicroTCA.4	Micro Telecommunications Computing Architecture enhancements for rear I/O and precision timing
MLO	Master Laser Oscillator
MO	Master Oscillator
OXC	Optical Cross Correlator
PCIe	Peripheral Component Interconnect Express
PI	Proportional-Integral
PLL	Phase Locked Loop
PPL	Pump Probe Laser
PRB	Pseudo Random Binary
REFM-OPT	Optical Reference Module
RHP	Right Half Plane
RMS	Root Mean Square
RTM	Rear Transition Module
SSA	Signal Source Analyzer
VHDL	VHSIC Hardware Description Language
VME	Versa Module Europa
VSA	Vector Signal Analyzer
XFEL	European X-ray Free Electron Laser
ZOH	Zero Order Hold

Bibliography

[Abr02] Abramovitch, D. Y.: Phase-Locked Loops: A Control Centric Tutorial. In: *Proceedings of the 2002 American Control Conference*. Anchorage, Alaska, 2002

[Abr15] Abramovitch, D. Y.: The Multinotch, Part I: A Low Latency, High Numerical Fidelity Filter. In: *Proceedings of American Control Conference*. Chicago, IL, 2015

[Alt+07] Altarelli, M. et al.: *The European X-Ray Free-Electron Laser Technical design report*. Technical report. Hamburg, Germany: Deutsches Elektronen-Synchrotron, 2007

[ÅM08] Åström, K. J. ; Murray, R. M.: *Feedback Systems: An Introduction for Scientists and Engineers*. Princeton University Press, 2008. URL: http://press.princeton.edu/titles/8701.htm

[Bal+04] Balas, G. J. et al.: Next generation of tools for robust control. In: *Proceedings of American Control Conference*. Volume 6. 2004, pages 5612–5615

[Bay99] Bay, J. S.: *Fundamentals of Linear State Space System*. Electrical Engineering Series. McGraw-Hill, 1999

[Ben48] Bennett, W. R.: Spectra of Quantized Signals. In: *Bell System Technical Journal* (1948)

[Boc12] Bock, M. K.: *Measuring the Electron Bunch Timing with Femtosecond Resolution at FLASH*. PhD thesis. University of Hambug, 2012

[Bom99] Bomar, B. W.: Digital Signal Processing Handbook. In: CRC Press LLC, 1999. Chapter Finite Wordlength Effects

[CC09] Chui, C. K. ; Chen, G.: *Kalman Filtering with Real-Time Application*. Springer-Verlag Berlin Heidelberg, 2009. DOI: 10.1007/978-3-540-87849-0

[DFT92] Doyle, J. C. ; Francis, B. A. ; Tannenbaum, A. R.: *Feedback Control Theory*. Macmillan Publishing Company, 1992

[Dyk28] Dyke, K. S. van: The Piezo-Electric Resonator and Its Equivalent Network. In: IEEE (editor): *Proceedings of the Institute of Radio Engineers*. Volume 16 6. June 1928. DOI: 10.1109/JRPROC.1928.221466

[ESQ11] Estrada, J. C. ; Servin, M. ; Quiroga, J. A.: Noise robust linear dynamic System for phase unwrapping and smoothing. In: *Optics Express* 19 (2011) Nr. 6

[Fel+15] Felber, M. et al.: Implementation of MTCA.4-based Controls for the Pulsed Optical Synchronization Systems at DESY. In: *Proc. 37th International Free Electron Laser Conference*. 2015

[Fel+14] Felber, M. et al.: New MTCA.4-based hardware developments for the control of the optical synchronization systems at DESY. In: *Proc. 3rd International Beam Instrumentation Conference*. 2014

[FPE14] Franklin, G. F. ; Powel, J. D. ; Emami-Naeini, A.: *Feedback Control of Dynamic Systems*. Seventh Edition. Harlow Pearson Education Limited, 2014

[Gar05] Gardner, F. M.: *Phaselock Techniques*. Wiley, 2005

[Gaw04] Gawronski, W. K. (editor): *Advanced Structural Dynamics and Active Control of Structures*. Mechanical Engineering Series. Springer New York, 2004. doi: 10.1007/978-0-387-72133-0

[Gün+11] Günther, C. M. et al.: Sequential femtosecond X-ray imaging. In: *Nature Photonics 5*. 2011, pages 99–102

[Heu+14a] Heuer, M. et al.: Comparison of Feedback Controller for Link Stabilizing Units of the Laser-Based Synchronization System used at the European XFEL. In: *Proc. 3rd International Beam Instrumentation Conference*. 2014

[Heu+15a] Heuer, M. et al.: Developments of XFEL Master Laser Oscillator Controls based on MicroTCA.4. In: *5th Mini-Workshop on Longitudinal Diagnostics for FELs*. 2015

[Heu+16] Heuer, M. et al.: Feedback Control for Optical Synchronization. In: *4th ARD ST3 Workshop - Matter and Technology*. 2016. url: https://indico.desy.de/getFile.py/access?contribId=58&sessionId=8&resId=0&materialId=poster&confId=14765

[Heu+14b] Heuer, M. et al.: Modeling of the Master Laser Oscillator Phase Noise for the European XFEL using Fractional Order Systems. In: *Proc. 19th IFAC World Congr.* 2014

[Heu+15b] Heuer, M. et al.: Plant Modeling for Observer-Based Control of the Link Stabilizing Units at the European X-ray Free-Electron Laser. In: *Proc. 2015 American Control Conference*. 2015

[HB06] Hogan, N. ; Breedveld, P. C.: Mechatronics: An Introduction. In: Bishop, R. H. (editor). CRC, 2006. Chapter The Physical Basis of Analogies in Physical System Models

[Hor96] Horenstein, M. N.: *Microelectronic Circuits and Devices*. Second. Prentice Hall, 1996

[HSO11] Hussain, Z. M. ; Sadik, A. Z. ; O'Shea, P.: *Digital Signal Processing - An Introduction with MATLAB and Applications*. Springer-Verlag Berlin Heidelberg, 2011. doi: 10.1007/978-3-642-15591-8

[Jan+06] Janaideh, M. A. et al.: Generalized Prandtl-Ishlinskii Hysteresis Model: Hysteresis Modeling and Its Inverse for Compensation in Smart Actuators. In: *Proceedings of the 47th IEEE Conference on Decision and Control*. 2006

[Jan+14] Janas, E. et al.: Design and Integration of the Optical Reference Module at 1.3 GHz for FLASH and the European XFEL. In: *Proceedings of IPAC 2014*. Dresden, Germany, 2014

[Kil+15] Killenberg, M. et al.: Drivers and Software for MicroTCA.4. In: *Proceedings of ICALEPCS 2015*. 2015

[Kil+14] Killenberg, M. et al.: Update on the MicroTCA.4 User Tool Kit (MTCA4U). In: *Proc. 3rd MicroTCA workshop for industry and research*. 2014

[KK10] Kim, J. ; Kärtner, F. X.: Attosecond-precision ultrafast photonics. In: *Laser & Photonics Reviews* 4 (2010) Nr. 3, pages 432–456. doi: 10.1002/lpor.200910003

[Kim+04] Kim, J. et al.: Large-Scale Timing Distribution and RF-Synchronization for FEL Facilities. In: *Proceedings of FEL Conference*. Triest, Italy, 2004

[Kim+07] Kim, J. et al.: Long-term femtosecond timing link stabilization using a single-crystal balanced cross correlator. In: *Optics Letters* 32 (May 2007) Nr. 9, pages 1044–1046. doi: 10.1364/OL.32.001044

[KK01] Krejci, P. ; Kuhnen, K.: Inverse control of systems with hysteresis and creep. In: *IEE Proceedings of Control Theory and Applications*. Volume 148. 3. IET, 2001. doi: 10.1049/ip-cta:20010375

[LZ06] Landau, I. D. ; Zito, G.: *Digital Control Systems*. 1st edition. Springer-Verlag London, 2006. doi: 10.1007/978-1-84628-056-6

[Lau+87] Laub, A. J. et al.: Computation of System Balancing Transformations and Other Applications of Simultaneous Diagonalization Alotithms. In: *IEEE Transactions on Automatic Control*. Volume AC-32 2. 1987

[Lju15] Ljung, L.: System Identification: An Overview. Englishin: Baillieul, John ; Samad, Tariq (editors): *Encyclopedia of Systems and Control*. Springer London, 2015, pages 1443–1458. isbn: 978-1-4471-5057-2. doi: 10.1007/978-1-4471-5058-9_100. url: http://dx.doi.org/10.1007/978-1-4471-5058-9_100

[Lju99] Ljung, L.: *System Identification - Theory for the User*. Upper Saddle River, NJ, USA: Prentice-Hall, 1999. url: http://liu.diva-portal.org/smash/record.jsf?pid=diva2:562142

[LE11] Lurie, B. ; Enright, P.: *Classical Feedback Control: With MATLAB and Simulink, Second Edition*. CRC Press, 2011

[Man15] Manthey, F.: *Design and Implementation of a Minimum Variance Controller of the Master Laser Oscillator of the European X-ray Free Electron Laser*. 2015

[MP05] Mirkin, L. ; Palmor, Z. J.: Control Issues in Systems with Loop Delays. In: Hristu-Varsakelis, D. ; Levine, W. S. (editors): *Handbook of Networked and Embedded Control Systems*. Birkhäuser, 2005, pages 627–648

[MR76] Mullis, C. T. ; Roberts, R. A.: Synthesis of Minimum Roundoff Noise Fixed Point Digital Filters. In: *IEEE Transactions on Circuits and Sytems*. Volume CAS-23. 9. 1976

[NC07] Normey-Rico, J. E. ; Camacho, E. F.: *Control of Dead-time Processes*. Springer London, 2007. doi: 10.1007/978-1-84628-829-6

[Pas08] Paschotta, R.: *Encyclopedia of Laser Physics and Technology*. 1st edition. Wiley, 2008

[PL12] Petersson, D. ; Löfberg, J.: Model Reduction using a Frequency-Limited H2-Cost. In: *ArXiv e-prints* (2012). url: http://arxiv.org/abs/1212.1603

[Pfe14] Pfeiffer, S.: *Symmetric Grey Box Identification and Distributed Beam-Based Controller Design for Free-Electron Lasers*. PhD thesis. Hamburg University of Technology, 2014. doi: http://dx.doi.org/10.15480/882.1191

[Pfe+12] Pfeiffer, S. et al.: Fast Feedback Strategies for Longitudinal Beam Stabilization. In: *Proceedings of IPAC 2012*. New Orleans, Lousiana, 2012

[Poh95] Pohlmann, K. C.: *Principles of Digital Audio*. Edited by 3. McGraw-Hill, 1995

[Pre+14] Predki, P. et al.: Rapid FPGA development framework using a custom Simulink library for MTCA.4 modules. In: *Proc. 19th Real-Time conference*. 2014

[Pre+15] Predki, P. et al.: Rapid-X - An FPGA Development Toolset Using a Custom Simulink Library for MTCA.4 Modules. In: *IEEE Transactions on Nuclear Science* (2015)

[Pre06] Preumont, A.: *Mechatronics: Dynamics of Electromechanical and Piezoelectric Systems*. 1st edition. Volume 136. Solid Mechanics and Its Applications. Springer Netherlands, 2006. doi: 10.1007/1-4020-4696-0

[Prz+14] Przygoda, K. et al.: MTCA.4 Module for Cavity and Laser Piezo Operation. In: *Proc. 5th International Particle Accelerator Conference*. 2014

[Şaf+15] Şafak, K. et al.: All fiber-coupled, long-term stable timing distribution for free-electron lasers with few-femtosecond jitter. In: *Structural Dynamics* 2 (2015) Nr. 4. doi: http://dx.doi.org/10.1063/1.4922747

[Sch10] Schmidt, C.: *RF System Modeling and Controller Design for the European XFEL*. PhD thesis. Hamburg University of Technology, 2010

[Sch11] Schulz, S.: *Implementation of the Laser-Based Femtosecond Precision Synchronization System at FLASH*. PhD thesis. University of Hambug, 2011

[Sch+13] Schulz, S. et al.: Past, Present and Future Aspects of Laser-Based Synchronization at FLASH. In: *Proc. 2nd International Beam Instrumentation Conference*. Oxford, UK, Sept. 2013, pages 753–756. URL: http://accelconf.web.cern.ch/AccelConf/IBIC2013/papers/wepc32.pdf

[SP01] Skogestad, S. ; Postlethwaite, I.: *Multivariable Feedback Control: Analysis and Design*. Chichester, U.K.: Wiley, 2001

[Smi59] Smith, O. J. M.: A controller to overcome dead time. In: *ISA Journal* 6 (1959), pages 28–33

[Smi99] Smith, S. W.: *The Scientist and Engineer's Guide to Digital Signal Processing*. Second. San Diego, CA, USA: California Technical Publishing, 1999. URL: dspguide.com

[TIA98] Takatsu, H. ; Itoh, T. ; Araki, M.: Future needs for the control theory in industries—report and topics of the control technology survey in Japanese industry. In: *Journal of Process Control* 8 (1998) Nr. 5-6. DOI: http://dx.doi.org/10.1016/S0959-1524(98)00019-5

[VPA13] Vuillemin, P. ; Poussot-Vassal, C. ; Alazard, D.: A Spectral Expression for the Frequency-Limited H2-norm. In: *ArXiv e-prints* (2013). URL: http://arxiv.org/abs/1211.1858

[WM05] Wang, F. ; Mechefske, C. K.: Modal analysis and testing of a thin-walled gradient coil cylinder model. In: *Concepts in Magnetic Resonance Part B: Magnetic Resonance Engineering* 27B (2005) Nr. 1, pages 34–50. ISSN: 1552-504X. DOI: 10.1002/cmr.b.20045. URL: http://dx.doi.org/10.1002/cmr.b.20045

[Wid61] Widrow, B.: Statistical analysis of amplitude-quantized sampled-data systems. In: *Transactions of the American Institute of Electrical Engineers, Part II: Applications and Industry* 79 (1961) Nr. 6, pages 555–568. DOI: 10.1109/TAI.1961.6371702

[Win08] Winter, A.: *Fiber Laser Master Oscillators for Optical Synchronization Systems*. PhD thesis. University of Hambug, 2008

[Zem+14] Zembala, L. et al.: Master Oscillator for the European XFEL. In: *Proceedings of IPAC 2014*. 2014

[ZDG96] Zhou, K. ; Doyle, J. C. ; Glover, K.: *Robust and Optimal Control*. Prentice Hall, 1996

[Zöl08] Zölzer, U.: *Digital Audio Signal Processing*. Edited by 2nd. Wiley, 2008

Application Notes, Data Sheets and Norms

[DM] DESY, Deutsches Elektronen-Synchrotron: *GISFMS*. Accessed: 01.08.2016. URL: http://maps.desy.de

[IEEE1139] IEEE Standard Definitions of Physical Quantities for Fundamental Frequency and Time Metrology - Random Instabilities. In: *IEEE Std 1139-2008* (1999), pages c1–35. DOI: 10.1109/IEEESTD.2008.4797525

[MT017] Analog Devices: *Oversampling Interpolating DACs*. Tutorial MT-017. 2011. URL: http://www.analog.com/media/en/training-seminars/tutorials/MT-017.pdf

[ORIG15] Onefive GmbH: *Origami-15 – Ultra-Low-Noise Soliton Femtosecond Laser Module*. Data Sheet. URL: http://www.onefive.com/ds/Datasheet%20Origami%20LP.pdf

[PI2014] PI Ceramic GmbH: *Piezoelectric Actuators*. 2014

[PZ2] Optiphase: *PZ2 Mid-range Fiber Stretcher*. Data Sheet. URL: http://www.optiphase.com/data_sheets/PZ2%20Data%20Sheet%20Rev%20F.pdf

[PZT4] eicSys GmbH: *ERTM-PZT4, 4 Channel Piezo Driver*. Data Sheet. URL: http://www.eicsys.de/index_htm_files/ERTM-PZT4.pdf

[SLAN118] Silicon Laboratories Inc.: *Improving ADC Resolution by Oversampling and Averaging*. Application Note 118. 2013. URL: https://www.silabs.com/Support%20Documents/TechnicalDocs/an118.pdf

[SLAN256] Silicon Laboratories Inc.: *Integrated Phase Noise*. Application Note 256. 2011. URL: https://www.silabs.com/Support%20Documents/TechnicalDocs/an256.pdf